

AD 667228

54

Bulletin 37  
Part 3  
(of 7 Parts)

(1)

# THE SHOCK AND VIBRATION BULLETIN

JANUARY 1968

A Publication of  
THE SHOCK AND VIBRATION  
INFORMATION CENTER  
Naval Research Laboratory, Washington, D.C.



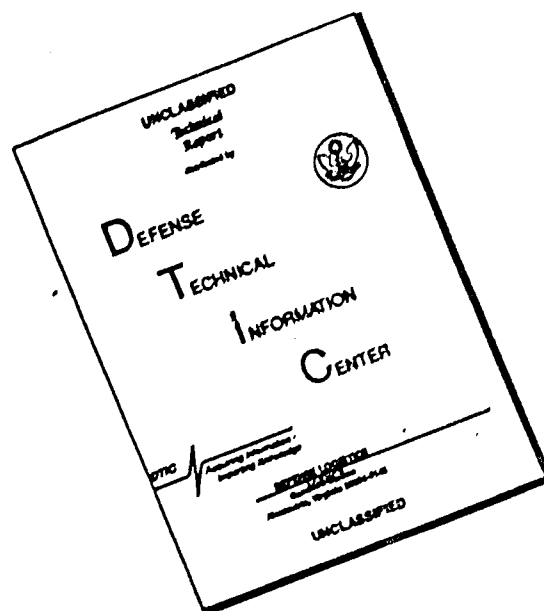
Office of  
The Director of Defense  
Research and Engineering

OFFICE OF THE DIRECTOR OF DEFENSE RESEARCH AND ENGINEERING  
JAN 19 1968

This document has been approved for public release and sale; its distribution is unlimited

234

# DISCLAIMER NOTICE



THIS DOCUMENT IS BEST QUALITY AVAILABLE. THE COPY FURNISHED TO DTIC CONTAINED A SIGNIFICANT NUMBER OF PAGES WHICH DO NOT REPRODUCE LEGIBLY.

## **SYMPOSIUM MANAGEMENT**

### **THE SHOCK AND VIBRATION INFORMATION CENTER**

William W. Mutch, Director  
Henry C. Pusey, Coordinator  
Rudolph H. Volin, Coordinator  
Katherine G. Jahnel, Administrative Secretary

#### **37th Program Committee**

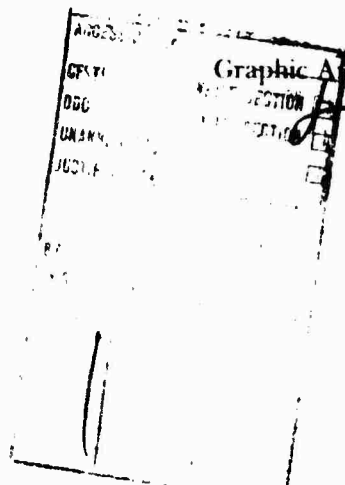
David Askin, U.S. Army Frankford Arsenal  
Jerry Sullivan, Naval Ship Systems Command Hdq.  
Robert F. Wilkus, Systems Engineering Group, W-PAFB  
Dennis J. Martin, NASA Langley Research Center

#### **Navy Liaison**

Naval Training Device Center

William Powell  
Allan Collier

#### **Bulletin Production**



Graphic Arts Branch, Technical Information Division,  
Naval Research Laboratory

**Bulletin 37**  
**Part 3**  
**(of 7 Parts)**

# **THE SHOCK AND VIBRATION BULLETIN**

**JANUARY 1968**

**A Publication of  
THE SHOCK AND VIBRATION  
INFORMATION CENTER  
Naval Research Laboratory, Washington, D.C.**

The 37th Symposium on Shock and Vibration was held in Orlando, Florida, on 24-26 October 1967. The U.S. Navy was host.

**Office of  
The Director of Defense  
Research and Engineering**



# CONTENTS

## PART 3

### Vibration Testing

|   |     |
|---|-----|
| ADVANCES IN NUMEROLOGY.....   | 1   |
| J. P. Salter, Royal Armaments Research and Development Establishment, Fort Halstead, Sevenoaks, Kent, England                           |     |
| INTERNAL VIBRATION OF ELECTRONIC EQUIPMENT RESULTING FROM ACOUSTIC SHAKER INDUCED EXCITATION.....                                       | 7   |
| A. D. Houston, Lockheed Missile & Space Company, Sunnyvale, California  |     |
| RANDOM-VIBRATION RESPONSE DATA FOR ORBITING GEOPHYSICAL OBSERVATORY: FLIGHT, ACOUSTIC, AND VIBRATION TEST.....                          | 21  |
| W. G. Elsen, NASA Goddard Space Flight Center, Greenbelt, Maryland  |     |
| RANDOM-VIBRATION TEST LEVEL CONTROL USING INPUT AND TEST ITEM RESPONSE SPECTRA.....   | 47  |
| A. J. Curtis and J. G. Herrera, Hughes Aircraft Company, Culver City, California  |     |
| RANDOM-FORCE VIBRATION TESTING.....   | 61  |
| J. V. Otts and N. F. Hunter, Jr., Sandia Corporation, Albuquerque, New Mexico   |     |
| CONTROL POINT AVERAGING FOR LARGE SPECIMEN VIBRATION TESTS.....   | 75  |
| H. R. Berkman, Litton Systems, Inc., Van Nuys, California   |     |
| VIBRATION METHODS FOR MULTIPLE RANDOM EXCITATION.....   | 89  |
| W. E. Noonan, McDonnell Company, St. Louis, Missouri  |     |
| DYNAMIC TESTING OF FULL-SCALE SATURN LAUNCH VEHICLES.....   | 99  |
| B. R. Jacobs, Northrop Northronics, Huntsville, Alabama   |     |
| BUFFET RESPONSE MEASUREMENTS OF A SEVEN PERCENT AEROELASTICALLY SCALED MODEL OF VARIOUS TITAN III CONFIGURATIONS.....                   | 121 |
| J. T. Uchiyama and F. W. Peters, Martin-Marietta Corporation, Denver, Colorado  |     |
| HIGH-FORCE VIBRATION TESTING OF THE SATURN S-IVB STAGE.....   | 137 |
| L. G. Smith, McDonnell Douglas Corporation, Huntington Beach, California  |     |
| SIMPLIFIED METHOD OF CONDUCTING A DUAL RANDOM-VIBRATION INTEGRATED SYSTEM TEST.....   | 151 |
| J. G. Colt, Radio Corporation of America, Burlington, Massachusetts   |     |
| CONTROL STABILIZATION FOR MULTIPLE SHAKER TESTS.....  | 155 |
| N. F. Hunter, Jr., Sandia Corporation, Albuquerque, New Mexico, and J. G. Helmuth, Chadwick-Helmuth Company, Inc., Monrovia, California |     |
| THE SHIMMING ISOLATION.....   | 163 |
| L. H. Weinstein, Jr., Lord Manufacturing Company, Erie, Pennsylvania  |     |

### Test Facilities

|  |     |
|--|-----|
| ADVANCED COMBINED ENVIRONMENTAL TEST FACILITY.....                                       | 175 |
| E. J. Kirchman and C. J. Arcilesi, NASA Goddard Space Flight Center, Greenbelt, Maryland |     |
| DEVELOPMENT OF SIMULATED AIRCRAFT DELIVERY USING A ROCKET SLED.....                      | 193 |
| W. R. Kampfe and K. M. Timmerman, Sandia Corporation, Albuquerque, New Mexico            |     |
| AERODYNAMIC NOISE INVESTIGATION IN A SHORT-DURATION SHOCK TUNNEL.....                    | 203 |
| D. H. Ross, Aerospace Corporation, El Segundo, California                                |     |
| IMPACT TESTING WITH A FOUR-INCH AIR GUN AND LEAD TARGETS.....                            | 219 |
| H. J. Davis, Harry Diamond Laboratories, Washington, D. C.                               |     |

PAPERS APPEARING IN PART 1  
Part 1 - Classified  
(Titles Unclassified)

RECENT WORK ON SHOCK AT N. C. R. E.

A. M. MacIntosh, Naval Construction Research Establishment, Dunfermline, Fife, Scotland

STATE OF SHOCK IN THE NAVY, 1967

H. L. Rich, Naval Ship Research and Development Center, Washington, D. C.

NAVY DYNAMIC DESIGN ANALYSIS METHOD - PANEL SESSION

SHOCK HARDENING RIVERINE WARFARE CRAFT FOR VIETNAM

O. H. Porter and F. Weinberger, Naval Ship Research and Development Center, Washington, D. C.

SHOCK TESTING OF SONAR TRANSDUCERS -- A STATUS REPORT

G. M. Mayer and C. D. Johnson, Navy Underwater Sound Laboratory, New London, Connecticut

AN EXPLOSION SHOCK-TESTING METHOD FOR SHIPBOARD EQUIPMENT

R. R. Higginbotham, Naval Ship Research and Development Center, Portsmouth, Virginia

RIGID BODY RESPONSE OF NAVAL SURFACE VESSELS TO AIR BLAST

J. T. Irick, AVCO Corporation, Lowell, Massachusetts, S. Silverman and W. E. Baker, Southwest Research Institute, San Antonio, Texas

REACTION OF MILD STEEL TARGETS TO EXPLODING MUNITIONS

J. W. Apgar, Ballistic Research Laboratories, Aberdeen Proving Ground, Maryland

RESPONSE OF A MISSILE STRUCTURE UNDER HIGH VELOCITY IMPACT

C. Riparbelli, General Dynamics/Pomona, Pomona, California

AIM4D/F4 CAPTIVE-FLIGHT VIBRATION LOADS AND ENVIRONMENTAL MEASUREMENTS PROGRAM

C. D. Knauer, Jr. and P. E. McHorney, Hughes Aircraft Company, El Segundo, California

PAPERS APPEARING IN PART 2

Instrumentation and Analysis

PORTABLE LASER INSTRUMENT FOR VIBRATION ANALYSIS AND TRANSDUCER CALIBRATION

G. A. Massey and R. R. Carter, Sylvania Electronic Systems, Mountain View, California

HIGH-FREQUENCY MICROPHONE CALIBRATION USING A SUPERSONIC FREE-FLIGHT RANGE

C. D. Hayes, Jet Propulsion Laboratory, Pasadena, California, and R. C. Binder, University of Southern California, Los Angeles, California

METHOD OF MEASURING VIBRATORY DISPLACEMENTS IN TERMS OF A LIGHT WAVELENGTH

J. L. Goldberg, National Standards Laboratory, Sydney, Australia

CALIBRATION OF ACCELEROMETERS BY IMPULSE EXCITATION AND FOURIER INTEGRAL TRANSFORM TECHNIQUES

J. D. Favour, The Boeing Company, Seattle, Washington

BIDIRECTIONAL SHOCK AND HIGH-IMPACT EFFECTS ON SHOCK TRANSDUCERS

V. F. DeVost and P. S. Hughes, Naval Ordnance Laboratory, Silver Spring, Maryland

INFLUENCE OF FIXTURE STRESS CONCENTRATIONS ON RING ACCELEROMETERS

J. A. Nagy and C. E. Henley, Jr., NASA Goddard Space Flight Center, Greenbelt, Maryland

SONAR TRANSDUCER VIBRATION REQUIREMENTS AND MEASUREMENT TECHNIQUES

G. M. Mayer and E. G. Marsh, Navy Underwater Sound Laboratory, New London, Connecticut

AUTOMATED VIBRATION ANALYSIS

R. J. Pabich and W. H. Sellers, Raytheon Company, Bedford, Massachusetts

A COMPACT, LOW-COST SHOCK-SPECTRUM ANALYZER

W. W. Mebane, Naval Ordnance Laboratory, Silver Spring, Maryland

DYNAMIC PHASE PLOTTING

T. E. Smart, Sandia Corporation, Albuquerque, New Mexico

RANDOM VIBRATION-INDUCED ERRORS IN A MISSILE CAUSED BY NONLINEAR INERTIAL ACCELEROMETERS

N. A. Leifer, Bell Telephone Laboratories, Inc., Whippany, New Jersey

VIBRATION DISTRIBUTIONS IN MULTIPANEL STRUCTURES: COMPARISON OF MEASUREMENTS WITH STATISTICAL ENERGY PREDICTIONS

E. E. Ungar and N. Koronaios, Bolt Beranek and Newman Inc., Cambridge, Massachusetts

CONSTANT BANDWIDTH FM DATA SYSTEM DESIGNED FOR SATURN S-1V/B/V VIBRATION TESTS

D. F. Redford, Thiokol Chemical Corporation, Brigham City, Utah

DYNAMICS PORTION OF GEMINI AGENA TARGET VEHICLE ENGINE MODIFICATION AND TEST PROGRAM (PROJECT SURE FIRE)

N. Angelopoulos, Lockheed Missiles & Space Company, Sunnyvale, California

DYNAMIC ANALYSIS OF COMPLEX STRUCTURES

M. D. Benton, G. K. Hobbs, Hughes Aircraft Company, El Segundo, California, and J. R. Dickerson, University of Texas, Austin, Texas

PAPERS APPEARING IN PART 4

Shock Analysis and Simulation

MEASUREMENT AND ANALYSIS OF SPACECRAFT SEPARATION TRANSIENT RESPONSE FOR MARINER-TYPE SPACECRAFT

P. Barnett, Jet Propulsion Laboratory, Pasadena, California

MECHANICAL SHOCK OF HONEYCOMB STRUCTURE FROM PYROTECHNIC SEPARATION

J. R. Olsen, J. R. West, Jr., H. Hirschblau, North American Rockwell Corporation, Los Angeles, California, C. D. Knauer, Jr., and P. E. McHerney, Jr., Hughes Aircraft Company, El Segundo, California

A SIMPLE STRENGTH CONCEPT FOR DEFINING PRACTICAL HIGH-FREQUENCY LIMITS OF SHOCK SPECTRUM ANALYSIS

M. Gertel and R. Holland, Allied Research Associates, Concord, Massachusetts

TRANSIENT VIBRATION SIMULATION

T. E. Fitzgerald and L. C. Kula, The Boeing Company, New Orleans, Louisiana

PREDICTING MECHANICAL SHOCK TRANSMISSION

J. E. Manning and K. Lee, Bolt Beranek and Newman Inc., Cambridge, Massachusetts

SHOCK DAMAGE MECHANISM OF A SIMPLE STRUCTURE

L. T. Butt, Naval Ship Research and Development Center, Portsmouth, Virginia

GENERAL MOTORS ENERGY-ABSORBING STEERING COLUMN AS A COMPONENT OF SHIPBOARD PERSONNEL PROTECTION

J. T. Hawkins and A. E. Hirsch, Naval Ship Research and Development Center, Washington, D. C.

HEAVY WEIGHT SHOCK TEST FIXTURES: DESIGN AND RESULTS

C. G. Schrader, San Francisco Bay Naval Shipyard, San Francisco, California

DERIVATION AND IMPLICATIONS OF THE NAVY SHOCK ANALYSIS METHOD

F. J. Heymann, Westinghouse Electric Corporation, Lester, Pennsylvania

DYNAMIC ANALYSIS OF A TYPICAL ELECTRONIC EQUIPMENT CABINET SUBJECTED TO NUCLEAR-WEAPON-INDUCED SHOCK

J. H. Putukian, Kaman Avidyne, Burlington, Massachusetts

DEVELOPMENT OF A ZERO-G COAST PHASE AIR GUN

S. Rodkin, General Electric Company, Philadelphia, Pennsylvania

DEVELOPMENT OF A MISSILE LAUNCH SHOCK TEST FACILITY FOR SHILLELAGH

R. W. Stevens, Martin-Marietta Corporation, Orlando, Florida

USE OF EXPLODING WIRE APPARATUS FOR LABORATORY SIMULATION OF SHOCK WAVES  
F. B. Safford, Mechanics Research Inc., El Segundo, California, and R. C. Binder, University of Southern California, Los Angeles, California

**NIKE-X SHOCK TUBE FACILITY**

R. G. Donaghy and J. J. Healy, Office of the Chief of Engineers, Department of the Army, Washington, D. C.

**DESIGN AND PERFORMANCE OF DUAL MODE SHOCK MACHINE**

W. D. Everett, Naval Missile Center, Point Mugu, California

Air Blast and Ground Shock

**INFLUENCE OF SHIP MOBILITY ON INTERNAL FORCES PRODUCED BY BLAST**

A. Chajes, F. J. Dzialo, and M. P. White, Department of Civil Engineering, University of Massachusetts, Amherst, Massachusetts

**DYNAMIC BEHAVIOR OF SHIPBOARD ANTENNA MASTS SUBJECTED TO BLAST-GENERATED OVERPRESSURES**

F. A. Britt and R. H. Anderson, Mechanics Research, Inc., El Segundo, California

**\*HARDENED ANTENNA TECHNOLOGY**

D. A. Benson, A. F. Gurdo, R. W. Mair and D. J. Waters, Rome Air Development Center, Griffiss AFB, New York

**ABSOLUTE UPPER AND LOWER BOUNDS FOR THE CRITICAL BLAST LOADING ENVIRONMENT OF TARGET ELEMENTS AND SYSTEMS**

E. Sevin and W. D. Pilkey, IIT Research Institute, Chicago, Illinois

**ELASTIC-PLASTIC COLLAPSE OF STRUCTURES SUBJECTED TO A BLAST PULSE**

W. B. Murfin, Sandia Corporation, Albuquerque, New Mexico

**INTERNAL LOADING OF STRUCTURES BY BLAST WAVES**

J. F. Melichar, Ballistic Research Laboratories, Aberdeen Proving Ground, Maryland

**EFFECTS OF SLIDING ON BLAST LOADS REQUIRED TO OVERTURN STRUCTURES**

C. E. Gebhart, IIT Research Institute, Chicago, Illinois

**USE OF DETONABLE GAS EXPLOSIONS FOR BLAST AND SHOCK STUDIES**

M. R. Johnson and M. J. Balcerzak, General American Research Division, Niles, Illinois

**INCORPORATION OF SHOCK PROTECTION IN EXISTING ABOVEGROUND CYLINDRICAL STRUCTURES SUBJECTED TO NUCLEAR BLAST**

E. Cohen, S. Weissman and L. Sanchez, Ammann and Whitney, New York, New York

**PAPERS APPEARING IN PART 5**

Large Vibro-Acoustic Test Facilities

**VIBROACOUSTIC ENVIRONMENTAL SIMULATION FOR AEROSPACE VEHICLES**

K. McK. Eldred, Wyle Laboratories, El Segundo, California

**\*RTD SONIC FATIGUE FACILITY, DESIGN AND PERFORMANCE CHARACTERISTICS**

A. W. Kolb and H. A. Magrath, Air Force Flight Dynamics Laboratory, Wright-Patterson AFB, Ohio

**OPERATIONAL CHARACTERISTICS OF A 100,000 CUBIC FOOT ACOUSTIC REVERBERATION CHAMBER**

F. M. Murray, Wyle Laboratories, Huntsville, Alabama

**CONCEPT, DESIGN, AND PERFORMANCE OF THE SPACECRAFT ACOUSTIC LABORATORY**

R. J. Wren, W. D. Dorland, J. D. Johnston, Jr., NASA Manned Spacecraft Center, Houston, Texas, and K. McK. Eldred, Wyle Laboratories, El Segundo, California

**THEORETICAL STUDY OF ACOUSTIC SIMULATION OF IN-FLIGHT ENVIRONMENTS**

R. W. White, Wyle Laboratories, Huntsville, Alabama

\*This paper appears in Shock and Vibration Bulletin 37, Supplement.

DATA HANDLING METHODS FOR LARGE VEHICLE TESTING  
D. J. Bozich, Wyle Laboratories, Huntsville, Alabama

DEVELOPMENT AND VERIFICATION OF THE VIBRATION TEST REQUIREMENTS FOR THE APOLLO COMMAND AND SERVICE MODULES  
D. E. Newbrough, General Electric Company, Houston, Texas, R. A. Colonna, NASA Manned Spacecraft Center, Houston, Texas, and J. R. West, North American Rockwell Corporation, Downey, California

DEVELOPMENT AND VERIFICATION OF THE APOLLO LUNAR MODULE VIBRATION TEST REQUIREMENTS  
D. E. Newbrough, General Electric Company, Houston, Texas, M. Bernstein and E. F. Baird, Grumman Aircraft Engineering Company, Bethpage, New York

SATURN S-II, S-IVB, AND INSTRUMENT UNIT SUBASSEMBLY AND ASSEMBLY VIBRATION AND ACOUSTIC EVALUATION PROGRAMS, PARTS 1 AND 2  
R. W. Schock, J. M. Everitt, NASA Marshall Space Flight Center, Huntsville, Alabama, and J. R. Seat, Brown Engineering Company, Huntsville, Alabama

DEVELOPMENT OF ACOUSTIC TEST CONDITIONS FOR APOLLO LUNAR MODULE FLIGHT CERTIFICATION  
W. D. Dorland, R. J. Wren, NASA Manned Spacecraft Center, Houston, Texas, and K. McK. Eldred, Wyle Laboratories, El Segundo, California

\*FACILITY SONIC FATIGUE PROOF TESTING  
O. F. Maurer, Air Force Flight Dynamics Laboratory, Wright-Patterson AFB, Ohio

VIBROACOUSTIC TEST METHODS FOR VIBRATION QUALIFICATION OF APOLLO FLIGHT HARDWARE  
R. W. Peverley, General Electric Company, Houston, Texas

ACOUSTICAL QUALIFICATION OF S-IC FIN STRUCTURES  
C. J. Beck, Jr., The Boeing Company, Huntsville, Alabama, and D. R. Kennedy, Brown Engineering Company, Huntsville, Alabama

\*SIMULATION OF ACOUSTIC FATIGUE FAILURE IN THE WIDEBAND NOISE TEST FACILITY OF THE AIR FORCE FLIGHT DYNAMICS LABORATORY  
R. C. W. van der Heyde, Air Force Flight Dynamics Laboratory, Wright-Patterson AFB, Ohio

REAL-TIME COMBINED ACOUSTIC-VACUUM TESTING OF SPACECRAFT  
L. J. Demas, NASA Goddard Space Flight Center, Greenbelt, Maryland

#### PAPERS APPEARING IN PART 6

##### Helicopter Environments

HELICOPTER VIBRATIONS  
C. D. Roach, U. S. Army Aviation Materiel Laboratories, Fort Eustis, Virginia

HELICOPTER VIBRATION -- A MAJOR SOURCE, ITS PREDICTION AND AN APPROACH TO ITS CONTROL  
R. P. White, Jr., and F. A. DuWaldt, Cornell Aeronautical Laboratory, Inc., Buffalo, New York

\*IN-FLIGHT VIBRATION AND ACOUSTIC STUDY ON THE UH-1F HELICOPTER  
C. E. Thomas and J. T. Ach, Air Force Flight Dynamics Laboratory, Wright-Patterson AFB, Ohio

HELICOPTER FUSELAGE VIBRATION PREDICTION BY STIFFNESS MOBILITY METHODS  
J. J. Sciarra, The Boeing Company, Morton, Pennsylvania

ISOLATION OF HELICOPTER ROTOR-INDUCED VIBRATIONS USING ACTIVE ELEMENTS  
P. C. Calcaterra and D. W. Schubert, Barry Research & Development, Watertown, Massachusetts

HYBRID VIBRATION-ISOLATION SYSTEM FOR HELICOPTERS  
D. A. Bies and T. M. Yang, Bolt Beranek and Newman Inc., Los Angeles, California

\*This paper appears in Shock and Vibration Bulletin 57, Supplement.

RECENT ADVANCES IN THE STUDY OF SYNCHRONOUS VIBRATION ABSORBERS  
A. V. Srinivasan, Kaman Corporation, Bloomfield, Connecticut

OPTIMIZING THE DYNAMIC ABSORBER TO INCREASE SYSTEM DAMPING  
G. K. Jones, NASA Goddard Space Flight Center, Greenbelt, Maryland

APPLICATION OF THE DYNAMIC ANTIRESONANT VIBRATION ISOLATOR TO HELICOPTER  
VIBRATION CONTROL  
R. Jones and W. G. Flannelly, Kaman Corporation, Bloomfield, Connecticut

#### PAPERS APPEARING IN PART 7

##### Environmental Data

SURVEY OF THE CARGO-HANDLING SHOCK AND VIBRATION ENVIRONMENT  
F. E. Ostrem, General American Research Division, Niles, Illinois

A NEW LOOK AT TRANSPORTATION VIBRATION STATISTICS  
J. W. Schlue and W. D. Phelps, Jet Propulsion Laboratory, Pasadena, California

RECENT SHOCK AND VIBRATION MEASUREMENTS ON THE M-151 (JEEP) VEHICLE  
R. D. Brunner and G. M. Pomonik, Hughes Aircraft Company, Canoga Park, California

LATERAL IMPACT SHOCK DURING SHIP LOADING OF THE A3 POLARIS MISSILE  
E. G. Fischer, C. R. Brown, and A. J. Molnar, Westinghouse Electric Corporation, Pittsburgh, Pennsylvania

\*RF-4C VIBRATION AND ACOUSTIC ENVIRONMENT STUDY  
J. F. Dreher, Air Force Flight Dynamics Laboratory, and W. D. Hinegardner, Systems Engineering Group, Wright-Patterson AFB, Ohio

EMPIRICAL CORRELATION OF FLIGHT VEHICLE VIBRATION RESPONSE  
W. H. Roberts, Martin-Marietta Corporation, Orlando, Florida

VIBRATION DATA SUMMARY OF MINUTEMAN WING VI FLIGHT TEST MISSILES  
R. R. Burnett and R. E. Morse, TRW Systems, Redondo Beach, California

SPACECRAFT VIBRATION: COMPARISON OF FLIGHT DATA AND GROUND TEST DATA  
G. Kachadourian, General Electric Company, Philadelphia, Pennsylvania

MEASUREMENT AND ANALYSIS OF GUN FIRING AND VIBRATION ENVIRONMENTS OF THE  
RIVER PATROL BOAT  
R. S. Reed, Naval Ordnance Laboratory, Silver Spring, Maryland

\*RESPONSE OF THE AIM-9D (SIDEWINDER) MISSILE TO CAPTIVE-FLIGHT VIBRATION  
W. W. Parmenter, Naval Weapons Center, China Lake, California

SCALE-MODEL WIND-TUNNEL ACOUSTIC DATA  
J. R. Baratoro and F. A. Smith, Martin-Marietta Corporation, Denver, Colorado

---

\*This paper appears in Shock and Vibration Bulletin 57, Supplement.

# VIBRATION TESTING

## ADVANCES IN NUMEROLOGY

J. P. Saker

Royal Armaments Research and Development Establishment  
Fort Halstead, Sevenoaks, Kent, England

The fundamental basis of vibration testing is discussed, with particular emphasis on the arbitrary and misleading nature of specifications, the difficulty of generating and measuring test forces, and the errors resulting from an attempt to attain consistency. The realities of shock and vibration are untidy, complex, and incommensurable. In the author's view the attempt to use precise, defined numerical values to represent these realities is itself unrealistic. The use of simpler and more empirical techniques is urged, and two simple examples are given.

It is an easy and fatal step to think that the accuracy of our arithmetic is equivalent to the accuracy of our knowledge about the subject in hand. We suffer from "delusions of accuracy." Once an enthusiast gets this disease, he and all who depend on his conclusions are damned.—M. J. Moroney, "Facts from Figures"

Immaturity — whether in tribal development, in the human individual, or in a form of art or science — is characterized by an unwillingness to face up to the complexity of reality, and by an insistence on simplification which degenerates on occasion into an escape into the realms of magic and of fantasy.

—Retlaski

It may be questioned whether quotations such as these have any place in a technical bulletin devoted to shock and vibration in the year 1967. Nevertheless, the implications will be quite obvious to individuals actively engaged in the "art or science" of shock testing or vibration testing. Little is to be lost, and much may be gained, by considering whether they are justified.

Our field of work is a difficult and somewhat untidy one. Do we, in fact, tend to turn our backs on the complexity of the reality and escape into a world of make-believe? Are we exercising mature judgement, or are we playing with our numeric bricks, when we argue whether  $0.1 \text{ g}^2/\text{eps}$  is better than  $10 \text{ g}$ , whether

$6\text{-msec}$  pulses of  $40 \text{ g}$  can be swapped for  $50\text{-msec}$  pulses of  $10 \text{ g}$ , and whether the specified acceleration level should be maintained to within 1 percent or 10 percent?

### NUMERICAL EQUIVALENCE

Few will deny that we have become somewhat obsessed with purely numerical accuracy in a field where our basic understanding is somewhat limited. An analogy from the world of commerce may help to put the matter in better perspective. The development of international currencies has made it possible for us to define a precise numerical equivalence (in units of dollars and rupees) between the reality of a silo of grain in the United States and the reality of a masterpiece of oriental silverware in Benares, India. Yet the equivalence is purely notional. It is in terms of a single concept — monetary value — which ignores countless other facets of the two realities. Neither the stomach of the silversmith nor the aesthetic senses of the connoisseur would accept the suggestion that there was any equivalence.

In much the same way, the development of the ubiquitous accelerometer has enabled us to postulate a numerical equivalence (in units of  $\text{g}$ ) between a laboratory shock test and a ride as cargo in the back of a truck, or between a vibration test and a ride in a guided missile. But again the equivalence in each case relates to a single facet of the two realities: the acceleration of a single point in a single dimension. If we propose to disregard all the other

features which contribute to a true equivalence — all those, in fact, to which we cannot ascribe simple numerical values — is not our preoccupation with accuracy a little intemperate?

### TIDYING UP THE REALITY

To some of us, the oblique reference to tribal ritual touches on a raw spot. It has become completely taboo for a test agency to permit a node to develop at the attachment points of an article undergoing a vibration test. It is a salutary exercise to look back and try to discover why.

The thought processes which have led us to this decision are quite logical — up to a point. Our accelerometers have enabled us to measure the motion at countless locations on countless articles forming part of countless vibrating systems. Our wave analyzers and x-y plotters have presented the information as curves of acceleration amplitude plotted against frequency, each curve relating to just one of the myriad combinations. On each curve, one or two prominent peaks have borne witness to a high level of acceleration at the frequencies of system resonance. On each curve, one or two distinctive troughs have done their best to remind us that, no matter what point within a flexing structure we may care to select, there will always be one or more spot frequencies at which the point will coincide with a motional node. Understandably, we have found the reality complex and intractable, even in terms of motion in a single direction. With a sense of relief, we have recollected that it is the high levels of acceleration, represented by the resonant peaks, that cause the structural failures. So we have concentrated our attention on the peaks, and swept the remainder of our hard-won information under the carpet — out of sight and out of mind.

It now takes no more than a pencil line to envelop the peaks of as many curves as we may care to superimpose; we can even rule in an envelope enclosing a number of envelopes. We are now in possession of a number, a simple unit of international intelligence. With this number we can indicate the worst level of vibration likely to exist at any point in a variety of structures under conditions of mechanical resonance.

At this stage we have, admittedly, tidied up the reality very extensively. But as long as we can keep firmly in mind that the level of acceleration indicated by the envelope — the so-called "envelope level" — is appropriate solely to antinodal points in structures which are excited at

their frequencies of mechanical resonance, we shall be keeping some grip upon reality. But now we are faced with a further problem: that of devising a laboratory test to establish whether an article would survive the kind of environment defined by the envelope. Is it at this stage that our grip on reality slackens, and we begin our retreat into a world of fantasy?

### THE ONSET OF AMNESIA

In a fit of absentmindedness, which a psychologist would have no difficulty explaining, we conveniently "forget" that our original curves displayed troughs as well as peaks. We conveniently forget that for a complete system even to be capable of resonance there must be frequencies at which sections of that system become antiresonant, and nodal behavior is imposed at their boundaries. We conveniently forget that the laws of dynamics know nothing of the existence of subassemblies, test articles, and attachment points; that they are quite oblivious of the boundary lines between the units into which we subdivide a system for the purposes of contract action or ease of manufacture; and that they distribute both nodes and antinodes throughout a structure as a whole with complete disregard for our conventions.

Projected by our amnesia, we see no illogicality in using the envelope level as the acceleration test level. We see nothing unreasonable in demanding that the test agency generate precisely that level of vibration at the attachment points of an article at all frequencies within the test band. We see nothing odd in transferring to a natural nodal point a level of vibration which we have previously accepted as appropriate only to antinodal points in a system at resonance. And we are quite content to blame the designer or the manufacturer for any failure of the article to survive such treatment.

### UNREALITY AUTOMATED

In retrospect, it is hard to deny that our approach to these problems has been just a little odd. Can we boost our morale by pointing to all the effort and money we have poured into the development and introduction of random-vibration test facilities? This work, surely, has made a genuine contribution to the realism of our test methods. So, too, have our recent proposals that shock test be defined in terms of shock spectra rather than of pulse shape. Unhappily for us, any attempt to argue along these lines involves lifting the edge of our carpet and



being reminded of much that we have preferred to forget.

The transposition of a single, measured shock pulse from the time domain to the frequency domain undoubtedly helps us to get a clearer appreciation of the response which the shock must have excited in the remainder of the structure on which it was measured. It also significantly increases the precision with which the severity of one shock pulse can be compared with the severity of another. But if the raw data have already been generalized by means of an envelope-drawing operation, the increased precision with which the resulting test shock can be defined, and (in theory) generated, merely increases the intrinsic unreality of the test. We are limiting still further the freedom of the test article to influence the motion at its attachment points.

Perhaps we owe more than we know to the rough-and-ready methods of the typical test laboratory. Perhaps we should be thankful that it is still possible for them to turn a blind eye to the significant discrepancies between the shock pulse defined in the specification and the shock pulse they are actually administering.

But the introduction of fully automatic equipment for the control of spectral density has blocked this loophole during a random-vibration test. Here, it matters not whether the response of the article is resonant or anti-resonant at any particular frequency; the electronic control system is ever alert to detect the slightest discrepancy between the medicine prescribed and the medicine administered. It carries out its duties conscientiously — and quite ruthlessly.

#### THE PRICE OF CONSISTENCY

In trying to justify our actions, we soon find ourselves in an embarrassing dilemma — a dilemma, ironically enough, which is largely of our own making. We have long poured scorn upon the poor ignorant fellows who would call for the use of a particular test machine, rather than for the generation of a specific acceleration waveform, or spectral density. "There's no consistency of test between one test machine and another," we have pointed out; "haven't our accelerometers proved it? Haven't we all heard of the manufacturer's product which was accepted when tested on one machine but rejected when tested on another? By insisting upon the generation of precisely the same test waveform by all test agencies we are at least achieving consistency of test."

But dare we use this argument any longer? Are we in fact even generating a common waveform? Could it be that that full-bellied rumble which we hear in our test laboratories is not, after all,  $1 \text{ g}^2/\text{cps}$  plus-or-minus 3 db (precisely), but is merely a distant echo of the sardonic mirth of the gods? Are we only now, in 1967, realizing that it is one thing to put a tight tolerance upon a mathematical abstraction (a stroke of the pen will suffice to do that), but quite another thing to devise and to install throughout the land a practical filter system which will measure the true spectral density at the bottom of a notch to within even 30 db, bearing in mind that the fatigue life of the test article sets a limit to the integrating time we can tolerate, and that the national purse is not, after all, bottomless?

If we cannot measure, how can we standardize? If we cannot standardize, what becomes of our consistency of test? It would be unkind to break in upon the stunned silence that has recently descended upon a certain committee of experts: a committee that has been attempting to standardize all our random-vibration tests and has come face to face with the problem of spectral density tolerances — and has now done its homework...

Looking back, we can see so much that we have sacrificed upon the altar of "consistency." Time and again, we have been forced to compromise with reality — to jettison successive facets of the truth — by excluding from our tests any physical effect which was not amenable to numerical definition in the very simplest of terms. It will be a bitter pill to swallow if we are forced to admit that the sacrifice has been in vain — that we have not even achieved consistency of test.

#### WHOM ARE WE FOOLING?

Nevertheless, the time has come for us to ask ourselves, quite brutally, whom we think we are fooling. We may be fooling the customer — the ultimate user of the article. We may be fooling the designer of the article, or the manufacturer. We may even be fooling ourselves. But we are not fooling the article. It knows with complete certainty that the physical experience of being mated with the shake table is quite unlike the physical experience of being mated to its parent assembly over the years that follow. Its reactions in each case are perfectly appropriate, but quite different.

An increasing number of skeptics, quite unimpressed by our skills in juggling with numbers, are already beginning to side with the

small boy in the fairytale who pointed out that while the Emperor's New Clothes might be clearly visible to the eyes of those mentally attuned to the requirements of The Establishment, yet they appeared to him to give little protection to the user. It could well be that the time is not far off when the distant and derisive mirth of the gods finds a human echo somewhat closer at hand -- and at our expense. Maybe it is not just by chance that it is the down-to-earth marketing organizations which have evolved a carton for the safe transport and handling of the domestic egg -- a carton which for cheapness, simplicity, and effectiveness is unequaled by anything in the world of military packaging.

If, by numerical methods, we have failed to achieve either realism or consistency of test, then maybe, just maybe, we ought now to face up to the fact that in the world of shock and vibration the reality is untidy, is complex, is incommensurable.

#### THE INDIRECT APPROACH

Maybe we ought to spend a little time and money reassessing the possibilities of those test machines which our fathers had to use before the advent of the accelerometer; the machines which produced comparable patterns of failure rather than comparable levels of acceleration; the machines which, without benefit of Fourier or Laplace, could yet separate the sheep from the goats by generating a test environment which was every bit as complex, as untidy, as indescribable as those found in reality.

A suitably located carrot is all that is needed to excite a donkey's back into realistic motion. As a practical test of numerous qualities in riders of all shapes and sizes, the combination is both simple and effective. Here, as is often the case, the indirect approach is the best one. If we would be content to adopt a similarly indirect approach to our problem of environmental testing -- guilefully stimulating nature, rather than using brute force -- we should be far more successful.

Two practical examples are described below. In each case the investment of money and manpower by the author's establishment has been relatively trifling, yet each gives promise of significant returns. It is hoped that the brief details presented will be sufficient to prompt others to explore similar methods.

#### THE BOUNCER

The first example concerns what we are deliberately calling a "bounce" test. When articles travel as cargo in the back of a truck, some are eager to bounce on the floor of the truck, others are most reluctant to do so. Some will bounce vigorously upon one of their sides, but remain relatively quiescent when turned onto another. In determining the punishment they receive, their own dynamic characteristics are quite as important as the basic motion of the floor.

As reported elsewhere [1] it can be demonstrated that the acceleration pulses experienced by various resiliently packaged articles when bounced upon a commercial "transportation simulator" correlate very satisfactorily with the pulses experienced when the selfsame articles are transported as cargo in a truck traversing a rough track. This particular simulator ("bouncer") comprises merely a suitably reinforced wooden platform mechanically constrained to execute a simple form of quasi-sinusoidal motion at an amplitude of around 1.5 g.

But measurement of the motion of a single point in one dimension falls far short of defining the damage potential of either environment. It tells us nothing of the effects of intercargo jostling and hammering, the effects of multi-layer loading, the spatial distribution of damage within a package, damage to hermetic seals and to protective finishes, the distortion or unlatching of clip fasteners, or the lamentable consequences of including just one chisel-cornered item in the cargo. Recent work, therefore, has been oriented toward the correlation of failure patterns, embracing as many as possible of the modes of failure listed above.

The victims have comprised a number of containers each holding from 15 to 150 damageable items. Some of the containers have been of pressed-steel construction and some have been of wood. Some have provided a degree of resilient cushioning for their contents, while others have allowed considerable freedom for the contents to rattle between unyielding surfaces.

As regards the contents, an overriding requirement has been that they should be readily available in large numbers, so as to provide a homogeneous population from which extensive samples could be drawn at random. Various forms of pharmaceutical glassware (ampoules, jars, etc.), domestic light bulbs, and a simple form of commercial "shock indicator" have provided items whose mode of failure would be

catastrophic rather than fatigue induced. Domestic alarm clocks have provided items whose deterioration would tend to be progressive rather than catastrophic.

The results have been both encouraging and infuriating.

They have been encouraging because of the high confidence levels at which statistically significant correlation between the two environments has been demonstrated for various failure patterns and various combinations of containers, interior furnishings, and contents.

The results have been infuriating because of the relentlessness with which each session on the test track has hammered home afresh the simple lessons learned the hard way by any serviceman who has ever found himself a helpless item of human cargo in the back of a military truck: that there is a severe damage gradient along the length of the truck; that the degree of abrasion of a protective coating is closely related to the amount of sand and grit on the floor; that the various layers of cargo experience quite different environments; and that in the final analysis, given a determined and well-protected driver, a robust and lightly laden truck, a location near the tailboard, and the "right" combination of speed, surface, and suspension, there is virtually no limit to the severity of the punishment.

In short, we were approaching the problem from the wrong end. We were seeking an answer to the wrong question. Prompted by the natural concern of the potential customer that the article "survive truck transportation," we were asking, "Does the bouncer produce the same damage, and the same patterns of failure, as truck transportation?" — as if the term "truck transportation" had meaning.

More realistic questions would have been: Is there a definable range of truck environments for which the patterns of failure correlate acceptably with those produced by the bouncer?; and, Is it one which reasonable parties to a contract — producer and user — would accept as being a fair test of a well-designed article?

If both of these questions can be answered in the affirmative, there seems little reason for a bounce test failing to gain wider official acceptance. Test results to date suggest that the first question can be answered affirmatively with considerable confidence. The answer to the second question is a matter of personal judgment: the author's verdict would be "Yes," and he believes

that this view would find widespread acceptance if authoritative opinion were to be canvassed.

## A RANDOM-VIBRATION TEST

The second example relates to the development of a simple random-vibration test in a form which would make it practicable to set reasonable tolerances to the level of spectral density. The prototype system has been described elsewhere in the literature [2].

The carrot in this case is a randomly varying force whose spectral density has some simple slope (in terms of decibels per octave) between defined frequency limits. The force spectral density can thus be established without uncertainty by a conventional wave analyzer and confirmed by an rms measurement.

The donkey is a multiresonant structure whose resonances are spaced equally at close intervals of frequency and whose dynamic characteristics can be reproduced by normal manufacturing processes and verified by conventional mobility measurement techniques. The design is such that the peaks of the mobility curve lie along an easily defined line: the application of a sinusoidal force of unit amplitude generates a range of resonant peaks to which a simple envelope can be ascribed.

With random excitation, the combination of a random force of known spectral texture and intensity with a structure of known mobility results in a motion whose spectral density can be deduced with an accuracy far greater than that achievable by direct measurement with conventional equipment.

The test thus involves three major departures from generally accepted practice:

1. The envelope level derived from field measurements of service environments is no longer used as the test level itself; it provides a common yardstick for the equating of test environment and service environment.

2. The article to be tested is no longer mated to a surface of infinite mechanical impedance; it is attached to a mechanical foster-parent whose impedance is of the same order as its own and with which it forms a complete system capable of natural resonance under the influence of a very modest force.

3. The desired motion is no longer generated directly, nor is any attempt made to measure it directly; it is excited by the application of a known force to a known structure.

The intriguing feature of the test results to date has been the remarkable simplicity of coloration of the random force that has sufficed to reproduce two particular classes of service environment: that relating to air transport in general, as defined by an overall envelope of the type depicted in a recent review [3]; and that defined by a more closely tailored envelope, such as would normally be derived from a family of spectral density curves relating to a specific missile. As yet the evidence is limited, and any association of ideas may be quite unwarranted; but if we recollect that vibration of aerodynamic origin is merely the outcome of the interaction between a flexible structure and a steady stream of air, it would not be too surprising if the relationship between the required energy and frequency followed quite a simple law.

## SUMMARY

In short, it is suggested that we have unknowingly become dissociated from the realities of our subject and have got caught up in a circle of activity of considerable intellectual interest but of little relevance to our main purpose. A conscious effort will be necessary if we are to break out of this posture, but the rewards for doing so are considerable.

It may be that this suggestion is unwarranted. But if so, it is high time that somebody said so — in print and with evidence in rebuttal.

## REFERENCES

1. J. P. Salter and N. W. Lee, "The Response of Packaged Military Stores to Truck Transportation — Real and Simulated," RARDE Memorandum 53/65
2. J. P. Salter, "A Vibration Exciter Having Generalized Mobility Characteristics, J. Environmental Sci., p. 18 August (1966)
3. R. W. Schock and W. E. Paulson, "A Survey of Shock and Vibration Environments," Shock and Vibration Bull. No. 35, Part 5, p. 1 (1966)

\* \* \*

# INTERNAL VIBRATION OF ELECTRONIC EQUIPMENT RESULTING FROM ACOUSTIC AND SHAKER-INDUCED EXCITATION\*

Allan D. Houston  
Lockheed Missiles & Space Company  
Sunnyvale, California

The many mission configurations of upper stage boosters developed by LMSC have required the design, development, fabrication, and vibration qualification testing of many pieces of electronic equipment. To improve the methods and criteria for designing and qualifying this equipment, the Research and Development Division of Lockheed Missiles and Space Company began empirical studies of the nature of vibration environments existing within equipment.

The primary objectives of the studies were: (a) to determine whether estimated vibration responses within equipment during flight are compatible with vibration test criteria of electronic piece parts; (b) to investigate the validity of shaker excitation techniques in simulating flight-type acoustically induced environments; (c) to evaluate the effectiveness of viscoelastic fabrication materials in reducing responses within equipment.

The first phase of the experimental work was a series of reverberant chamber acoustic tests conducted on a 60-in.-diameter cylindrical airframe containing internal support structure with several packages of electronic equipment attached to it. This equipment, having a variety of packaging designs, was extensively instrumented internally and externally with special miniature vibration transducers to measure absolute response of elements within the package and also to obtain transmissibility data between internal and external package environments. Another package was specially fabricated and tested to compare viscoelastic vibration attenuation materials with existing fabrication materials.

The second phase of the experimental work was conducted using shaker excitation techniques on a number of packages evaluated during the acoustic test. These packages, instrumented as in the acoustic test, were attached to rigid fixtures (as they would normally be in a vibration qualification test) and exposed to the random-vibration environments measured at the mounting interface during the acoustic test. Reduced and analyzed data from one such test is presented.

On the basis of these experiments, it has been determined that: (a) shaker-induced vibration of equipment produced responses of elements within equipment from 2 to 10 times more severe than those produced by an acoustically induced excitation when the equipment is installed on launch vehicle structure; (b) environments measured within equipment differ in form from those used in qualification tests of electronic piece parts, such as electromagnetic relays; (c) sparse use of viscoelastic materials within a package resulted in a 20 to 35 percent reduction of vibration transmissibilities, as measured between package mounts and internal structure.

The results of this preliminary work indicate that existing industry-wide shaker vibration test techniques and criteria for both electronic packages and electronic piece parts require careful reevaluation, and that development of improved package fabrication methods should continue.

## INTRODUCTION

The development of many Lockheed Missiles and Space Company (LMSC) upper stage booster configurations has resulted in the design, development, fabrication, and test of

many pieces of packaged electronic equipment. The method currently in use at LMSC, and many other companies, for demonstrating that this equipment will survive in-flight environments consists of the application of vibration excitation by means of electromagnetic shakers.

\*This paper was not presented at the Symposium.

At LMSC, two types of shaker vibration tests are conducted on equipment. First, there is the qualification test, which is applied to a random sample from a production batch of equipment to verify the adequacy of the basic package design. Levels somewhat in excess of those expected in flight are used in this test to allow for the fact that there are variations of material quality and workmanship standards in a given batch. The second type of shaker test conducted at LMSC is the acceptance test, which is performed solely to detect workmanship flaws and faulty material on each piece of equipment to be flown. The test levels used during acceptance testing are approximately one half of those used in qualification testing.

Equipment malfunctions have occurred during both of the above types of test, resulting in equipment redesign or repair. Lockheed Missiles and Space Company's Research and Development Division has embarked upon a study to define the nature of vibration environments found within equipment which will minimize failures during qualification and acceptance testing while maintaining or increasing the present high standard of LMSC equipment flight reliability. The primary objectives of the study are as follows:

1. To investigate the validity of shaker excitation techniques in simulating in-flight acoustically induced vibration environments. The intent in this phase of the study is to determine whether shaker tests, as presently conducted, produce overstress conditions beyond those considered necessary for qualification purposes. In other words, LMSC wants to be sure that flightworthy equipment is not being rejected because of an overly severe test.

2. To determine whether the character and levels of vibration responses existing within equipment are compatible with those applied to electronic piece parts, such as electromagnetic relays, during qualification and acceptance testing of these devices.

3. To evaluate the effectiveness of limited use of viscoelastic fabrication materials in reducing responses within equipment.

This paper presents the data acquired and the conclusions reached thus far in the continuing effort to improve package design, fabrication, and test techniques.

## EXPERIMENTAL WORK

### Acoustic Tests

The purposes in conducting the acoustic tests were:

1. To survey the level and characteristics of vibrations existing within typical electronic packages when they are attached to large airframe structures and exposed to acoustic environments similar to in-flight conditions.

2. To obtain data relating vibration levels at the package external mounting points to the levels existing within the equipment, in an acoustic environment. This data would later be compared with corresponding information gathered from shaker vibration tests on packages.

3. To evaluate the effectiveness of sparsely used viscoelastic damped package fabrication materials in reducing vibration responses of electronic piece parts, such as electromagnetic relays.

The airframe of the acoustic test specimen was not a portion of an actual booster airframe but resembled one structurally. It consisted of a cylindrical shell 5 ft in diameter and 5 ft in length, having a skin of 0.04-in. gage aluminum, which was stiffened by six rings and six longe-rons. An inner truss structure, used for equipment support, was attached to the outer shell at eight locations. Several electronic packages, which have been used in various programs and which represent a wide variety of design, were then attached to these truss members by means of intermediate secondary structure such as Z-shaped members or suitably stiffened shelves. (Figure 1 shows the specimen with a particular set of equipment installed, while Figs. 2 through 5 illustrate the packaging designs of some of the equipments surveyed.) The specimen was then closed off by a hemispherical plug at one end and an ogive-shaped plug at the other end, each containing sound suppression material.

The acoustic tests were performed in a reverberant chamber (25 ft long, 15 ft wide, and 11 ft high) with excitation provided by two Ling type 94B 4000-w transducers and horns which exhausted into a common exponential horn. The horn exhaust was directed into a corner of

the room, producing a reverberant field there, with the specimen suspended from the ceiling using "bungee" cord to isolate it from seismic vibrations existing in the room walls (see Fig. 6).

The instrumentation for the test consisted of Endevco type 2220 and Columbia type 606 miniature vibration transducers weighing 0.042 and 0.028 oz, respectively, which were considered to have little effect on the dynamic characteristics of the structures being monitored. Typical installations of this instrumentation attached to package mount points and package internal structure are shown in Figs. 2 through 5. Four microphones were suspended from the chamber ceiling to monitor the acoustic environment external to the specimen shell approximately 1 ft from the shell. Two microphones were installed within the cylindrical shell to monitor internal acoustic excitation.

The acoustic environment measured in the chamber during the test is shown by the octave

band plot in Fig. 7, with the environment measured within the specimen. Also shown in Fig. 7 is the maximum external acoustic level encountered by a vehicle during flight which, because of power limitations of the excitation equipment, it was not possible to achieve during test.

The experimental package which was built to evaluate the effectiveness of viscoelastic materials consists of a relay support beam and a circuit card (Fig. 8). This package is not intended to be representative of a superior package design but is merely a "test rig" on which these materials can be evaluated as a means of reducing vibration responses. An initial test was conducted with the relay support beam fabricated from plain L-section aluminum and the circuit card from laminated Fiberglas. Prior to the second test run, viscoelastic damped L-shaped beams were substituted for the plain aluminum beams used in the first test, and a viscoelastic damped card was substituted for the Fiberglas card.

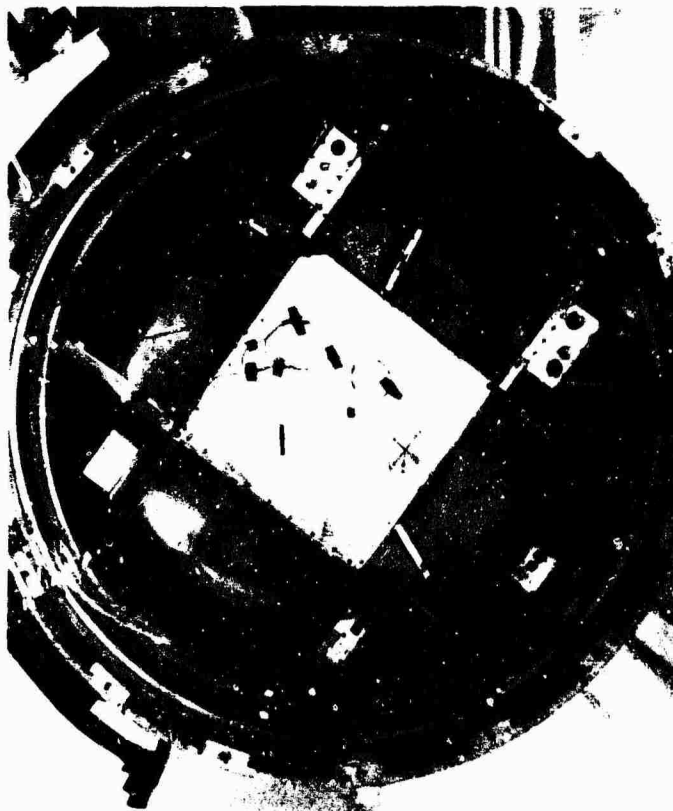


Fig. 1. Acoustic test specimen with packages installed

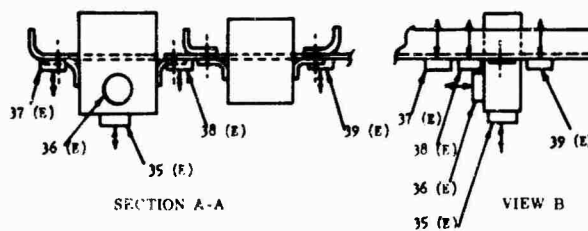
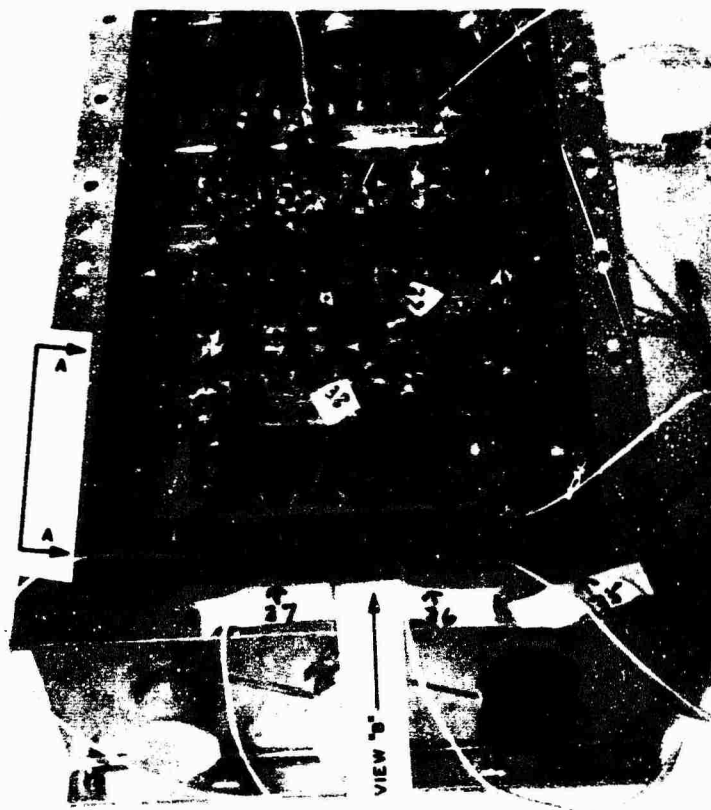


Fig. 2. Instrumentation within package 1



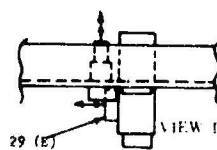
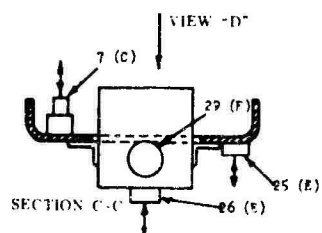
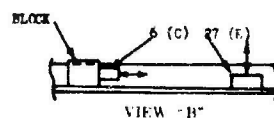
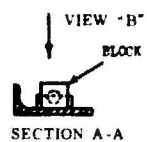


Fig. 3. Instrumentation within package 2



Fig. 4. instrumentation within package 3  
(cover removed)

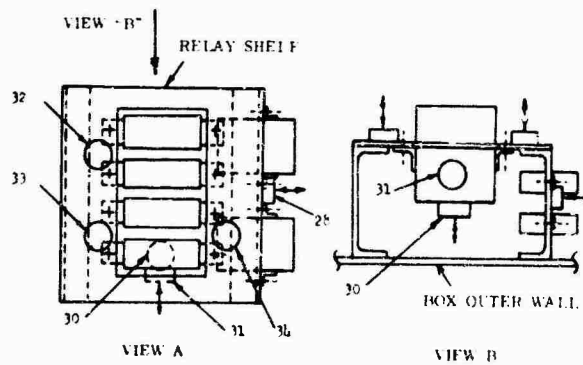
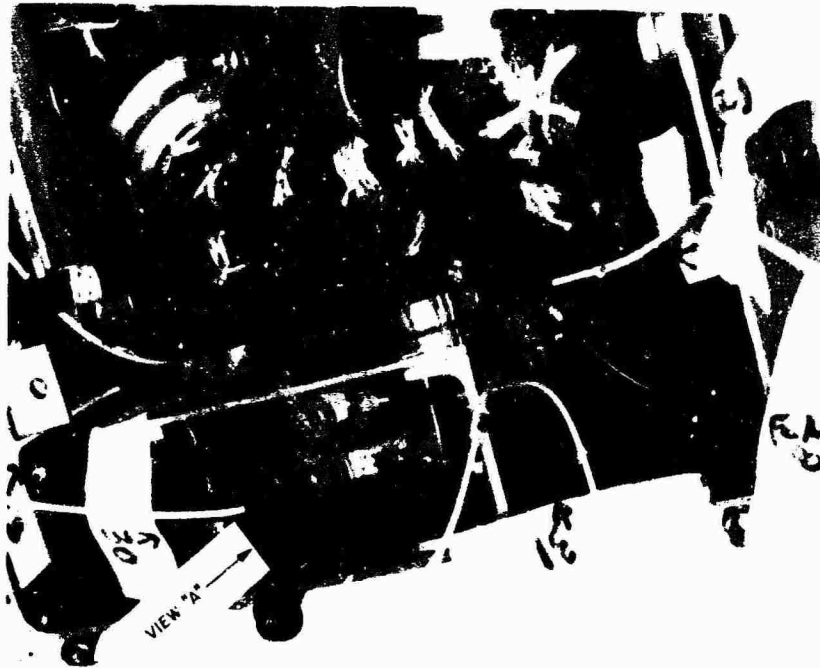


Fig. 5. Instrumentation within package 4

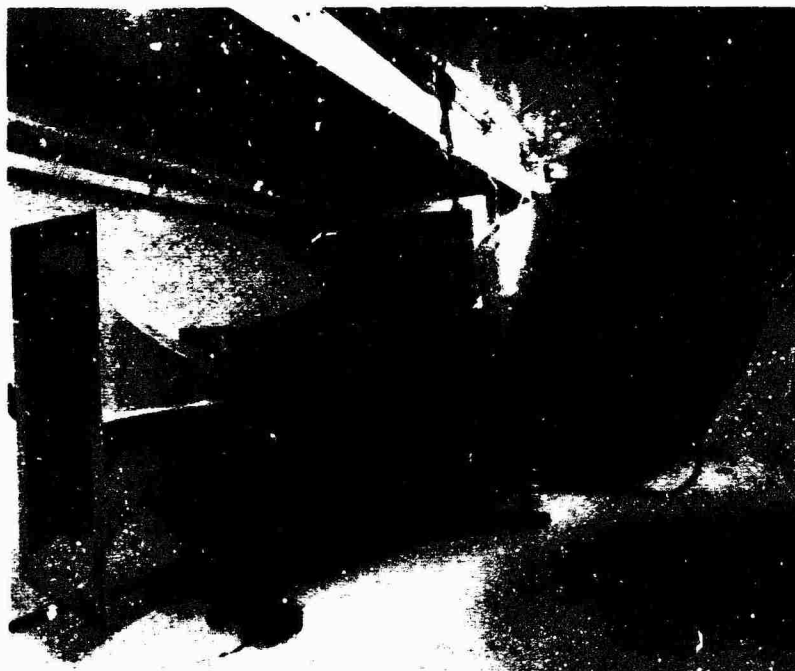


Fig. 6. Specimen installed in reverberant chamber

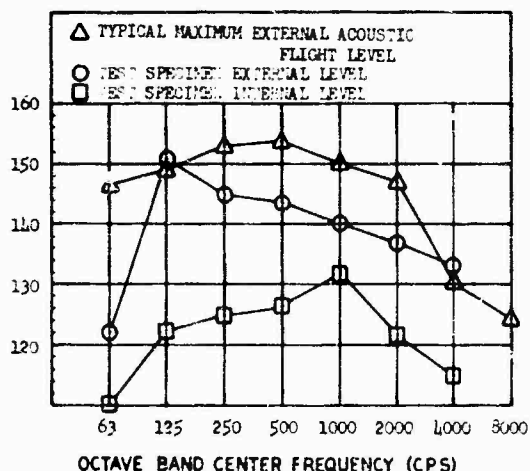


Fig. 7. Specimen acoustic test levels

Acoustic excitations occurring during flight at launch and at transonic and supersonic Mach numbers differ in character from those present in a reverberant chamber. For example, time and spatial correlations of these various fields differ; the extent of these differences is being investigated by LMSC and other organizations. However, since the specimen airframe and the

package samples are essentially flight hardware and since the fundamental mechanism whereby vibrations are acoustically induced in the outer shell and transmitted to packages, the data acquired from this test are considered to be worthy of evaluation.

#### Shaker Vibration Tests

The principal objective of these tests is to compare shaker-induced internal responses of electronic packages with those measured during the acoustic test. In this manner, the validity of the shaker test as a means of simulating in-flight acoustically induced environments can be examined. Also, further testing was conducted on the experimental package to evaluate the effectiveness of the viscoelastic materials.

Package samples used during the acoustic test were attached to rigid fixtures (having no resonances below 2000 cps) as they normally are during qualification and acceptance testing at LMSC. Excitation control accelerometers were placed on the fixture at locations corresponding to those where vibration measurements were made during the acoustic test. The instrumentation installations within the packages were identical to those used during the acoustic tests. The test setup for the shaker tests on one sample of equipment is shown in Fig. 9.

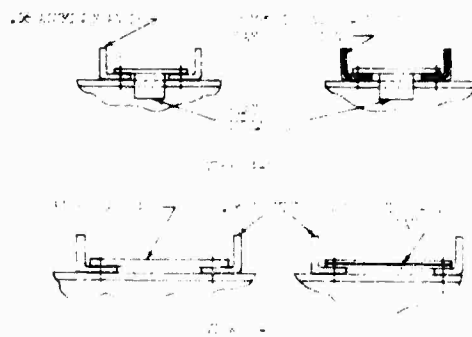
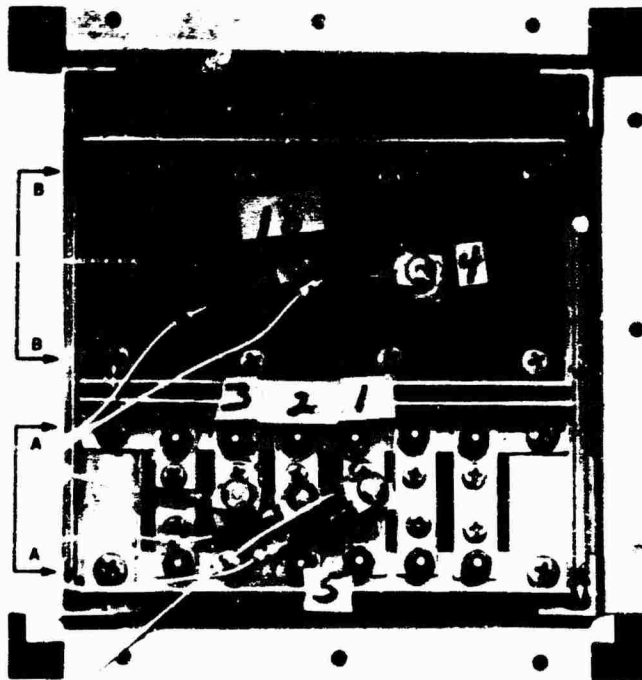


Fig. 8. Experimental package used to evaluate viscoelastic materials

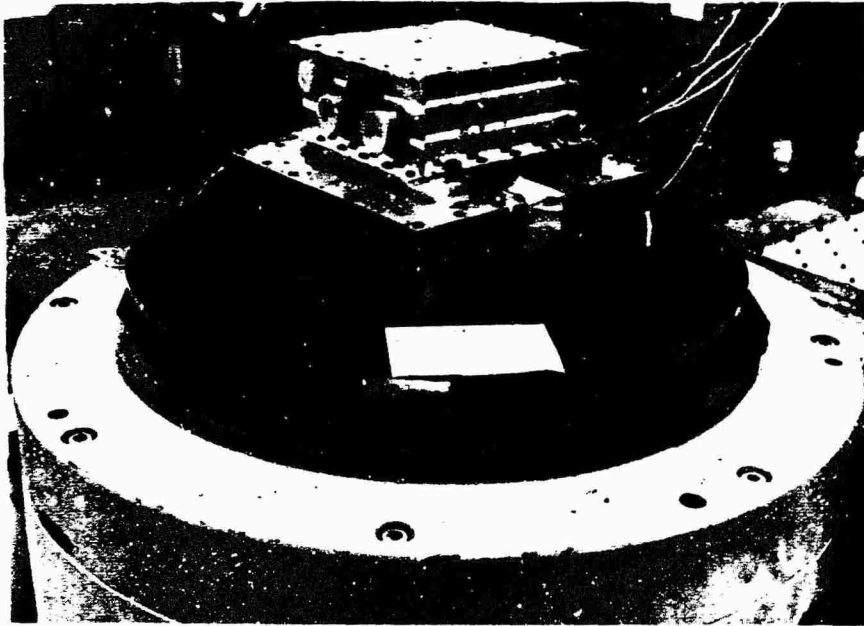


Fig. 9. Installation of package on shaker

The excitation applied to the packages by the shaker was controlled using a tape-recorded loop of vibrations measured on the packaged foundation structure during the acoustic test. The loop was played into the shaker power amplifier system and the amplifier setting adjusted until the overall rms g level achieved was the same as that measured during the acoustic test. In this way, PSD's of vibration applied to the equipment during shaker testing were made essentially the same as those of vibrations measured during the acoustic test. Sinusoidal sweep tests were performed on the experimental package used to evaluate the viscoelastic materials; the tests were conducted on both the plain sheet metal and damped configurations using a level of  $\pm 3$  g from 20 to 2000 cps.

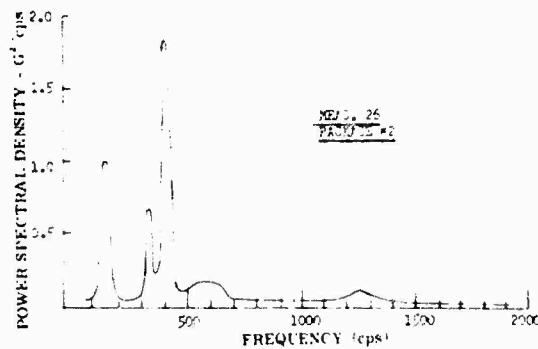


Fig. 10. Typical PSD plot of vibration measured within package during acoustic test

## TEST RESULTS

### Vibration Environment Within Packages

The data obtained from the acoustic test revealed that the vibration environment present within the packages surveyed consisted generally of low-level background random vibration, with superimposed concentrations ("spikes") of narrow-band random vibration, as shown by the typical PSD plot in Fig. 10.

As indicated in the discussion of the acoustic tests, it was not possible to achieve excitation levels within the reverberant chamber comparable to those which exist external to LMSC vehicles during their worst missions. Therefore, it was necessary to adjust the vibration levels measured within the equipment in accordance with the difference between acoustic test and maximum flight environment. This was done by assuming a linear relationship between mean square SPL and mean square vibration levels. Figure 11 is the PSD plot of

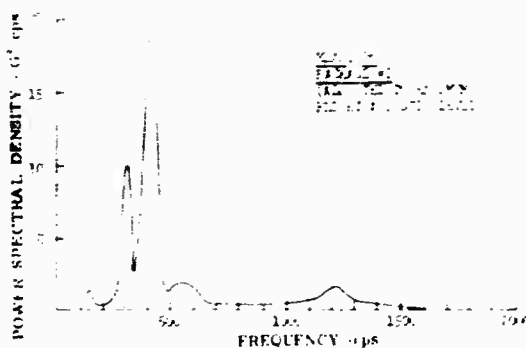


Fig. 11. Typical PSD plot, adjusted to maximum acoustic flight levels

the above typical vibration measurement, obtained during the acoustic test, projected to maximum flight conditions. Special interest is attached to the rms g level present in the concentrations (spikes) of narrow-band random vibrations which appeared in all internal package vibration measurements: Table 1 summarizes the significant rms g levels measured which have been adjusted to maximum anticipated flight levels.

Vibration qualification and acceptance testing of many electronic piece parts, such as relays, transistors, diodes, etc., consist of

either a sinusoidal sweep test or a random-vibration test using an essentially flat spectrum. For example, a typical specification for an electromagnetic relay calls for either a 30-g sinusoidal sweep test from 20 to 3000 cps or a random-vibration test defined by the spectrum shape  $0.2 \text{ g}^2 \text{ cps}$  (20 - 400 cps) and  $0.4 \text{ g}^2 \text{ cps}$  (400 - 2000 cps).

On the basis of the appearance and levels of vibration observed during the acoustic test survey, it is apparent that the above specification is inconsistent with the environment to which electronic piece part components are exposed. The essentially flat broad-band random-vibration specification is not severe enough, considering that a severe narrow-band excitation, such as that measured during the acoustic tests, may coincide with a critical frequency within an electronic piece part. By contrast, the sinusoidal sweep test appears to be much too severe in comparing the damage potential of a 30-g sinusoidal excitation with, say, 55 g rms of random-vibration excitation, the maximum level measured during the acoustic test. (The 30-g sinusoidal test has the ability to build up full resonant amplification in an element of a component, whereas narrow-band random excitation, using the levels measured, does not.)

A more realistic method for qualification and acceptance testing of piece parts, which is

TABLE 1  
Significant rms g Levels Observed Within Equipment

| Package | Measurement | Levels Contained in PSD Spikes<br>(rms g) |                                       |
|---------|-------------|---|---------------------------------------|
|         |             | Measured in<br>Acoustic Test              | Maximum<br>Projected<br>Flight Levels |
| 1       | 36          | 9 (450 - 500 cps)                         | 30                                    |
| 1       | 35          | 10 (250 - 300 cps)                        | 26                                    |
| 1       | 35          | 2.5 (750 - 800 cps)                       | 8.5                                   |
| 2       | 27          | 10.5 (500 - 550 cps)                      | 35                                    |
| 2       | 25          | 6.5 (350 - 400 cps)                       | 22                                    |
| 3       | 12          | 15 (300 - 400 cps)                        | 34                                    |
| 3       | 13          | 17 (600 - 750 cps)                        | 55                                    |
| 3       | 13          | 4 (950 - 1050 cps)                        | 15                                    |
| 3       | 8           | 4.2 (650 - 750 cps)                       | 14                                    |
| 3       | 11          | 4.2 (650 - 800 cps)                       | 14                                    |
| 4       | 32          | 7.5 (350 - 500 cps)                       | 25                                    |
| 4       | 30          | 10 (750 - 850 cps)                        | 32                                    |

within state of the art, would be the application of sweeping narrow-band random excitation. The nature and level of such a test is beyond the scope of this paper and requires further investigation.

### Package Shaker Test

As previously discussed, the vibrations applied to a package by the shaker were controlled in such a way that the PSD of the vibration present at the package-fixture interface was essentially the same as the PSD of vibration measured on foundation structure of that package during the acoustic test. Power spectral density plots were then processed from vibration measurements obtained within the package from both the shaker test and the acoustic test. Curves of transfer functions,  $H(\omega)$ , were then plotted relating vibrations existing at a package mount point to vibrations present within the package.  $H(\omega)$  is given by:

$$H(\omega) = \frac{\ddot{x}_i}{\ddot{x}_e}$$

where  $\ddot{x}_i$  is the PSD of vibration measured within the package and  $\ddot{x}_e$  is the PSD of the vibration measured at the package external mount point.

Two typical curves, obtained from shaker tests on package 2, are shown in Fig. 12. It is seen that the shaker tests induce responses on structures and electronic components within the package significantly higher than those induced by the acoustic test. The value of  $H(\omega)$  for the shaker test at 350 cps, the resonant frequency of the beam structure upon which the measurement was made, is in one case 4 times more severe and in another case 10 times more severe than corresponding values obtained from the acoustic tests. At the higher frequencies, the differences in the ability of the two types of test to do damage becomes larger, and at 1200 cps, the resonant frequency of a relay on its local mount, the value of  $H(\omega)$  for shaker test is 40 to 100 times more severe than in the acoustic test.

The relative severity of the two types of test, in terms of induced stresses, will be approximately proportional to the square root of  $H(\omega)$ . Therefore, this package was subjected to stress levels at 350 cps during shaker testing from 2.0 to 3.3 times more severe than during the acoustic testing; at 1200 cps the relative severity of the two tests varied from 6.3 to 10 times.

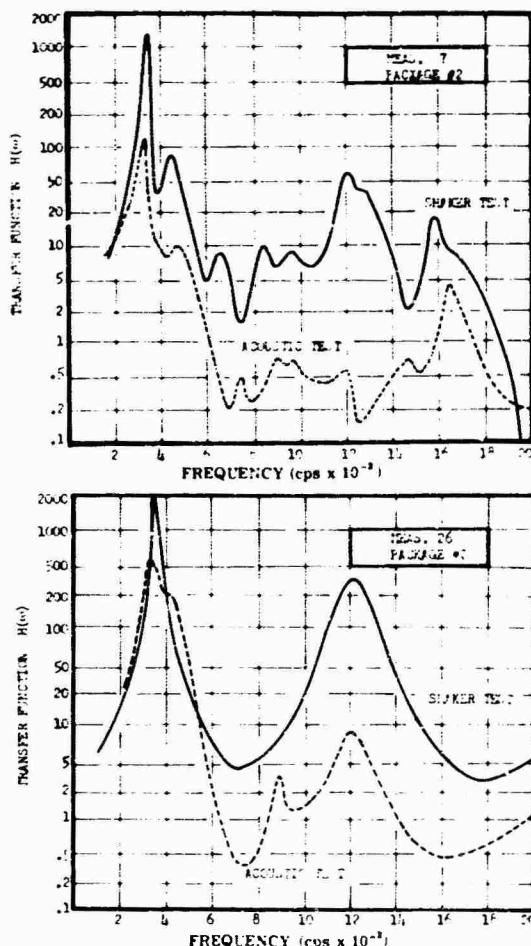


Fig. 12. Transfer functions  $H(\omega)$  for package 2 measured in acoustic and shaker tests

Lockheed is continuing analysis of data obtained from similar shaker tests conducted on other packages to verify whether the data trends uncovered during tests on this one package applied generally to all packages. It will also investigate the reasons for the differences between the two types of test, believed to be principally that vibrations at all package mounting points are more closely correlated than in an acoustically induced environment.

The investigation performed thus far, and other considerations which are beyond the scope of this paper, has led LMSC to believe that the preferable test for formal qualification and final acceptance testing of packages is an acoustic test conducted on the entire vehicle system. In this way, the needless rejection of flightworthy hardware because of overtest



during shaker qualification can be minimized. Even more important, acoustic tests performed on a vehicle system as an acceptance test of all vehicles to be flown will minimize the danger of shortening service life of the package and provide for better simulation of flight conditions. Lockheed is presently constructing large acoustic facilities, capable of performing both qualification and acceptance testing of complete vehicle systems.

#### Evaluation of Viscoelastic Materials

The results of limited acoustic and shaker tests conducted on the experimental package reveal that very sparse use of viscoelastic materials can reduce peak responses within packages by 20 to 35 percent. Figure 13 presents acoustic test data which compare the PSD of a typical vibration measurement on the relay shelf, fabricated from sheet metal, with the corresponding measurement on the shelf fabricated from viscoelastic damped materials; the overall rms g is reduced from 35 to 27 g rms. Similar results were obtained during the sinusoidal shaker test on the experimental package, as shown in Table 2, which compares

resonant amplification (Q) values of the internal structures for the sheet metal and viscoelastic damped configurations.

It was hoped that limited use of viscoelastic materials would substantially reduce environments to which electronic piece parts are exposed. The results obtained so far indicate that the response reductions achieved were far below the values being sought to justify procurement and qualification of these materials at this time. More liberal use of these materials within a given package will likely produce more encouraging results, since this will reduce the large resonant amplifications of structures within the package which have not been treated with these materials. The resonances of structures adjacent to the viscoelastic damped structures tested are believed to be the reason for the disappointing results in this series of tests. More liberal use of these materials results in a weight penalty since stiffness/weight ratios of these materials are smaller than for conventional structures. This factor will have to be weighed against the reduction of responses achieved and the rates of package failure, when more realistic package test requirements are implemented.

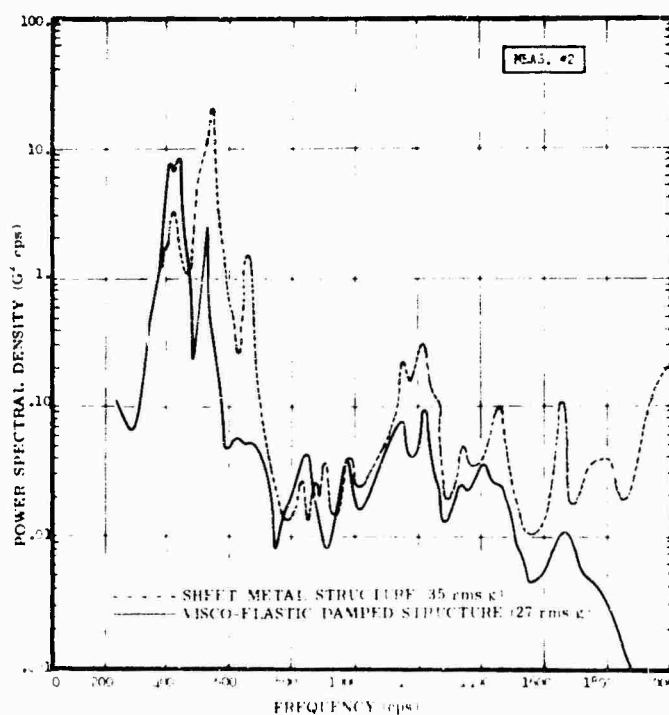


Fig. 13. PSD plot of measurements within experimental package, sheet metal configuration vs viscoelastic damped configuration

**TABLE 2**  
**Results of Evaluation of Viscoelastic Materials Using Shaker**

| Configuration                  | Q Values (Amplification at Resonance) |            |            |            |              |
|--------------------------------|---------------------------------------|------------|------------|------------|--------------|
|                                | Relay Shelf                           |            |            |            | Circuit Card |
|                                | Meas.<br>1                            | Meas.<br>2 | Meas.<br>3 | Meas.<br>5 | Meas.<br>4   |
| Sheet metal structures         | 35                                    | 37         | 40         | 20         | 50           |
| Viscoelastic damped structures | 25                                    | 28         | 26         | 15         | 40           |
| Percent reduction              | 35                                    | 25         | 35         | 25         | 20           |

#### CONCLUSIONS AND SUMMARY

The results of a survey of vibration environments existing within electronic packages reveal that the character of that environment is inconsistent with commonly used piece-part qualification and acceptance test criteria. It is proposed that a new method for testing such components, worthy of investigation, is the use of a sweeping narrow-band random test, which is within state of the art and existing facility capability.

The internal response characteristics of components within a package obtained during shaker testing were compared with corresponding responses measured within the package installed on the airframe, which was exposed to a flight-like acoustic environment. The results indicated that the shaker test induced responses within the package that were from 2 to 10 times more severe than the acoustic test. It is proposed that realistic qualification and final acceptance testing of packages be conducted on an

airframe with an acoustic environment applied. This will minimize the possibility of rejection of flightworthy hardware because of overtest.

Evaluation of sparsely used viscoelastic materials in package internal beam structures and circuit cards, as a means of reducing internal vibration responses, reveals that reductions are not enough to justify procurement and qualification of these materials at this time. More liberal use of the materials throughout a package will be investigated with respect to inherent weight penalty, current package failure rate, and reduction of responses achieved.

#### ACKNOWLEDGMENT

The author expresses appreciation to R. Gonzales of LMSC for his valuable contribution in the implementation of the laboratory experiments.

\* \* \*

# **RANDOM-VIBRATION RESPONSE DATA FOR ORBITING GEOPHYSICAL OBSERVATORY: FLIGHT, ACOUSTIC, AND VIBRATION TEST**

William G. Elsen  
NASA Goddard Space Flight Center  
Greenbelt, Maryland

Random-vibration response data for the Orbiting Geophysical Observatory are presently available from three sources: launch phase of flight spacecraft, acoustic test, and random-vibration test. A study was made to determine how well ground tests (acoustic and vibration) can duplicate the actual flight random environment, and how well a random-vibration test can simulate an acoustic test. Results of this study are presented.

Comparison of flight response and acoustic test response indicates that below 300 Hz the acoustic test was conservative. This difference is partially explained by the fact that the acoustic test levels in the low-frequency bands were higher than desired, and probably resulted from ground reflection of the longer wavelengths associated with the low-frequency acoustic energy. However, above 300 Hz the data show that the acoustic test was a reasonable approximation of the flight environment. The data were digitized and a small computer program was developed to compare the two test responses. The program produced plots of average PSD vs frequency per axis, and plots of average PSD vs frequency for all three axes together, for both acoustic and vibration data. Standard deviations of these averages are also plotted on the same graphs.

Comparison of the average response levels in the lateral axes shows that the vibration test seems to do a fairly good job of simulating the acoustic test except below 50 Hz, where the acoustic test response was excessively high because of ground reflection. In the longitudinal axis, the vibration test response was much higher than the acoustic test response between 50 and 700 Hz. This result is probably caused by the fact that the modes of vibration in the longitudinal axis are at higher frequencies than the lateral modes and therefore the amount of isolation is less.

Conclusions are as follows:

1. An acoustic test can produce a good duplication of the flight environment if the basic input acoustic spectrum is modified to compensate for facility peculiarities and unrealistic boundary conditions.
2. A random-vibration test can be a fairly good simulation of an acoustic test. However, there are other drawbacks of a vibration test: energy transmission paths are unrealistic; energy is introduced into the spacecraft only one axis at a time; and to get a sufficiently high level of vibration into many parts of the spacecraft, it is necessary to input a considerable amount of energy at the base of the spacecraft.

Therefore, an acoustic test is still the best simulation of the random-vibration portion of the flight environment and should be performed where possible instead of a random-vibration test.

## **INTRODUCTION**

Random-vibration response data for the Orbiting Geophysical Observatory (OGO) spacecraft are presently available from three sources: launch phase of flight spacecraft, acoustic test, and vibration test.

Launch data are available from two OGO launches (OGO-A and OGO-C) and include mean squared acceleration density plots (or power spectral density, PSD) from both the liftoff portion and the maximum dynamic pressure portion (max Q) of flight. The acoustic test data (also in the form of PSD plots) come

from the acoustic test of the OGO structural model spacecraft conducted at the Langley Research Center, Hampton, Virginia. The vibration test data (PSD plots) originate from a well-instrumented random-vibration test of the OGO prototype spacecraft conducted at TRW Systems Group, Redondo Beach, California.

The existence of these data provided an excellent opportunity for a comparison study. This study attempts to determine how well ground tests (acoustic and vibration) can duplicate the actual flight random environment and how well a random-vibration test can simulate an acoustic test. The results of this study are presented here.

#### SOURCES OF DATA

The flight data for this study were obtained from the launches of OGO-A and OGO-C. Each of these spacecraft had two accelerometers mounted on the spacecraft-Agena adapter (interstage) just underneath the separation plane. In each case one of the accelerometers was oriented to measure longitudinal acceleration (spacecraft y axis) and the other to measure lateral acceleration (spacecraft z axis) (Fig. 1). The data from these accelerometers were telemetered to ground receivers during the powered portion of flight and recorded on tape as an acceleration time history. From this tape, tape loops were made from the liftoff portion and the maximum dynamic pressure

max Q portion of flight. Then a plot of PSD vs frequency was obtained by analysis from each tape loop.

The acoustic data used for this study came from an acoustic test of the OGO structural model spacecraft conducted at Langley Research Center [1]. This test was well instrumented, with 41 accelerometers mounted throughout the entire spacecraft at the following locations for each of the x, y, and z axes:

1. Bottom corner of spacecraft box
  2. Top corner of spacecraft box
  3. Solar array - hinge top corner
  4. Upper +Z experiment panel
  5. Lower +Z experiment panel
  6. Upper -Z experiment panel
  7. Lower -Z experiment panel
  8. Base of orbital plane experiment package 1 box
  9. Base of experiment package (EP) 1 box
  10. Base of EP-2 box
  11. Base of EP-3 box
  12. Base of EP-4 box
  13. Base of EP-5 box
  14. Base of EP-6 box (x and z axes only)
- } Body-mounted experiments  
 } Boom-mounted experiments

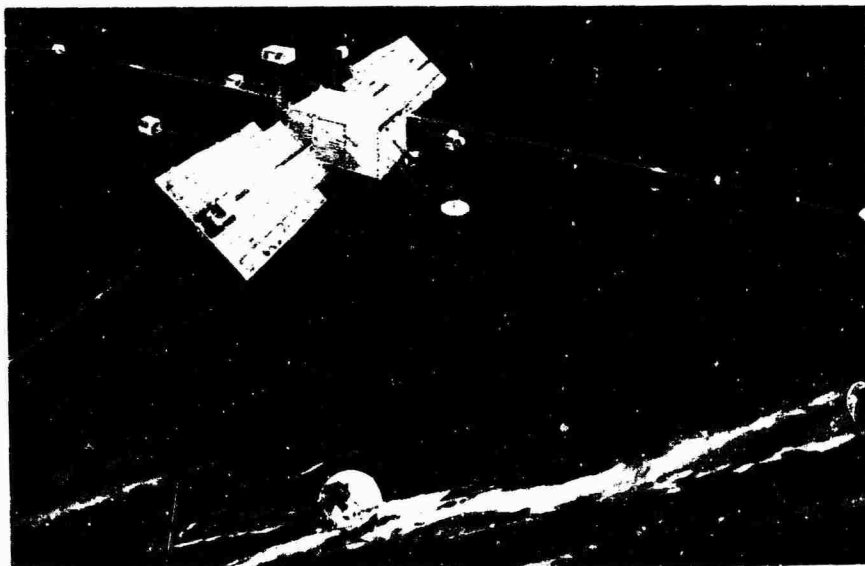


Fig. 1. Orbiting Geophysical Observatory spacecraft

The test subjected the OGO structural model spacecraft to a simulated launch acoustic environment which was generated by the exhaust of the Langley 9 by 6 ft thermal structures wind tunnel. Output signals from the accelerometers (responses) were recorded on magnetic tape. Tape loops from these data were analyzed in the Data Analysis Laboratory, and PSD vs frequency plots were generated.

The vibration response data used for this study were obtained from a random-vibration qualification test of the OGO prototype spacecraft conducted at TRW Systems Group. This test was instrumented with accelerometers mounted in the same locations as those for the acoustic test. The random response was recorded on magnetic tape from which tape loops were made, and PSD vs frequency plots were generated.

## COMPARISON OF DATA

Some general trends can be seen from looking at the PSD plots of flight response and acoustic test response (Figs. 2 through 5). Below about 400 Hz, the response at the liftoff portion of flight is greater than the response at the max Q portion of flight. Above 400 Hz, the reverse is true: max Q response is greater than liftoff response. Below about 300 Hz, the response during the acoustic test is considerably greater than the response during flight excitation. Above 300 Hz, there is good agreement between acoustic test response and the liftoff portion of flight response. However, above 300 Hz, the response during the max Q portion of flight is slightly greater than the response during acoustic test. Table 1 gives a comparison of the overall spectrum levels at the bottom corner of the spacecraft box.

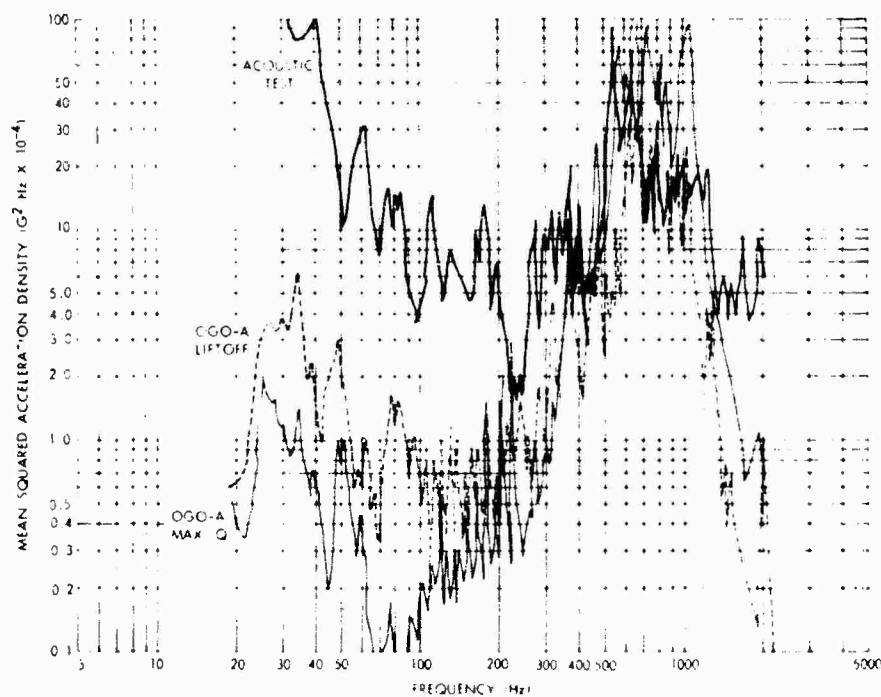


Fig. 2. Comparison of acoustic test and OGO-A flight: z axis (lateral), bottom corner of spacecraft box, PSD vs frequency

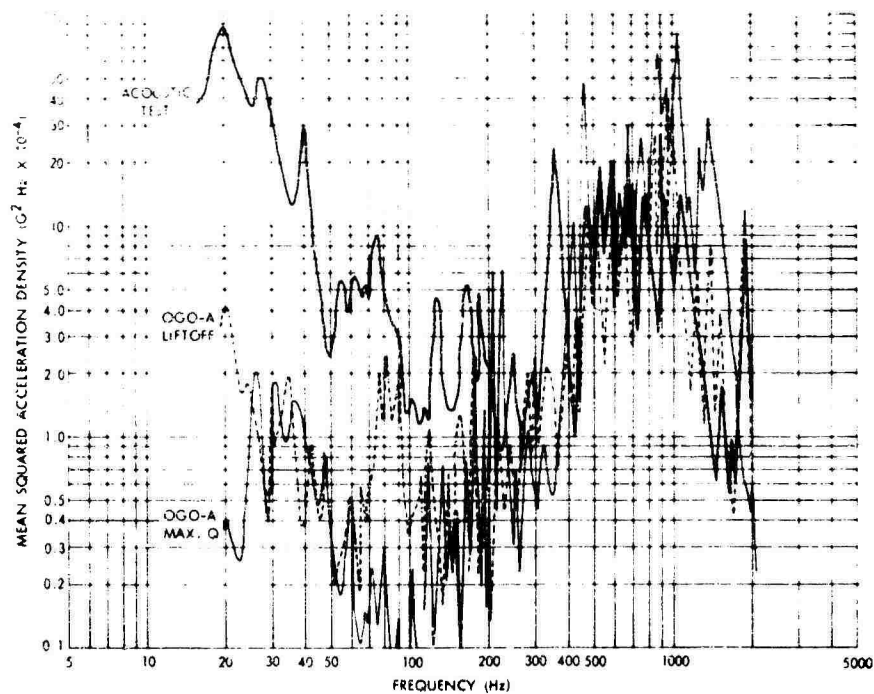


Fig. 3. Comparison of acoustic test and OGO-A flight: y axis (longitudinal), bottom corner of spacecraft box, PSD vs frequency

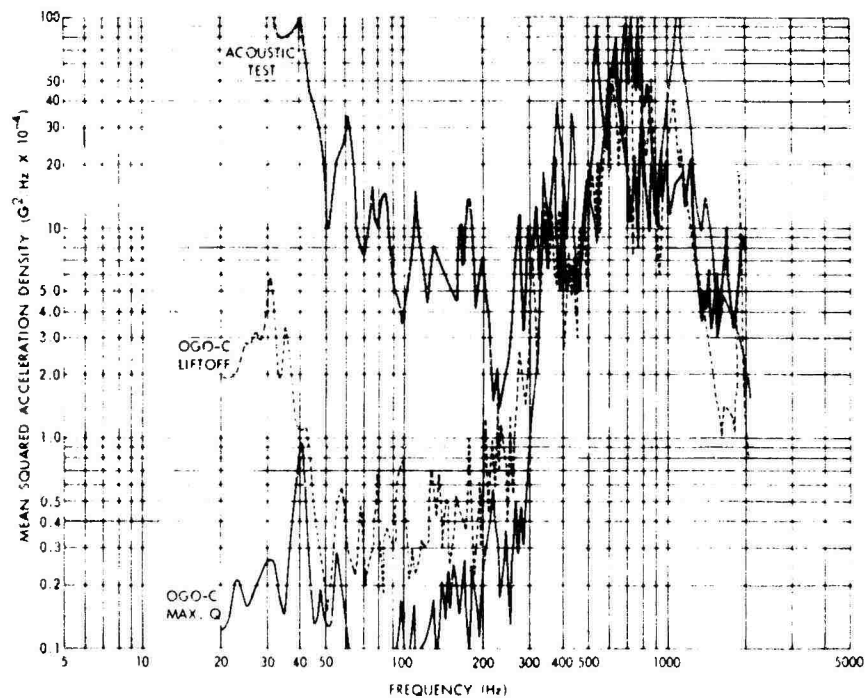


Fig. 4. Comparison of acoustic test and OGO-C flight: z axis (lateral), bottom corner of spacecraft box, PSD vs frequency

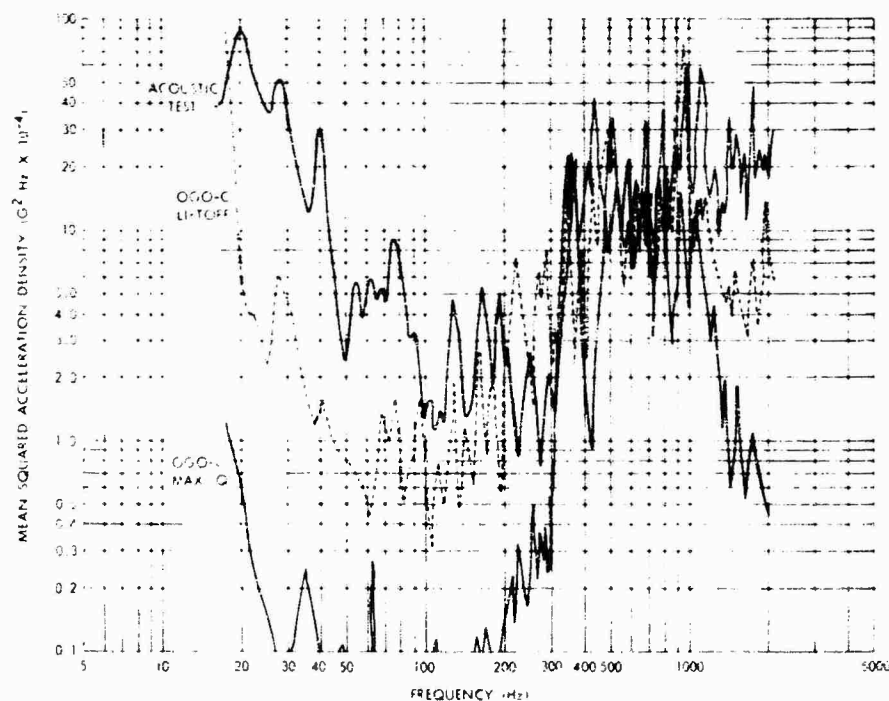


Fig. 5. Comparison of acoustic test and OGO-C flight: y axis (longitudinal), bottom corner of spacecraft box, PSD vs frequency

TABLE 1  
Overall Spectrum Levels: Flight and Acoustic Test

| Axis of Measurement | Level <sup>a</sup> (rms g) |                |       |              |       |
|---------------------|----------------------------|----------------|-------|--------------|-------|
|                     | Acoustic Test              | Flight Liftoff |       | Flight max Q |       |
|                     |                            | OGO-A          | OGO-C | OGO-A        | OGO-C |
| z (lateral)         | 2.2                        | 1.1            | 1.6   | 2.1          | 2.2   |
| y (longitudinal)    | 1.1                        | 1.2            | 1.5   | 1.9          | 2.2   |

<sup>a</sup>Bottom corner of spacecraft box.

Responses plotted in Figs. 2 through 5 indicate that below 300 Hz the acoustic test was conservative in comparison to the actual flight environment. This difference is partially explained by the fact that the acoustic test levels in the low-frequency bands were higher than desired [1], and probably resulted from ground reflection of the longer wavelengths associated with the low-frequency acoustic energy. However, above 300 Hz the data show that the acoustic test was a reasonable approximation of the flight environment.

A comparison of the vibration test level with the acoustic test response at the bottom corner of the spacecraft box (Figs. 6, 7, 8) shows that the vibration level is much more severe than the acoustically induced level. This finding is attributed to the fact that this point, near the adapter-spacecraft interface (separation plane), was the control point for the vibration test, and the spectrum in the figures is the actual input.

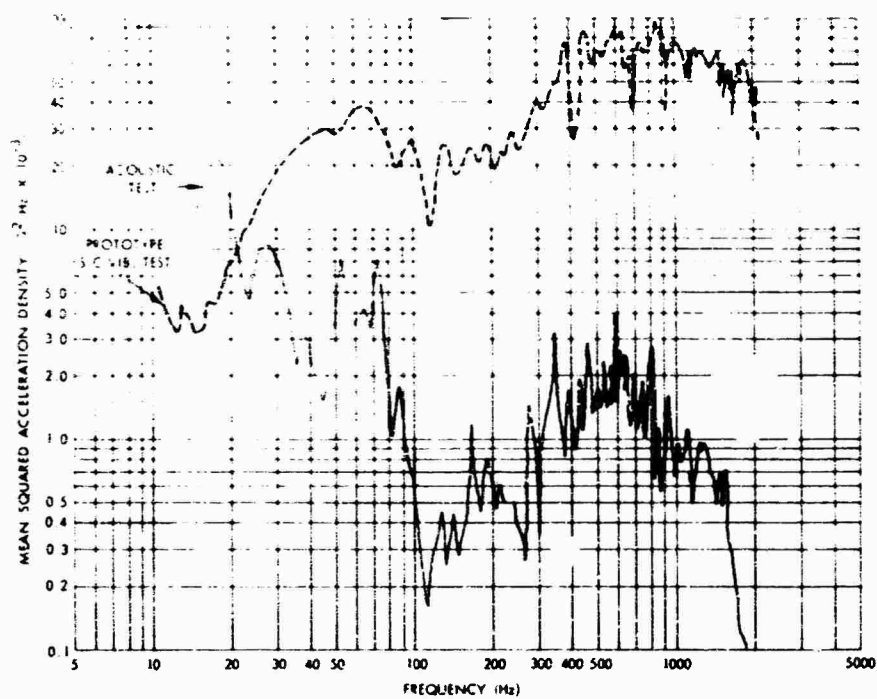


Fig. 6. Comparison of acoustic test and vibration test: x axis, bottom corner of spacecraft box, PSD vs frequency

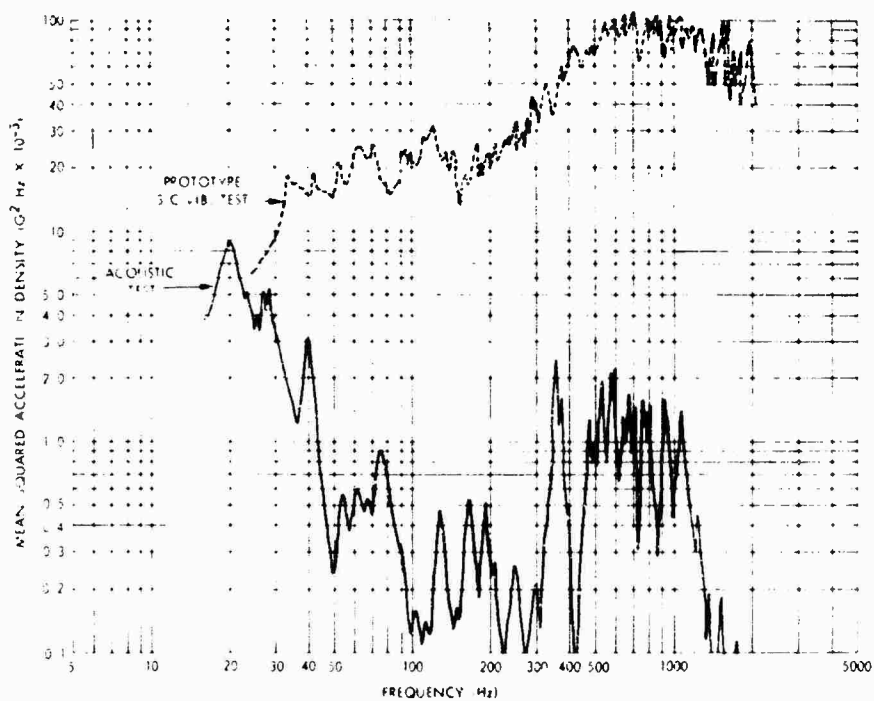


Fig. 7. Comparison of acoustic test and vibration test: y axis, bottom corner of spacecraft box, PSD vs frequency



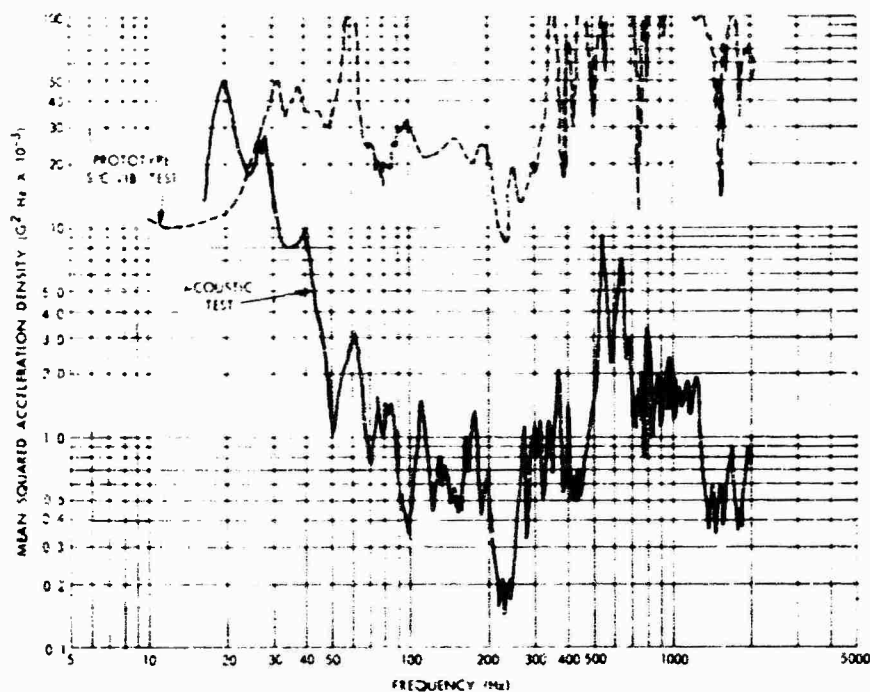


Fig. 8. Comparison of acoustic test and vibration test: z axis, bottom corner of spacecraft box, PSD vs frequency

The acoustic test response data and the random-vibration test response data for the 41 measurement points on the spacecraft were plotted on common coordinates for comparison. In examining these data, it was difficult to form an opinion as to how the acoustic and vibration responses compare since there is so much variance between points on the spacecraft. In an attempt to clarify this area of comparison, it was decided to digitize the data and obtain average PSD levels vs frequency. Therefore, all the analog plots of PSD vs frequency from the prototype spacecraft random-vibration test and the structural model spacecraft acoustic test were converted to tables of digital data. This was done by choosing 48 frequency points in the test band between 10 and 2000 Hz and listing the PSD level at each frequency. These data were entered into punch cards for use in a digital computer program. The data cards were read and processed on the CDC 3100 computer. Plot tapes generated by this computer are plotted on the 165 Calcomp digital incremental plotter by a smaller computer, the CDC 160-A.

The computer program was set up to provide several types of plotted data: plots of average PSD vs frequency for each axis and plots of average PSD vs frequency for all three axes together, for both acoustic and vibration data.

Standard deviation of these averages has also been plotted on the same graphs by plotting the average plus the standard deviation and the average minus the standard deviation (see Figs. 9 through 20).

Figures 21, 22, and 23 present comparisons of the acoustic test average PSD curve and the vibration test average PSD curve for each of the three axes of measurement (x, z, y). Figure 24 presents a comparison of the acoustic test average PSD curve and the vibration test average PSD curve for all measurements (three axes).

It should be noted that the random-vibration test responses presented here were obtained from a qualification level vibration test which was intended to be more severe than flight levels (50 percent greater overall level and 125 percent greater acceleration density levels). Therefore, in order to compare them with the acoustic test responses which were produced by a simulated launch environment, the vibration response curves (PSD levels) in Figs. 21 through 24 have been corrected by reducing the measured values by a factor of 4.9. The shaded area on these four figures denotes the ±3-dB tolerance allowed by specification in random-vibration testing [2].

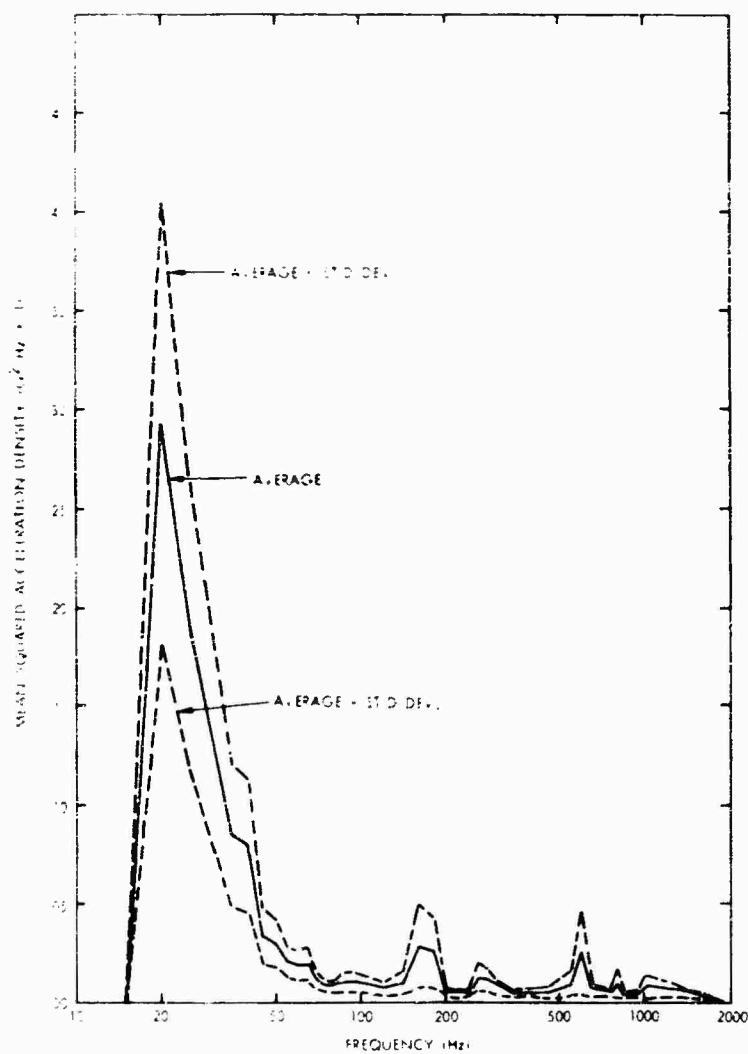


Fig. 9. Acoustic test: x-axis average, PSD vs frequency with standard deviation

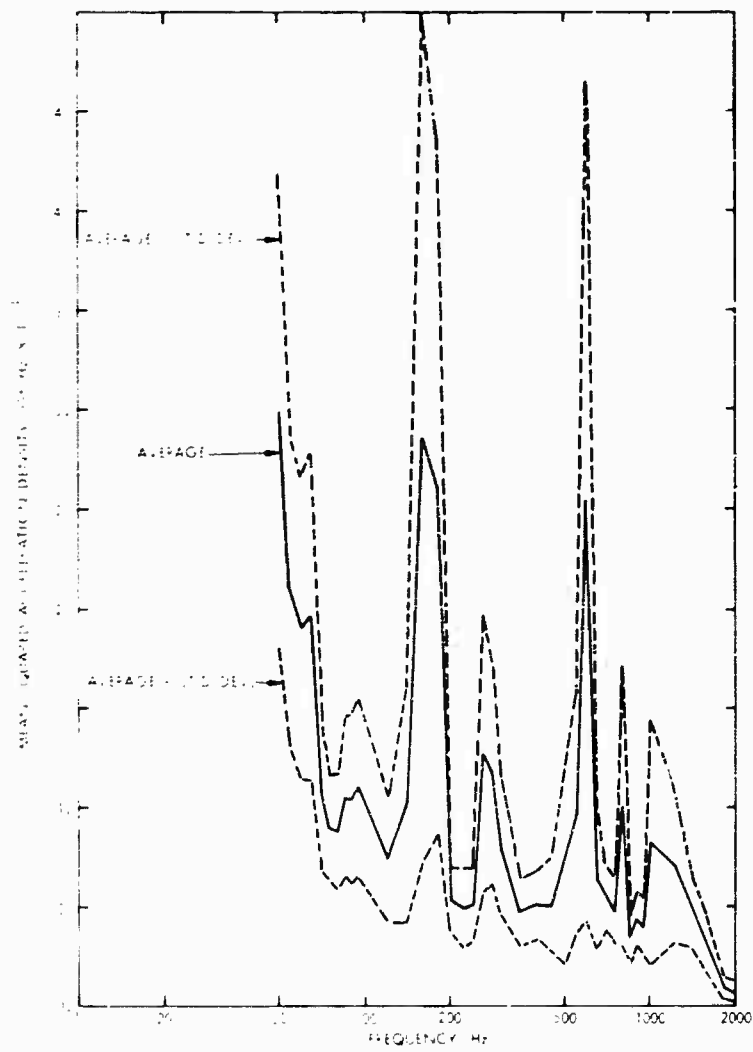


Fig. 10. Acoustic test: x-axis average, PSD vs frequency with standard deviation (expanded scale)

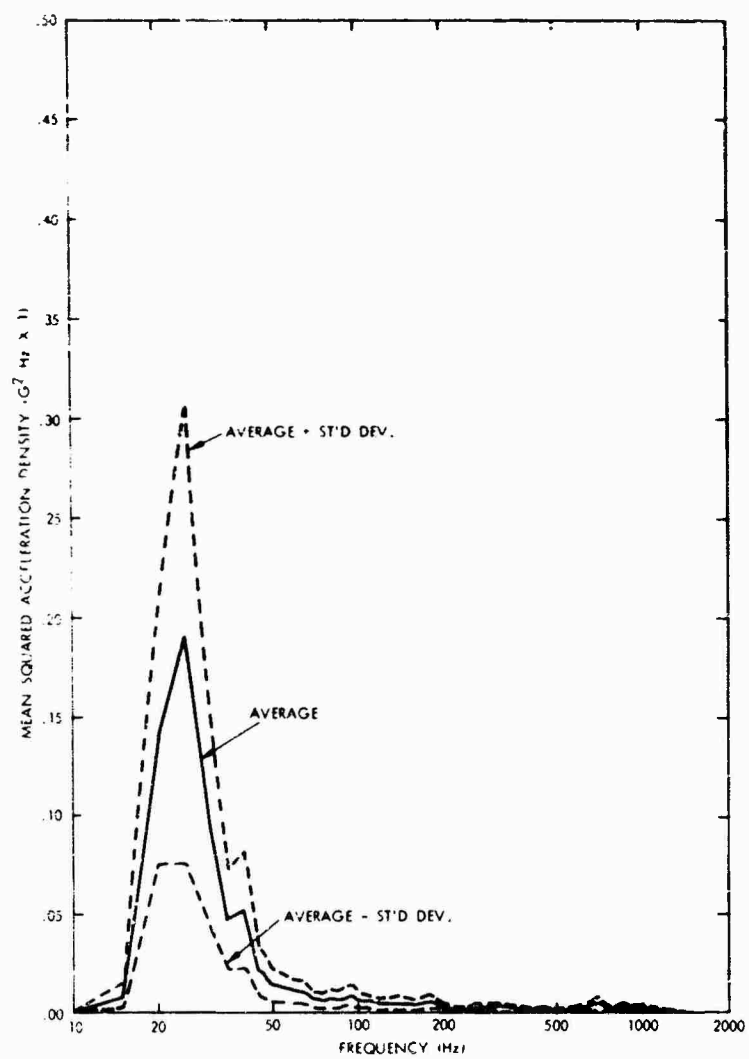


Fig. 11. Acoustic test: y-axis average, PSD vs frequency with standard deviation

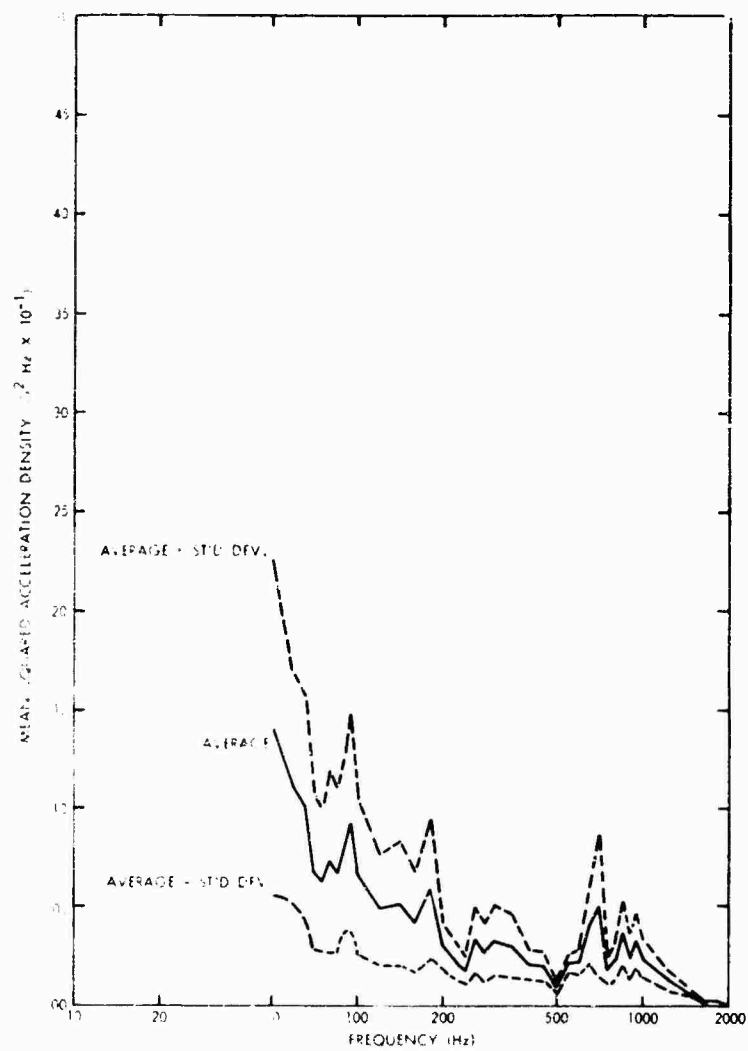


Fig. 12. Acoustic test: y-axis average, PSD vs frequency with standard deviation (expanded scale)

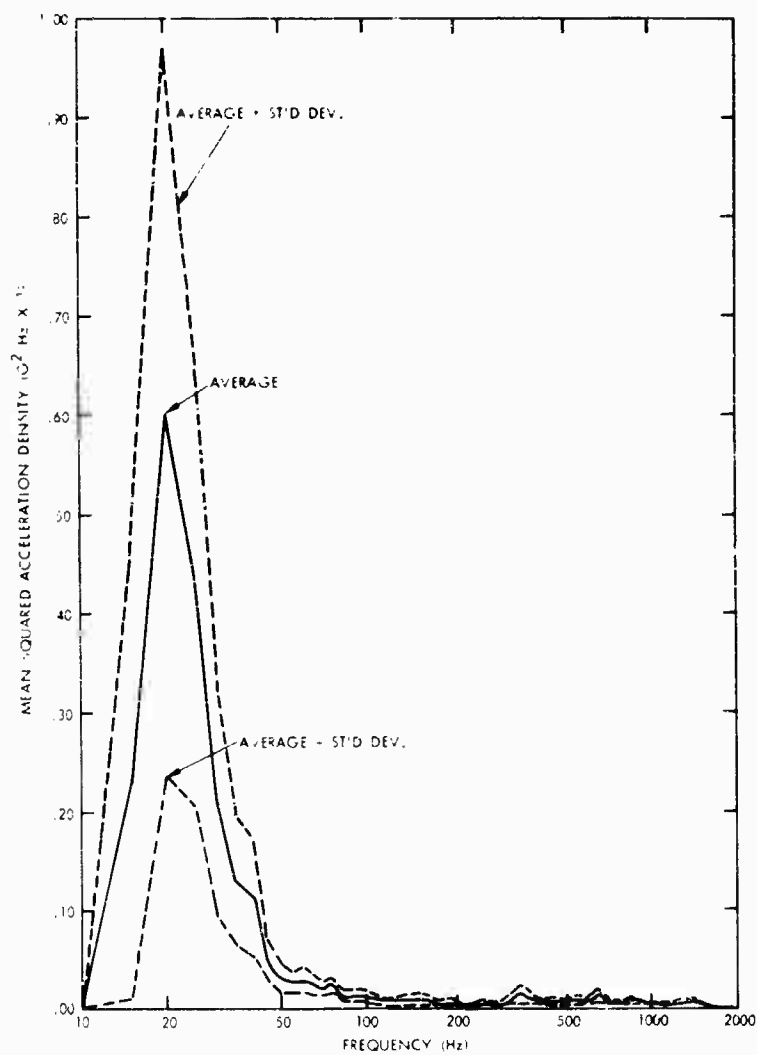


Fig. 13. Acoustic test: z-axis average, PSD vs frequency with standard deviation

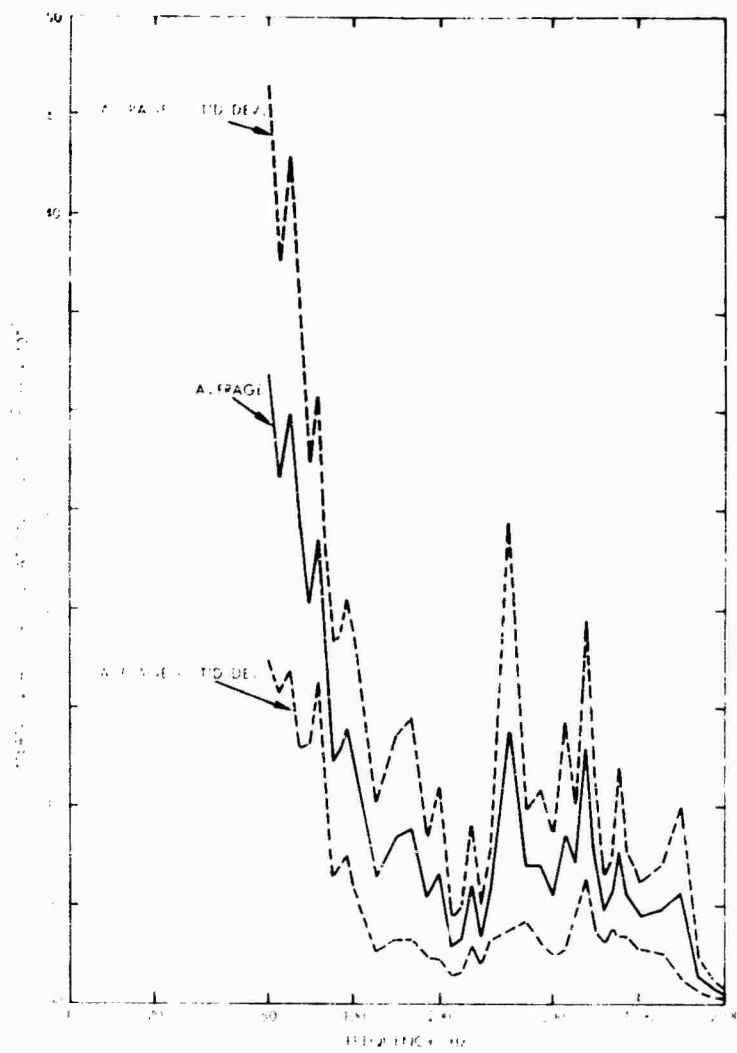


Fig. 14. Acoustic test:  $z$ -axis average, PSD vs frequency with standard deviation (expanded scale)

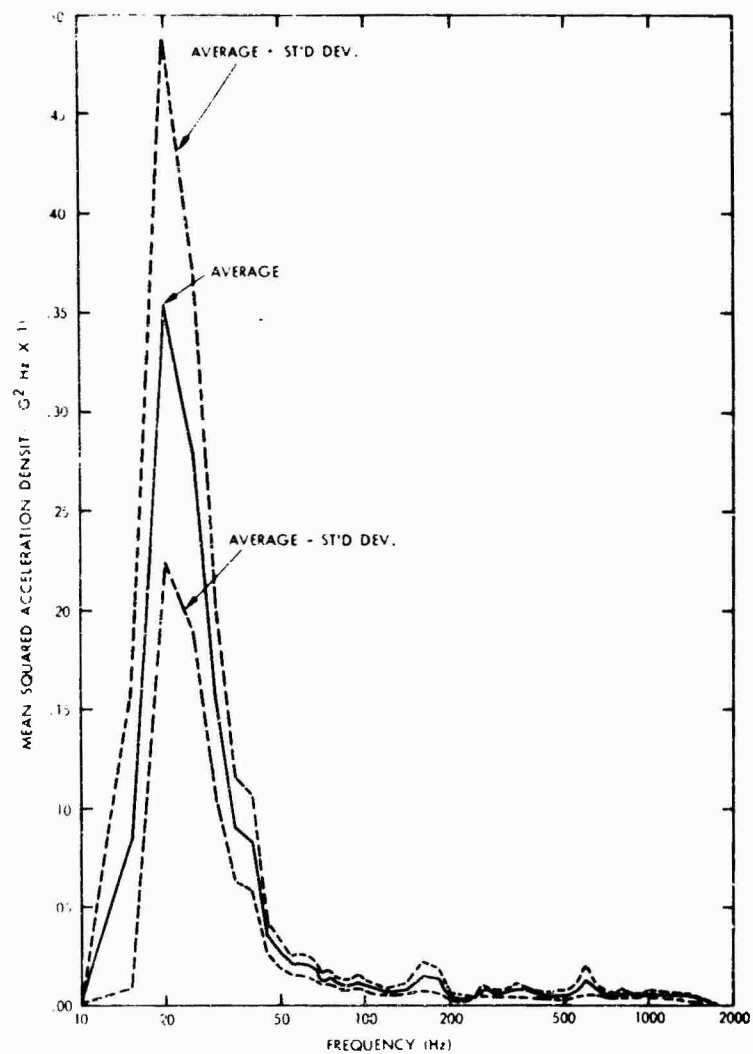


Fig. 15. Acoustic test: three-axis average, PSD vs frequency with standard deviation



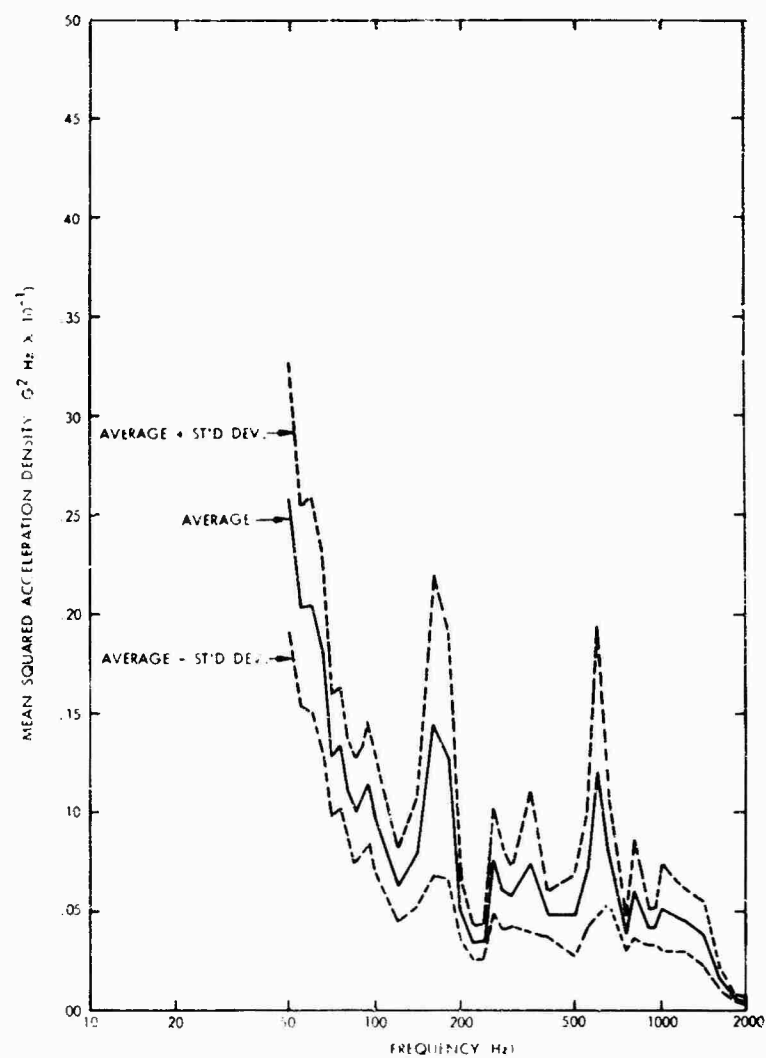


Fig. 16. Acoustic test: three-axis average, PSD vs frequency with standard deviation (expanded scale)

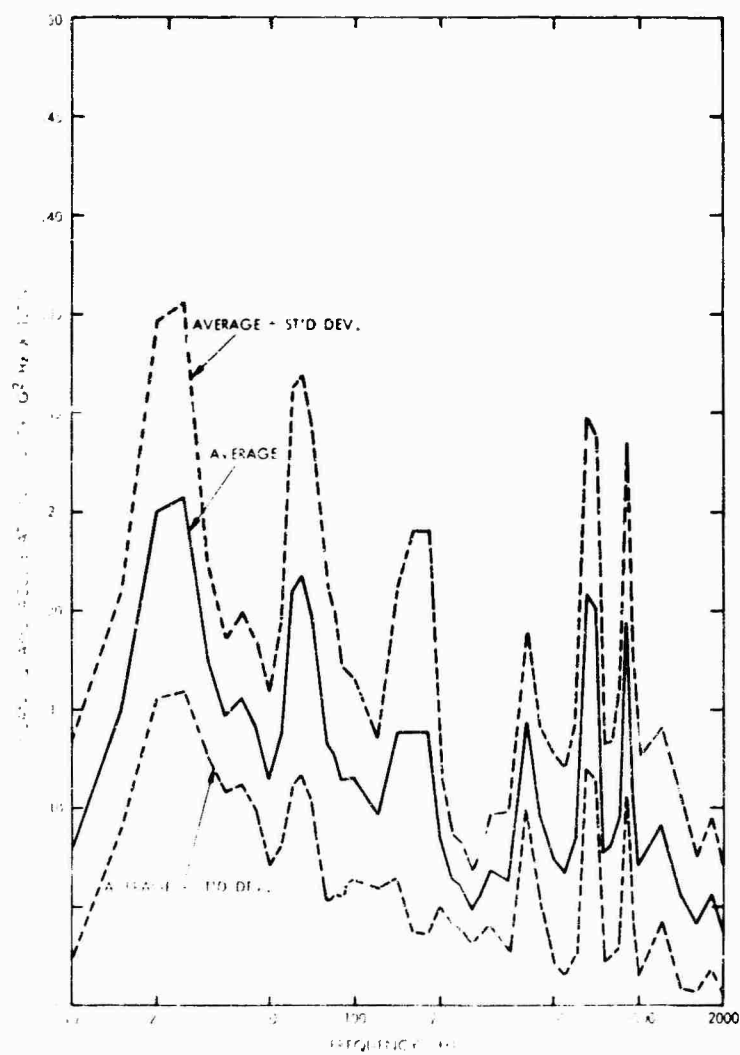


Fig. 17. Vibration test: x-axis average, PSD vs frequency with standard deviation

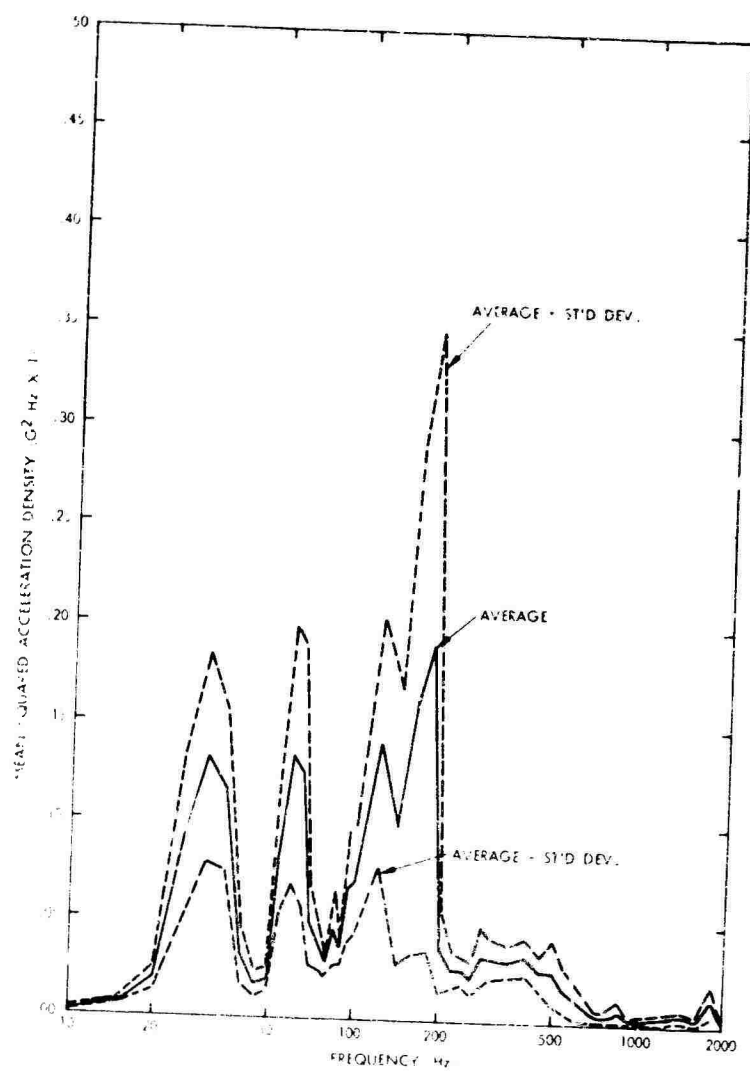


Fig. 18. Vibration test: y-axis average, PSD vs frequency with standard deviation

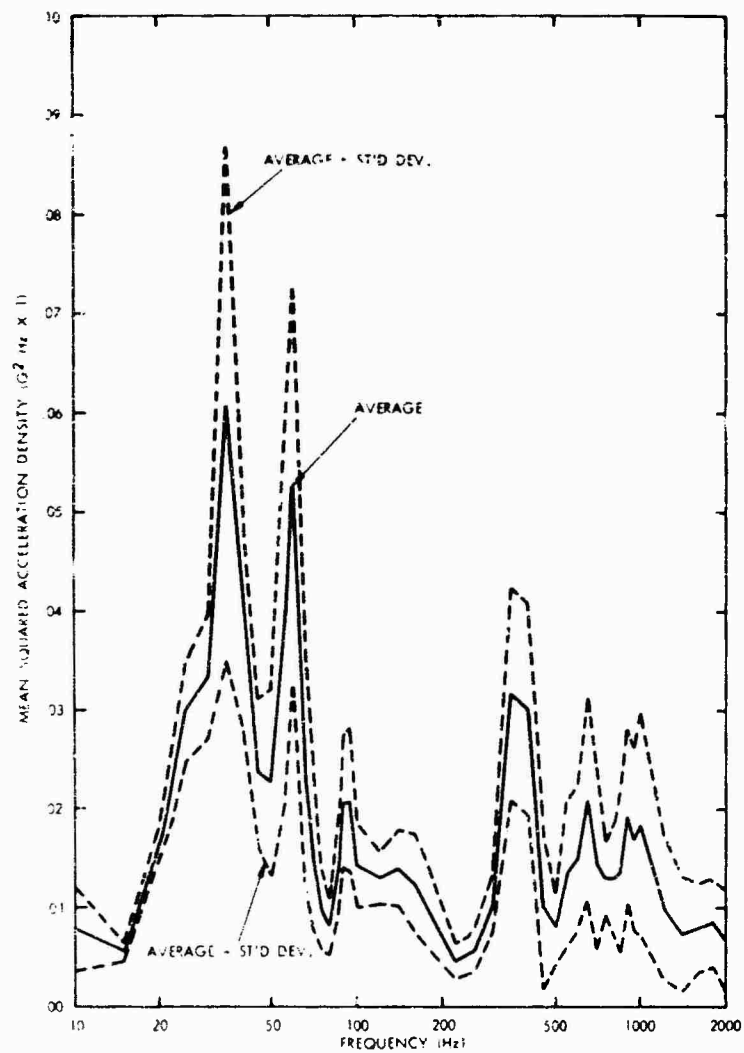


Fig. 19. Vibration test: z-axis average, PSD vs frequency with standard deviation

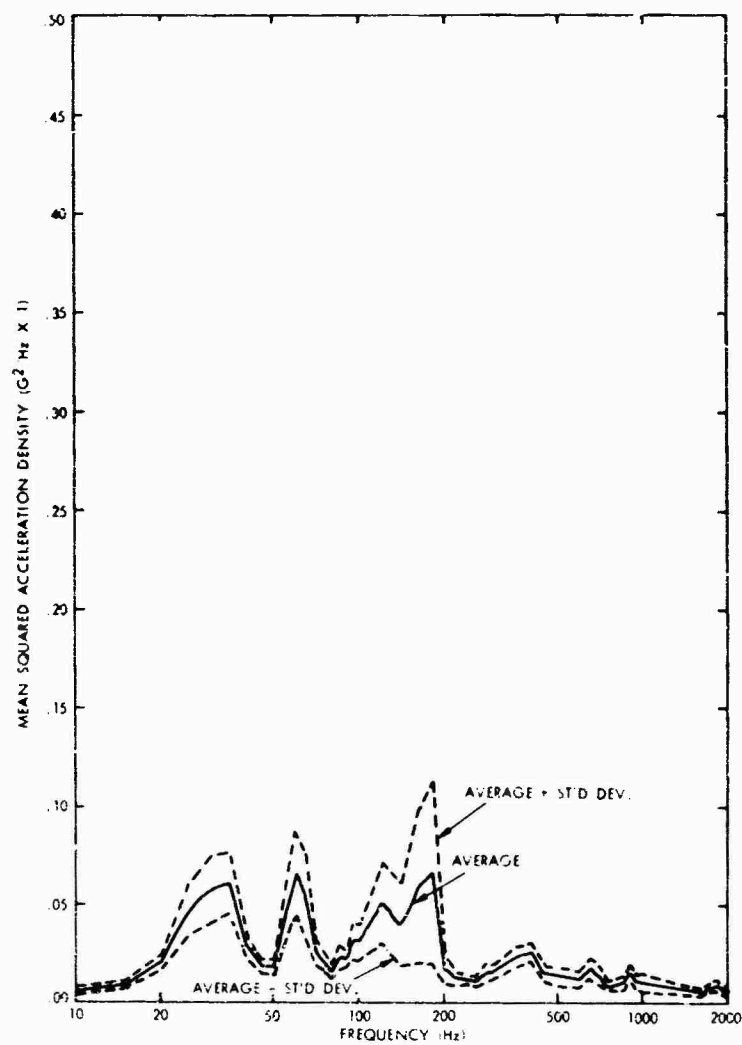


Fig. 20. Vibration test; three-axis average, PSD vs frequency with standard deviation

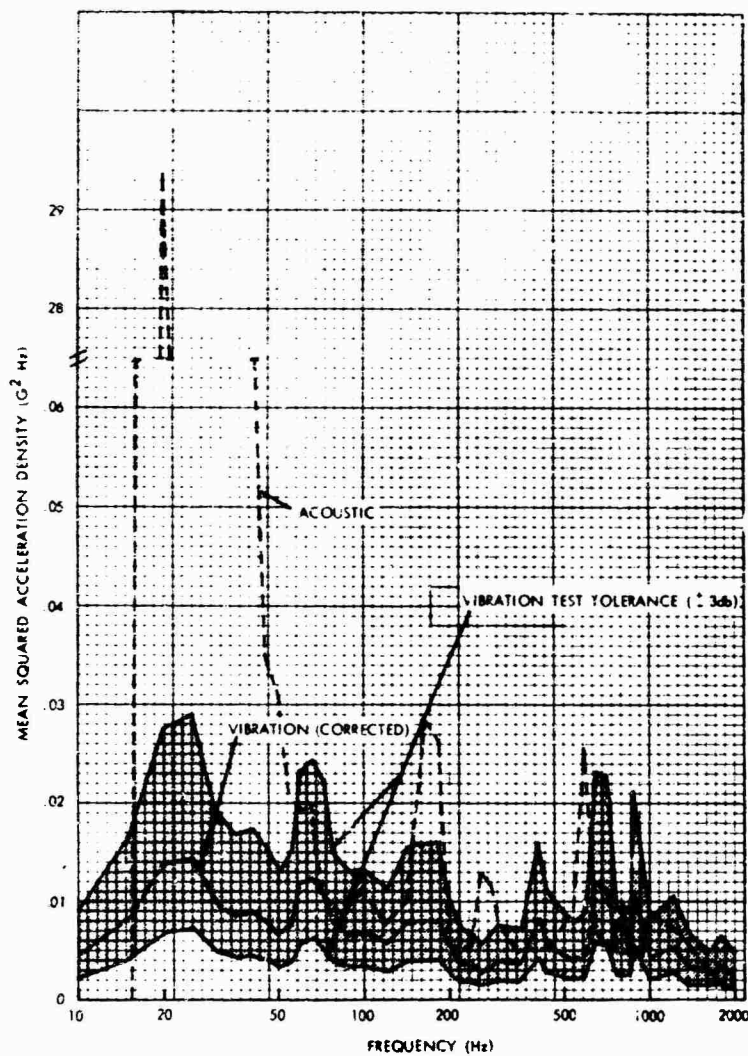


Fig. 21. Comparison of acoustic test and vibration test:  
x-axis average, PSD vs frequency

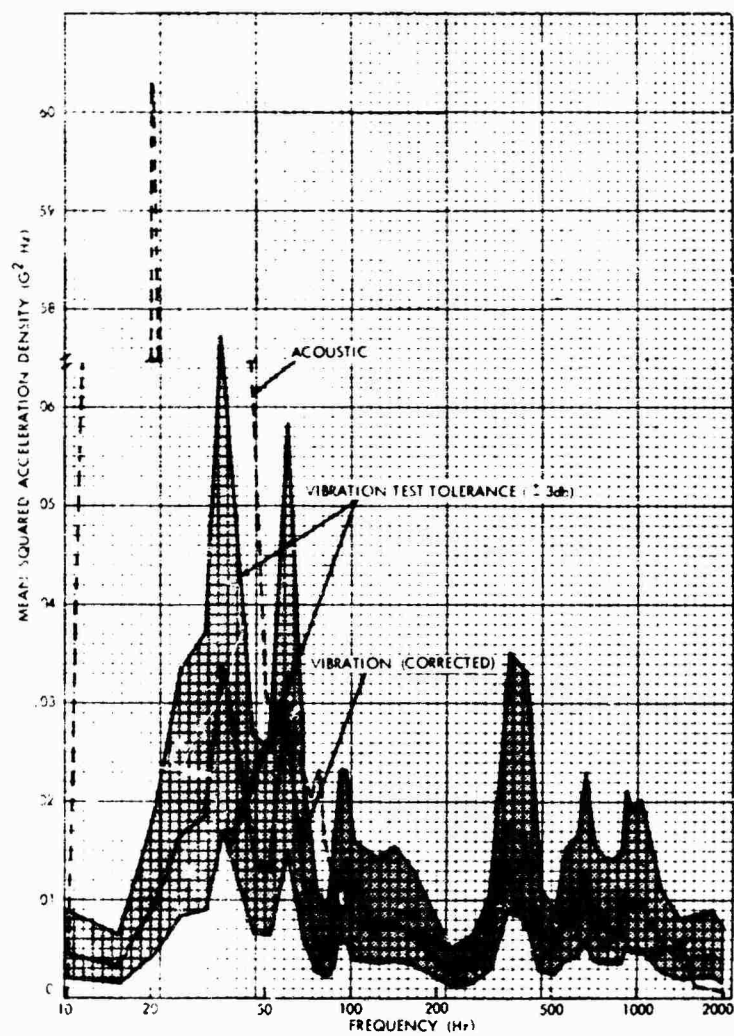


Fig. 22. Comparison of acoustic test and vibration test:  
z-axis average, PSD vs frequency

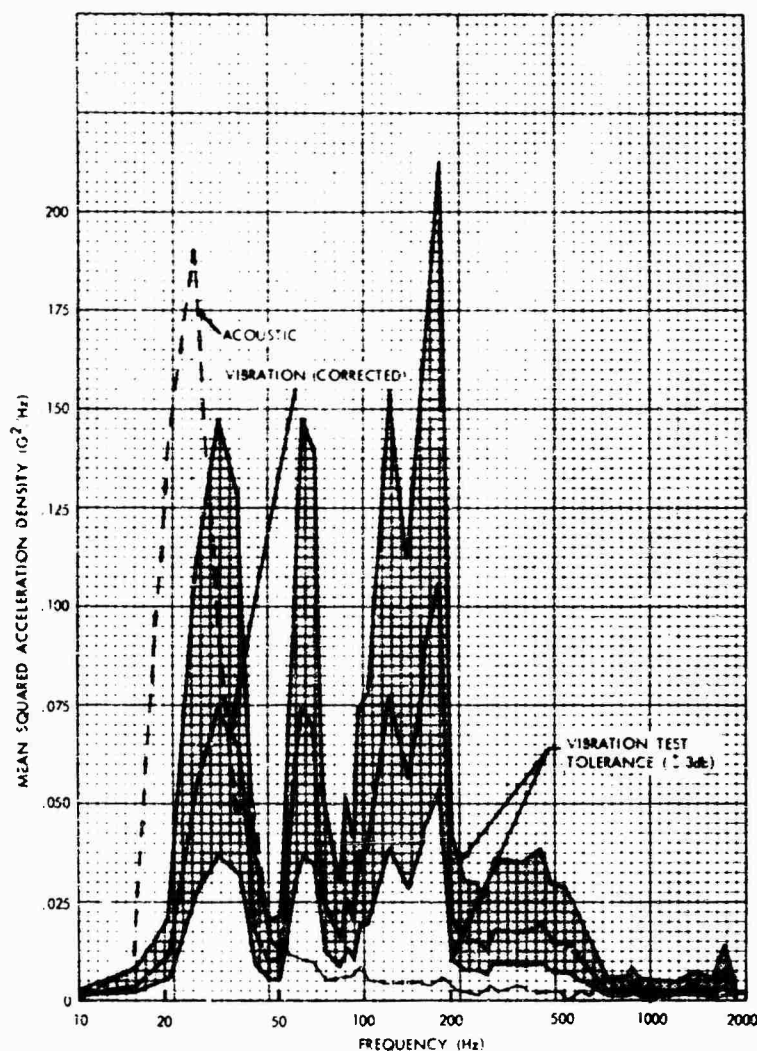


Fig. 23. Comparison of acoustic test and vibration test: y-axis average, PSD vs frequency

In both the x-axis and z-axis plots (Figs. 21 and 22), it can be seen that, in the frequency band from 15 to 50 Hz (approximately), the acoustic test response is much higher than the vibration test response. For the remaining frequency band (50 to 2000 Hz), the two responses are fairly close. In contrast to the x- and z-axis comparisons, the y-axis (longitudinal) comparison plot (Fig. 23) shows a different trend. In the frequency band from approximately 50 to 700 Hz, the vibration response is considerably greater than the acoustic response. The agreement in the 15- to 50-Hz band is much better, however, than occurred in the lateral axes (x and z). The acoustic response between 15 and 30 Hz still exceeds the vibration response, but not by nearly as great

a margin as occurred in this frequency band in the lateral axes. In the triaxial plot (Fig. 24), the acoustic test response is much higher than the vibration test response in the 10 to 50 Hz frequency band. In the remainder of the test band (50 to 2000 Hz), the vibration test response agrees fairly well with the acoustic test response.

## RESULTS

The data indicate that the acoustic test was conservative in the low-frequency region (below 300 Hz) compared to the actual flight levels. If the acoustic test levels in this frequency region had been reduced, a better duplication of



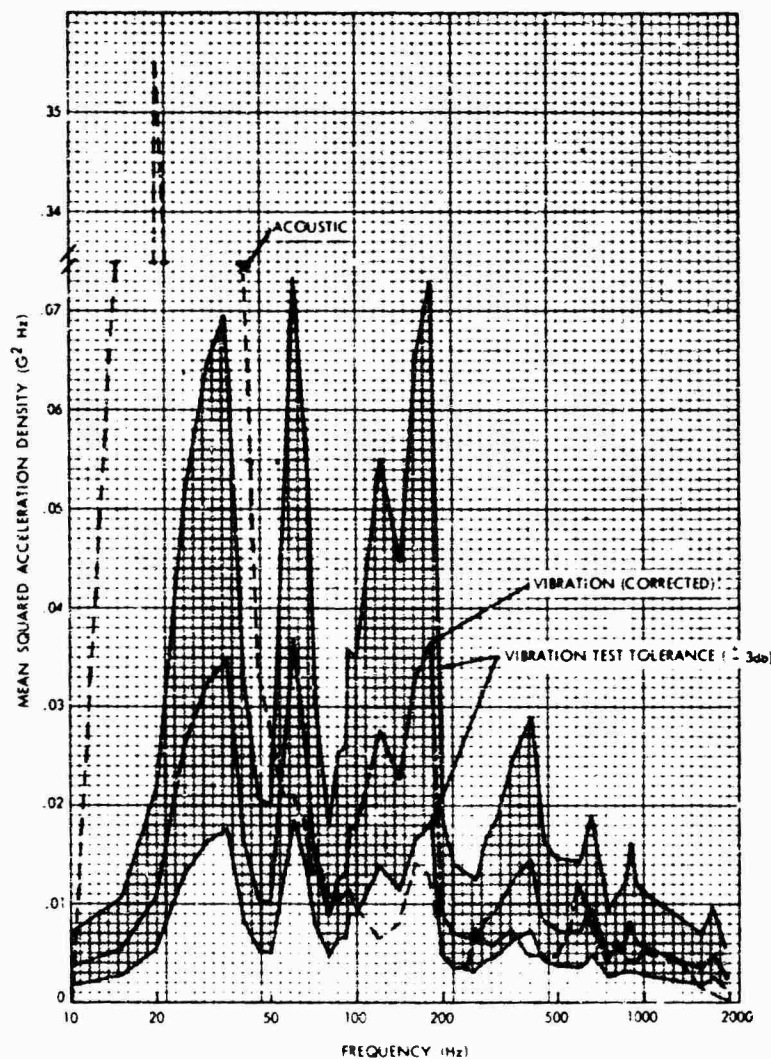


Fig. 24. Comparison of acoustic test and vibration test: three-axis average, PSD vs frequency

the flight environment would have been obtained over the entire frequency range of significance. Therefore, it can be concluded that an acoustic test can produce a good duplication of the flight environment if the basic input acoustic spectrum is modified to compensate for the anomalies produced by the particular test facility being used.

On the other hand, the simulation of an acoustic test by a random-vibration test presents problems. First, the energy transmission paths to any point in the spacecraft are significantly different between acoustic and vibration tests. In an acoustic test the energy arriving at a given point comes through two paths: air and structure. In a vibration test,

all the energy is structure borne and it is introduced into the spacecraft at one location (base of the spacecraft box). Furthermore, in a vibration test, the energy is introduced into the spacecraft only one axis at a time as opposed to the somewhat omnidirectional acoustic field. To get a sufficiently high level of vibration into many parts of the spacecraft, it is necessary to input a considerable amount of energy at the base of the spacecraft in a vibration test. (Structure, of course, attenuates much of the vibration, especially in the high-frequency region.)

Comparison of the average response levels in the lateral axes (x and z) shows that the vibration test seems to do a fairly good job of

simulating the acoustic test, except below 50 Hz, where the acoustic test response was excessively high, as mentioned above. This high response below 50 Hz was probably caused by the long wavelengths of the low-frequency energy being reflected from the ground into the spacecraft. This agrees with the high, out-of-specification, measured sound pressure levels in the 20- to 75-Hz octave band [1]. In the longitudinal axis (y), the vibration test response is excessive between 50 and 700 Hz. This probably results from the fact that the modes of vibration in the longitudinal axis are at higher frequencies than the lateral modes and therefore the amount of isolation is less. To summarize, then, the specified random-vibration test in the present general Agena test specification [2] produced responses that compare with the acoustic test responses as follows:

1. Good agreement in the lateral axes at frequencies over 50 Hz (tolerance is  $\pm 3$  db on PSD input levels in the vibration test specification [2]);

2. Poor agreement in the lateral axes at frequencies under 50 Hz, and in the longitudinal

axis over a large portion of the frequency range (50 to 700 Hz).

## CONCLUSION

It appears that a random-vibration test can be a fairly good simulation of an acoustic test if (as in this case of OGO) the vibration input levels in the longitudinal direction of test were somewhat less, in certain frequency bands, than the lateral input levels.

However, an acoustic test is still the best simulation of the flight (launch) environment and should be performed, where possible, instead of a random-vibration test. In accordance with this belief, our present philosophy in the Test and Evaluation Division at the Goddard Space Flight Center is to make use of the acoustic test capability of our new launch phase simulator and, whenever possible, test spacecraft acoustically as a preferred alternate to random-vibration testing or a vibration generator. The Test and Evaluation Division is recommending that revisions reflecting this philosophy be made in the general test specifications for spacecraft issued by the Goddard Space Flight Center.

## REFERENCES

1. Paul J. Alfonsi, "The Vibration Response of an Orbiting Geophysical Observatory Spacecraft Full-Scale Structural Model to a Simulated Launch Acoustic Environment," NASA Rept. X-320-66-353, Aug. 1966
2. "General Environmental Test Specification for Spacecraft and Components Using Launch Environments Dictated by Atlas-Agena, Thor-Agena, or Thrust-Augmented Thor-Agena Launch Vehicles." NASA-GSFC Specification S-320-A-1, Oct. 1965

## DISCUSSION

Mr. Parmenter (Naval Weapons Center): Could you establish stationarity in the vibration data?

Mr. Elsen: For the flight response we have PSD's from both liftoff and max Q. In each area the data were locally stationary over the period for which we analyzed it. It isn't really stationary data, strictly speaking, but it is close enough to give satisfactory results for what we were doing.

Dr. Morrow (LTV Research Center): There is no such thing as a stationary random vibration, but the concept is still a useful one.

Mr. Smith (Martin-Marietta Corp.): I am interested in the manner in which your acoustic test was conducted.

Mr. Elsen: The test was conducted at Langley in a 9 by 6 ft blowdown tunnel which generates fairly interesting sound fields for test purposes. The spacecraft in its shroud is set on a truck bed on an isolated mount in this sound field at a point chosen by a sound pressure level survey. It was oriented to give an acoustic input spectrum that matched, as best we could, the flight spectrum. A report of this acoustic test on the overall structural model was in the 34th Shock and Vibration Bulletin.

Mr. Mustain (Douglas Space Systems Center): Is the acoustic test specification based on liftoff or max Q?

Mr. Elsen: It was based on a combination of both.

Dr. Morrow: Generally speaking, you indicated a preference for the acoustic noise test over the vibration test. The example that you gave was a spacecraft, so one could infer that you are talking only about spacecraft. Is this

true or were you talking about everything in general?

Mr. Elsen: I was talking about spacecraft.

\* \* \*

## RANDOM-VIBRATION TEST LEVEL CONTROL USING INPUT AND TEST ITEM RESPONSE SPECTRA

A. J. Curtis and J. G. Herrera  
Hughes Aircraft Company  
Culver City, California

Testing which simulates the predicted aircraft flight vibration environment for an equipment rack or assembly made up of a number of black boxes plus the supporting rack structure is discussed. The rack may be considered an extension of the aircraft structure, and the vibration level is defined at the attachment points of the individual units to the rack, and possibly at the attachments of the rack to the aircraft. To a reasonable approximation, the center frequencies of the narrow-band spikes which occur at unit attachment points are defined by the transmission characteristics of the loaded rack structure. Therefore a test method has been devised in which the control of the vibration level uses both the input spectrum, defined by the power average of the acceleration at the assembly attachment points, and the response spectra, measured at the attachment points of the individual units. The maximum input spectrum corresponds to the predicted broad-band random vibration. The maximum response, averaged over the appropriate narrow frequency band and measured at any unit attachment point, corresponds to the predicted narrow-band vibration, which is also an extreme value. If, with the maximum input, the maximum response is exceeded in test, the input is reduced in the corresponding frequency band to limit the response to the predicted maximum value. However, a minimum input spectrum which will avoid the acceptance of a poor rack structure may also be defined.

In this way, the impedance characteristics of the equipment are empirically accounted for by allowing a resonant response within the assembly to force a notch in the spectrum at the attachment points. Similar action will occur in the aircraft installation, analogous to the operation of a dynamic vibration absorber.

The method of implementing an assembly test using input and response control is also described. Because of nonlinearities of response, the method requires an iterative procedure in which the shaped input spectrum is refined as the input level is increased in steps up to the maximum level.

The use of hybrid analog-digital spectral analyzer, with further use of the digital portion for computation of the shaped input spectrum for each iteration, is described. The results of using this method on an air-to-air guided missile are presented.

### INTRODUCTION

Another paper [1] describes the statistical prediction of the aircraft flight vibration environment, for a given flight dynamic pressure, at the attachment points of an individual electronic unit, i.e., black box. It was shown that the environment can be described by a broad-band random vibration with approximately constant spectral density, plus several narrow-band random-vibration spikes superimposed. While the envelope and bandwidths of these spikes are predicted, the center frequencies of the spikes cannot be predicted but are determined by the (unknown) impedance characteristics of the aircraft structure and the equipment. Figure 1, reproduced from Ref. [1], shows the predicted

broad-band base level  $W(\bar{K}_i)$  and the envelope of the spikes  $W(\bar{K}_i + 2.33 S_i)$ , with simplified spectra for design and test requirements shown by the solid line and hat sections, respectively.

A second paper [2] describes the use of combined broad-band and stepped narrow-band random vibration for design verification of individual hard-mounted units or black boxes. Figure 2, reproduced from Ref. [2], shows the general spectrum employed; Ref. [2] describes the method of programming the narrow-band excitation through the frequency range to verify the design for any occurrence of the center frequencies.

The present paper, completing the trilogy, is concerned with the method of testing which

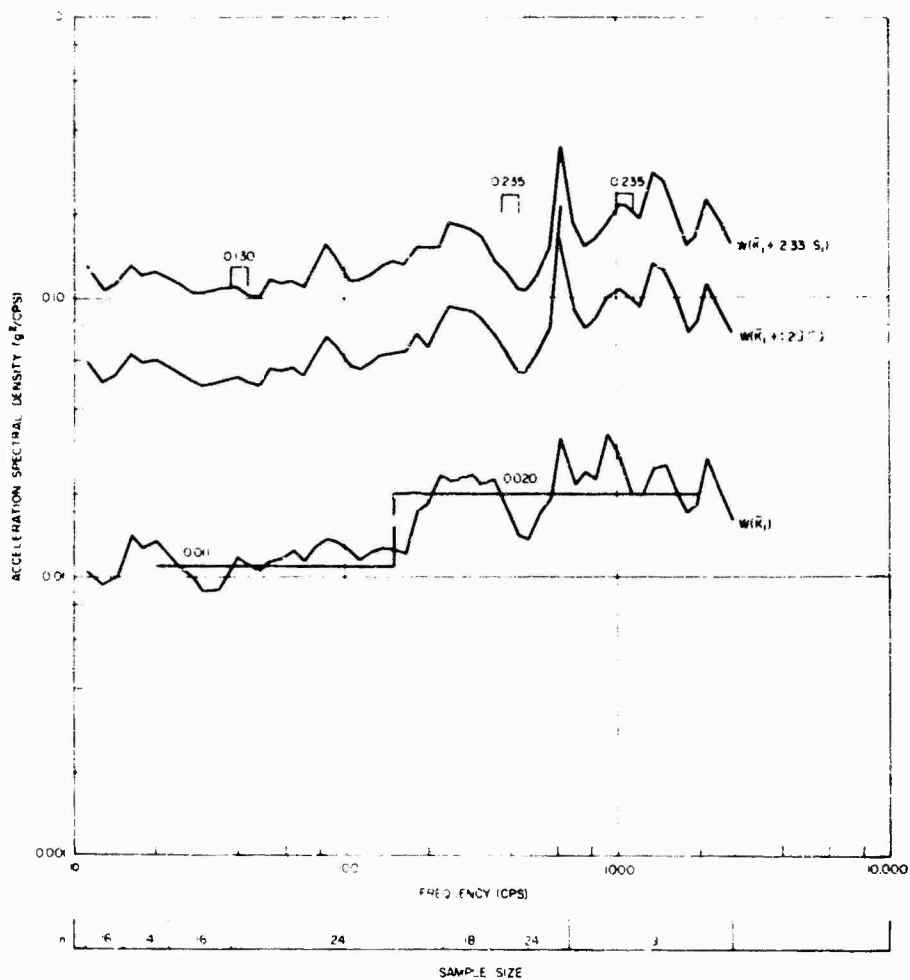


Fig. 1. Predicted spectral density, exposed equipment, all directions

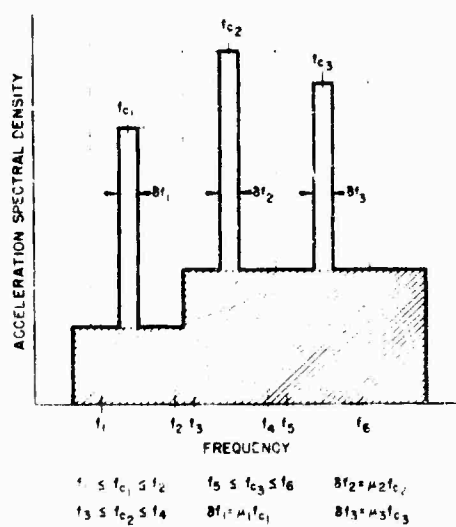


Fig. 2. General broad-band plus constant percentage narrow-band random-vibration spectrum

simulates the predicted environment for larger test items, made up of a number of black boxes and classified as assemblies.

#### DEFINITION OF ASSEMBLY

To differentiate classes of test items requiring different methods of test level control, larger test items, such as an equipment rack containing a number of individual units or a complete missile, are defined as assemblies. The classification of a test item as an assembly is not based solely on the weight or size of the test object but rather on the following two judgment factors. First, as shown schematically in Fig. 3, the test item contains a number of units whose attachment points to the supporting rack or structure are points at which the vibration environment is predicted by the method of Ref. [1]. Also, these unit attachment points are removed from the attachment points of the assembly to the test fixture at which the test level is to be actively controlled. Of course, these latter points could also be points at which the environment is predicted using Ref. [1]. Alternatively, an item classified as an assembly includes a number of points at which accelerometers would logically be located in a program to measure the flight vibration environment of the equipment. Thus a single large unit, such as an antenna, could well be classified as an assembly. Second, the test item is such that resonant response can be expected to "load down" the aircraft structure to which it is attached, in the manner of a dynamic vibration absorber [3].

It is necessary to differentiate between hard-mounted and vibration-isolated assemblies. Only hard-mounted assembly testing is discussed here.

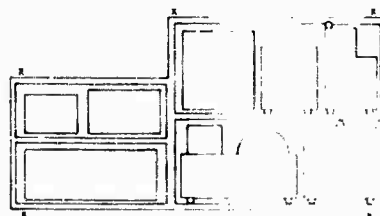
#### TEST LEVEL CONTROL FOR ASSEMBLY TEST

In developing an appropriate method for control of the test level for an assembly test, it is important to recall that the maximum or extreme spectral density of the spikes predicted in Ref. [1], can occur at any frequency but will not occur at every frequency. Nor will the spectral density of a spike necessarily reach the extreme value. Further, the frequency resolution employed for test level control must be consistent with the frequency resolution employed in the prediction method. Thus, for consistency with Ref. [1], a constant 10 percent bandwidth analysis is required.

Considering a hard-mounted assembly as represented in Fig. 3, the equipment rack in which the units are mounted may be considered as an extension of the aircraft structure. Therefore the dynamic characteristics of the rack approximately define the center frequencies of the spikes (and notches) which may be observed at any of the unit attachment points. Because of differences in impedance characteristics between the actual installation and the vibration test fixture, the center frequencies of peak responses in test do not exactly duplicate those in the aircraft. However, the theory of dynamic absorbers [3] indicates that the shifts should be minor. Further, this approximation is no more significant than in traditional methods of test control.

Therefore, if random vibration at the broad-band level of Fig. 2 is applied to the assembly attachment points, it is consistent with the prediction method to limit the response spectral density at any unit attachment point, averaged over any 10 percent bandwidth, to the value of the spikes in Fig. 2. This is achieved

Fig. 3. Schematic of equipment rack classified as an assembly.  $\circ$  = unit attachment points (typical) -- response control points.  $\Delta$  = assembly attachment points -- input control points



- $\circ$  UNIT ATTACHMENT POINTS (TYPICAL)  
-RESPONSE CONTROL POINTS
- $\Delta$  ASSEMBLY ATTACHMENT POINTS  
-INPUT CONTROL POINTS

by reducing the broad-band input spectral density in the narrow frequency band corresponding to the peak in a response. In this way empirical account is taken of the impedance characteristics of the assembly. In other words, the test level is reduced at the resonant frequencies of the assembly, where the actual environment of the assembly attachment points exhibits a minimum in spectral density level. The appropriate degree of reduction is determined by limiting the response level to the maximum level which is expected in flight.

An initial reaction to the above method might be to argue that the method merely allows the input level to be reduced until the assembly can "pass the test." However, upon reflection, it will be realized that the reduction of input level is not so great as might first be supposed. Since the bandwidth over which the response spectral density is analyzed remains constant, 10 percent in this case, the reduction in input spectral level is proportional to the increase in the  $Q$  of the resonance rather than to  $Q^2$  as might be first supposed. This is consistent with the operation of a dynamic absorber, where the extent to which it forces a node at the lower mass increases as the  $Q$  of the absorber increases, although it does so over a narrower frequency bandwidth.

In some cases, it may be desirable to set a lower limit below which the input spectrum may not be reduced. From the data used in Ref. [1], it was observed that the most likely spectral density is approximately 25 percent of the mean spectral density  $W(\bar{K})$  in Fig. 1. This level is suitable for use as the minimum input level to the assembly.

A further reaction to the proposed method might be to argue that no "extreme" or spike spectral density values will be introduced at the assembly attachment points. As previously mentioned, the prediction method and good judgment both lead to the expectation of the occurrence of extreme values at those locations. This, of course, is the familiar dilemma of having to define an input level for testing on the basis of measured data which can only be the response at a point on a dynamic system.

While no logical method of purposefully introducing spikes at these points has been developed, it is considered that the simulation and test severity are not significantly degraded by their absence, for the following reasons. First, a spike at the input in a frequency range where the assembly responds like a rigid body would probably be of no significance from a damage aspect. Second, a spike at the input where the

assembly responds elastically can only occur at frequencies other than the resonant frequencies of the assembly, i.e., in frequency bands of low impedance, where again significant damage effects are unlikely. Third, any test item which can be classified as an assembly will have a number of attachment points separated by some distance. If the power average of the accelerations measured at the attachment points is controlled to the input test level, then variations between the levels at the attachment points caused by both the assembly and the test fixture dynamic characteristics are permitted to occur naturally.

The specification of an assembly test for an assembly for which Fig. 1 describes the environment is shown in Fig. 4. Control of the test level employs both the input and the test item response spectra.

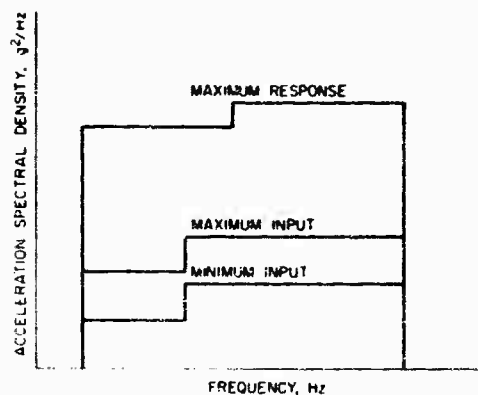


Fig. 4. Typical specification for input and response spectra control

#### IMPLEMENTATION OF ASSEMBLY TEST

It is readily apparent that implementation of an assembly test employing control of the input and as many as 15 or 20 response spectra is neither simple nor inexpensive. On the other hand, any test item which is classified as an assembly is also neither simple nor inexpensive, so that the use of sophisticated test methods is amply justified.

It would be desirable to monitor displays of the response spectra continuously during test to adjust the input spectrum in accordance with the requirements of Fig. 4. However, the equipment requirements, e.g., as many spectral analyzers as response spectra, and the operational

complexity from a human factors standpoint make such an approach completely impractical. More importantly, however, the bandwidth characteristics of commercial random-vibration equalization systems are not compatible with the required bandwidth characteristics. In the low-frequency region, up to approximately 200 Hz, the equalization channels are too broad, while in the high-frequency region the channels are narrower than necessary and must be "ganged" together to give sufficient bandwidth.

In view of these factors, it is necessary to achieve the proper test levels by an iterative process as follows:

1. After initial equalization has been achieved at low level, e.g., 10 db down, the assembly is vibrated at the minimum input level of Fig. 4 for approximately 1 min, i.e., enough time to record data for spectral analysis. If no minimum level is specified, the maximum input level reduced by an agreed-upon factor, say 10 db, is employed.

2. The data recorded in step 1 are analyzed, and the required shaped input spectrum is computed.

3. After equalization at low level, the shaped spectrum is applied to the assembly for approximately 1 min at full level.

4. The data from step 3 are analyzed, and a new shaped input spectrum is computed.

5. Steps 3 and 4 are repeated until a satisfactory input spectrum is achieved.

The necessity for employing an iterative process arises from the need to start at low level so that the maximum response level is not exceeded, coupled with the effects of the typical nonlinearities in the system which modify the frequency response characteristics as the input level is increased.

For consistency with the derivation of the specified test levels, the spectral analysis in the above iteration must employ a constant 10 percent bandwidth. However, for test control with commercial equalizers, the input spectrum must be defined in terms of and controlled within the bandwidths of these equalizers. Figure 5 illustrates, on a logarithmic frequency scale, the 52 bandwidths of a 10 percent comb filter starting at 20 Hz and the bandwidths of commercial 40- and 80- (actually 45 and 85)

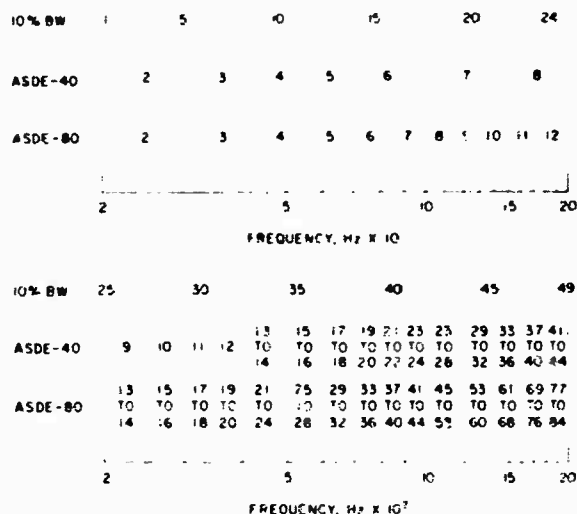


Fig. 5. Filter bandwidths of 10 percent comb filter, 40-channel and 80-channel equalizers

channel equalizer systems. The vertical lines on Fig. 5 are drawn at the crossover frequencies separating adjacent filter channels. A decision must now be made regarding which channel(s) of the equalizer system is (are) controlled by which channel(s) of the analysis system. Table 1 lists the equalizer channels in numerical order, with the analysis system channel number(s) by which they are controlled. It is seen that at the low-frequency end, several analysis system channels govern a single equalizer channel, with the converse occurring at the high end of the spectrum.

It was decided that where several analysis system channels governed one equalizer channel the minimum of the computed input spectral densities among the several analysis system channels would define the input spectral density for the corresponding equalizer channel. This decision creates a lower-than-desired test level on each side of the notch in the input. However, this is considered preferable to exceeding the test level at the notch in the input which corresponds to a peak in a response spectrum and therefore a resonance of the assembly.

In other respects, the implementation of this type of test is identical to normal random-vibration tests which specify a shaped input spectrum. The actual control signal may be from a single accelerometer or from a "power-averaged" signal from several accelerometers.



**TABLE 1**  
**Channel Conversion Table**

| Equalizer<br>Channel<br>Number | Controlling Analysis<br>System Channel<br>Number |                | Equalizer<br>Channel<br>Number | Controlling Analysis<br>System Channel<br>Number |                |
|--------------------------------|--|----------------|--------------------------------|--|----------------|
|                                | For<br>ASDE-80                                   | For<br>ASDE-40 |                                | For<br>ASDE-80                                   | For<br>ASDE-40 |
| 2                              | 1-5  | 1-5            | 28                             | 36   | 43, 44         |
| 3                              | 6-8  | 6-8            | 29                             | 37   | 44             |
| 4                              | 9-11   | 9-11           | 30                             | 37   | 44             |
| 5                              | 12-14  | 12-14          | 31                             | 37, 38   | 45             |
| 6                              | 14-16  | 14-17          | 32                             | 38   | 45             |
| 7                              | 16, 17   | 18-21          | 33                             | 38   | 45, 46         |
| 8                              | 18, 19   | 22-25          | 34                             | 39   | 46             |
| 9                              | 19, 20   | 25-27          | 35                             | 39   | 46             |
| 10                             | 21, 22   | 28, 29         | 36                             | 39   | 46, 47         |
| 11                             | 22, 23   | 29-31          | 37                             | 40   | 47             |
| 12                             | 24, 25   | 31, 32         | 38                             | 40   | 47             |
| 13                             | 25, 26   | 33             | 39                             | 40   | 47, 48         |
| 14                             | 27   | 34             | 40                             | 40, 41   | 48             |
| 15                             | 28   | 35             | 41                             | 41   | 48             |
| 16                             | 29   | 36             | 42                             | 41   | 48             |
| 17                             | 30   | 37             | 43                             | 41   | 49             |
| 18                             | 30, 31   | 38             | 44                             | 42   | 49             |
| 19                             | 31   | 38, 39         | 45-47                          | 42   |                |
| 20                             | 32   | 39             | 48-51                          | 43   |                |
| 21                             | 32, 33   | 40             | 52-56                          | 44   |                |
| 22                             | 33   | 40, 41         | 57-61                          | 45   |                |
| 23                             | 34   | 41             | 62-67                          | 46   |                |
| 24                             | 34   | 41, 42         | 67-73                          | 47   |                |
| 25                             | 35   | 42             | 74-80                          | 48   |                |
| 26                             | 35   | 42, 43         | 81-84                          | 49   |                |
| 27                             | 36   | 43             |                                |  |                |

## COMPUTATION OF INPUT SPECTRUM

Computation of the shaped spectrum to be used as the test input may be divided into two phases: (a) spectral analysis of the input control and each response control acceleration signal measured during the previous iteration step; and (b) from the results of (a), computation of the shaped spectrum which satisfies the test specification, such as Fig. 4.

### Spectral Analysis

A detailed discussion of the analysis system employed for spectral analysis is beyond the scope of this paper. However, a brief description is appropriate to illustrate the practicality of the test method. Figure 6 is a simplified block diagram of the system. The features of the system significant to expeditious computation of the input spectrum are: (a) by use of the IRIG B time code translator/tape search and control unit, no dubbing or tape loop cutting is required; (b) the data sample length is selectable, in 12.5-msec increments, anywhere between 5 and approximately 40 sec; (c) by simultaneous detection of the output of every filter, a single playback in real time of the accelerometer signal is enough to complete the analysis; (d) the spectrum is computed and recorded on digital tape in engineering units less than 5 sec after the data sample playback is completed; (e) printing or listing of the computed spectrum as illustrated in Fig. 7 requires approximately 3 min, although this is not necessary for computation of the shaped input spectrum. With allowances for location of data sample for analysis, switching tape playback channels, adjusting of system gains, etc., listed spectra can be produced at a rate in excess of 10 per hour.

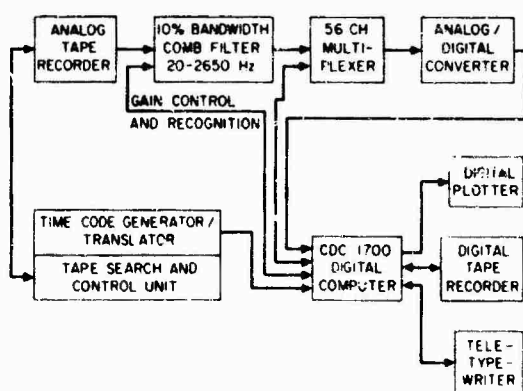


Fig. 6. Simplified block diagram of spectral analysis system

| CH. | FREQ.  | G**2/HZ     |
|-----|--------|-------------|
| 01  | 20.00  | 00.00207936 |
| 02  | 22.58  | 00.00320356 |
| 03  | 24.84  | 00.00268324 |
| 04  | 27.32  | 00.00357604 |
| 05  | 30.05  | 00.00381924 |
| 06  | 33.06  | 00.00379456 |
| 07  | 36.36  | 00.00244036 |
| 08  | 40.00  | 00.00236196 |
| 09  | 44.00  | 00.00478864 |
| 10  | 48.40  | 00.00425104 |
| 11  | 53.24  | 00.00285156 |
| 12  | 58.56  | 00.00256036 |
| 13  | 64.42  | 00.00238144 |
| 14  | 70.86  | 00.00360000 |
| 15  | 77.95  | 00.00258064 |
| 16  | 85.74  | 00.00529984 |
| 17  | 94.32  | 00.00181476 |
| 18  | 103.8  | 00.00147456 |
| 19  | 114.1  | 00.00092416 |
| 20  | 125.5  | 00.00166464 |
| 21  | 138.1  | 00.00163216 |
| 22  | 151.9  | 00.00125316 |
| 23  | 167.1  | 00.00197136 |
| 24  | 183.8  | 00.00183184 |
| 25  | 202.2  | 00.00150544 |
| 26  | 222.4  | 00.00142884 |
| 27  | 244.6  | 00.00171396 |
| 28  | 269.1  | 00.00145924 |
| 29  | 296.0  | 00.00155236 |
| 30  | 325.6  | 00.00161604 |
| 31  | 358.2  | 00.00160000 |
| 32  | 394.0  | 00.00153664 |
| 33  | 433.4  | 00.00148996 |
| 34  | 476.7  | 00.00164836 |
| 35  | 524.4  | 00.00161604 |
| 36  | 576.8  | 00.00168100 |
| 37  | 634.5  | 00.00169744 |
| 38  | 698.0  | 00.00168100 |
| 39  | 767.8  | 00.00163216 |
| 40  | 845.0  | 00.00155236 |
| 41  | 929.5  | 00.00164836 |
| 42  | 1022.0 | 00.00173056 |
| 43  | 1124.0 | 00.00155236 |
| 44  | 1236.0 | 00.00163216 |
| 45  | 1360.0 | 00.00142884 |
| 46  | 1496.0 | 00.00132496 |
| 47  | 1646.0 | 00.00132496 |
| 48  | 1811.0 | 00.00142884 |
| 49  | 1992.0 | 00.00080656 |
| 50  | 2191.0 | 00.00002704 |
| 51  | 2410.0 | 00.00001024 |
| 52  | 2651.0 | 00.00001600 |
| 53  | LPASS  | 00.00001761 |
| 54  | HPASS  | 00.00001792 |

CH.53 & 54 ARE  $\times 10^{**+5}$  g RMS

Fig. 7. Acceleration spectral density listing; control acceleration -10 db initial iteration

### Input Spectrum Computation

Computation of the input spectrum for each step in the previously described iteration process employs the digital computer and its peripherals, which are part of the analysis system of Fig. 6. During spectral analysis, the spectrum of the input control signal, followed by the spectra of each of the response control signals, are sequentially recorded on digital tape and suitably identified, e.g.,  $C_1, R_1, R_2 \dots R_n$ . With the assembly test program now entered into the computer memory, the test specification shown in Fig. 4 is requested by and entered through the teletypewriter. Figure 8 illustrates this entry which permits different specification levels for each 10 percent bandwidth channel, should this be desired. The computer now stores the control spectrum in memory. Next, the maximum response spectral density in each analysis system channel and the control location at which it occurred is determined by sequentially calling in the response spectra and comparing them channel by channel. This spectrum, which represents the envelope of all the response control spectra, is now normalized with respect to the input spectrum. Normalization is necessary to account for variations between the specified and achieved input levels. The normalized spectrum is now compared with the previously entered test specification, and the maximum input spectral density which will cause a response equal to the specified maximum response is computed for each channel. If this computed value is greater than the specified maximum input, the latter value is retained. On the other hand, if the computed value is less than the specified minimum input, then the minimum input is retained. When the computed value is between these specified limits, it is retained. The desired input control spectrum is now complete in terms of the analysis system channels. The computer then defines the spectrum in terms of the equalizer channels and prints out the data shown in Figs. 9 and 10. Figure 9, the Engineering Report, lists, by analysis system channel number, the actual control spectral density, the maximum response spectral density with the response location at which it occurred, and the correction factor ( $\pm 1.0$ ) to be applied to the specified maximum input spectral density. Figure 10, the Operations Report, which is selectable for either the 40- or 80-channel equalizer, lists the input spectral density by equalizer channel number for use by the vibration test technician in controlling the next test.

The time to enter the assembly test program, make the computations, and print out the reports shown is approximately 10 min. The

overall time from acquiring analog data to printout of the shaped spectrum for 15 response control accelerometers is, on the average, approximately 2 hr.

### TESTING EXPERIENCE

The primary purpose of this paper is to propose, for test level control of larger test objects, a logical method which achieves improved simulation of the usage environment. To illustrate the practicality of the method, it is appropriate to describe some experience with it.

A recent test of an air-to-air missile was defined in three phases: (a) 30 min of low-level vibration 6 db down from the reference spectrum; (b) 1 min of vibration 2.5 db down from the reference spectrum; and (c) 1 min of vibration at the reference spectrum, i.e., 0 db. No minimum input was specified (see Fig. 4). The initial vibration run was conducted 10 db down from the specified maximum input. Table 2 shows the correction factors from the engineering report (Fig. 9) for each run, while Fig. 11 is a plot of these factors vs run number using an arbitrary horizontal scale. Channels which are omitted from Table 2 for brevity consistently showed unity correction factors. Criteria for acceptance or rejection of a spectrum were: (a) if less than 1.5-db change occurred in any channel, accept spectrum for test; (b) if greater than 3-db change occurred in any channel, iterate once more; and (c) if any changes exceeded 1.5 db but none exceeded 3 db, accept or reject on judgment basis. From Table 2 it is seen that iteration to the desired input spectrum took three runs, one at -10 db, two at -6 db. It should be noted that the two 1-min runs at -6 db were considered as part of the 30-min test duration. The computation after 25 min of low-level vibration exposure just prior to the high-level vibration was conducted to adjust the input spectrum, if necessary, to account for changes in missile response resulting from accumulated vibration exposure. The computed spectrum at 0 db was computed from data during the 1-min exposure at the high level. While not used actually to control the test, since it was by then completed, it did show the variation between the spectrum actually used and the spectrum which should have been used.

It should be noted that the correction factors in Table 2 and Fig. 11 are corrections to spectral density, i.e., mean square acceleration. Also, locations 2 and 3 were at the same missile bulkhead but separated 180 deg circumferentially so that almost identical responses were expected. Further, changes in tabulated location

| ASSEMBLY TEST PROGRAM |              |                     |          |                        |
|-----------------------|--------------|---------------------|----------|------------------------|
| SPECIFICATION REQUEST |              |                     |          |                        |
| TODAY'S DATE 10-6-67  |              |                     |          |                        |
| FIRST<br>CHAN         | LAST<br>CHAN | SPECIFICATION INPUT |          | SPECIFICATION RESPONSE |
|                       |              | MINIMUM             | MAXIMUM  | MAXIMUM                |
| XX                    | XX           | XX.XXXXX            | XX.XXXXX | XX.XXXXX               |
| 01                    | 17           | 00.00001            | 00.03000 | 00.12500               |
| 18                    | 33           | 00.00001            | 00.01500 | 00.12500               |
| 34                    | 49           | 00.00001            | 00.01500 | 00.15000               |
| 50                    | 52           | 00.00001            | 00.00001 | 00.00001               |
| END INPUT SPEC        |              |                     |          |                        |
| C                     |              |                     |          |                        |
| R                     |              |                     |          |                        |
| R                     |              |                     |          |                        |
| R                     |              |                     |          |                        |
| R                     |              |                     |          |                        |
| R                     |              |                     |          |                        |
| R                     |              |                     |          |                        |
| R                     |              |                     |          |                        |
| R                     |              |                     |          |                        |
| R                     |              |                     |          |                        |
| R                     |              |                     |          |                        |
| END OF FILE           |              |                     |          |                        |

Fig. 8. Assembly test program, specification input (C = control spectrum, number of R's = number of response spectra; for zero minimum input specification, 0.00001 is entered)

# ASSEMBLY TEST PROGRAM ENGINEERING REPORT

| CHAN<br>NO | ACTUAL<br>CONTROL | TEST MAX<br>RESPONSE | ACCEL<br>ID | CORR<br>FACE |
|------------|-------------------|----------------------|-------------|--------------|
| 001        | 00.00207936       | 00.00553536          | R003        | 100          |
| 002        | 00.00320356       | 00.01032256          | R003        | 100          |
| 003        | 00.00268324       | 00.00788544          | R002        | 100          |
| 004        | 00.00357604       | 00.01166400          | R002        | 100          |
| 005        | 00.00381924       | 00.01557504          | R002        | 100          |
| 006        | 00.00379456       | 00.01721344          | R002        | 091          |
| 007        | 00.00244036       | 00.01459264          | R003        | 069          |
| 008        | 00.00236196       | 00.02611456          | R002        | 037          |
| 009        | 00.00478864       | 00.02585664          | R014        | 077          |
| 010        | 00.00425104       | 00.01345600          | R009        | 100          |
| 011        | 00.00285156       | 00.01982464          | R002        | 059          |
| 012        | 00.00256036       | 00.05017600          | R002        | 021          |
| 013        | 00.00238144       | 00.06471936          | R002        | 015          |
| 014        | 00.00360000       | 00.03444736          | R002        | 043          |
| 015        | 00.00258064       | 00.01700416          | R014        | 063          |
| 016        | 00.00529984       | 00.01478656          | R014        | 100          |
| 017        | 00.00181476       | 00.00595984          | R006        | 100          |
| 018        | 00.00147456       | 00.00760384          | R006        | 100          |
| 019        | 00.00092416       | 00.00577600          | R006        | 100          |
| 020        | 00.00166464       | 00.00518400          | R006        | 100          |
| 021        | 00.00163216       | 00.00160000          | R003        | 100          |
| 022        | 00.00125316       | 00.00529984          | R003        | 100          |
| 023        | 00.00197136       | 00.01254400          | R003        | 100          |
| 024        | 00.00183184       | 00.00322624          | R003        | 100          |
| 025        | 00.00150544       | 00.00078400          | R003        | 100          |
| 026        | 00.00142884       | 00.00046656          | R003        | 100          |
| 027        | 00.00171396       | 00.00021024          | R003        | 100          |
| 028        | 00.00145924       | 00.00033856          | R014        | 100          |
| 029        | 00.00155236       | 00.00027556          | R003        | 100          |
| 030        | 00.00161604       | 00.00021316          | R003        | 100          |
| 031        | 00.00160000       | 00.00026244          | R002        | 100          |
| 032        | 00.00153664       | 00.00030976          | R002        | 100          |
| 033        | 00.00148996       | 00.00026568          | R002        | 100          |
| 034        | 00.00164836       | 00.00013688          | R002        | 100          |
| 035        | 00.00161604       | 00.00008648          | R002        | 100          |
| 036        | 00.00168100       | 00.00010200          | R005        | 100          |
| 037        | 00.00169744       | 00.00028224          | R006        | 100          |
| 038        | 00.00168100       | 00.00087616          | R009        | 100          |
| 039        | 00.00163216       | 00.00240100          | R009        | 100          |
| 040        | 00.00155236       | 00.00291600          | R009        | 100          |
| 041        | 00.00164836       | 00.00313600          | R009        | 100          |
| 042        | 00.00173056       | 00.00250000          | R009        | 100          |
| 043        | 00.00155236       | 00.00274576          | R004        | 100          |
| 044        | 00.00163216       | 00.00129600          | R004        | 100          |
| 045        | 00.00142884       | 00.00627264          | R004        | 100          |
| 046        | 00.00132496       | 00.03111696          | R004        | 042          |
| 047        | 00.00132496       | 00.05419584          | R006        | 024          |
| 048        | 00.00142884       | 00.01336336          | R005        | 100          |
| 049        | 00.00080656       | 00.00698896          | R005        | 100          |
| 050        | 00.00002704       | 00.00004096          | R014        | 100          |
| 051        | 00.00001024       | 00.00016900          | R014        | 100          |
| 052        | 00.00001600       | 00.00008464          | R014        | 100          |

Fig. 2. Engineering report from assembly test program.  
-10 db initial iteration

**TABLE 2**  
**Correction Factors from Successive Assembly Test Computations**

| Channel Number | Run I <sup>a</sup>        |                         | Run II <sup>b</sup>       |                         | Run III <sup>c</sup>      |                         | Run IV <sup>d</sup>       |                         | Run V <sup>e</sup>        |                         |
|----------------|---------------------------|-------------------------|---------------------------|-------------------------|---------------------------|-------------------------|---------------------------|-------------------------|---------------------------|-------------------------|
|                | Correc-<br>tion<br>Factor | Accel.<br>Loca-<br>tion | Correc-<br>tion<br>Factor | Accel.<br>Loca-<br>tion | Correc-<br>tion<br>Factor | Accel.<br>Loca-<br>tion | Correc-<br>tion<br>Factor | Accel.<br>Loca-<br>tion | Correc-<br>tion<br>Factor | Accel.<br>Loca-<br>tion |
| 5              | 1.00                      | 2                       | 1.00                      | 2                       | 1.00                      | 2                       | 1.00                      | 2                       | 1.00                      | 3                       |
| 6              | 0.91                      | 2                       | 1.00                      | 2                       | 1.00                      | 2                       | 1.00                      | 2                       | 1.00                      | 3                       |
| 7              | 0.69                      | 3                       | 1.00                      | 3                       | 0.91                      | 2                       | 0.88                      | 3                       | 0.94                      | 3                       |
| 8              | 0.37                      | 2                       | 0.68                      | 3                       | 0.58                      | 2                       | 0.54                      | 2                       | 0.69                      | 3                       |
| 9              | 0.77                      | 14                      | 1.00                      | 3                       | 1.00                      | 2                       | 1.00                      | 2                       | 1.00                      | 14                      |
| 10             | 1.00                      | 9                       | 1.00                      | 3                       | 1.00                      | 2                       | 1.00                      | 2                       | 1.00                      | 6                       |
| 11             | 0.59                      | 2                       | 0.84                      | 2                       | 0.79                      | 2                       | 0.70                      | 2                       | 0.83                      | 3                       |
| 12             | 0.21                      | 2                       | 0.52                      | 5                       | 0.75                      | 4                       | 0.27                      | 2                       | 0.51                      | 3                       |
| 13             | 0.15                      | 2                       | 0.26                      | 2                       | 0.26                      | 2                       | 0.16                      | 2                       | 0.28                      | 3                       |
| 14             | 0.43                      | 2                       | 0.24                      | 14                      | 0.31                      | 14                      | 0.31                      | 14                      | 0.66                      | 3                       |
| 15             | 0.63                      | 14                      | 0.53                      | 14                      | 0.55                      | 14                      | 0.62                      | 14                      | 1.00                      | 14                      |
| 16             | 1.00                      | 14                      | 1.00                      | 14                      | 1.00                      | 14                      | 1.00                      | 14                      | 1.00                      | 6                       |
| 17             | 1.00                      | 6                       | 1.00                      | 6                       | 1.00                      | 6                       | 1.00                      | 6                       | 0.59                      | 6                       |
| 18             | 1.00                      | 6                       | 1.00                      | 6                       | 1.00                      | 6                       | 1.00                      | 6                       | 1.00                      | 6                       |
| 45             | 1.00                      | 4                       | 1.00                      | 4                       | 1.00                      | 4                       | 1.00                      | 4                       | 1.00                      | 4                       |
| 46             | 0.42                      | 4                       | 0.52                      | 4                       | 0.50                      | 4                       | 0.49                      | 4                       | 0.59                      | 4                       |
| 47             | 0.24                      | 6                       | 0.45                      | 4                       | 0.36                      | 4                       | 0.45                      | 4                       | 0.41                      | 4                       |
| 48             | 1.00                      | 5                       | 1.00                      | 5                       | 1.00                      | 5                       | 1.00                      | 5                       | 1.00                      | 5                       |
| 49             | 1.00                      | 5                       | 0.91                      | 5                       | 0.77                      | 5                       | 0.82                      | 5                       | 0.97                      | 5                       |
| 50             | 1.00                      | 14                      | 1.00                      | 4                       | 1.00                      | 4                       | 1.00                      | 4                       | 1.00                      | 4                       |

<sup>a</sup>Initial computation, input 10 db down from maximum input.

<sup>b</sup>Second computation, input 6 db down from initial computation.

<sup>c</sup>Third computation, input 6 db down from second computation.

<sup>d</sup>Computation from response measured after 25-min excitation at 6 db down from third computation.

<sup>e</sup>Computation from response measured during 1-min excitation at level from fourth computation (0 db).

# ASSEMBLY TEST PROGRAM OPERATIONS REPORT

| CHAN<br>NO | ASDE<br>80  |     |             |
|------------|-------------|-----|-------------|
| 002        | 00.00030000 | 043 | 00.00015000 |
| 003        | 00.00011305 | 044 | 00.00015000 |
| 004        | 00.00017978 | 045 | 00.00015000 |
| 005        | 00.00004589 | 046 | 00.00015000 |
| 006        | 00.00013062 | 047 | 00.00015000 |
| 007        | 00.00030000 | 048 | 00.00015000 |
| 008        | 00.00015000 | 049 | 00.00015000 |
| 009        | 00.00015000 | 050 | 00.00015000 |
| 010        | 00.00015000 | 051 | 00.00015000 |
| 011        | 00.00015000 | 052 | 00.00015000 |
| 012        | 00.00015000 | 053 | 00.00015000 |
| 013        | 00.00015000 | 054 | 00.00015000 |
| 014        | 00.00015000 | 055 | 00.00015000 |
| 015        | 00.00015000 | 056 | 00.00015000 |
| 016        | 00.00015000 | 057 | 00.00015000 |
| 017        | 00.00015000 | 058 | 00.00015000 |
| 018        | 00.00015000 | 059 | 00.00015000 |
| 019        | 00.00015000 | 060 | 00.00015000 |
| 020        | 00.00015000 | 061 | 00.00015000 |
| 021        | 00.00015000 | 062 | 00.00006386 |
| 022        | 00.00015000 | 063 | 00.00006386 |
| 023        | 00.00015000 | 064 | 00.00006386 |
| 024        | 00.00015000 | 065 | 00.00006386 |
| 025        | 00.00015000 | 066 | 00.00006386 |
| 026        | 00.00015000 | 067 | 00.00003667 |
| 027        | 00.00015000 | 068 | 00.00003667 |
| 028        | 00.00015000 | 069 | 00.00003667 |
| 029        | 00.00015000 | 070 | 00.00003667 |
| 030        | 00.00015000 | 071 | 00.00003667 |
| 031        | 00.00015000 | 072 | 00.00003667 |
| 032        | 00.00015000 | 073 | 00.00003667 |
| 033        | 00.00015000 | 074 | 00.00015000 |
| 034        | 00.00015000 | 075 | 00.00015000 |
| 035        | 00.00015000 | 076 | 00.00015000 |
| 036        | 00.00015000 | 077 | 00.00015000 |
| 037        | 00.00015000 | 078 | 00.00015000 |
| 038        | 00.00015000 | 079 | 00.00015000 |
| 039        | 00.00015000 | 080 | 00.00015000 |
| 040        | 00.00015000 | 081 | 00.00015000 |
| 041        | 00.00015000 | 082 | 00.00015000 |
| 042        | 00.00015000 | 083 | 00.00015000 |

Fig. 10. Operations report from assembly test program, -10 db initial iteration

where a unity correction factor is listed merely indicate a change in the location at which the maximum response was observed, regardless of the magnitude of the response.

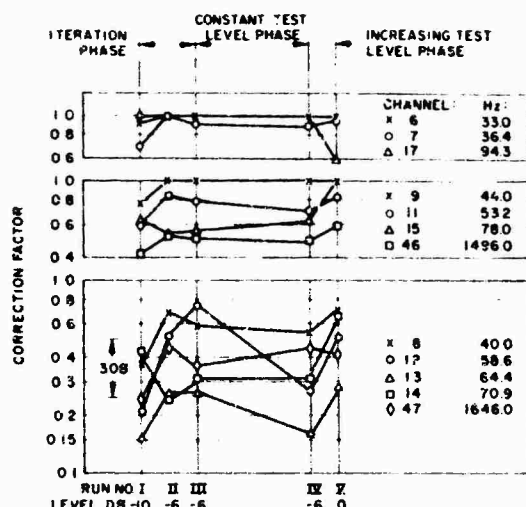


Fig. 11. Variation of correction factors with successive assembly test computations (run I: initial computation, input 10 db down from maximum input; run II: second computation, input 6 db down from initial computation; run III: third computation, input 6 db down from second computation; run IV: computation from response measured after 25-min excitation at 6 db down from third computation; run V: computation from response measured during 1-min excitation at level from fourth computation (0 db))

Examination of Table 2 and Fig. 11 leads to the following observations:

1. The greatest fluctuation in correction factor, particularly during the constant test level phase, occurs in channels 12 and 13, with center frequencies at 58.6 and 64.4 Hz, respectively. Fortunately, the same equalizer channel is controlled by both these analysis channels, and therefore the correction factor for channel 13 governed. The change during this phase is just under 2 db for this channel. It would be easy to conclude that this fluctuation, particularly in channel 12, results entirely from typical 60-Hz signal/noise problems. Undoubtedly this explains part of the fluctuation, particularly since the control location changes for runs II and III. However, it is noted that the correction factor for channel 11, centered at 53.2 Hz, is approximately 0.75 and has the same control location as channel 13, which has a correction factor of approximately 0.2. Thus a small change in the frequency of peak response as the

excitation level changed could cause significant change in the correction factor for channel 12, since it appears to be centered on the slope of the notch.

2. The trend in correction factors during the iteration phase is to increase as test level increases, i.e., the required notch in input level is not as deep for higher inputs. This is consistent with the generally accepted decrease in  $Q$  with increased excitation.

3. The tendency of the correction factor for run II to be larger than for run III is indicative of "overshoot" in the iteration and could perhaps be anticipated.

4. During the constant test level phase, the changes in correction factor, except as noted in item 1, indicate that changes in system response were relatively minor. This is crucial to the use of the proposed test method, since it permits the use of input and response spectra control without continuous on-line analyses of many response accelerometers. As mentioned previously, the method would be impractical had such on-line analysis been required.

5. The general trend of increasing correction factor between runs IV and V with a 6-db change in excitation level means that the short-duration high-level input was notched more deeply than it should have been, although the error did not exceed 3 db.

6. The error discussed in Item 5 indicates that this test method may be less readily applicable to very short duration tests than to longer tests at constant level. Of course, a new one-step iteration at the 0-db level could be made. However, statistical accuracy in spectral analysis at the lower frequencies can be maintained only with data sample duration approaching the test duration, if the analysis bandwidth is narrow enough to avoid excessive smoothing of the response spectra.

## CONCLUSION

This paper has described a vibration test method for larger test objects which achieves, through the control of both input and response spectra, a closer simulation of the usage environment. This simulation improvement is gained by empirically accounting for the impedance characteristics of the test object through appropriate notching of the input spectrum on the basis of measured responses. Application of the method as described requires a statistical description of the environment as developed elsewhere [1]. However, if the environment is described only in terms of response envelopes, adaptation of the method to this situation appears quite straightforward. Implementation of the test method is more expensive than traditional test methods. However, with the use of high-speed data reduction facilities, it is believed the additional costs are readily justified when weighed against the probable value of the test object and the improved validity of test results.

## REFERENCES

1. A. J. Curtis, "A Statistical Approach to Prediction of the Aircraft Flight Vibration Environment," Shock and Vibration Bull., 33 Part 1, pp. 1-13, Feb. 1964
2. A. J. Curtis, J. G. Herrera, and R. F. Witters, "Combined Broadband and Stepped
3. S. Timoshenko, Vibration Problems in Engineering, pp. 240-251, Van Nostrand, New York, 1937

## DISCUSSION

Mr. Smith (Douglas Aircraft Co.): In slide 4 you showed an envelope of both input and response levels. What was the ratio between those two levels? I don't believe you mentioned that.

Mr. Curtis: The ratio was approximately 5 to 1 for this particular test. Some of the others we've had, using this approach, are 10 or 15 to 1 between the maximum input and the maximum response. The ratio of minimum



input to maximum response has been as high as 80 or so.

Mr. Smith: On the Saturn S-IV B/V high force tests we looked at the results in a similar way. We compared the input to a large number of panels to the response of the panels by enveloping the two. The envelopes of responses and inputs were practically indistinguishable. I think the maximum ratio was something like two. Perhaps this shows that the bigger you get the more the difference diminishes.

Mr. Curtis: I think that is probably true. Another thing was surprising to me. In the 2 kc bandwidth there were something like 49 ten percent bandwidths and I think the correction factor was other than unity for roughly 12 of these. I rather expected that the shaped input would be more complex than it turned out to be. Perhaps one can conclude that either the minimum input was too low or the maximum response was too high.

Voice: What was the reason for attenuating the amplified response points? I think we all would agree that there are many definitions for environment, but the more generally accepted one is the input to the base rather than the response.

Mr. Curtis: The approach is that we would like to control the test at the points at which we have predicted and think we know what the environmental level is. We have predicted it at the attachment points, but we are exciting it and wish to control actively the test at a point on

the structure somewhat removed from that. If there is a resonant frequency at some point, and you go out and measure the environments at the assembly attachment points, you can be pretty sure that you will see a notch in the environment at that resonant frequency. This is because the assembly will act as a dynamic vibration absorber. Now, if you exert control and don't allow for that, you can very severely overstress that rack because the supporting structure just doesn't have enough energy to drive it up to that level. Somebody could accuse us of trying to legalize not being able to drive the test item hard enough at those frequencies because of the limitations in the shaker. We should simply recognize that many times we start driving a large test item to some specification level, and when we try to drive it at its resonant frequency it takes more power and causes greater stresses in the attachment points than the real supporting structure could ever deliver. You are empirically adjusting for the dynamic loading for whatever it is you are testing.

Dr. Morrow (LTV Research Center): I take it that when you get data it is primarily from the unit mounting points rather than the rack mounting points and the controlling specifications are primarily for the units.

Mr. Foley (Sandia Corp): This is not so much a question as it is a comment. We've considered this particular technique sufficiently worthwhile to incorporate it in AEC standards since about 1963 and it has been quite successful.

\* \* \*

## RANDOM-FORCE VIBRATION TESTING\*

John V. Otts and Norman F. Hunter, Jr.  
Sandia Corporation  
Albuquerque, New Mexico

Several phases of random-force vibration testing are discussed: (a) force-controlled random vibration input; (b) electronic simulation of a foundation's apparent weight during a random test where the input is force controlled; (c) measurement of a structure's apparent weight using random force and random acceleration data; and (d) random response predictions and/or calculations using random field data and the appropriate apparent weight data.

The Vibration Division of Sandia Corporation has, over the past three years, been actively involved in force-controlled vibration testing, force limiting during acceleration-controlled tests, electronic simulation of a structure's apparent weight, apparent weight analyses, and vibration response predictions. Until recently, all of these categories had been restricted to sinusoidal sweep testing and discrete frequency analyses due to limited technology.

To meet specific test requirements and anticipated test specifications, an investigation was initiated to develop the capabilities for accurate and economical testing in the area of random-force vibration. Results of this investigation are reported.

### INTRODUCTION

The Vibration Division of Sandia Corporation has been actively involved with the development and utilization of force-controlled vibration testing, apparent weight ( $W_A$ ) analysis, apparent weight simulation, and environmental response predictions. Apparent weight  $W_A$  is defined as the complex ratio of applied force  $F$  to the resulting acceleration  $g$ . This property is represented in terms of magnitude and phase angle vs frequency. Apparent weight  $W_A$  is related to mechanical impedance  $Z$  by a factor of  $j\omega$ . The type of force-controlled vibration test normally used is one where the input vibratory force is controlled below a test system which consists of the test specimen and its foundation from the field environment. The arguments for this type of test are presented by Otts (1). Further, the foundation  $W_A$ , as seen by the test specimen, is normally simulated electronically during the laboratory test. This technique is described and proved by Hunter and Otts (2).

Until recently, these areas of testing had been limited to sinusoidal sweep inputs and discrete frequency analyses because of limited

technology and development. However, to meet both specific and anticipated test requirements in the future, an investigation in the areas of random force testing and analyses was started. The results of this investigation are presented here, and include the following:

1. Random vibration response predictions;
2.  $W_A$  measurement with random force and acceleration data;
3.  $W_A$  simulation through electronics during random force-controlled vibration tests.

### RANDOM VIBRATION RESPONSE PREDICTION

To obtain meaningful and repeatable random data, several parameters should be carefully considered. These parameters are filter bandwidth, averaging time, and sweep rate. Filter bandwidth determines the frequency resolution obtained on response plots. Bandwidth is particularly important when analyzing high Q peaks and notches. The effects of filter bandwidth on measured peak response are predicted

\*This work was supported by the United States Atomic Energy Commission.

by Forlifer (3) and these predictions are verified by experimental data. Best resolution requires the narrowest available filter, though a narrow filter requires a long averaging time and a slow sweep rate (4). A 10-cps bandwidth filter was chosen as a compromise. For most data analysis, the parameters used were then:

|                  |                    |
|------------------|--------------------|
| Filter bandwidth | 10 cps             |
| Averaging time   | 3.55 sec           |
| Sweep rate (log) | 0.0667 decades/min |

Consider the electrical "mobility" analog of a mechanical test item and foundation as shown in Fig. 1. This might represent a typical rocket motor-payload system. The simulated random force input (generator S in Fig. 1) is a flat spectrum  $I^2/\text{cps}$  from 20 to 2000 cps. A list of analogous mechanical and electrical quantities appears in Table 1 and shows, for example, that force is analogous to current.

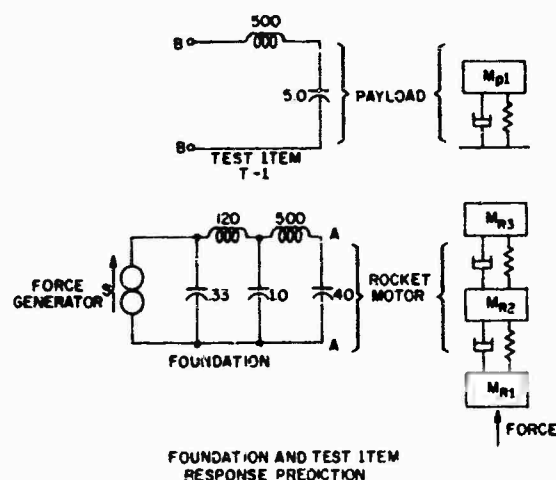


Fig. 1. Simulated rocket motor-payload system

Interface response of the rocket motor-payload system is desired without an actual run being made with the two connected. This response may be predicted if data are available of:

1. Foundation impedance  $Z_F$  ( $I_F/V_F$ ) mhos
2. Test item impedance  $Z_{TI}$  ( $I_{TI}/I_1$ ) mhos
3. Unloaded foundation response  $(V_{wo})^2$  volts<sup>2</sup>/cps

TABLE 1  
Mechanical-Electric Analogies

| Mechanical                     | Mass Capacitance Analogy    |
|--------------------------------|-----------------------------|
| Force F                        | Current i                   |
| Damping C                      | Conductance 1/R             |
| Mass M                         | Capacitance c               |
| Compliance 1/K                 | Inductance L                |
| Velocity v                     | Voltage E                   |
| Acceleration a                 | dE/dt                       |
| Blocked force                  | Short circuited current     |
| Freely suspended system        | Open circuit                |
| Thrust irregularities          | Current generator           |
| Mechanical impedance $Z = F/v$ | Electrical admittance $i/E$ |
| Apparent weight $W_A$          | $i/(dE/dt)$                 |

Foundation and test item impedance are obtained from sine analysis by applying a constant voltage to the items, and measuring the resulting current. Source S is a current (force) generator and is replaced by an open circuit during impedance measuring. Unloaded foundation response is determined by applying input  $I^2/\text{cps}$  at S (Fig. 1) and plotting the resulting  $V_{wo}^2$  volts<sup>2</sup>/cps at the interface (AA).

The interface response with foundation and test item connected may be determined from Thevinin's theorem as

$$V_w^2 = \left( \frac{Z_F}{Z_F + Z_{TI}} \right)^2 V_{wo}^2 \quad (1)$$

Experimental data obtained on the quantities in Eq. (1) are shown in Figs. 2, 3, and 4. The interface response  $V_w$  is calculated by using Eq. (1) and is measured experimentally. This is shown in Fig. 5. Note the correlation between predicted and measured values in Fig. 5.

The terms  $Z_F$  and  $Z_{TI}$  in Eq. (1) are sine impedances. However, they were also measured by using the techniques described below in  $W_A$  analysis. These "random" impedances are shown in Figs. 6 and 7. Calculations of  $V_w$  are again made and compared with the measured response in Fig. 8.

#### APPARENT WEIGHT

Typically,  $W_A$  characteristics are determined during a sinusoidal sweep vibration test. The input force and resultant acceleration are

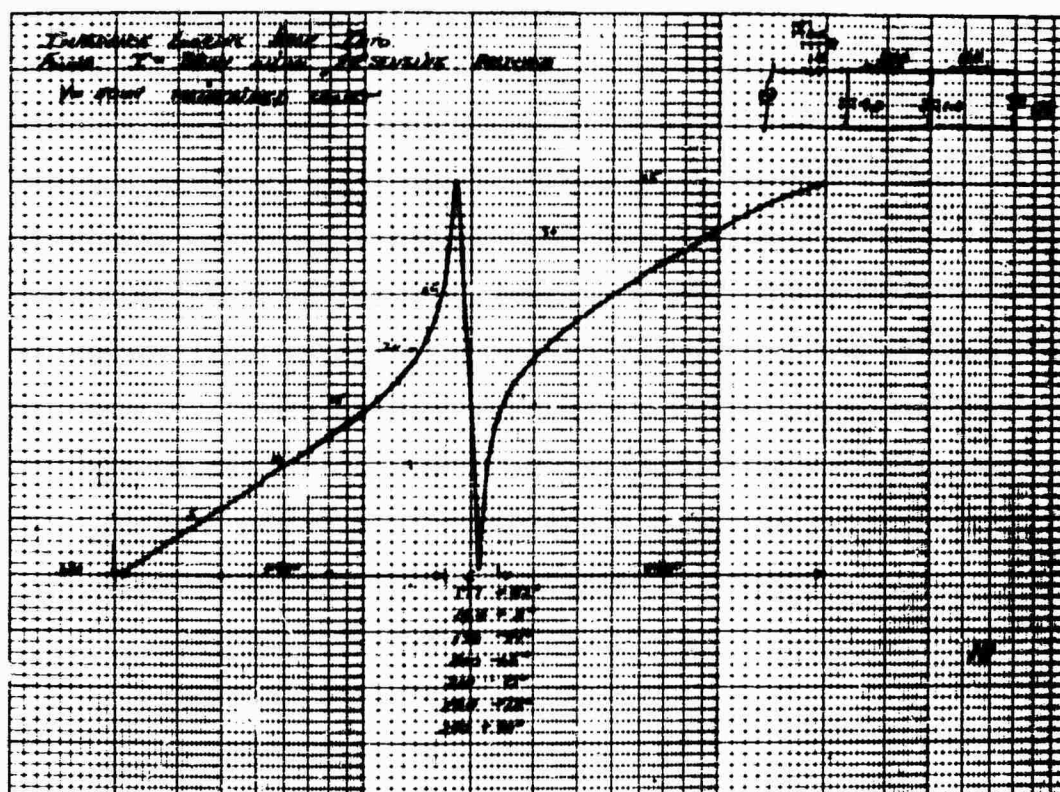


**Fig. 2. Foundation impedance**

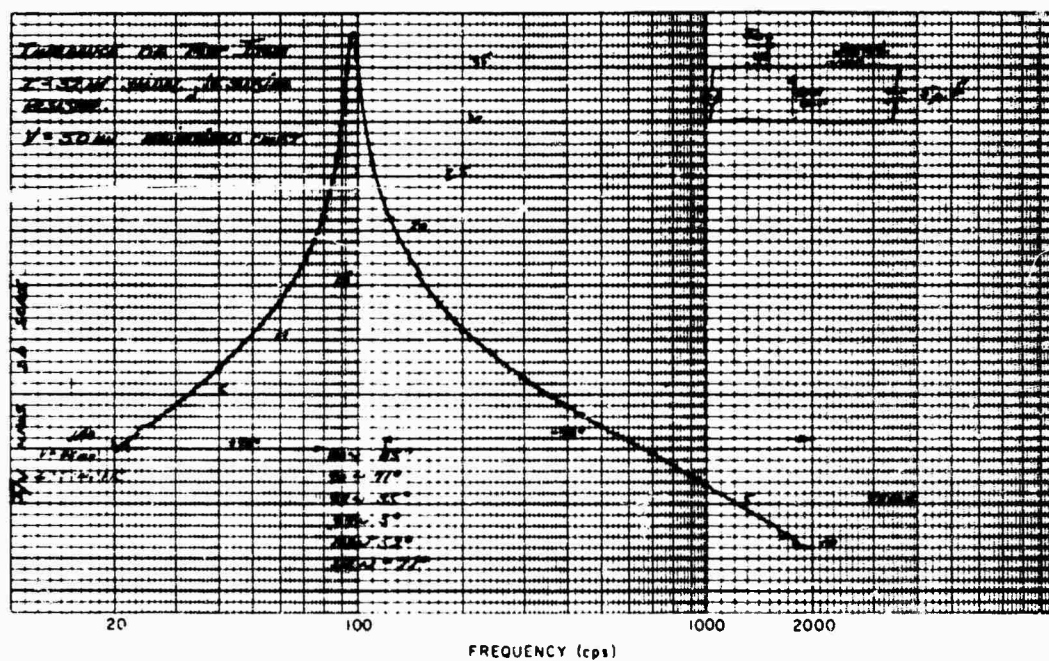


Fig. 3. Test item impedance

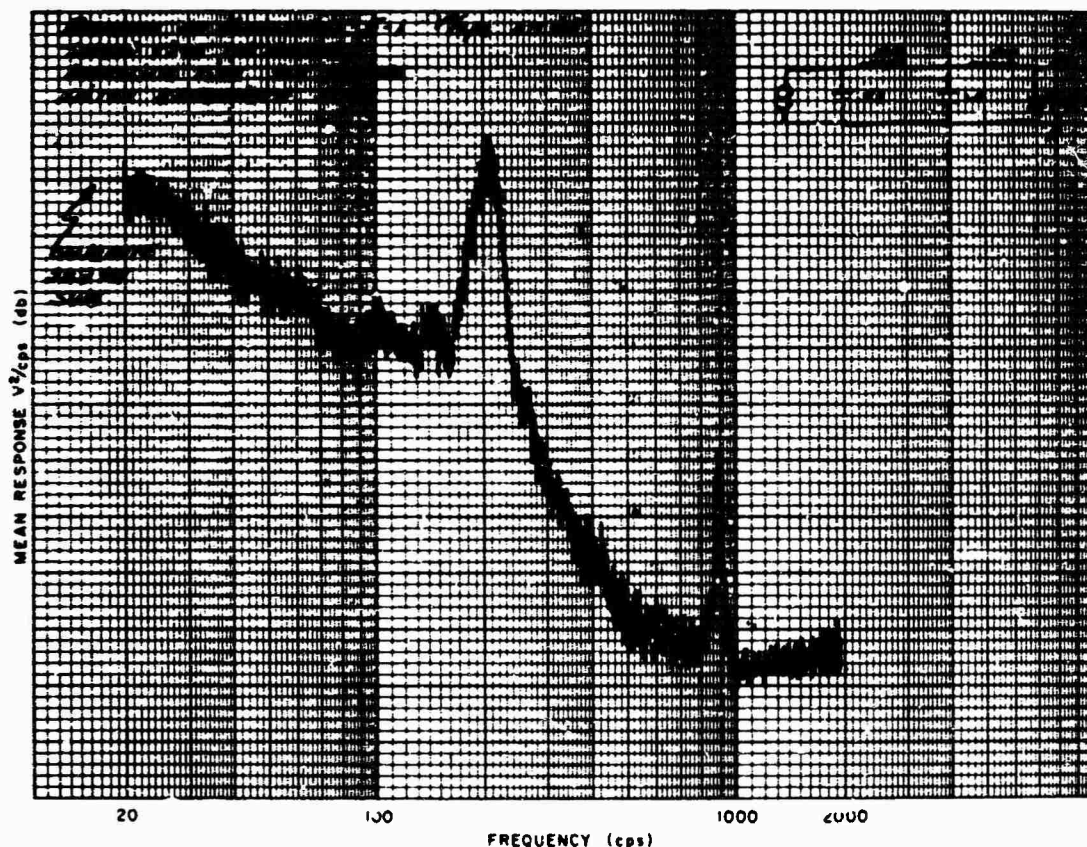


Fig. 4. Unloaded foundation response

used to obtain plots of  $F/g$  and phase angle vs frequency. Due to the sine sweep, the analysis requires approximately 15 min. If the  $W_A$  could be determined from a short burst of random vibration, the unit test time could be reduced (a critical factor in many cases), and sine testing could be eliminated in cases where random testing was specified.

An investigation was conducted to determine (a) the best random technique, (b) the accuracy that could be expected, and (c) how phase could be measured. The results are considered below.

The  $W_A$  analysis can be accomplished by two methods. First, the acceleration spectrum is equalized flat over the frequency range, and the required force spectrum is recorded. A plot of the force spectrum, in decibels, then represents the magnitude of  $F/g$  since the  $g$  spectrum was flat. The results of this technique are shown in Fig. 6. Also shown for comparison is the plot obtained during a sine analysis. In general, a 2- to 3-db loss in resolution

is noted at the peak and notch frequencies. This error, however, is predictable from Ref. (3).

Another technique still being investigated is to take the ratio of the narrow-band rms values of force and acceleration and plot this ratio as the center frequencies of the filters are swept across the frequency range. These results are not as yet conclusive enough for reporting.

Two choices are available for determination of the phase angle. The best method involves comparing the narrow-band force spectrum to the narrow-band random spectrum on an oscilloscope or oscillograph record. Such a comparison is shown in Fig. 9. The second method is to assume the phase angle based upon known relationships and experience. In the past, this method has proved surprisingly accurate.

#### APPARENT WEIGHT SIMULATION TECHNIQUE

In general, a foundation's apparent weight ( $W_A$ ) may be simulated with the control circuit



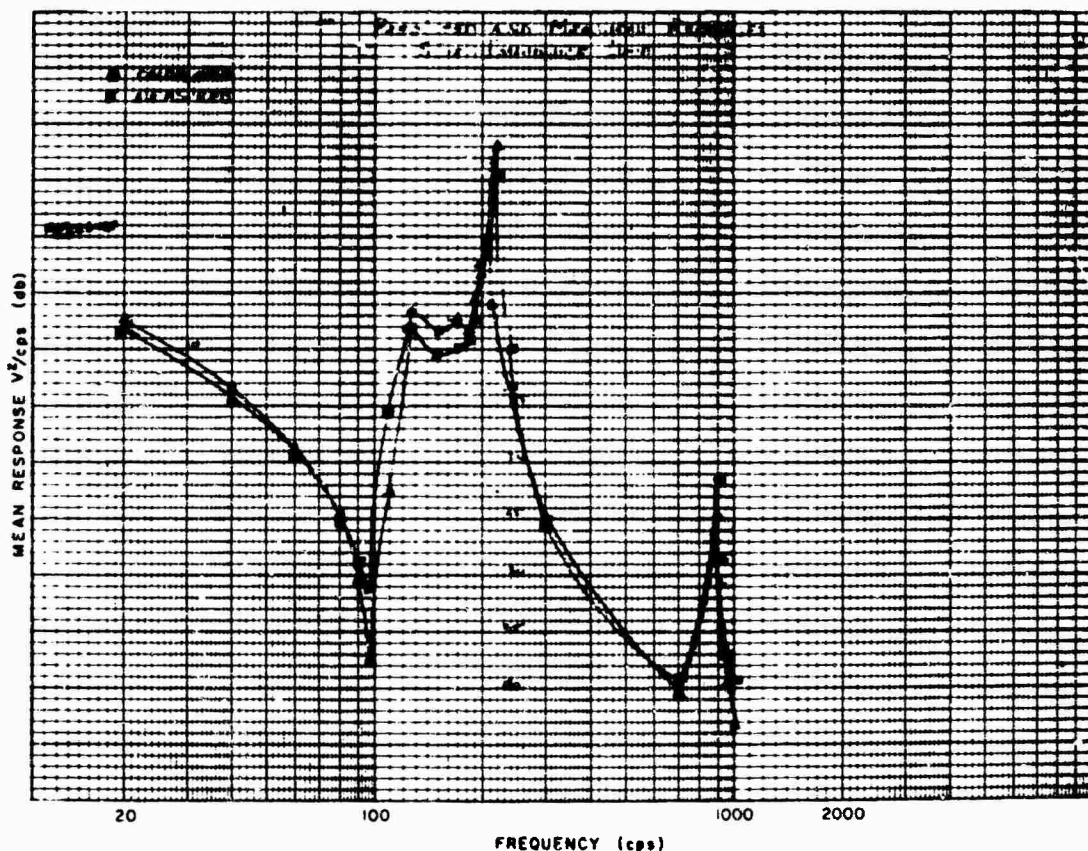


Fig. 5. Predicted and measured responses, sine impedance data

of Fig. 10. Proof of this may be found in Nuckolls (5) and also Otts and Hunter (2). The force signal is fed to the summer through line C. A portion of the acceleration signal is fed through amplifier A and subtracted from the force signal to cancel fixture  $W_A$ . Foundation mass (0 deg) or springlike (180 deg) characteristics are added by amplifier B. Since normally foundation  $W_A$  will change with frequency, amplifier B should have variable gain. The gains and phases required for some common foundation impedances are listed in Table 2.

While a foundation may be approximately simulated with a step gain and phase change, better simulation results if smoothly changing gain and phase are used. A set of peak notch equalizers (basically a variable gain, variable Q resonant circuit) provide the gain and phase vs frequency characteristics required for multi-degree-of-freedom foundations.

A peak notch filter also has the advantage that its transfer function exists at all frequencies simultaneously. This allows use of the

TABLE 2  
Required Gain for Foundation Simulation

| Foundation Simulation Desired | Gain Required | Phase Required (deg)   |
|-------------------------------|---------------|------------------------|
| Mass                          | Constant      | 0                      |
| Spring                        | -12 db/octave | 180                    |
| Damper                        | -6 db/octave  | 90                     |
| Resonant system               | Variable      | Smooth Change 0 to 180 |

mass addition circuit of Fig. 11 for random apparent weight simulation. Amplifier B of Fig. 10 has been replaced with a peak notch equalizer set for the proper gain (and therefore phase) function. Following the summing amplifier, another set of equalizers and a random console simulate the foundation blocked force. With

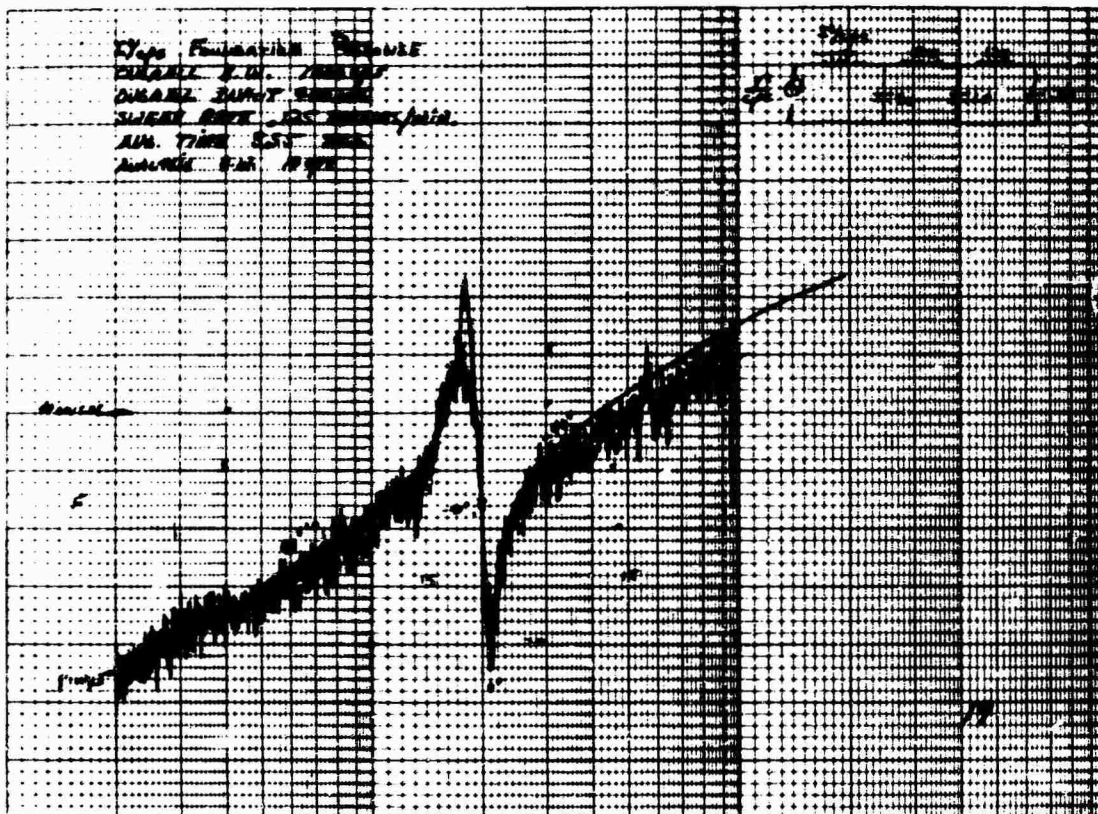


Fig. 6. Random foundation impedance

this system, gains within 10 percent of those necessary for ideal simulation were obtained at all frequencies as shown in the following example.

#### EXAMPLE OF $W_A$ SIMULATION DURING RANDOM TESTING

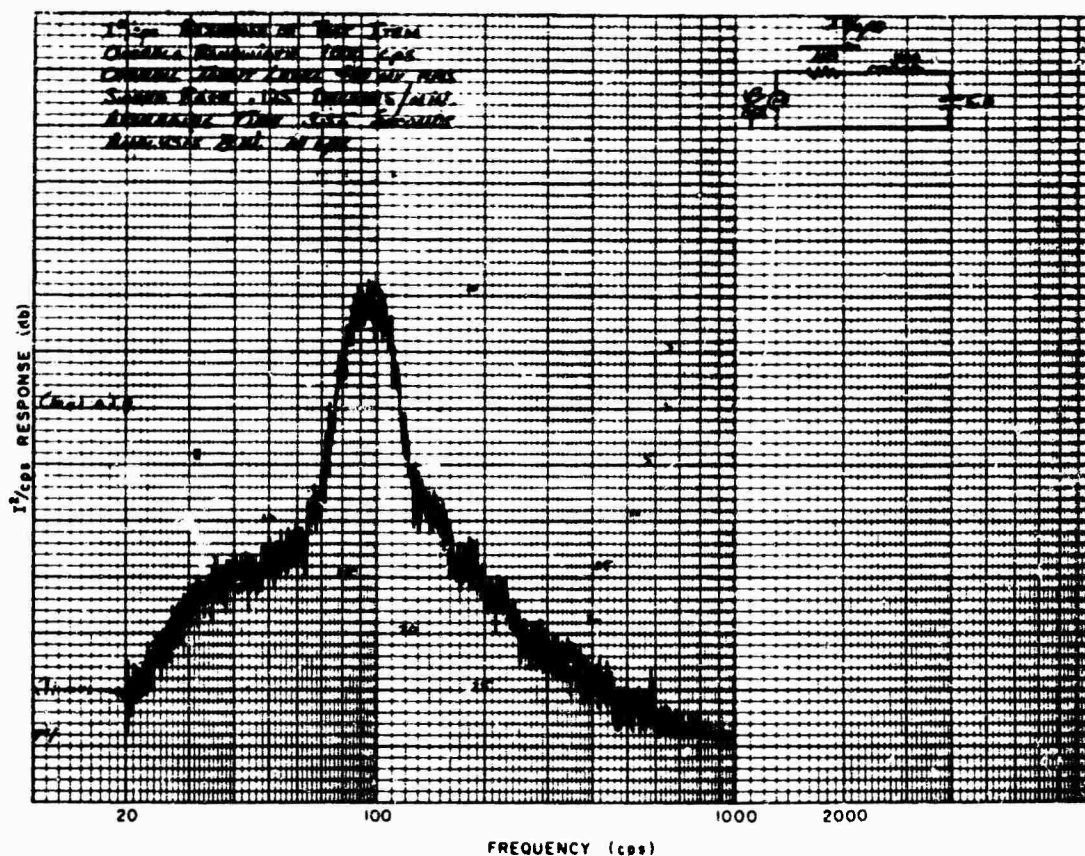
An electrical analog of a mechanical system will be used to demonstrate (a) the validity and accuracy of  $W_A$  simulation during random testing, and (b) one of the laboratory procedures used to simulate vibration environments existing in the field. This procedure is identical to that reported by Otts and Nuckolls (6) with the exception that random input and responses will be used in place of the sinusoidal test (swept from 20 to 2000 cps). Figure 12 depicts an assumed rocket motor-payload system. The vibratory input is the random force generated at the nozzle of the rocket motor. Practically speaking, this assumption is valid since all  $W_A$  measurements are at the motor-payload interface.

The mass-capacitance analogy in Table 1 is used to depict the passive analog of the

mechanical system (Fig. 12a) and is shown in Fig. 12b. The random vibration input in the field, which results from burning irregularities, will be assumed to be a flat spectrum between 20 and 2000 cps as shown in Fig. 13. The response of the payload element  $C_{P2}$  to the field input is shown in Fig. 14. The procedure used to simulate this response in the laboratory is outlined below:

1. The input force to be controlled during the laboratory test is the force spectrum at the interface between the rocket motor and the payload. This force spectrum is obtained through a blocked force test (short circuit) where the motor is fired into a massive test block and the force between the motor and test block measured. This spectrum, obtained during a short circuit, is shown in Fig. 15.

2. The  $W_A$ ,  $[1/(dE/dt)]$ , of the motor, as seen by the payload, is also required. These characteristics are depicted in Fig. 16. This is the characteristic to be electronically simulated during the laboratory test, by using the  $W_A$  simulation technique described above.



3. The laboratory test will be equivalent to controlling the interface random force spectrum (Fig. 15) below the test system consisting of the motor  $W_A$ , as seen by the payload, and the payload itself. Using the procedure previously outlined, the force spectrum will be controlled at the output of the  $W_A$  simulator. The  $W_A$  will be electronically simulated. The

response of  $C_{P2}$  under the above conditions is compared with the actual field response in Fig. 17. The validity of the technique, particularly  $W_A$  simulation with electronics, is obvious from this example. It might be noted that the same analysis parameters (bandwidth, sweep rate, etc.) were used for each response plot.

## REFERENCES

1. John V. Otts, "Force Controlled Vibration Tests: A Step Toward Practical Application of Mechanical Impedance," Shock and Vibration Bull. 34(Part 5) p. 45 (1965)
2. John V. Otts and Norman F. Hunter, "Electronic Simulation of Apparent Weight in Force Controlled Vibration Tests," paper presented at Instrument Society of America 22nd Annual Conference and Exhibit, Chicago, Ill., Sept. 1967
3. W. R. Forlifer, "The Effects of Filter Bandwidth in Spectrum Analysis of Random Vibration," Shock and Vibration Bull., 33(Part 2) p. 273 (1963)
4. Laurie R. Burrow, "Some Analog Methods for Power Spectral Density Analysis," paper presented at Instrument Society of America 20th Annual Conference and Exhibit, Oct. 1965.
5. C. E. Nuckolls, "An Approximate Method of Simulating Mechanical Impedance in Vibration Testing," Institute of Environmental Sciences 1965 Annual Technical Meeting Proceedings pp. 577-581
6. John V. Otts, and C. E. Nuckolls, "A Progress Report on Force Controlled Vibration Testing," Shock and Vibration Bull., 35(Part 2) p. 117 (1966)



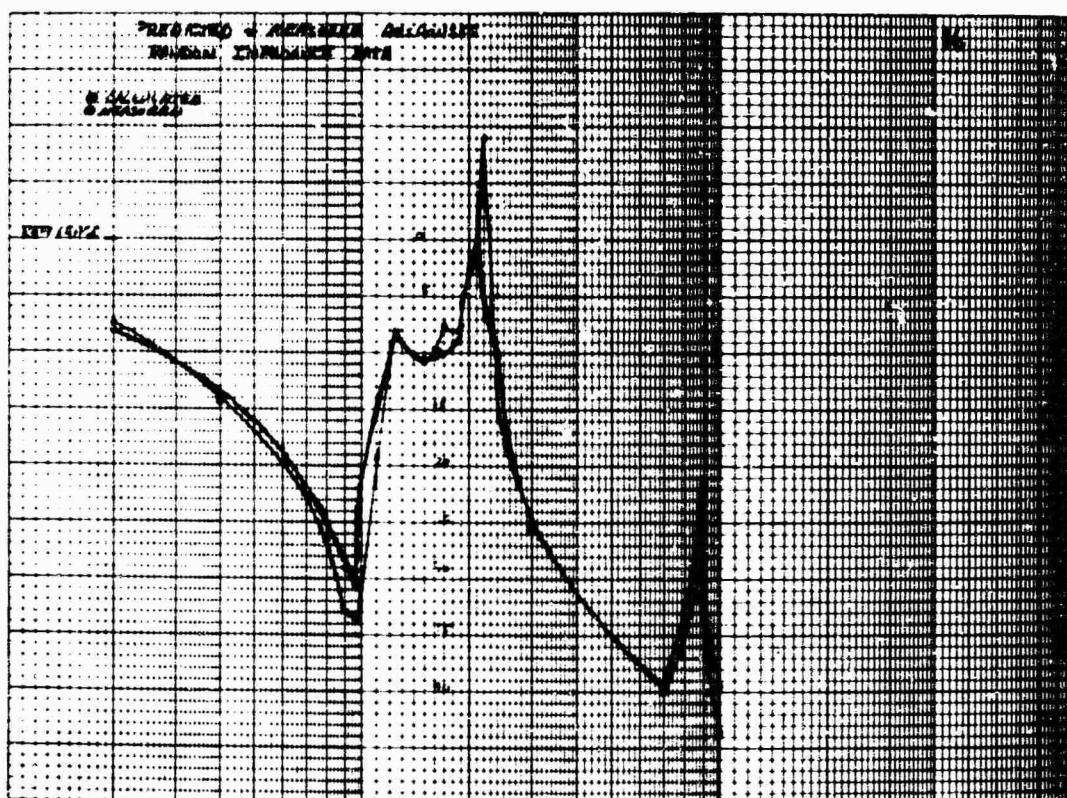


Fig. 8. Predicted and measured responses, random impedance data

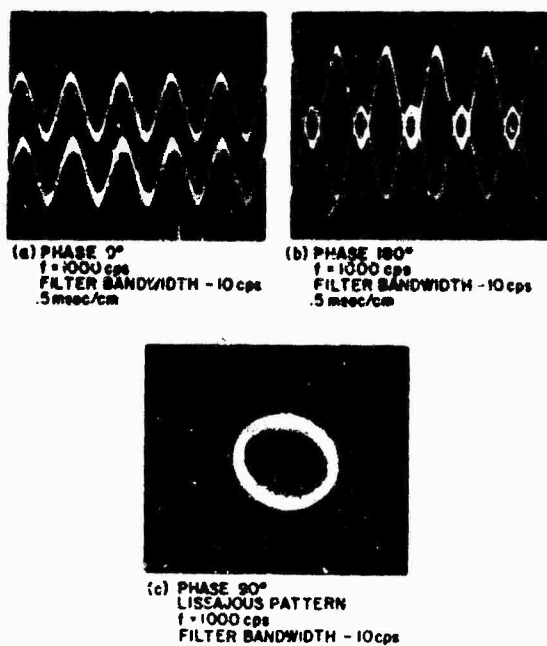


Fig. 9. Narrow-band random phase comparisons

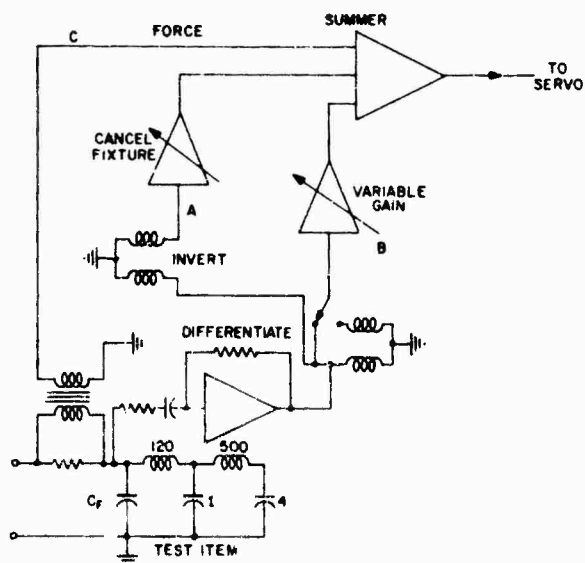


Fig. 10. Mass addition circuit

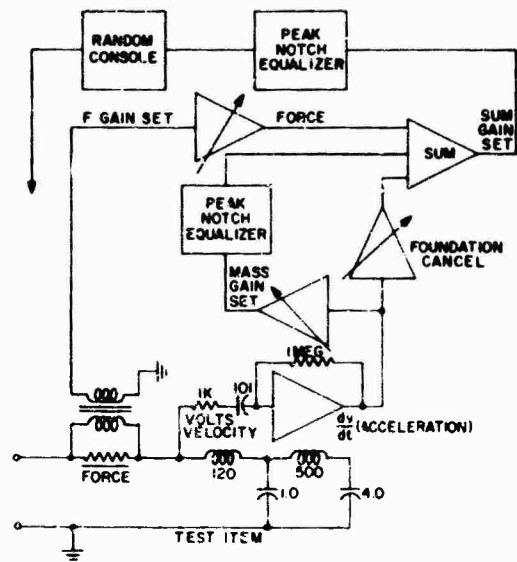


Fig. 11. Random mass addition circuit

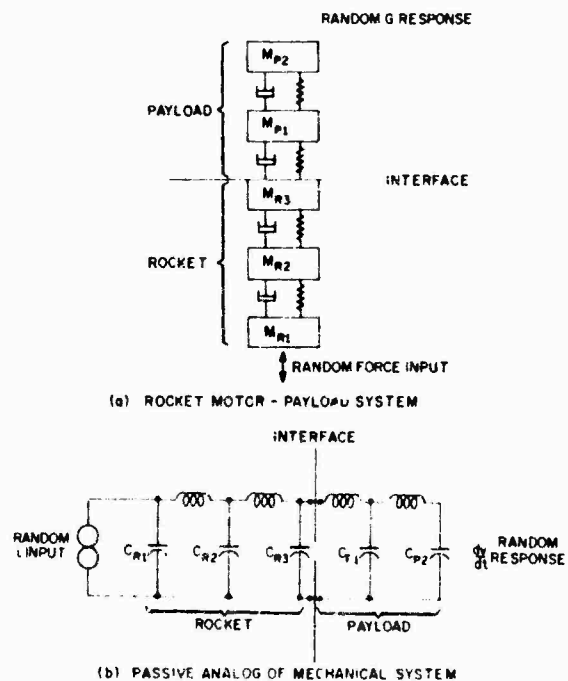


Fig. 12. Rocket motor - payload system

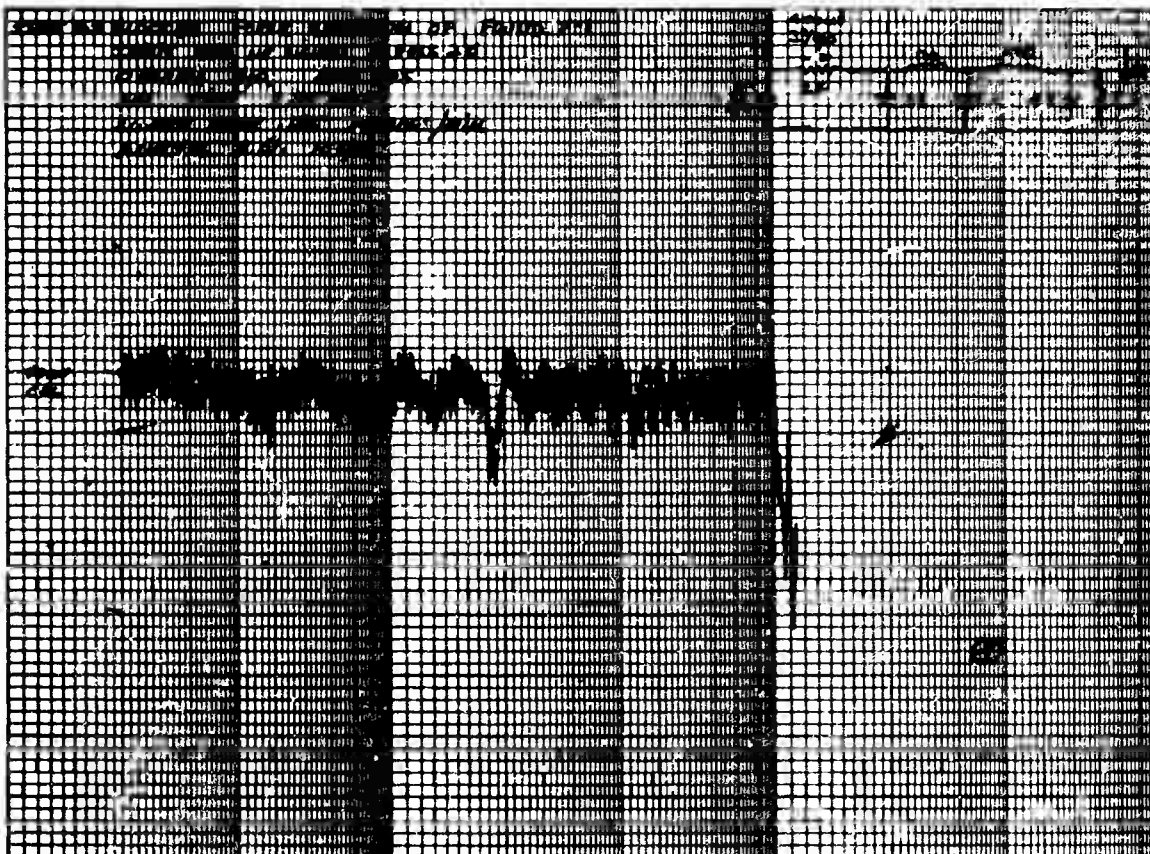


Fig. 13. Foundation force input spectrum

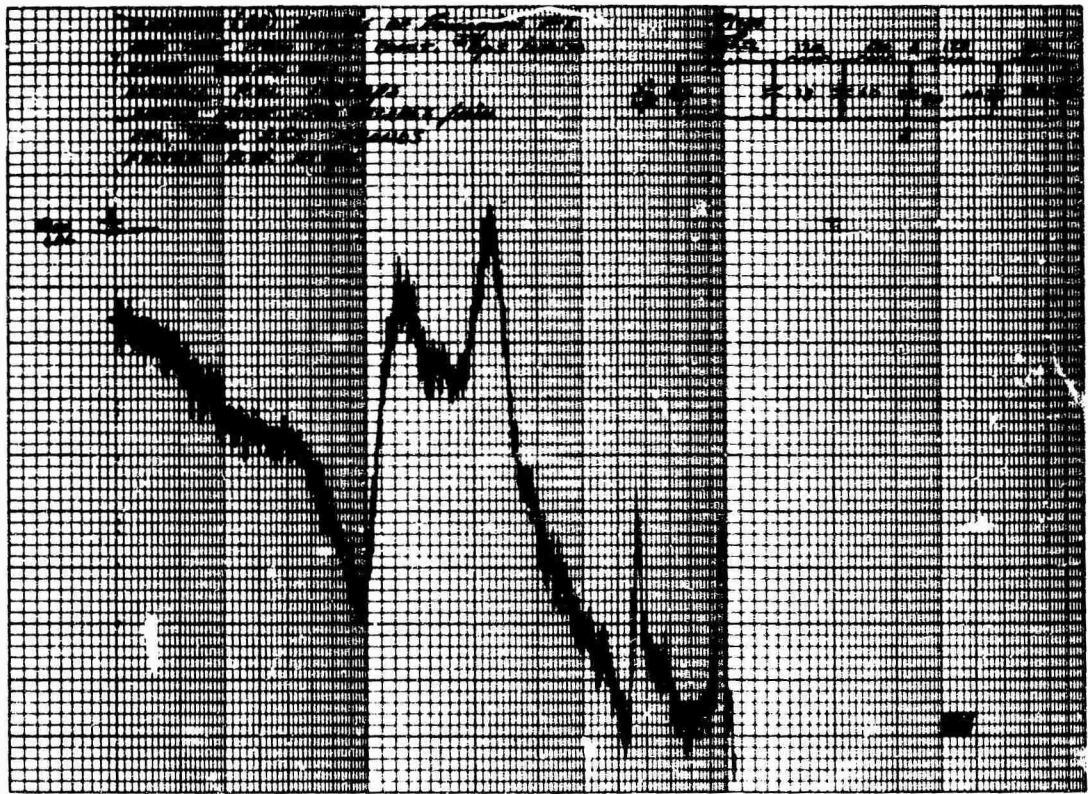


Fig. 14. Test item response to field excitation

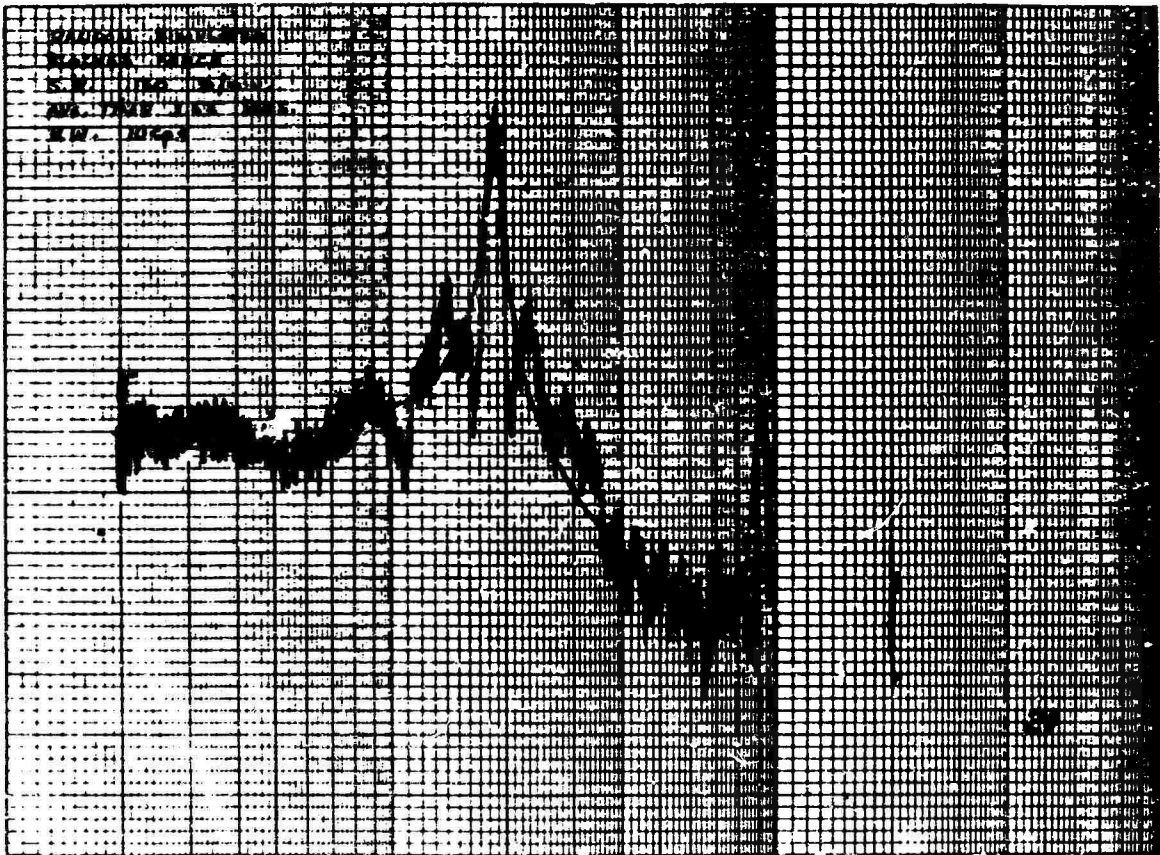


Fig. 15. Foundation blocked force

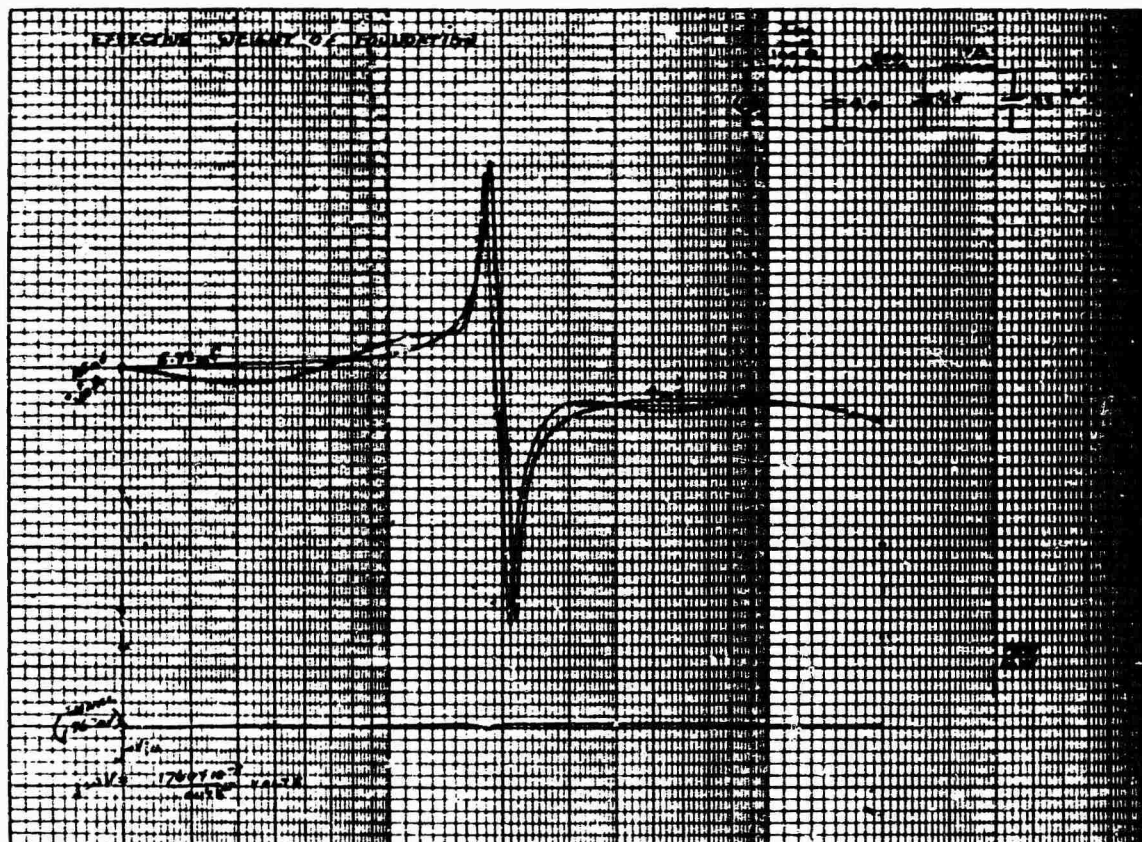


Fig. 16. Foundation apparent weight



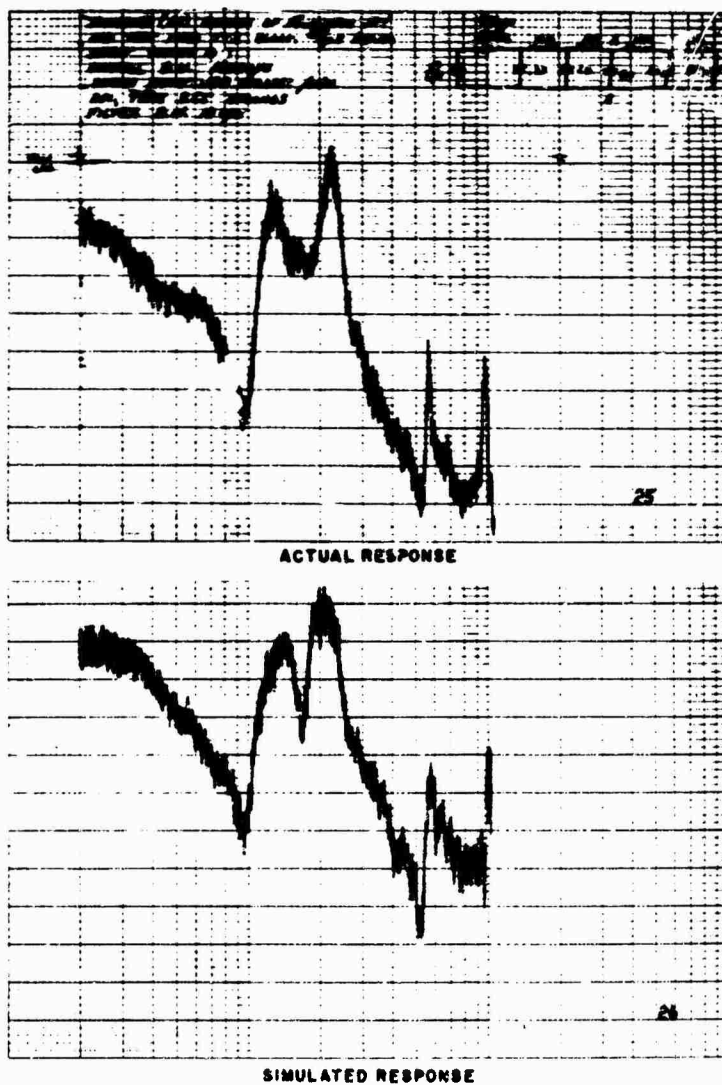


Fig. 17. Simulated and field responses

\* \* \*

## CONTROL POINT AVERAGING FOR LARGE SPECIMEN VIBRATION TESTS

Herbert R. Berkman  
Litton Systems, Inc.  
Van Nuys, California

Vibration tests currently being performed on a large computer programmer employ an averaging system for input control. The effectiveness of this system in conjunction with a large test fixture has been evaluated through preliminary tests with a mockup specimen. Arguments are presented in favor of the averaging concept as a valid test method, with emphasis on defining new terminology to relate specified vibration levels directly to the averaged control level. Data acquired in the tests is presented in a manner particularly suited for averaged control and is used to emphasize the difficulty in applying a specified environment uniformly in a large package test. A system of defining the range of variation allowable between the averaged control points is presented which is then directly related to a proposed new tolerance term which, if incorporated into future specifications or amended to present ones, would allow averaging to become more universally acceptable.

### INTRODUCTION

The conception of controlling the input level to a vibration test by sensing the levels at more than one point and using their average value as the control signal to the servo is not new. It probably occurred to the first test engineer who ever encountered a fixture resonance. It has found widespread usage only recently, primarily because of a scarcity of reliable equipment designed specifically for this purpose. This problem has now nearly been eliminated by an outpouring of new products from instrumentation manufacturers.

This presentation is an effort toward analyzing the uses and limitations of the technique of averaging, defining its unique conceptions and terminology, and promoting general acceptance of its validity throughout the testing community. The discussion is based on recent experience in planning qualifications tests on a large electronic package now being developed at Litton Industries, Data Systems Division.

The equipment being tested is an advanced airborne microelectronic computer programmer. Its physical size is about 4 ft long, 4 ft high, and 1.5 ft deep. It weighs approximately 600 lb and is mounted on a unique isolation system which is C.G. oriented in two axes, but is quite asymmetric in the third. The characteristics of this mounting system were one of the

major factors preventing the specimen from being placed on its side to attain a lower profile during vibration testing.

In order to conduct this test properly, it was necessary to design and fabricate a large fixture. The required dimensions of the fixture made it obvious that resonance would occur within the 500-Hz test range and that definition of control point locations would be a serious problem; hence the technique of a multiple-point-averaged control system was proposed. After much discussion, the many technical and philosophical doubts regarding the validity of this method were dispelled, and averaging was incorporated into the test plan. Preliminary tests have been conducted to evaluate both the fixture and control system. The resulting data which is presented graphically here emphasizes the efficacy of this method for conducting a better understood and more well-controlled test.

### RATIONALE FOR AVERAGING

In developing a vibration test plan, a basic step is to decide at which points of the specimen levels are to be applied. Normally this is "the point" at which the unit attaches structurally to the source of environment, be it a building, a vehicle, a shaker, or a test fixture. This point, which is actually several points or even a distributed area, is easily definable for relatively



small items having a characteristic dimension no larger than, say, the diameter of the shaker head. In this range, it is not unreasonable to assume that the vibration at the source is essentially the same at each of the attachment points. As the size of the specimen (and necessarily of the fixture) becomes larger than this arbitrary threshold, the assumption is no longer valid. It becomes increasingly absurd to speak in terms of "the" input point, since there are as many input points as there are load-carrying attachment points, and they each may be receiving a different input.

It is a common misconception that the only reason this occurs is that fixture resonances may exist within the test range because the fixture has been improperly designed. Hence any plea for averaged control is considered an admission of failure. Those who adhere to this line of thought have probably not had a first-hand opportunity to design a large vibration fixture and are thus unaware of the tremendous tradeoffs required to attain that next 50 or 100 Hz of resonance-free performance. A seldom considered point is that even at frequencies below resonance there are significant differences in response at the various locations.

The most obvious cause of this is dynamic unbalance of the test specimen caused by the individual resonances of its component masses. Any large specimen is bound to be made up of a multitude of smaller components, subassemblies, and removable modules, each of which may resonate and cause the effective C.G. to be constantly shifting. Unless the fixture is several times more massive than the specimen, which seldom occurs because of shaker force-pound limitations, it will tend to deform under the eccentric loading.

Another more significant cause of variation between input locations which occurs in the Litton test is eccentricity in specimen mounting. Although it is almost axiomatic that equipment should be mounted in such a way that it is balanced about its C.G. and no rotational modes are introduced, this cannot always be accomplished in practice. The result is that eccentricities do occur, rotational modes do occur, and asymmetrical loads must be accommodated in most of our large vibration fixtures. The larger the fixture, the greater the deformations that may be caused by these loads. Generally, the best that the fixture designer can do without knowing the modes before the test is to align the static C.G. of the fixture-specimen system with the centerline of the shaker. If some response information is known beforehand, the designer may be able to account for its effect by

compromising on the static alignment. It is, however, impossible to design against eccentricity at all frequencies.

Not only must it be conceded that even the best fixture will display some point-to-point variation, but it must be remembered that the conception of the infinitely rigid test fixture has itself always been open to doubt. It is self-evident that the very idea of providing an identical environment at each attachment point is something that could never happen in actual service, and that the derived specification is only an approximation of the real environment.

In light of these phenomena there is still an inescapable decision to be made as to where to control the vibration environment. Depending on who makes the decision, the results of the test could be drastically different. If it is the equipment designer, he may be quite sensitive to the possibility of exceeding the environment and choose a point which will cause attenuation at all other points. The customer on the other hand may be concerned about undertesting and choose a point which will avoid attenuation, but will allow amplification. Accordingly, the specimen may pass the test in the first case and fail in the second. To avoid these extremes some compromise must be reached. This generally requires a thorough resonance survey of the fixture, followed by an agreement that the control point will be changed from one point to another for particular frequency bands. This is a very cumbersome process and usually leads to tremendous confusion in interpreting the test data. For example, calculating transmissibility to various points on the specimen must take into account that the input changed at certain frequencies. Of course, this method cannot be used at all for random vibration.

## TERMINOLOGY

The conception of averaging offers a logical solution to the dilemma of deciding the input location and, in so doing, removes all of the arbitrariness associated with such a decision. In using the conception, however, a new domain of terminology is introduced which requires definition and understanding. This terminology is unique in that it allows reference to the specified environment as an abstract environmental field which does not exist at any given point but is present only as a property of the fixture and specimen regarded as an interrelated system.

Specifically the terms which are introduced are:

1. Test system
2. Field of excitation
3. Averaged control points
4. Averaged control level
5. Averaged control signal
6. Range of variation
7. Limits of allowable variation

They may be defined as follows:

1. Test system—the overall vibrating structural complex composed of the shaker armature, the test fixture, and the specimen, which is used to provide a particular field of excitation to the specimen;

2. Field of excitation—the abstract vibratory environment to which the specimen is to be exposed through its structural attachments to the test system; this is simply the input spectrum as defined for single-point control plus a tolerance in terms of allowable variation.

3. Averaged control points—those locations on the fixture through which load is applied to the specimen and which are to be instrumented with vibration transducers connected into the averaging instrumentation and servo control system;

4. Averaged control level—the magnitude of the absolute value average of the vibratory levels at each of the averaged control points; ideally, this is equal at all frequencies to the value of the field of excitation.

5. Averaged control signal—the output of the averaging device which is used as the feedback to the servo control system; this signal is calibrated to be proportional to the averaged control level.

6. Range of variation—the positive and negative values by which the levels at the averaged control points differ from the actual averaged control level, expressed as a ratio, log ratio, or percentage: e.g.,  $\pm 2$  to 1,  $\pm 3$  db, or  $\pm 50$  percent;

7. Limits of allowable variation—the positive and negative values by which the levels at the averaged control points are allowed to differ from the specified field of excitation, expressed as a ratio, log ratio, or percentage.

At first glance the necessity of each of these definitions may not be apparent. The definitions themselves may even seem rather pompous and superficial in relation to present usage. Nevertheless, in order to transform this technique from its present status as a tricky method of dealing with fixture resonance into a useful, philosophically acceptable test method, the stigma that we are tampering with the intent of the specification must be erased. In the past, whenever the state of the art has been advanced and new test equipment has been developed, new methods had to be developed for using it. We now have the equipment for averaging, but the methods are still undefined.

By referring to a "test system" we are better able to comprehend that the shaker, fixture, and specimen are dynamically interrelated and that what we are basically trying to do is control the average level of excitation at a given interface within the system. Since that interface possesses unique response characteristics, it is thus subjected not to a particular level at a point but to the field of excitation. The terms averaged control points and averaged control signal are straightforward and are defined simply as an aid to communication.

The value of the averaged control level is a direct indication of the accuracy of the averaging method. That accuracy is a direct function of the type of circuitry and its ability to respond to rapidly changing signals. Of course, if the averaging is ideal, the accuracy is directly proportional to the number of points being averaged.

The range of variation is a redefinition of a key conception used in averaging. This term is a physical property of a given test system. It is a function of the mechanical impedance between the fixture and specimen and as such is affected by the stiffness of each and by the damping and any dynamic unbalance in the system. It probably is quite nonlinear with changes in averaged control level.

The limits of allowable variation, or simply the allowable variation, have nothing whatsoever to do with the test system. It is purely a specified tolerance to be met in conducting the test. This is the club which the specification writer holds over the test engineer and which keeps this method from becoming a justification for poor fixtures. The fixture designer, although he is not required to produce a purely resonance-free fixture, must assure the imposers of the specification that his range of variation is within their limits of allowable variation or at least reasonably close to it. This may not be any

easier to do, but there is now a well-defined basis for negotiating their differences about how good the fixture must be.

The problem with implementing this philosophy is that specifications do not define the allowable limits. MIL-STD-810A, Method 514.1, contains a reference to averaging which amounts to nothing more than recognition that there is such a thing and that it is allowable (1). The test engineer is left completely on his own to decide that his test is large enough to warrant averaging, to decide how much variation to allow, and to convince his customer that there is nothing sacred about the specification. The important thing is that all parties are assured that the hardware possesses the integrity to perform its function and survive under the extremes of its service environment as approximated by the specification.

#### TEST EQUIPMENT AND INSTRUMENTATION

The test of the Litton computer programmer is being conducted using a Ling A249 shaker and associated instrumentation acquired for this program. Figures 1, 2, and 3 show the physical arrangement of the fixtures in each of the three test axes. In the horizontal axes the fixture is mounted on four team tables. The object mounted in the fixture for these evaluation tests was a wooden mockup simulating the weight and C.G. of the actual computer programmer. The

specimen is attached to the fixture through the 10 isolator mounts distributed along the lower inboard edge and the 10 isolator mounts distributed along the upper outboard edge.

The structural requirements of the aircraft include those for possible arrested landings and thus do not allow vertical loads be carried in the area of the upper attachment of the computer programmer. The upper mounts are therefore attached to the aircraft through an articulated hinge and drag beam assembly. This is simulated on the fixture by a stainless steel flexural element. The upper mounts are sandwich type which operate in shear only, and all vertical load is carried out through the lower mounts. The result is a C.G. isolated system at 26 Hz in the x and y axes (see Fig. 4). In the z axis, however, there is also a prominent rotational mode at 45 to 50 Hz.

The modes of isolation do not significantly affect the fixture, but there is a secondary requirement that the specimen be tested hard-mounted (2). To do this the isolators are replaced by similarly shaped solid aluminum mounts. The result of this mounting is the development of rigid body modes between 75 and 100 Hz which do significantly affect the fixture.

With this method of mounting there are 20 discrete load-carrying attachment points (10 in z axis), each of which could be a legitimate single accelerometer control point. To average all of them is beyond the capacity of present

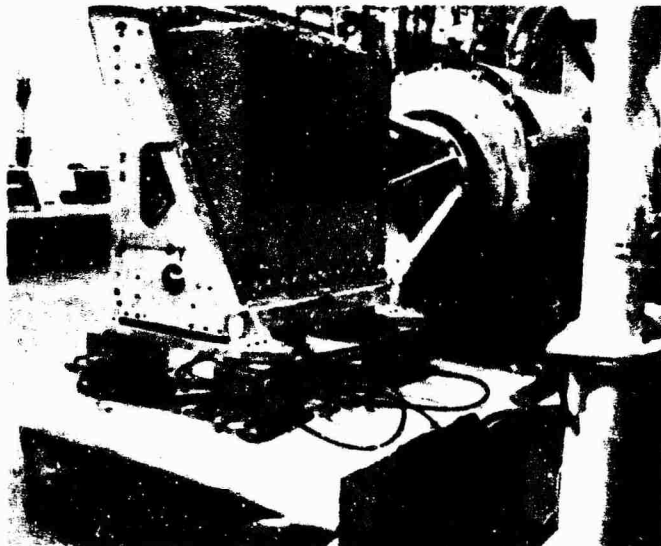


Fig. 1. Computer programmer fixture mounted in x axis

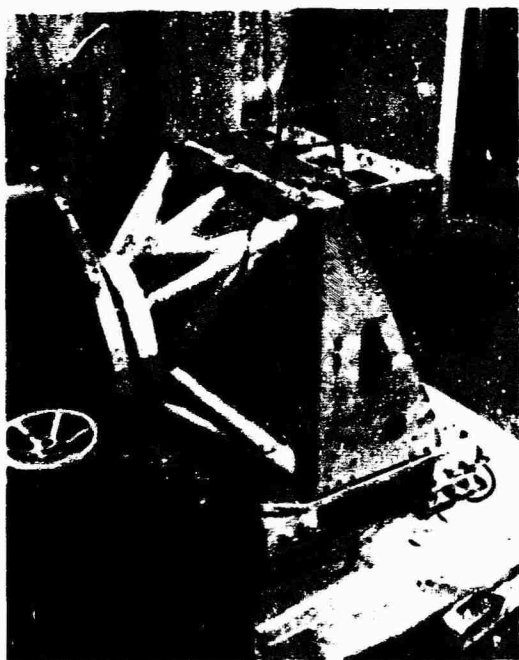


Fig. 2. Computer programmer fixture mounted in y axis

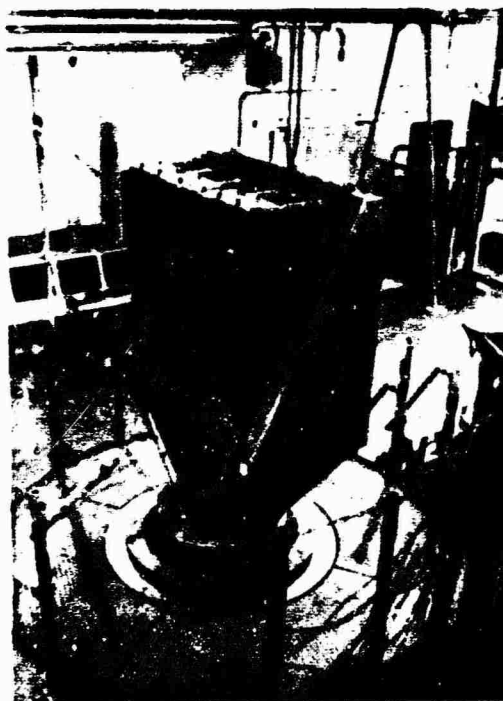


Fig. 3. Computer programmer fixture mounted in z axis

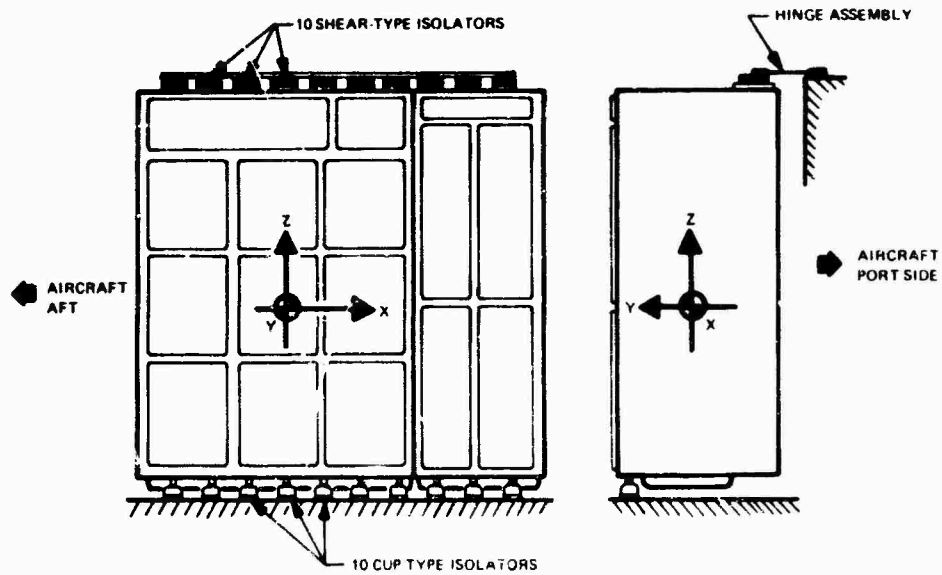


Fig. 4. Mounting configuration of airborne computer programmer

equipment and would be prohibitive in cost and complexity. Therefore, six locations were provided on the fixture for possible attachment of a control accelerometer. These are shown in Fig. 5. Of the six locations provided, in the x and y axes only four (F1, F2, F4, and F6) were actually used in the test because of limitations in equipment availability. In the z axis only three locations (F1, F2, F3) were used since the load is applied only through the bottom mounts as described earlier.

Figure 6 shows the entire instrumentation system, including control and averaging features as well as the data acquisition and plotting system. The heart of the system is the Unholtz-Dickie MAC-6B averager feeding into the spectral Dynamics SD-104, -105 sweep oscillator servo system. The averaged control accelerometer signals each pass through a 10-Hz Spectral Dynamics SD-101A tracking filter prior to entering the MAC-6B. The MAC-6B does not itself average the signals. What it does is multiplex them with a sampling rate synchronized to the fundamental excitation frequency. The synchronization is necessary to insure that one full cycle of each signal is sampled at all frequencies. This precludes introducing extraneous frequency components which are functions of the sampling rate. Oscilloscope traces of the multiplexed output of the MAC-6B are shown in Fig. 7.

The multiplexed signal is then coupled into the acceleration channel of the SD-105 servo where it undergoes detection within the meter circuit, and a value is indicated at the acceleration meter which is proportional to the absolute value average of the accelerometer signals (averaged control level).

Since several crossovers from acceleration to displacement are required by the isolated specimen, the Line MLP-101 multilevel programmer was used. At first, an effort was made to control constant displacement from the averaged control signal (which is the MAC-6B output), but since this would require the SD-105 to double integrate the multiplexed signal, it could not be done. Instead, a separate accelerometer was placed on the shaker head and coupled directly to the SD-105, where its output was double integrated to provide a displacement signal. Thus averaging was performed only during the constant acceleration portions of the spectrum.

#### PROCEDURE

The specified environments for the hard-mounted and the isolated conditions were from MIL-T-5422E, Curves II and IV, respectively (2). These spectra were transformed into fields of excitation inputs by adding the arbitrary

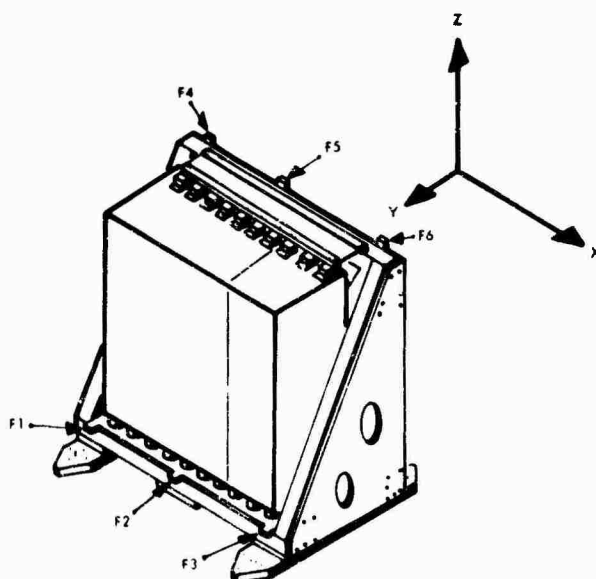


Fig. 5. Location of averaged control points on computer programmer fixture

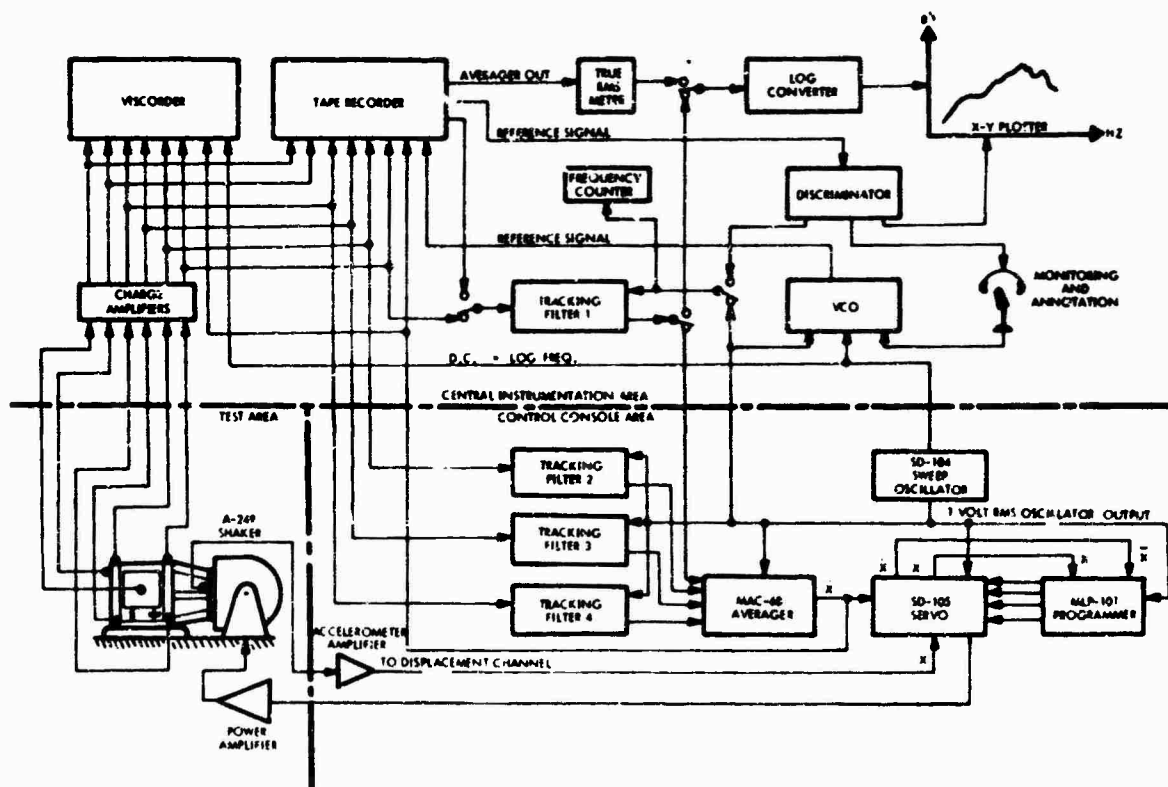


Fig. 6. Instrumentation diagram for computer programmer vibration test

allowable variation bands as shown in Figs. 8 and 9. These have the values of  $\pm 3\text{db}$  up to 300 Hz and  $\pm 6\text{db}$  from 300 to 500 Hz. The value of the band was based on expected fixture performance, which was determined from a previous series of tests (3).

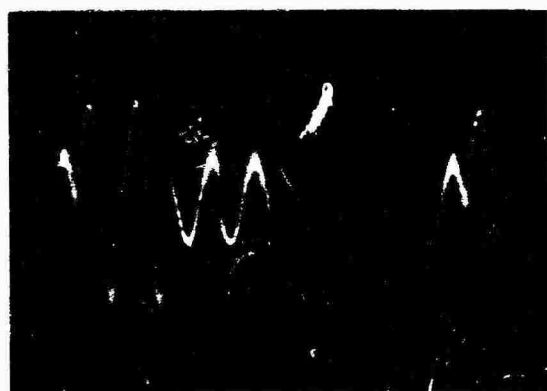
In all other respects, the test procedure conformed accurately to the MIL-T-5422E methods, i.e., logarithmic frequency sweeps were performed from 5 to 500 Hz in 7.5 min (.27 decades/min (2). The signals from each control accelerometer, as well as those which were not averaged, and six others mounted to monitor crosstalk were recorded simultaneously on the Visicorder and FM magnetic tape during sweeps from 5 to 500 Hz. The Visicorder traces were used for "quick look" to insure that the data were being recorded properly and that proper range settings were being used. The magnetic tapes were later replayed through a 10-Hz tracking filter and reduced to x-y plots. Modulated frequency reference data and voice annotation were recorded on a single AM channel as shown in Fig. 6.

A problem was encountered in obtaining x-y plots of the averaged control levels. The averaged

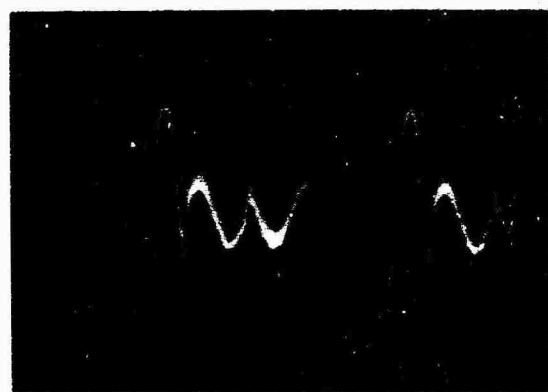
control signal was recorded at the multiplex output of the MAC-6B before being averaged by the SD-105. Although the result of the averaging process was observable at the SD-105 acceleration meter, there is no output provision for recording this metered signal. A solution was evolved by playing the multiplex signal into a true rms meter, patching the output of the meter's square-law amplifier into the x-y plotting system, and calibrating the recorder to the proper level. This gives a permanent record of the actual averaged control level for each sweep.

## RESULTS

An example of the data obtained is shown in Fig. 10 for the x axis, isolated. The four superimposed curves are the outputs of the four accelerometers at averaged control points F1, F3, F4, and F6. It is notable that the range of variation at frequencies below 80 Hz was so narrow that it could be represented by a single line. The information lost by using the single accelerometer from 5 to 20 Hz and from 33 to 73 Hz is negligible. It is quite obvious what would occur if any one of these locations had



(a) - INDICATED AVERAGE INPUT LEVEL =  $10_1$  AT 200 Hz  
(Y-AXIS ISOLATED)



(b) - INDICATED AVERAGE INPUT LEVEL =  $10_2$  AT 400 Hz  
(Y-AXIS ISOLATED)

Fig. 7. Typical multiplex outputs from  
MAC-6B averager

been used for single-point control. For instance, controlling at F3 would have caused a tremendous amplification at 310 Hz at location F6 and an unacceptable attenuation at 390 Hz at location F4.

This type of display is rather confusing, especially when six or more points are involved. In order to emphasize the range of variation, which is now a significant property of the system, it is a simple matter to envelop the upper and lower boundaries of the superimposed curves and ignore the data between unless they are needed for some specific reference. Then, by adding the curve of averaged control level we have a complete graphical display of the test system response when the specified field of excitation is imposed across its averaged control points. This is the type of display shown in Fig. 11 through 16 with the limits of allowable variation superimposed for all three axes, both hardmounted and isolated.

In this test it is immediately obvious that the range of variation exceeds the allowable variation at several frequencies. (It should be noted that subsequent to obtaining these data, fixture improvements have been made, but have not yet been released.) There are several avenues now open to dealing with this situation. The two most obvious would be either to relax the allowable variation or to make improvements in the fixture, such as adding damping to narrow the range of variation at fixture resonance or adding stiffness to increase the frequencies of resonance. Another approach is to examine both the response of the specimen and measurements of the actual service environment and determine if the frequencies at which the allowable variation is exceeded coincide with either a critical excitation or specimen response frequency. If not, the wide variations could be allowable, particularly if the bandwidth is quite narrow, as in the y axis hardmounted data at 400 Hz (Fig. 14). Examination of the data at each control point may indicate that the particular excessive variation occurred at only one relatively unimportant location. A third alternative would be to use a weighted average so as to increase the effect of one or more control locations with respect to others. This would have the effect of raising or lowering the entire range of variation envelope.

Examining Figs. 12 and 14 more closely, particularly in the range from 70 to 200 Hz, it is evident that there is a surprising amount of point-to-point variation in this range. This is the area of hardmounted rigid-body modes mentioned earlier. We know from direct observation during the tests that the resonant frequencies of the fixture are above 250 Hz; thus these low-frequency deformations are caused by the fixture reacting to the modes of the hardmounted specimen itself. This is a perfect illustration of the earlier statement that fixture resonance is not the only cause of control problems.

## CONCLUSION

It is difficult to deny that averaging control is a tremendous aid for increasing our understanding of the effect of fixture response on test specifications. It is also clear that it has limitations. One point above all others should be emphasized: average control provides complete assurance that at least some portion of the test specimen is exposed to the intended test level at all frequencies. This is not true of single-point control. In fact, at some frequencies, the single control point may be the only point at the proper level.

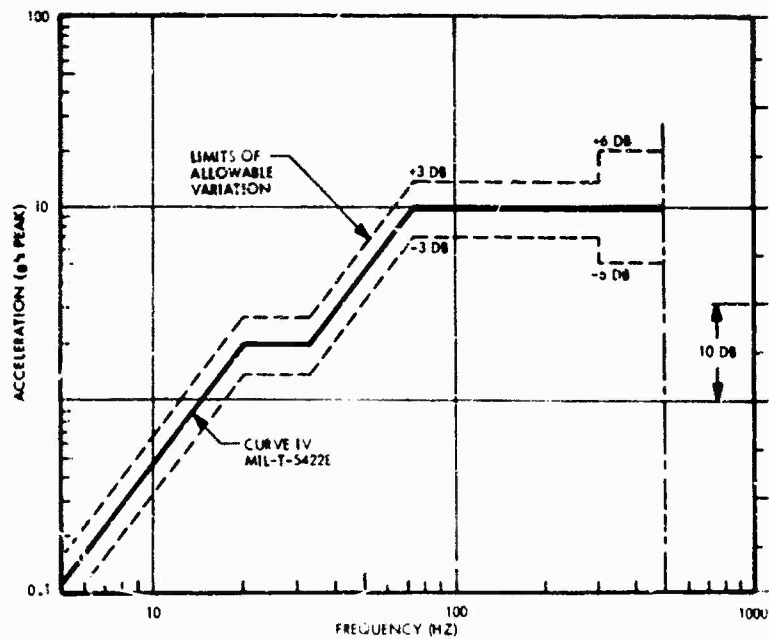


Fig. 8. Specified field of excitation for isolated computer programmer

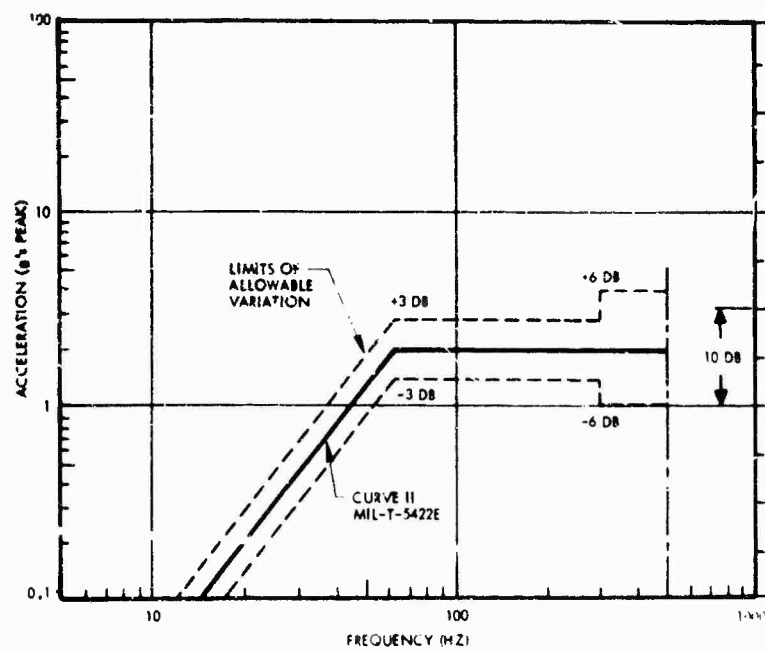


Fig. 9. Specified field of excitation for hardmounted computer programmer



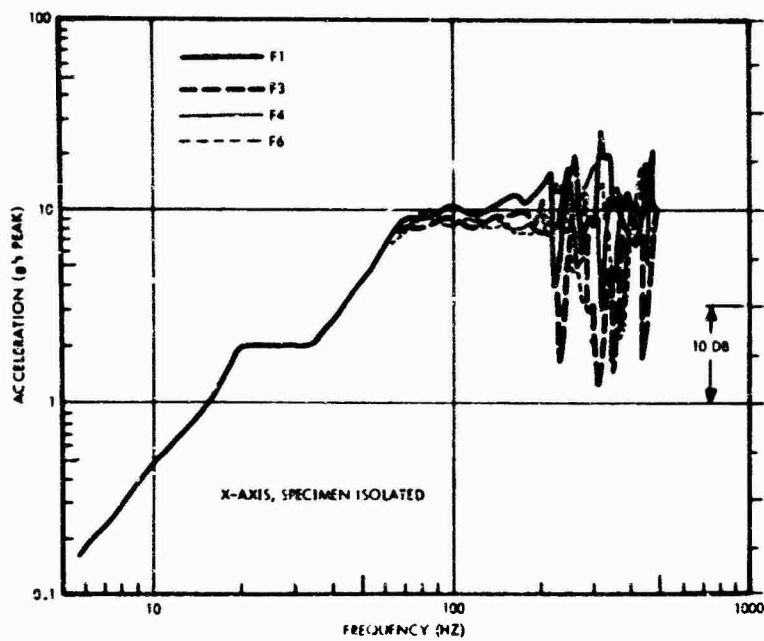


Fig. 10. Vibration levels at averaged control points on computer programmer fixture (x axis isolated)

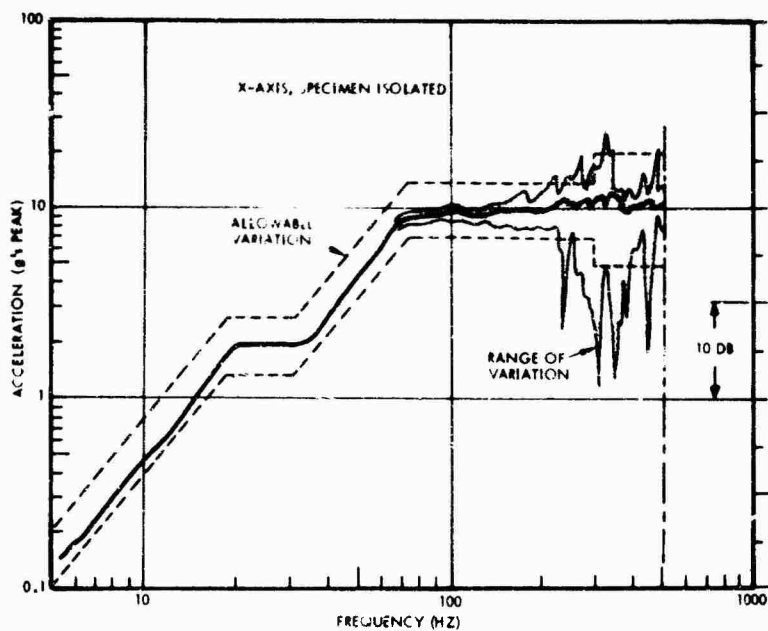


Fig. 11. Averaged control level and range of variation for computer programmer fixture (x axis isolated)

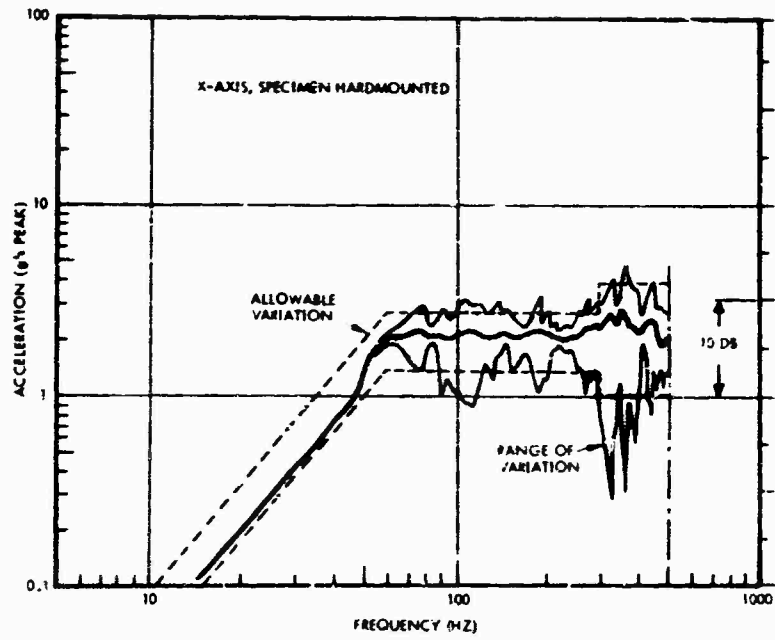


Fig. 12. Averaged control level and range of variation for computer programmer fixture (x axis hardmounted)

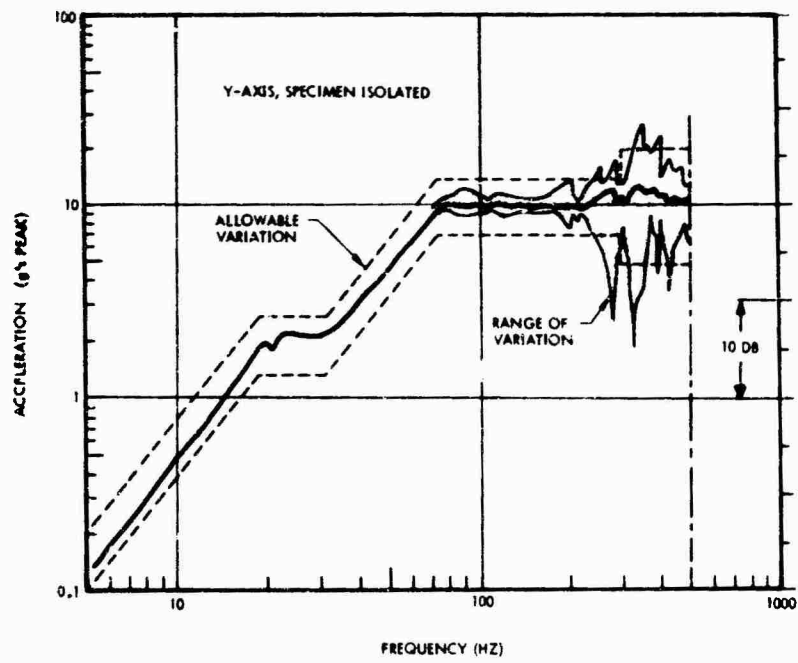


Fig. 13. Averaged control level and range of variation for computer programmer fixture (y axis isolated)

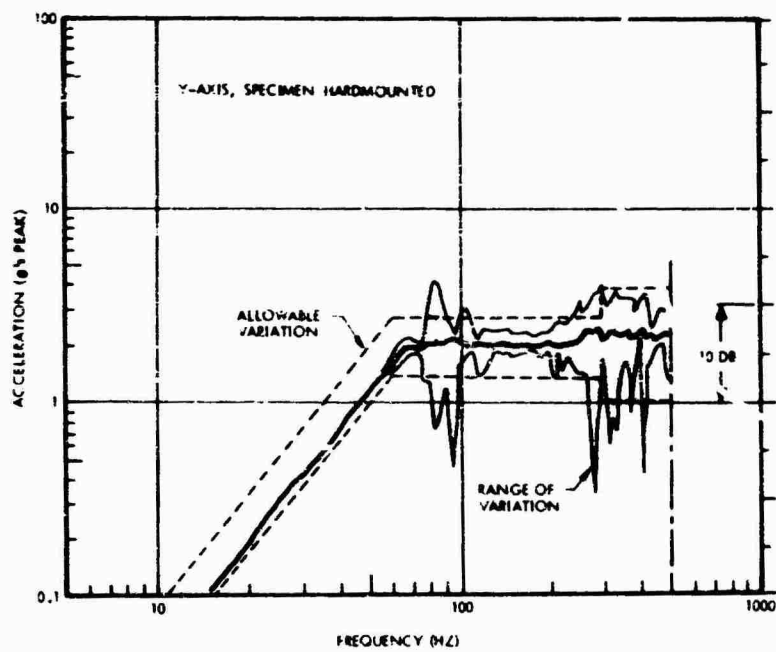


Fig. 14. Averaged control level and range of variation for computer programmer fixture (y axis hardmounted)

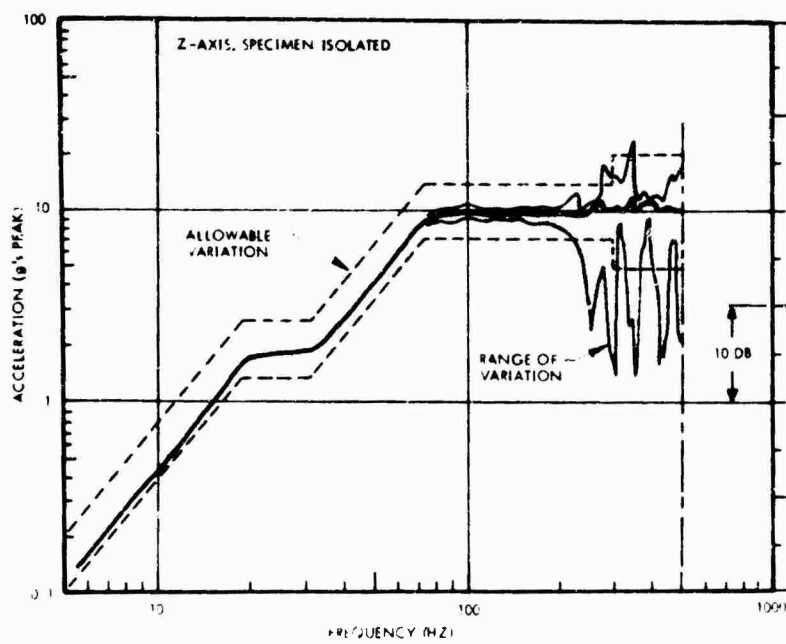


Fig. 15. Averaged control level and range of variation for computer programmer fixture (z axis isolated)

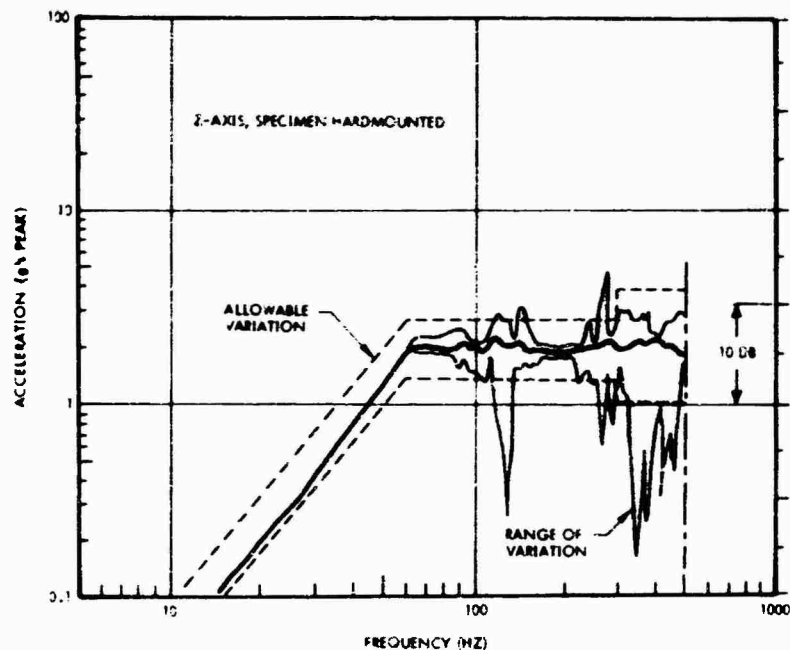


Fig. 16. Averaged control level and range of variation for computer programmer fixture (z axis hardmounted)

Average control is not a panacea for poor fixture design if reasonable limitations are fixed for the range of variation. In most cases, although some degree of resonance would be allowable, averaging allows the fixture performance to be scrutinized even more carefully since the total response is on display at once. Regarding the fixture as a component member of an integrated test system, however, cannot help but give the test engineer a much more realistic frame of reference in which to function.

The variety of equipment which is available to perform this type of test is increasing. The system used in these tests was but one of many combinations which could have been used. Much future work is required to evaluate the various methods of averaging transducer signals and to find those best suited for each type of application. With all the instruments available, however, there are still some voids. A good example is the lack of reliable devices for automatically performing multiple crossovers in a single

sweep without exceeding the dynamic range of the servo system.

It is the author's hope that this presentation will inspire others to comment on the use of averaging control systems and on the validity of the definitions presented here. It would be a significant step forward if the methods outlined here could gain in acceptance and find universal usage at all laboratories dealing with large package tests.

#### ACKNOWLEDGMENTS

The author is indebted to the management of the Litton Data Systems Division's Equipment Engineering Department and of the Engineering Project Office for their support and encouragement. Credit is also due to George Schaechtel of the Equipment Engineering Analysis Group for his aid in obtaining and preparing the data, as well as to Angelo Spandrio of the Point Mugu Environmental Laboratory for his assistance.

## REFERENCES

1. MIL-STD-810 (USAF), "Military Standard, Environmental Test Methods for Aerospace and Ground Equipment," June 1964
2. MIL-T-5422E (ASG), "Military Specification, Testing, Environmental, Aircraft Electronics Equipment," Apr. 1959
3. H. R. Berkman, "Computer Programmer Preliminary Fixture Evaluation," Litton, DSD, Engineering Test Rept. 546100-789, Sec. A, Dec. 1966

## DISCUSSION

Mr. Arone (Wyle Laboratories): On your instrumentation system you showed one accelerometer for your displacement control at the low frequency end which looked like it was close to the head of the shaker. You then switched over to your average control at around 50 cycles or so. Is there any particular reason why you didn't use a program to control your average all the way through your spectrum?

Mr. Berkman: This was mostly a matter of using the instrumentation available to us. We didn't have anything that would take accelerometer signals and double integrate to give displacement. We didn't feel that it was needed at the low end because there wasn't very much variation. We haven't lost very much accuracy.

Mr. Scharton (Bolt Beranek & Newman): I would like to commend you for your fine presentation of these very novel ideas. I have been in

favor of these ideas for several years. As you say, the main problem comes down to controlling these variations from point to point when you control on the average. One interesting thing that I would like to point out is that you can show that the magnitude of the spatial variations at a single frequency is proportional to the number of vibration modes of the fixture activated simultaneously. So, if a fixture is vibrating in one mode you will have quite a large variation, whereas if the fixture is vibrating in ten modes the spatial variations will be quite small. This is what has led us at Bolt Beranek & Newman to look at a way of developing fixtures that would have a lot of vibration modes, thereby reducing this spatial variation illustrated in your slides.

Mr. Berkman: This is very interesting. I thought about trying to develop a way of coming close to simulating an actual structure, but there are too many parameters. It is almost impossible.

\* \* \*

# VIBRATION METHODS FOR MULTIPLE RANDOM EXCITATION

William E. Noonan  
McDonnell Company  
St. Louis, Missouri

An investigation was conducted to establish a method, through applications of impedance techniques, for controlling a random environment resulting from multiple excitation. The output power spectral density (PSD) of a linear system was expressed in terms of system functions, input PSD's, and their cross PSD's.

A theoretical model was constructed, and the most simple multiple system (two degrees of freedom) was selected. The system response was determined, and the effects of uncorrelated and correlated forcing functions demonstrated. A result of this investigation revealed that arbitrary output PSD's cannot be obtained for independent applied sources. Arbitrary output spectra can impose a negative energy requirement on independent sources.

Experimental tests were conducted on a free-free beam. System functions were obtained through sinusoidal tests and were used in predicting the random response. The only independent parameter in the experimental system was the power amplifier input voltages. Random tests, conducted for uncorrelated power amplifier input voltages, resulted in good correlation between predicted and measured response.

Using the results of the theoretical and experimental investigations, a proposed test method is described for multiple random excitation.

## INTRODUCTION

The present trend in vibration testing of large specimens is toward the employment of multiple energy sources. This applies whether these sources are vibration exciters or acoustic transducers.

Currently, random-vibration tests on vehicle components are conducted by applying a specified acceleration power spectral density (PSD) using a single vibration source. These specified acceleration spectra are obtained by enveloping flight data obtained from flights of actual or similar vehicles. For single excitation, the control problem is concerned with only one system function. (System function is defined as the transfer function or frequency response function, both amplitude and phase.) The application of more than one vibration source results in multiple system functions.

This paper investigates the problems of multiple excitation and resolves these problems into a test procedure. The investigation is directed toward the application of impedance techniques. The question of phase is resolved in the consideration of cross PSD's. A theoretical investigation is made into the response

of a two-degree-of-freedom system when subjected to multiple random excitation, and the results of this investigation are experimentally applied to a physical system in the laboratory.

This paper represents a summary of the entire investigation. Detailed descriptions of the investigation and complete results are presented in Ref. [1].

## RESPONSE OF A LINEAR SYSTEM TO MULTIPLE RANDOM INPUTS

The infinitesimal output time function  $[df(t)_0]$  of a linear system can be expressed as a function of the input time function  $[f(t)_i]$  and the unit impulse response  $[h(t)]$  [2]:

$$df(t)_0 = f(t)_i \cdot h(t - \tau) \quad (1)$$

By summing all of the infinitesimal outputs from the beginning to the time  $t$ , the output time function can be expressed as a cumulative function of the input:

$$f(t)_0 = \int_0^t f(\tau)_i \cdot h(t - \tau) d\tau \quad (2)$$

Note that the instantaneous output of the system is dependent on everything which has occurred previously.

Using the above relations, the output autocorrelation function  $[R(\tau)]_o$  can be expressed as a function of the input autocorrelation:

$$R(\tau)_o = \lim_{T \rightarrow \infty} \frac{1}{T} \int_{-T}^T dt \int_{-T}^t h(\tau) f(t-\tau)_i d\tau$$

$$= \int_{-T}^T h(\tau) f(t-\tau)_i d\tau$$

$$R(\tau)_o = \int_{-T}^T h(\tau) d\tau \int_{-T}^T h(\tau) d\tau R(\tau-\tau)_i \quad (3)$$

The above expression gives the relation for the input to output autocorrelation for a single forcing function. For multiple inputs the above steps can be paralleled to arrive at the following expression [3]:

$$R_{rr}(\tau)_o = \sum_{n=1}^N \sum_{m=1}^M \int_{-T}^T h_{rn}(\tau) d\tau$$

$$= \int_{-T}^T h_{rn}(\tau) d\tau R_{nm}(\tau-\tau)_i \quad (4)$$

where  $R_{nm}$  represents the crosscorrelation of the  $n$ th and  $m$ th inputs, and  $R_{rr}(\tau)_o$  the autocorrelation of the  $r$ th output.

By transforming the autocorrelation from the time domain to the frequency domain, the output PSD can be expressed as a function of the input PSD:

$$S_{rr}(f)_o = \sum_{n=1}^N \sum_{m=1}^M \bar{H}_{rn}(2\pi f) H_{rm}(2\pi f) S_{nm}(f)_i \quad (5)$$

where  $H(2\pi f)$  = system function,  $\bar{H}(2\pi f)$  = conjugate system function.

The cross PSD's between the  $r$  and  $s$  output can be obtained in a similar manner:

$$S_{rs}(f)_o = \sum_{n=1}^N \sum_{m=1}^M \bar{H}_{rn}(2\pi f) H_{sm}(2\pi f) S_{nm}(f)_i \quad (6)$$

Equations (5) and (6) can be combined into a single matrix form of:

$$S(f)_o = H(f)_o H(f)_i^T S(f)_i \quad (7)$$

$S(f)_o$ ,  $\bar{H}(f)_o$ ,  $H(f)_i^T$  and  $S(f)_i$  are square  $N \times N$  complex matrices;  $\bar{H}(f)_o$  is the conjugate system function matrix and  $H(f)_i^T$  is the transpose of the system function matrix.

Equation (7) gives the relation for the output PSD's as a function of the system functions, the conjugates of the system functions, and the input PSD's. This expression is used extensively in predicting the response of the theoretical and experimental model. The system functions which are a measure of impedance determine the response for the forcing functions which can be periodic, transient, or random. Of equal importance is the reverse calculation. The input forcing functions can be determined for desired output PSD's.

## THEORETICAL MODEL

A theoretical model was constructed, and the most simple multiple system (two degrees of freedom) was selected [4]. The system was investigated to determine the effects of multiple excitation.

The investigation was directed toward determining system functions and the effects of forcing function correlation. The analyzed system, shown in Fig. 1, was assigned the following arbitrary values:

1. Undamped natural frequencies:  $\omega_{n2} = 2\omega_{n1}$ .
2. Spring rate:  $K_2 = 2K_1$ .
3. Mass:  $M_2 = 0.5M_1$ .
4. Damping in percentage of critical:  $\zeta_2 = 0.5\zeta_1 = 0.025$ .

The system functions are determined by solving the equations of motion and are expressed as follows:

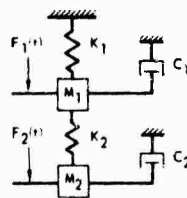


Fig. 1. Two-degree-of-freedom model

$$H_{11} = \frac{K_2}{\omega_{n2}^2} \left[ 1 - \left( \frac{\omega}{\omega_{n2}} \right)^2 + j 2\zeta_2 \left( \frac{\omega}{\omega_{n2}} \right) \right] \quad (8)$$

$$H_{12} = \frac{K_2}{\omega_{n2}^2} \quad (9)$$

$$H_{21} = \frac{K_2}{\dots} \quad (10)$$

$$H_{22} = \frac{K_1}{\dots} \left\{ \left[ 1 + \frac{K_2}{K_1} - \left( \frac{\omega}{\omega_{n1}} \right)^2 \right] + j 2 \zeta_1 \left( \frac{\omega}{\omega_{n1}} \right) \right\} \quad (11)$$

$$K_1 K_2 \left[ \frac{\omega^4}{\omega_{n1}^2 \omega_{n2}^2} - \left( \frac{1}{\omega_{n1}^2} + \frac{1}{\omega_{n2}^2} + \frac{4 \zeta_1^2 \omega^2}{\omega_{n1}^2 \omega_{n2}^2} + \frac{M_2}{K_1} \right) \omega^2 + 1 \right] \\ \cdot j 2 \zeta_1 K_2 \left[ \left( \frac{2 \zeta_2}{\omega_{n1} \omega_{n2}} - \frac{2 \zeta_1}{\omega_{n2} \omega_{n1}} \right) \omega + \left( \frac{2 \zeta_1}{\omega_{n1}} + \frac{2 \zeta_2}{\omega_{n2}} + \frac{C_2}{K_1} \right) \right] \quad (12)$$

Curves showing the response of the system with respect to  $F_1(t)$  are presented in Figs. 2 and 3. It is interesting to note that the ratio of the response of system 2 to system 1 is the single-degree-of-freedom response of mass 2.

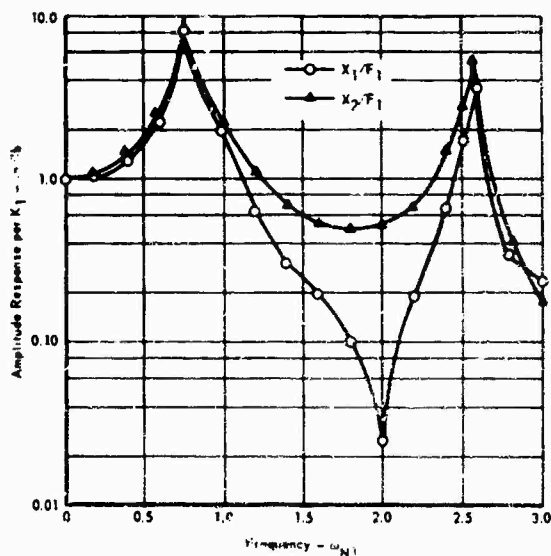


Fig. 2. Two-degree-of-freedom system response to force excitation at system 1; absolute value of amplitude with respect to force, systems 1 and 2

Based on the system functions above, the random response of the two-degree-of-freedom system was predicted for forcing functions having equal band-limited white PSD's. Figure 4 illustrates the response for correlated (in-phase) and uncorrelated (statistically independent) forcing functions. The effect of correlation increases the first mode response by 3 db and decreases the second mode response by 10 db.

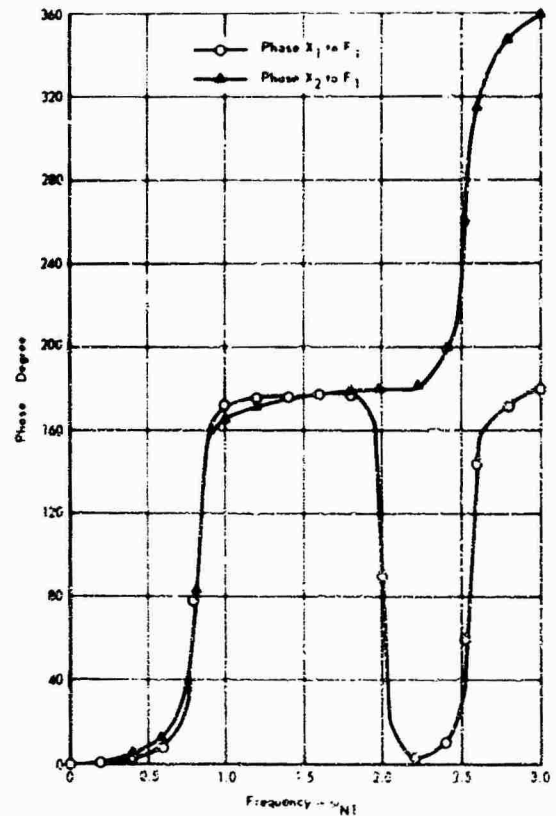


Fig. 3. Two-degree-of-freedom system response to force excitation at system 1; phase with respect to force, systems 1 and 2

The controlling parameter for this theoretical system is the force applied to each mass. The response of each mass is related to the force by a linear transformation. The transformation kernel in this case is the system function.

#### REQUIRED FORCING FUNCTIONS

The vibration spectra specified for laboratory test specimens are, in general, obtained by enveloping flight-test data. There are other considerations in determining level, but the shape of the PSD's is usually obtained by encompassing the peaks in flight-data spectra. For the laboratory test, the in-flight distributed forcing functions are combined into independent concentrated forces. Uncorrelated forcing functions are selected because the correlation between pressure disturbances approaches zero as the distance between the pressure disturbances is increased. Furthermore, if some



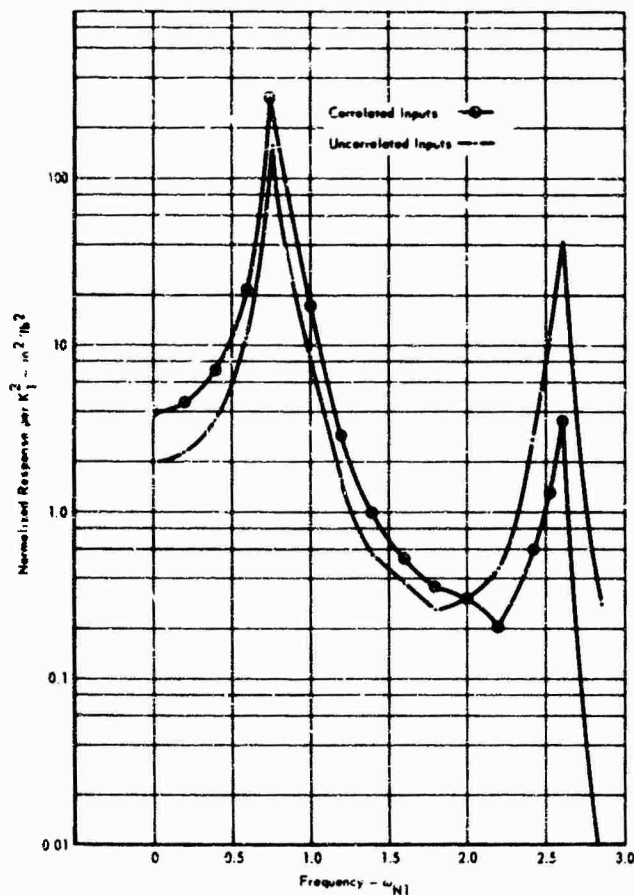


Fig. 4. Two-degree-of-freedom system response to multiple random inputs; response of system 1

degree of correlation in the forcing functions were desired, the forcing functions' cross PSD could not be controlled with present vibration control equipment. Therefore, for this discussion only statistically independent vibratory sources will be considered.

Desired acceleration PSD's are assigned to each mass in the two-degree-of-freedom model. The independent forcing functions required to obtain these spectra are computed by the following equations:

$$S_{a1} = H_{a1f1}^2 S_{f1} + H_{a1f2}^2 S_{f2} \quad (13)$$

and

$$S_{a2} = H_{a2f1}^2 S_{f1} + H_{a2f2}^2 S_{f2} \quad (14)$$

The solution of these equations for  $S_{f1}$  and  $S_{f2}$  when arbitrary spectra are assigned to  $S_{a1}$

and  $S_{a2}$  does not necessarily result in nonnegative PSD's. A negative PSD for  $S_{f1}$  and  $S_{f2}$  is an unrealistic solution. The ratio of  $S_{a1}$  and  $S_{a2}$  must lie within certain bands if the forcing function PSD is to remain nonnegative. For the two-degree-of-freedom system, these bands are obtained from Eqs. (13) and (14) and are specified as follows:

$$A \leq \frac{S_{a2}}{S_{a1}} \leq B \text{ for } A \leq B, \quad A > \frac{S_{a2}}{S_{a1}} > B \text{ for } A > B$$

$$A = \frac{H_{a2f2}^2}{H_{a1f2}^2}$$

and

(15)

$$B = \frac{H_{a2f1}^2}{H_{a1f1}^2}$$

If the ratio of the desired PSD's does not lie within these bands, then the desired spectra must be changed if reasonable control is to be achieved.

## EXPERIMENTAL TESTS

The results of the theoretical investigation were applied to a physical system in the laboratory. A beam, consisting of two aluminum channels, 1.75 in. by 6 in., bolted to two aluminum plates, 0.25 in. by 3.2 in. by 6 ft, was suspended at its first free-free mode nodal lines. The suspension wires were approximately 10 ft long, and all excitation was applied in the horizontal direction. Small 50 lb electromagnetic exciters were bonded to the sides of the beam at the locations shown in Fig. 5. Accelerometers were bonded at each exciter location and at a third location. A force transducer was installed in the exciter specimen attachment link to measure the force transmitted to the specimen.

System functions, both amplitude and phase, were measured with respect to the applied force. This was accomplished through sinusoidal tests from 10 to 500 Hz. Both exciter armatures were attached to the specimen and connected to their power amplifiers at all times to maintain continuously the effects of the exciter armature on the impedance of the system.

Typical amplitude and phase response curves are presented in Figs. 6 and 7. The

primary bending modes were 112 and 252 Hz. The first torsion mode was 180 Hz. The response of the drive link force number 2 when excitation was applied at position 1 is shown in Figs. 8 and 9. The elastic modes are reflected in the force transducer amplitude response. The rigid body modes, a function of the exciter location and restraint, are indicated in the phase response.

It is clearly demonstrated that the forces measured by the transducers are coupled to the response of the system. If both exciters are transmitting force, the output of the force transducers would not be independent. The only independent parameter which corresponds to the forcing function in the theoretical model is the power amplifier input voltage. The response of the excitation force with respect to the power amplifier voltage was measured and is shown in Figs. 10 and 11. For further experimental tests, the power amplifier input voltage was considered the forcing function.

Applying the results of the theoretical investigation to the experimental tests, the input voltages required to obtain arbitrary acceleration spectra were calculated using Eq. (7). The uncorrelated input voltage PSD was calculated for a band-limited white acceleration PSD of  $5 \times 10^{-4} \text{ g}^2/\text{Hz}$  at positions 1 and 2. Negative energy requirements resulted at 90, 252, 320, and 400 Hz for voltage number 1, and at 100, 113, 180, 257, and 300 Hz for voltage number 2.

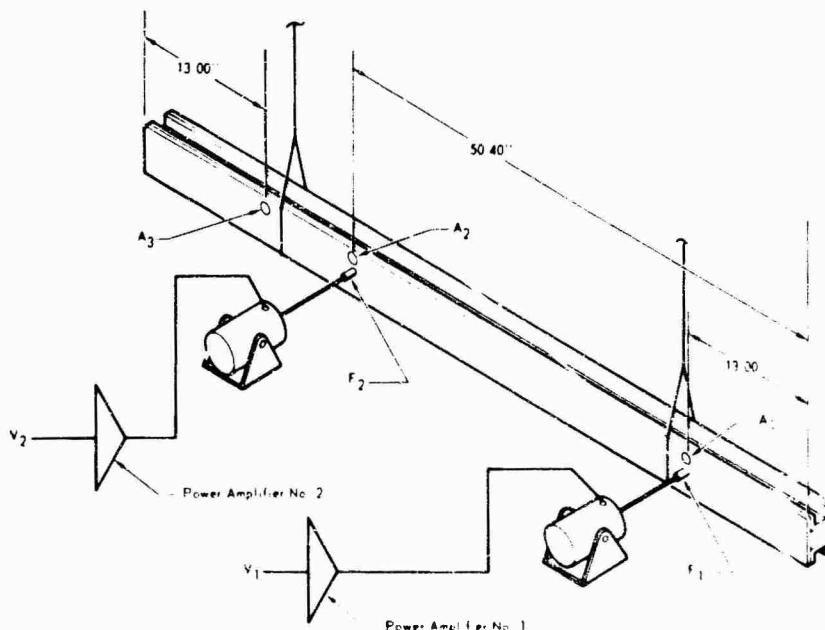


Fig. 5. Experimental test setup; vibration free-free beam

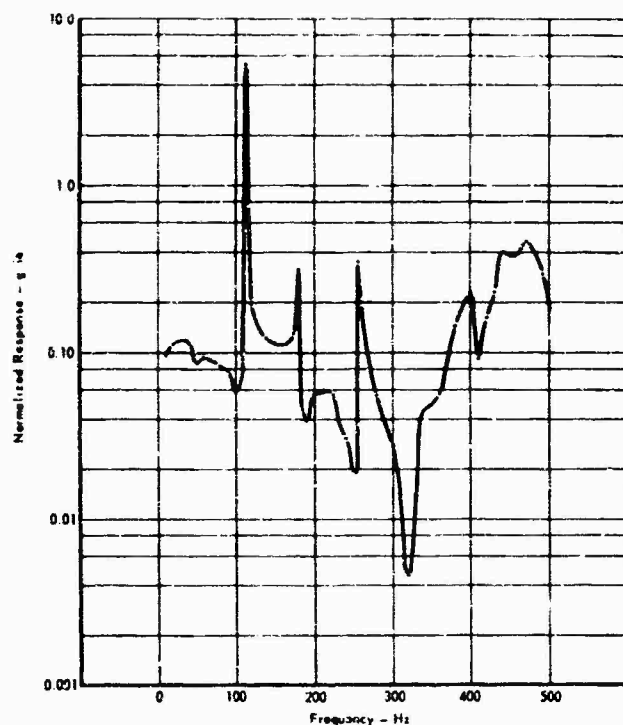


Fig. 6. System functions free-free beam force excitation at position 1; absolute magnitude acceleration 1 to force 1

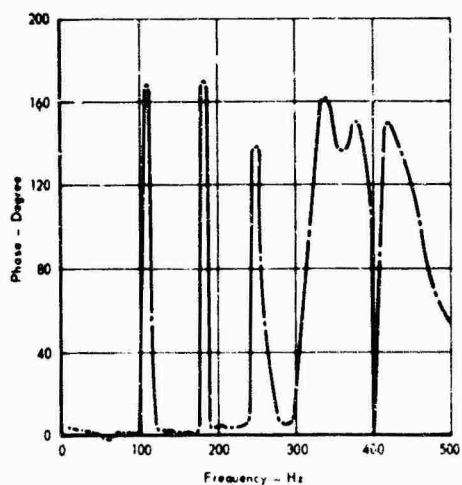


Fig. 7. System functions free-free beam force excitation at position 1; phase acceleration 1 to force 1

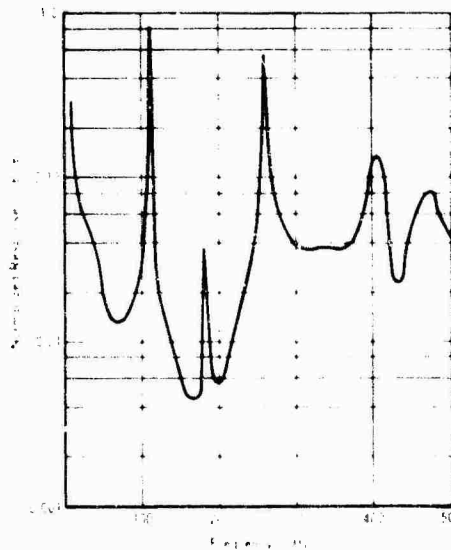


Fig. 8. System functions free-free beam force excitation at position 1; absolute magnitude of force 2 to force 1

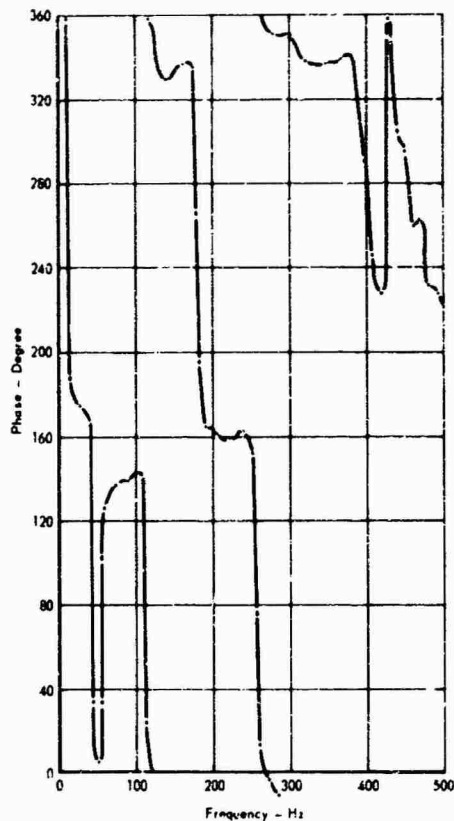


Fig. 9. System functions free-free beam force excitation at position 1; phase of force 2 to force 1

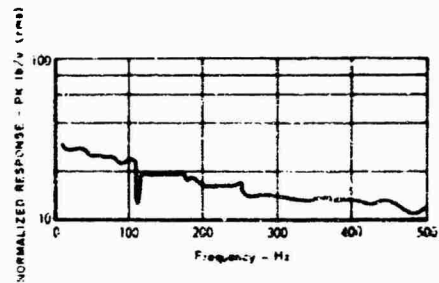


Fig. 10. System functions free-free beam force excitation at position 1; absolute magnitude force 1 to input voltage 1

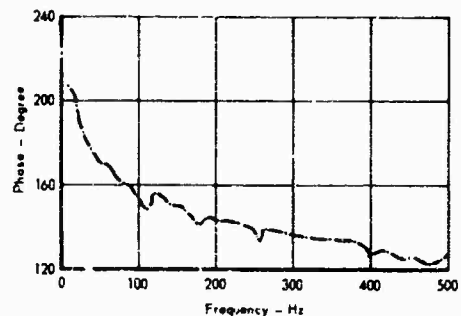


Fig. 11. System functions free-free beam force excitation at position 1; phase force 1 to input voltage 1

A random test was conducted by controlling the input voltage spectra with independent multi-channel equalizer-analyzers. An attempt was made to program the above-mentioned calculated voltage spectra except for the areas of negative energy requirements where the input spectra were given maximum attenuation. Because of improper power amplifier performance, the correct input voltage ratio could not be programmed. This resulted in acceleration PSD deviating considerably from the desired flat spectrum shapes.

Although an undesired voltage ratio was used, results substantiate the applicability of linear system relations. This applicability was a primary goal of the investigation.

A sampling of the results of the random tests is presented in Figs. 12, 13, and 14. These data represent the acceleration response of position 1 for individual and combined excitation. The circled data points are calculated data based on sinusoidal system functions and the measured input voltages. Good correlation between the

calculated and measured response is evidenced in the data. The average deviation of the calculated values was 20 percent.

## RESULTS AND CONCLUSIONS

The results of the theoretical and experimental investigation can be summarized as follows:

1. Linear system relations can be applied in predicting random response. The system function, which is a measure of impedance, is the transformation kernel for the input-output relation. The system function should be determined before conducting the random tests.

2. Arbitrary acceleration spectra cannot be obtained when independent sources are applied. The ratio of the acceleration spectra must lie within certain bands if nonnegative forcing function PSD's are to be obtained.

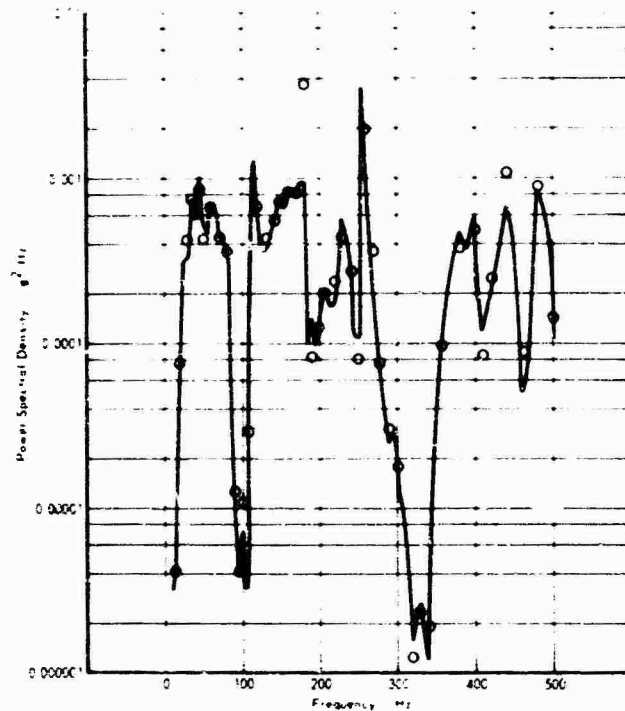


Fig. 12. Experimental random tests excitation at position 1; acceleration 1 PSD, rms level 0.44 g

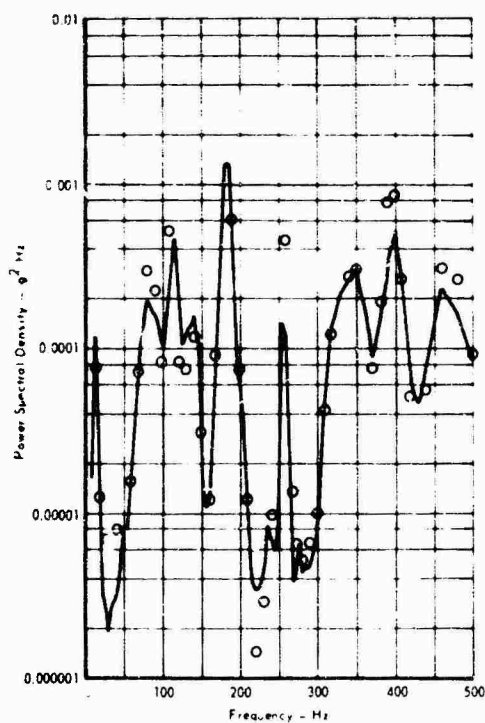


Fig. 13. Experimental random tests excitation at position 2; acceleration 1 PSD, rms level 0.31 g

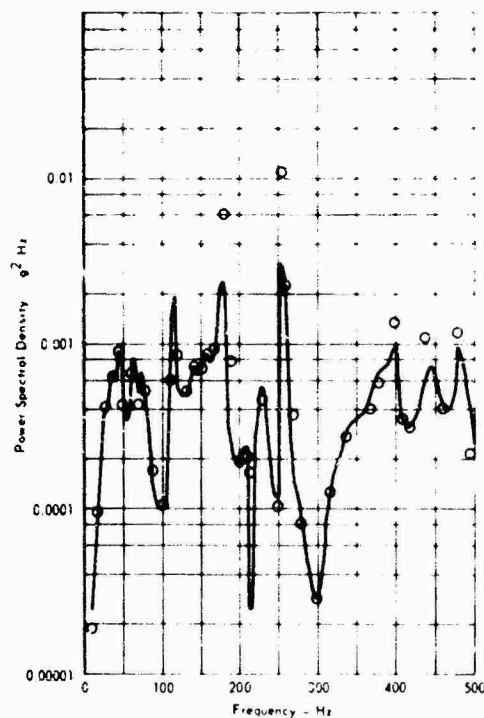


Fig. 14. Experimental random tests excitation at positions 1 and 2 uncorrelated; acceleration 1 PSD, rms level 0.54 g

3. The independent parameter in the experimental test was the power amplifier input voltage. This corresponded to the forcing function in the theoretical two-degree-of-freedom system.

Using the above results as a guide, a test method is proposed. System functions which are of primary concern can be obtained by impinging each exciter. A transient test is recommended since it requires a minimum of test time and still retains information at all frequencies. The system function is digitally calculated by performing a Fourier transform on

the time function. System functions calculated from a transient test indicated good agreement with those obtained from sinusoidal surveys. Figure 15 presents a comparison of system functions obtained from transient and sinusoidal tests on a stylized system. Based on system functions, limits for the acceleration spectrum ratios can be established and compared to the desired ratios. Any points in the acceleration spectrum having ratios outside these bands must be modified. Maintaining the same test setup, the random test can be conducted with a high degree of confidence that the applied environment will be controllable.

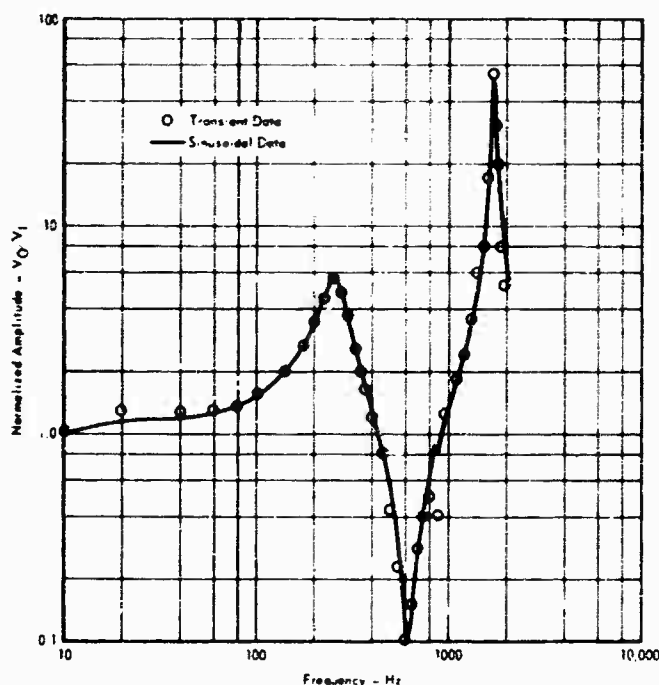


Fig. 15. Stylized system function transient and sinusoidal comparison test

#### REFERENCES

1. W. E. Noonan, "Vibration Methods for Multiple Random Excitation," unpublished thesis, St. Louis University, 1968
2. Y. W. Lee, *Statistical Theory of Communication*, pp. 323-351, Wiley, New York, 1961
3. W. B. Davenport and W. L. Root, *Random Signals and Noise*, pp. 87-109, and 171-185, McGraw-Hill, New York, 1958
4. S. H. Crandall and W. D. Mark, *Random Vibration In Mechanical Systems*, pp. 80-102, Academic Press, New York, 1963

\* \* \*

## DYNAMIC TESTING OF FULL-SCALE SATURN LAUNCH VEHICLES

B. R. Jacobs  
Nortronics Division, Northrop Corporation  
Huntsville, Alabama

A history of dynamic testing of full-scale Saturn launch vehicles at Marshall Space Flight Center is given. Methods and procedures, as well as instrumentation and facilities, are reviewed. The uses of full-scale tests are discussed, with a brief look at the uses of geometrically scaled models. Full-scale test results are compared with model test results, flight data, and mathematical models.

### INTRODUCTION

Experimental vibration surveys on full-scale Saturn launch vehicles were begun in the early 1960's. These programs were undertaken as a matter of necessity; there was no adequate theory relative to the dynamic response behavior of a complex vehicle, and test results were therefore necessary for the design of the vehicle control system. Later, as analysis methods improved, the test programs were used primarily to substantiate and verify structural analyses. Since the initial test program, which involved a Saturn I, Block I type of vehicle, was completed, these test series, through the program involving a Saturn V type of vehicle, have played an important role in the development of the Saturn vehicle at Marshall Space Flight Center (MSFC), Huntsville, Alabama.

### TEST SETUP

All dynamic testing on the full-scale Saturn-type vehicle has been performed at MSFC in the NASA dynamic test stands. The first dynamic test stand constructed is about 234 ft high; it accommodated both the Saturn I and Saturn IB series vehicle. The newest stand is approximately 365 ft high and is used for testing the Saturn V vehicle. The most important and distinguishing difference between the two towers (other than their height) is the complete enclosure of the Saturn V tower, affording both specimen and personnel protection from inclement weather.

To simulate a free-free condition, the Saturn I and IB test vehicles were suspended in

a vertical position by a cable-spring suspension system. The Saturn V test vehicle was also tested in the vertical position but was supported from below the thrust structure by means of hydrodynamic units. Figure 1 shows the first Saturn dynamic test vehicle (SA-1) erected in the test stand at MSFC.

The cable-spring suspension systems consisted of bridge-strand steel cables and helical springs employing hydraulic cylinders at the extreme upper end for lifting. Figure 2 shows the upper portion of the cable-spring system. Because of decreasing vehicle weight with increasing flight time, it was necessary to reduce the spring constant of the suspension system to maintain the closest approximation to a free-free condition. This reduction in spring constant was accomplished by decreasing the number of springs and cables supporting the vehicle. A test condition using the minimum number of cables and springs to support the vehicle and maintain its vertical stability was labeled a "soft" suspension condition. Conversely, one employing a number of springs and cables greater than that necessary for support and vertical stability was termed a "hard" suspension condition. Both hard and soft suspensions were used at certain flight times to determine the restraining effect on the natural frequencies, damping characteristics, etc. This was not altogether successful, and relatively insignificant differences were noticeable. Because of this fact and the ever-present tight scheduling of these test programs, the double suspension requirements were eventually eliminated.

Even though the cable-spring suspension system proved reliable and successful throughout the Saturn I and IB test programs, and even

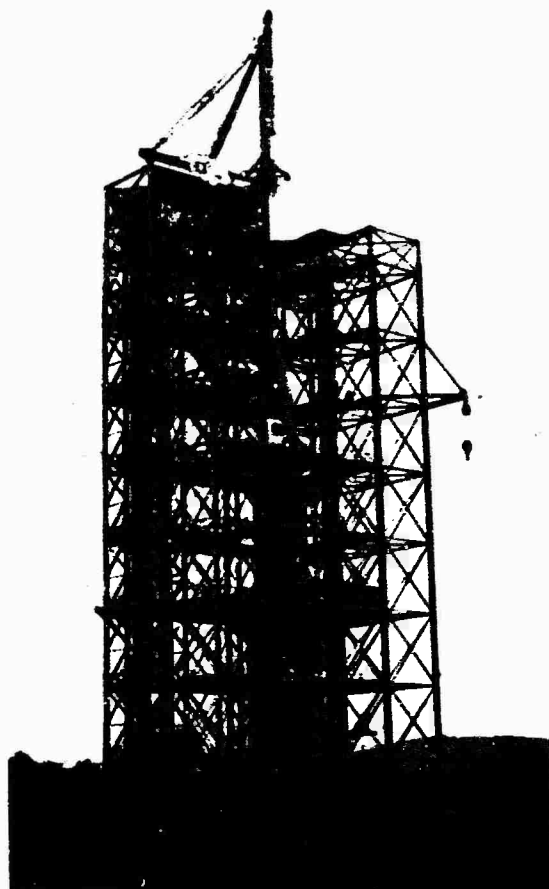


Fig. 1. First Saturn dynamic test vehicle erected in the test stand (note absence of wind screening and other structures)

though a similar system had been designed for the Saturn V dynamic test program, the latter program was to use a hydrodynamic suspension system. (See Table 1 for a summary of the cable-spring system characteristics. Figure 3 depicts the Saturn V with the cable-spring system in the tower.) The desire for a method other than the cable-spring type began almost as soon as the first Saturn I vehicle was tested; it reached a peak midway through the Saturn I program, and, for all practical purposes, the decision was made at that time to develop a new and more efficient suspension system. Many systems and methods were proposed, including compressed gas springs, liquid springs, and various arrangements of mechanical springs. Out of these the hydrodynamic system was chosen and subsequently designed and developed by the Martin-Marietta Company. The initial conception of this system came from MSFC.

The system for the Saturn V test vehicle has four hydrodynamic units, each placed upon a reinforced concrete and steel pedestal located at the four holddown points. The support system consists primarily of a piston within a cylinder fixed to the pedestal (Fig. 4). The piston is free to move vertically, but it is supported laterally by an oil gap, fed at high pressure, preventing piston-cylinder contact. The spring constant depends directly on a volume of trapped air, the size of which may be varied as desired. Lateral motion of the vehicle is provided for by a horizontal oil bearing on top of the pistons; rotational motion is permitted by means of a spherical bearing above the horizontal bearing.

Aside from the estimated cost savings of this system as compared with the cable-spring suspension system that would have been required





Fig. 2. Typical suspension point on cable-spring suspension system for Saturn I and IB tests (outer tanks of Saturn booster appear to right of springs)

TABLE 1  
Saturn V Cable-Spring Suspension System Characteristics

| Flight Time (sec) | Vehicle Weight (lb) | Number of Cables <sup>a</sup> | Number of Assemblies <sup>b</sup> | Total Spring Constant <sup>c</sup> (lb/in.) | Vehicle First Bending (cps) | Rocking Frequency (cps) | Translational Frequency (cps) | Static Stability Ratio <sup>d</sup> |
|-------------------|---------------------|-------------------------------|-----------------------------------|---|-----------------------------|-------------------------|-------------------------------|-------------------------------------|
| Liftoff           | 6,000,000           | 4                             | 55                                | 103,000                                     | 0.99                        | 0.165                   | 0.012                         | 1.30                                |
| 10                | 5,715,456           | 4                             | 55                                | 103,000                                     | 0.99                        | 0.165                   | 0.0148                        | 1.31                                |
| 35                | 5,032,550           | 3                             | 50                                | 89,230                                      | 1.00                        | 0.161                   | 0.015                         | 1.26                                |
| 78                | 3,780,558           | 2                             | 45                                | 73,448                                      | 1.08                        | 0.143                   | 0.015                         | 1.31                                |
| 112               | 2,613,109           | 2                             | 35                                | 60,747                                      | 1.09                        | 0.142                   | 0.016                         | 1.30                                |
| 150.6 (B.C.O.)    | 1,750,000           | 1                             | 15                                | 27,501                                      | 1.16                        | 0.121                   | 0.014                         | 1.18                                |

<sup>a</sup>Per suspension point; cables are 3.5-in. bridge strand with breaking strength of 724 tons and yield strength approximately 55 percent of breaking strength;  $E = 22 \cdot 10^6$  psi.

<sup>b</sup>Per suspension point; spring assembly consists of two 8.5-in. (O.D.) springs in series with spring constant for each assembly of 2430 lb/in. (spring wire diameter = 2.9 in.); free length (unloaded) of each assembly approximately 78 in.; extended length (loaded) of each assembly approximately 93 in.

<sup>c</sup>Per suspension point. Note.--A dynamic load factor of 0.1 g was used in determining the number of cables and spring assemblies required.

<sup>d</sup>The quotient of the restoring moment ( $M_R$ ) divided by the overturning moment ( $M_{OT}$ ) at a static condition.

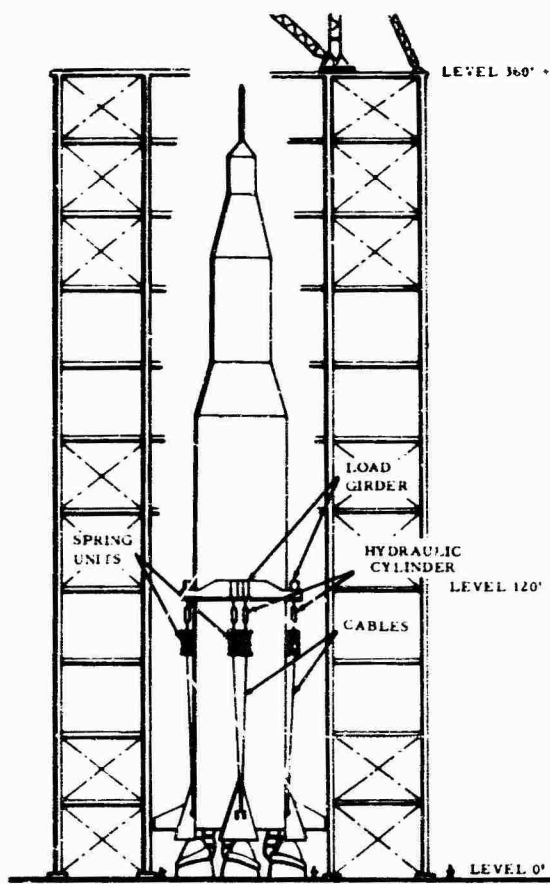


Fig. 3. Saturn V cable-spring suspension (vehicle in tower raised to test position)

for the larger Saturn V vehicle, the hydrodynamic support system possesses several advantages over its cable-spring predecessor. Some of these are:

**Analysis simplification**

Greatly reduced effective mass attached to specimen

Extremely low damping

Vehicle handling ease

Greater ease and flexibility in varying spring rates

Failure of one support will not damage the vehicle

Equally important in providing a satisfactory system of support for the vehicle was insuring that the proper weight and weight distribution were obtained for the test vehicle to exhibit the desired characteristics of the flight

vehicle to be simulated. This was accomplished at various flight times, varying from liftoff through various burn times of upper flight stages, by preparing and maintaining a weight and center of gravity summary sheet for both the test vehicle and flight vehicle. Accuracy in this phase of the testing was not good in the early days of full-scale vehicle testing; however, with the testing of the Saturn 8 and 9 vehicles, errors in accurately controlling weight and center of gravity were largely removed or, at least, could be determined readily. It is felt that some of the discrepancies appearing in the results from earlier test programs can be directly attributed to this type of error.

Propellant simulation for varying vehicle weights was accomplished by using deionized water as a simulant of lox and fuel. Since it is a little heavier than RP-1 and slightly lighter than lox, it was found that the total weight could be well represented with little or no change in vehicle center of gravity. Propellant simulation for liquid hydrogen was accomplished by using polystyrene balls 2 in. in diameter with a bulk density closely approximating that of the  $LH_2$ . These worked well for lateral excitation, but presented a problem during torsional tests because of an increased torsional moment of inertia. Eventually this requirement was dropped, and no propellant simulant was used in  $LH_2$  tanks in either the Saturn IB or Saturn V test programs.

To provide the excitation force desired, electrodynamic shakers were employed for excitation in the lateral, torsional, and longitudinal planes. These shakers were located so as to introduce the force at the approximate location of the engine gimbal plane for both the lateral and torsional excitation phases; they were positioned directly below the thrust structure for longitudinal vibration. Figure 5 is a typical shaker installation.

When not being tested the vehicle was lowered to a "complete rest" position. In this position the missile was supported in a manner comparable to that provided at the launch site. Lateral restraint was provided for additional security by snubbers at the upper tower levels. These snubbers were to prevent "bumping" between the outer missile skin and the tower structure during movement caused by inclement weather; also, they were cushioned and with minor repositioning served a similar purpose during excitation. The snubbers were particularly beneficial when the vehicle's rigid-body modes were excited.

Test vehicles were stacked in the test stands using equipment similar to that planned

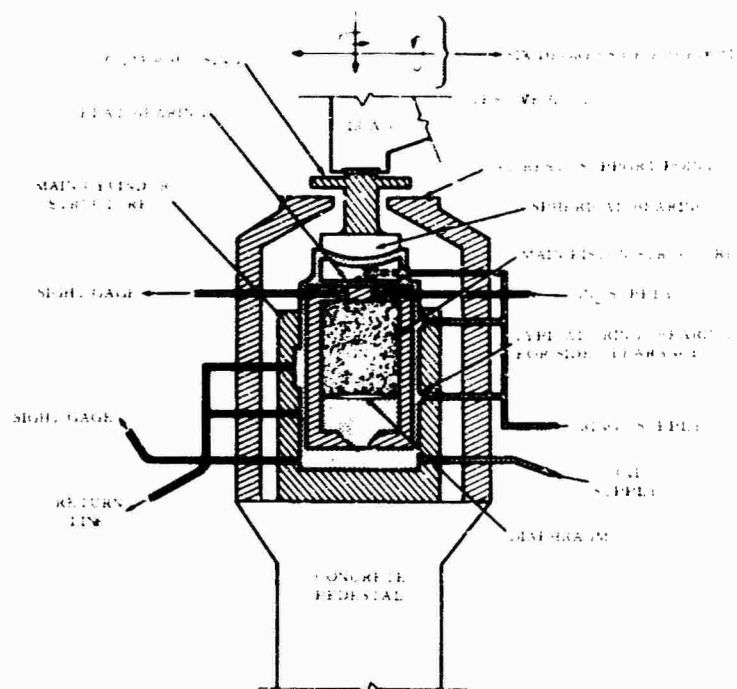


Fig. 4. Schematic of typical Saturn V dynamic test hydrodynamic vehicle support

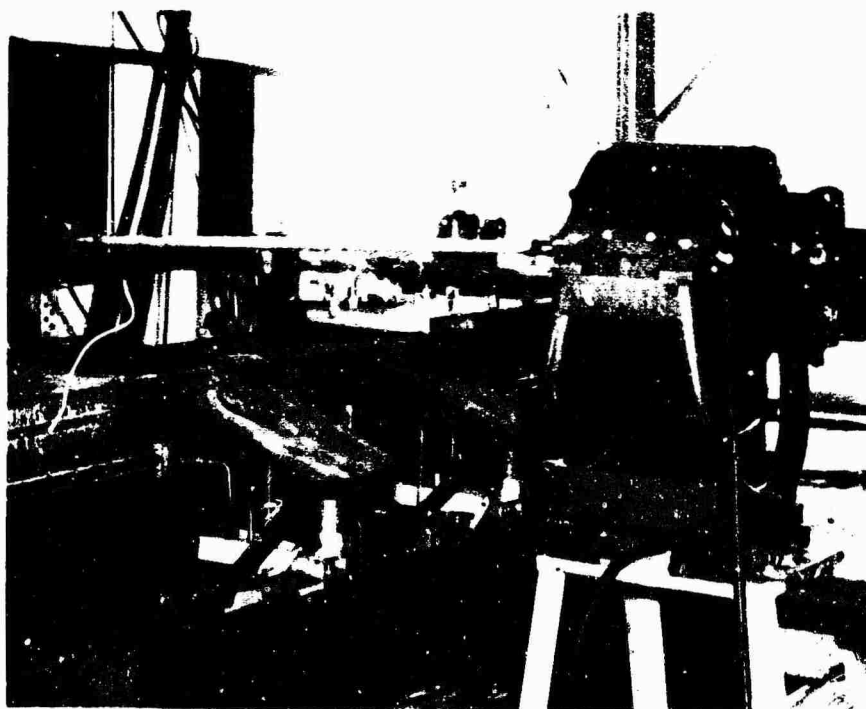


Fig. 5. A 500-lb shaker installed for lateral excitation during a second flight stage test series (load cell for monitoring applied force is installed adjacent to the vehicle)

for use at the launch site (see Figs. 6 through 9). It is interesting to note that, aside from the launch areas at the Kennedy Space Flight Center, MSFC is the only place where these vehicles are completely integrated in a vertical position. On various occasions specially designed tools, jigs, adapters, and mating methods were tried at the dynamic test stands to prevent trouble at the launch site.

### TEST PROCEDURE

Although the equipment has undergone a great deal of updating and many automatic operational and display capabilities now exist for Saturn V dynamic testing that were not available for Saturn I and Saturn IB testing, the primary procedures (whether automatic or manual) remain essentially the same; thus, the test crew themselves still have relatively the same

objectives, namely, to excite the vehicle sinusoidally and to locate and record its response characteristics in the lateral, torsional, and longitudinal planes. The procedures as stated subsequently are specifically related to the Saturn I and IB programs.

Excitation was accomplished with electrodynamic shakers, as follows:

| <u>Plane</u>     | <u>Shaker</u> | <u>Force Vector Output (Nominal)</u> |
|------------------|---------------|--------------------------------------|
| Pitch (lateral)  | One 1500-lb   | 1000 lb                              |
| Yaw (lateral)    | One 1500-lb   | 1000 lb                              |
| Roll (torsional) | Two 500-lb    | 500 lb each                          |
| Longitudinal     | Two 500-lb    | 500 lb each                          |

During torsional testing the shakers were diametrically opposed and operated 180 deg out

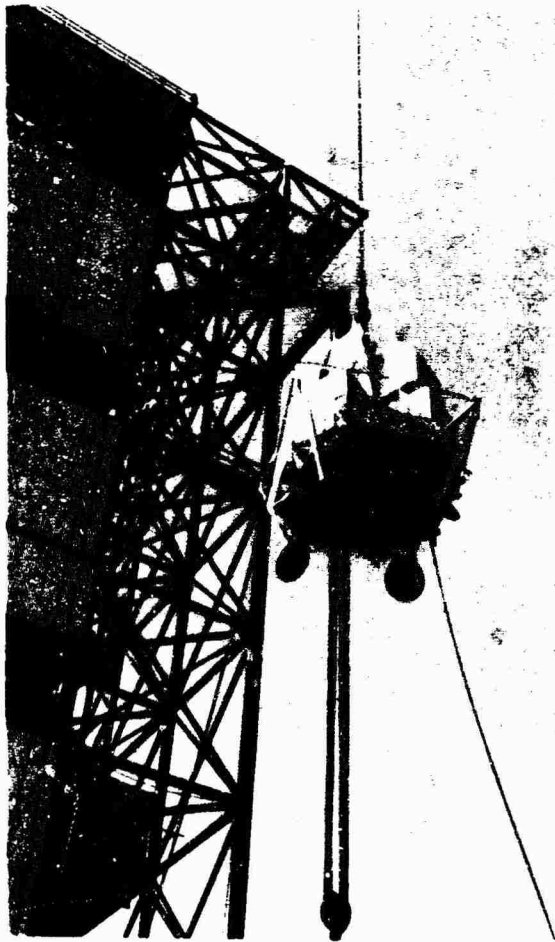


Fig. 6. Lunar excursion module test simulator being hoisted into place

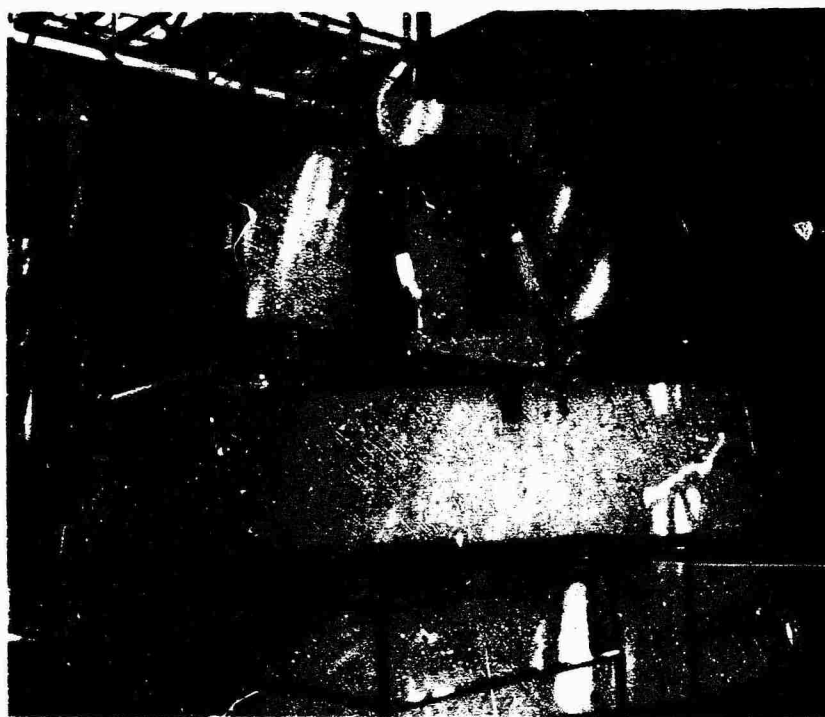


Fig. 7. Lunar excursion module test article in place and mated to the lower portion of the spacecraft lunar adapter

of phase; for longitudinal testing they were diametrically opposed and operated in phase.

Shaker force was usually a nominal force vector as shown above; however, for the purpose of defining system nonlinearity characteristics, reductions in 250-lb increments from the normal operational force vector to a 500-lb nominal force vector was accomplished in the pitch and yaw planes. This was performed only at intermittent flight times (i.e., it was not a routine procedure).

The testing of a particular flight time and shaker plane was commenced by exciting the vehicle to its rigid-body "rocking" mode to obtain proper phasing of the rate gyros. Because of the importance of the correct phasing of the rate gyros in data acquisition and reduction, the frequencies above and below the rocking frequency by 0.01 cps were also excited to ensure that the rocking frequency had indeed been correctly determined.

Resonant frequency searches were accomplished by manual frequency sweeps; resonances were detected by observing a display of selected accelerometer response vs shaker armature

current on an oscilloscope. Various accelerometers were selected for display until the test engineer was satisfied that all significant vehicle resonances were located. In general, the test engineer monitored approximately 60-70 accelerometers during resonance searches. Figure 10 is an actual sheet from the test engineer's log during the Saturn IB test program.

Once a resonant frequency was established, data recording was initiated. The procedure consisted of recording steady-state vibration at the peak followed by recording "ring-out" data. Ring-out was obtained by sudden cutoff of shaker armature current and permitting a minimum of 10 cycles of damped free vibration. Resonance searches above 15 cps were not accomplished, and only rarely were searches carried out above 10 cps. Because of guidance system characteristics, it was felt that searches above these frequencies were not necessary. It should be noted that this decision was not made until the latter portion of the Saturn I series program and at the initial stages of the Saturn IB program; therefore, there were sufficient vehicle performance characteristics available from both flight and test programs on which to base such a judgment.



Fig. 8. Command module, service module, and upper spacecraft lunar adapter section being positioned for mating (note tower wind screening and structural changes along with Saturn V dynamic test stand in contrast to Fig. 1)

To ensure that all major resonances had been detected and located correctly, two types of frequency sweeps were performed: (a) a short incremental sweep for locating the peaks accurately, and (b) a long incremental sweep for detecting any resonances not located during resonant searches. Short incremental sweeps of approximately 11 increments were performed around the peak of each major vehicle resonance. For peaks occurring below 10 cps, increments of 0.01 cps were used; for resonances above 10 cps, increments of 0.02 cps were employed. The long incremental frequency sweeps were performed over a frequency range of 1.3 to 10 cps. The frequency increments varied from 0.05 cps (for excitation frequencies up to 5 cps) to 0.10 cps (for excitation frequencies from 5.0 to 10.0 cps).

#### INSTRUMENTATION AND DATA ACQUISITION

Basically, there were two types of transducers used to measure the dynamic response of the vehicle:

1. Test (or ground) types of sensors were (a) strain-gage, viscous-damped accelerometers with a range of  $\pm 1.0$  g, and (b) inertial spring-mass, viscous-damped accelerometers with a range of 0.5 to 5.0 g. A typical test transducer installation is shown in Fig. 11.

2. Airborne (or flight) types of systems sensors were (a) inertial spring-mass, viscous-damped accelerometers with a range of 10 m/sec<sup>2</sup> and 25 m/sec<sup>2</sup>, and (b) rate gyros having a full-scale range of 10 deg/sec.

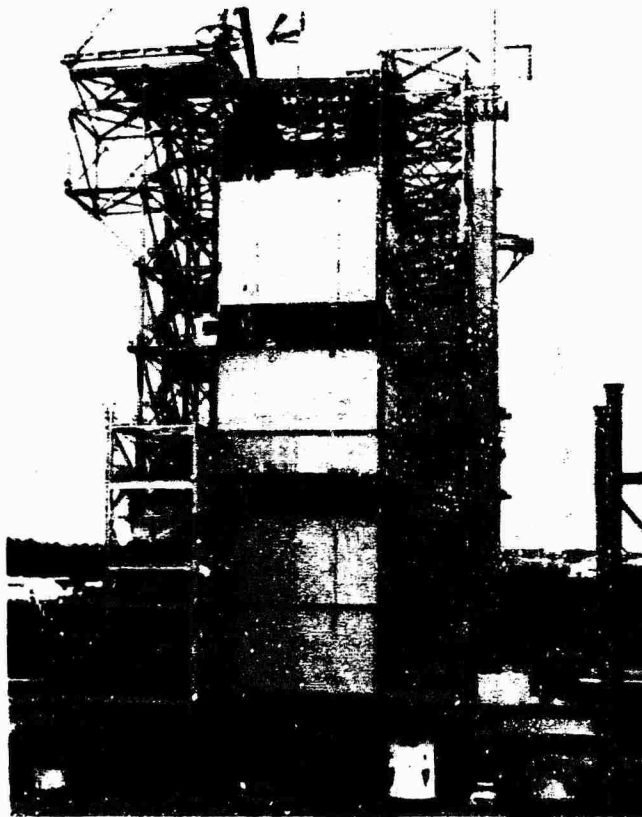


Fig. 9. Saturn IB test facilities (service and command modules are at base of tower; note area and structural buildups compared to Fig. 1)

Transducer locations were depicted by drawings. Test-type sensor drawings were made for each test condition, i.e., pitch at lift-off, yaw at lift-off, pitch at max Q, yaw at max Q, etc. Figure 12 is a typical acceleration location drawing. In general, such sketches provide (a) transducer location, (b) direction of sensitivity, and (c) number of sensors to be used for a given test.

The instrumentation equipment required for the Saturn I and Saturn IB dynamic test programs was contained in two trailers located at the base of the test stand. Since at the inception of the full-scale test programs the work was performed by NASA personnel directly assigned to the individual MSFC laboratories, the trailers acquired designations stemming from the laboratory personnel operating them; thus we had a Propulsion and Vehicle Engineering (P&VE) trailer and an Astrionics trailer. These designations remained for the life of the Saturn I and IB test programs.

The P&VE trailer contained equipment for supplying and controlling vehicle excitation and for monitoring numerous accelerometers located on the test vehicle. The Astrionics trailer contained equipment for monitoring the outputs of numerous accelerometers and rate gyros located on the test vehicle.

Input signals to the P&VE trailer were processed by a CEC Model 5-123 oscillograph and a Systems Engineering Laboratory (SEL) computer. The magnetic tape used on the SEL was 0.50 in. at 112.50 in./sec for a data sampling word rate of 31.25 cps. This routine was established to permit data reduction by both the GE 235 and IBM 7094 digital data computers used at MSFC. Reduction of the analog data was performed manually.

Input signals to the Astrionics trailer were processed by Brush recorders, oscilloscope display, and, for digital recording, by an SEL computer. The SEL used a tape procedure similar

Weather Clear and Cool (11 p.m.)

SATURN II DYNAMIC TEST PROJECT

TEST PERFORMANCE LOG

PAGE 7 OF

TESTER: B. R. JACOBS

DATE: 6 - AUGUST - 1965

TEST CONFIGURATION: SA-202 UNRES STAGE FLIGHT TIME: 10:40/11:55

LOG REC NOT RECORDING

| TEST NAME OR ACTION           | PERIOD (T) | PERI. (F) | TRANSDUCER MONITORED | TIME            |
|-------------------------------|------------|-----------|----------------------|-----------------|
|                               | 0.0170     |           |                      | 132200          |
| <u>End Log Rec</u>            |            |           |                      |                 |
| <u>BEGIN RESONANCE SEARCH</u> |            |           |                      |                 |
| Tors (Pitch & Yaw)            | 0.4467     | 2.25      | 20.15                | 132201          |
| +damping                      | "          | "         | "                    | 132202          |
| Excite                        | 0.3350     | 4.251     | 114                  | 132203          |
| "                             | "          | "         | "                    | 132204          |
| +damping                      | "          | "         | "                    | 132205          |
| 2nd Landing off Eng           | 0.1297     | 7.71      | 26.116               | 132206          |
| +damping                      | "          | "         | "                    | 132207          |
| Tors                          | 0.0963     | 10.58     | 26                   | 132210          |
| +damping                      | "          | "         | "                    | 132211          |
| Excite Tors                   | 0.0458     | 22.05     | 26.114               | 132212 $\Delta$ |
| "                             | "          | "         | "                    | 132213          |
| +damping                      | "          | "         | "                    | 132214 $\Delta$ |
| +damping                      | "          | "         | "                    | 132215          |
| R6                            | 0.0429     | 23.32     | 15.114               | 132216 $\Delta$ |
| +damping                      | "          | "         | "                    | 132217          |

< Standard Resonance continued

Fig. 10. Typical test performance log

to that employed in the P&VE trailer and was addressed by a Flexowriter with tape punch/read capability.

The major equipment for each instrumentation trailer is listed:

| Equipment                             | Quantity |
|---------------------------------------|----------|
| <b>P&amp;VE Trailer</b>               |          |
| Accelerometer, CEC type 4-205-0107    | 125      |
| Digital data acquisition system (SEL) | 1        |
| Amplidyne and drive motor, GE         | 2        |
| Electrodynamic shaker, Ling, 1500 lb  | 1        |
| Electrodynamic shaker, Ling, 500 lb   | 4        |
| Power amplifier, Ling, 12 kw          | 1        |
| Oscillator                            | 2        |
| Oscillograph                          | 1        |
| Oscilloscope                          | 2        |

#### Equipment

Quantity

#### Astrionics Trailer

|  |    |
|--|----|
| Accelerometer, Donner 4310/5310        | 52 |
| Accelerometer (control), Statham A311D | 9  |
| Rate gyro, Honeywell, JRS-102          | 30 |
| Counter, CMC 727B                      | 1  |
| Data acquisition system, SEL 600       | 1  |
| Flexowriter, Friden                    | 1  |
| Oscillator                             | 1  |
| Oscilloscope                           | 1  |
| Brush recorder, 11-1603-00             | 6  |

Flow diagrams for each of the trailers are shown in Figs. 13 and 14.

Significant improvements were made in the instrumentation and data acquisition systems



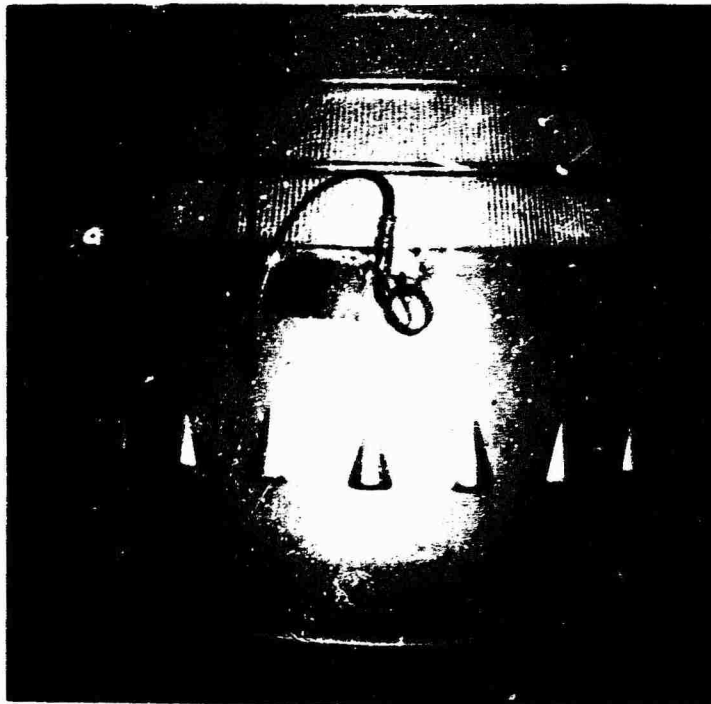


Fig. 11. Typical accelerometer mounting (accelerometers in pitch and yaw planes mounted on an outboard engine of the S-1B booster; note aluminum mounting blocks between transducer and engine)

for the Saturn V dynamic test program, not only from an operational standpoint but in efficiency as well. No detailed write-up of the system is presented here; however, some noteworthy improvements included the following:

1. An automatic mode shape display showing the elastic shape of the vehicle during excitation;
2. Automatic scanning of transducers and initiation of frequency sweeps;
3. Closed-circuit TV system permitting direct observation by the test engineer of critical areas along the vehicle;
4. Location of all instrumentation within one trailer;
5. On-site data evaluation (limited capability).

#### RESULTS AND DATA COMPARISONS

In reviewing full-scale dynamic test results and presenting data comparisons, one is

faced with a staggering amount of test data, preflight analysis, flight results, and correlation efforts from many sources. These sources include Saturn I, Block I launch vehicles, Saturn I, Block II launch vehicles, Saturn IB (updated Saturn) launch vehicles, Saturn V launch vehicles, Saturn I, Block I 1/5 scale model, Saturn V 1/10 scale model, and Saturn V 1/40 scale model.

It is beyond the scope of this paper to present a detailed discussion of test results and the corresponding correlations and comparisons with all these sources. Indeed, it is beyond the scope of this paper to present a detailed analysis involving even one of these sources. Therefore, the effort here is to present in a general form some of the results from several of the above sources and limited comparisons between these results in the earlier stages of the full-scale dynamic test programs and those of the later test program stages. In this respect, areas of interest are the following selected sources (detailed results for a comprehensive study may be obtained from Refs. 1 through 7):

1. Saturn I, Block I and Block II launch vehicles

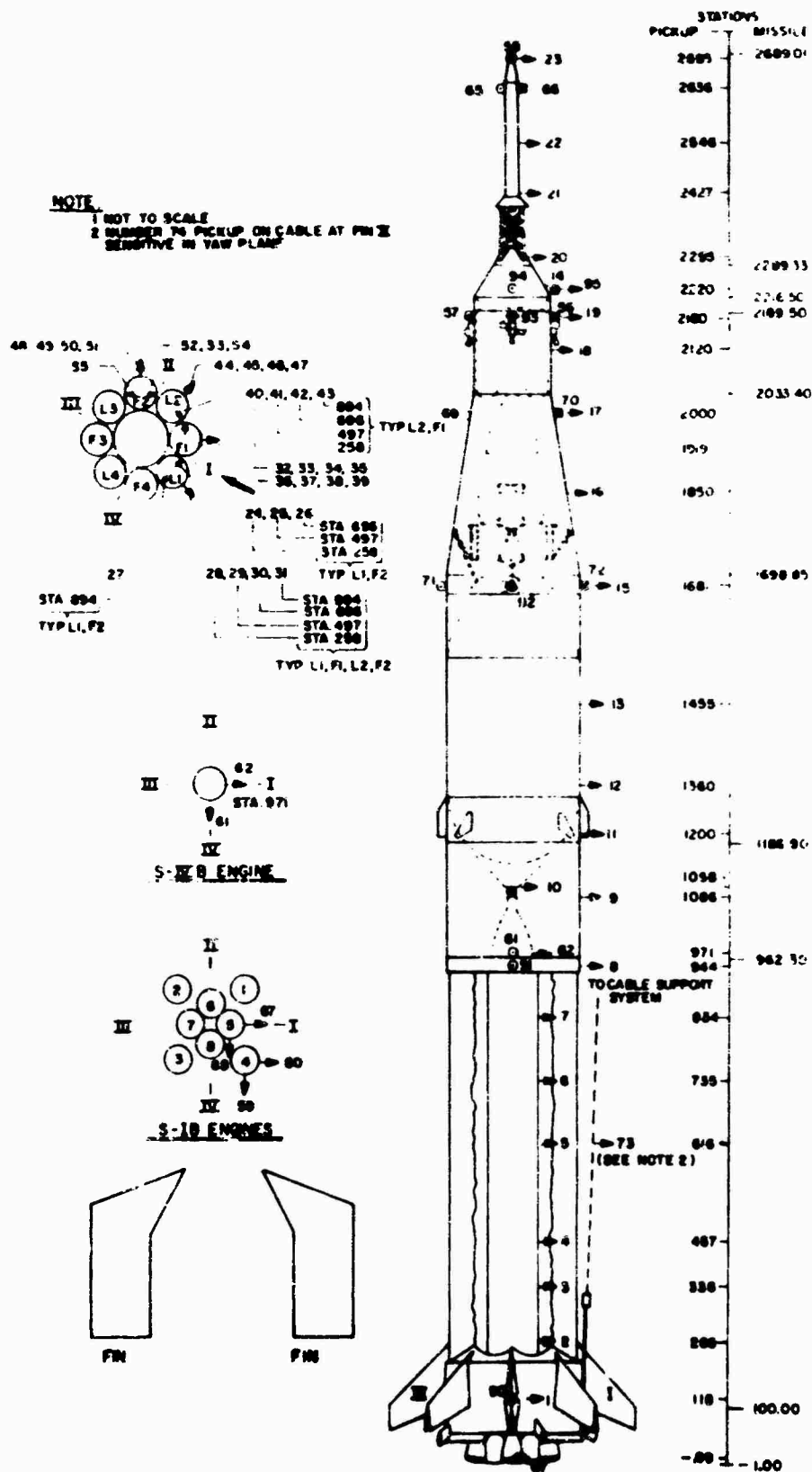


Fig. 12. SA-206, pitch excitation--accelerometer locations



## 2. Saturn IB launch vehicles

### 3. Saturn I, Block I 1/5 scale model

First, consider the results of data pertaining to the first vehicle of the Saturn I, Block I series to be tested. This was the SAD-1 dynamic test vehicle representing the first Saturn flight vehicle, SA-1. Figure 15 shows the variations in resonant frequencies for both the SA-1 full-scale test vehicle and the Saturn I 1/5 scale model. Table 2 presents a comparison of calculated, full-scale test, and model test result frequencies for SA-1. In addition, Fig. 16 shows the second bending mode shape for the SA-1 vehicle as defined at liftoff by the full-scale test results, model test results, and the calculated values.

In general, most of the information and data set forth above pertaining to the SA-1 vehicle are in fair agreement, the largest discrepancies or deviations occurring with respect to the analytical. Now, if we consider that the 1/5 model, even though it was a very good geometrically scaled vehicle, does contain certain inherent characteristics that would prevent complete agreement with full-scale test results (such as

excessive stiffness in the outer tanks and questionable similitude for the booster engines), and that some 16,000 to 20,000 lb of water was not accounted for in the full-scale test vehicle tank pumps and lines, we can say that fairly good representation was provided by the model, at least as far as resonant frequencies and response are concerned. Overall damping values for the model and full-scale vehicle agreed well.

The disagreement between test results, both full-scale and model, and the calculated values is obviously quite large. The major problem here was that the theory used was simply inadequate to cope with the complex vehicle structure represented by the Saturn. A single-beam theory was employed at this time to analyze the vehicle. This theory used a simplifying assumption that a single equivalent stiffness could represent the booster, which was composed of a center tank and surrounded by eight outer tanks subject to their own movements and associated resonances in addition to coupling effects. For the 1/5 scale model, eight major response peaks were found; for this same frequency range, the analysis provided the basis for locating only three (Fig. 17). Note

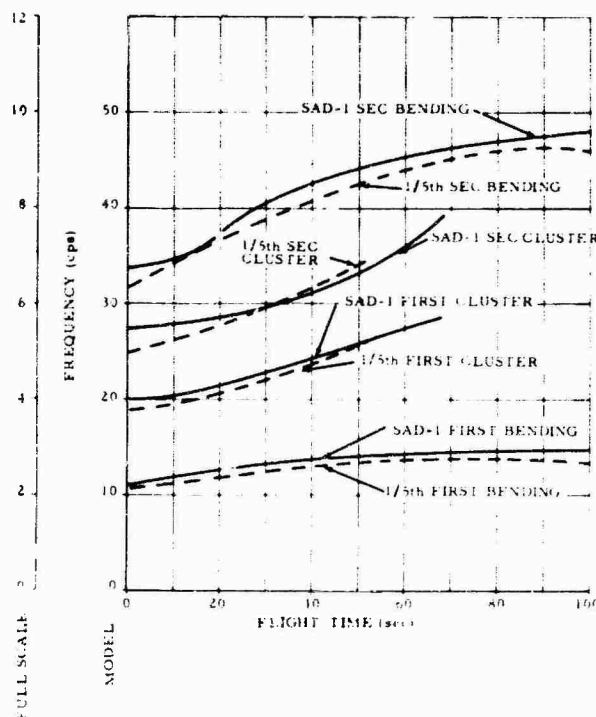


Fig. 15. Bending mode frequencies vs flight time, Saturn vehicle SA-1 full-scale and 1/5 model

TABLE 2  
SA-1 Saturn Vehicle Frequency Comparison

| Resonant Condition | Flight Time    | Frequency (cps) |                         |            |
|--------------------|----------------|-----------------|-------------------------|------------|
|                    |                | Full-Scale Test | Model Test <sup>a</sup> | Calculated |
| 1st Bending        | Liftoff        | 2.20            | 2.16                    | 1.44       |
| 2nd Bending        | Liftoff        | 6.74            | 6.1                     | 5.32       |
| 1st Bending        | max Q          | 2.83            | 2.66                    | 2.15       |
| 2nd Cluster        | max Q          | 7.83            | 7.72                    | 6.82       |
| 1st Bending        | Booster cutoff | 2.95            | 2.66                    | 2.52       |
| 2nd Bending        | Booster cutoff | 9.79            | 8.9                     | 9.45       |

<sup>a</sup>Frequencies listed for the 1/5 scale model are reduced from actual model frequency by the scale factor:

$$\text{Lateral frequency: } \frac{f_M}{f_F} = \left( \frac{EI_M m_M L_F}{EI_F m_F L_M} \right)^{1/2} \quad 5.$$

where M = model characteristics, and F = full-scale or prototype characteristics.

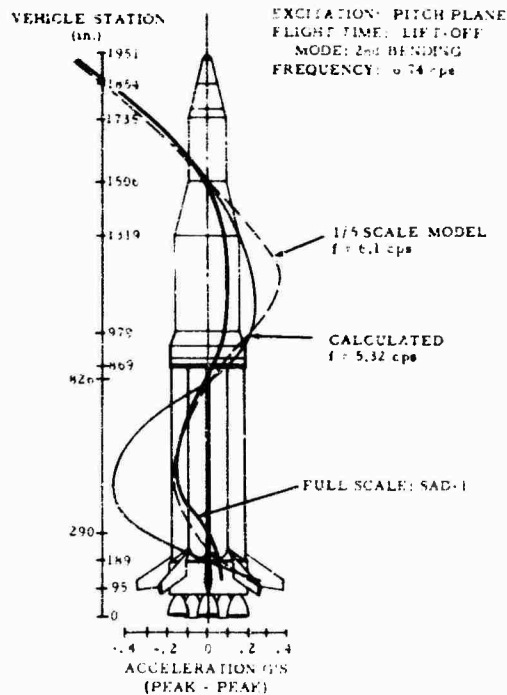


Fig. 16. Second bending mode shape at liftoff pitch: SA-1 vehicle (full-scale test, model test, and calculated modes)

also that not only did the analysis fail to locate the majority of the resonances, but it also missed on those it predicted, with a 100-percent miss on its third prediction. Results such as this were equally applicable to the full-scale test results.

Additional shortcomings of this single-beam analysis method and an obvious indication of the importance and necessity (at this time in the development stage of the Saturn vehicle) of the full-scale dynamic test programs is exhibited by a comparison of frequencies (cps) obtained from theory with those obtained from dynamic tests and flight tests of the Saturn I, SA-2 vehicle:

| Experimental | SA-2 Flight | Theoretical, Free Flight (Single-Beam Analysis) |
|--------------|-------------|---|
| 2.2          | 2.2-2.3     | 1.69  |
| 2.31         | —           | —   |
| 2.92         | —           | —   |
| 4.02         | —           | —   |
| 6.74         | —           | 6.60  |
| 11.7         | —           | 9.56  |

Note that the single-beam analysis was close at only one frequency, missed entirely three modes (these were tank modes involving clustered movements of the multiple tanks) and was "off" more than 20 percent on its prediction of the first major mode. It is significant that this is probably the most important mode as far as control system design is concerned. This 20 percent error is unacceptable in control system design, as is the fact that other modes close by were missed. Thus the dynamic test results were the only acceptable data upon which to base the design of the control system.

At the time of the SA-5 vehicle dynamic test program, theory had improved considerably with the use of a multiple-beam analysis which took into account the multiple-tank configuration

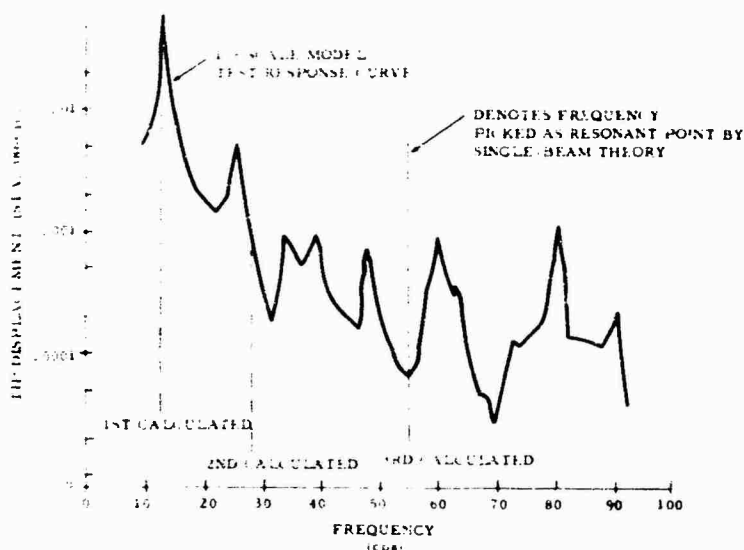


Fig. 17. Saturn I 1/5 scale model response plots for tip displacement vs frequency, model station 386

of the Saturn booster and considered the clustered and independent motion of these tanks. An expanded version of the comparison above illustrates this improvement (see Table 3). The second and third columns show the improvement when the vehicle is analyzed by the multiple-beam method. Since the theory is so close to the experimental values, an understandable optimism would result in the conclusion, "We've got it made." Unfortunately this is not the case. While the new analysis was far superior, and, in fact, did provide the basis for the control system design of vehicles subsequent to SA-5 (which design was verified with the dynamic test), there were still parameters and response characteristics that could not always be predicted. Among these were resonances not encountered on previous tests or previously predicted, local response phenomena, dynamic

crosscoupling, and, one of the most important, total vehicle structural damping.

A look at some of the test and theoretical results for the later Saturn IB dynamic test program is now in order. The Saturn IB dynamic test program involved the testing of four different vehicle configurations: AS-202, AS-203, AS-206, and AS-207. Table 4 presents a summary of lateral bending frequencies obtained from the full-scale tests and the multibeam model for vehicle configurations AS-202 and AS-203. These bending mode frequencies are given for only two flight times and, for the most part, agree very well. Some of the differences noted have been attributed to several factors:

1. Sloshing effect of propellant in S-IVB stage;

TABLE 3  
Saturn I, Block I, SA-2 Vehicle Frequency (cps) Comparison

| Experimental | Multiple-Beam Analysis       |                          | Single-Beam Analysis     |
|--------------|------------------------------|--------------------------|--------------------------|
|              | Theoretical, with Suspension | Theoretical, Free Flight | Theoretical, Free Flight |
| 2.2          | 2.27                         | 2.21                     | 1.69                     |
| 2.31         | 2.42                         | 2.31                     | -                        |
| 2.92         | 2.95                         | 2.84                     | -                        |
| 4.02         | 4.07                         | 4.12                     | -                        |
| 6.74         | 6.65                         | 6.38                     | 6.60                     |
| 11.7         | 11.78                        | 11.05                    | 9.56                     |

TABLE 4  
Saturn IB Vehicle Bending Mode Frequency (cps) Comparison

| Bending Mode        | Vehicle AS-202  |                    | Vehicle AS-203    |                    |
|---------------------|-----------------|--------------------|-------------------|--------------------|
|                     | Full-Scale Test | Mathematical Model | Full-Scale Test   | Mathematical Model |
| Liftoff             |                 |                    |                   |                    |
| 1st Bending         | 1.35            | 1.19               | 2.30              | 2.17               |
| 1st Fuel radial     | 1.66            | 1.61               | 1.60              | 1.60               |
| 1st Lox radial      | 2.10            | 2.06               | 2.05              | 2.06               |
| 2nd Bending         | 2.27            | 2.12               | 5.34 <sup>a</sup> | 5.88               |
| 1st Fuel tangential | 2.45            | 2.45               | —                 | 2.55               |
| S-IVB Engine        | —               | —                  | —                 | —                  |
| 3rd Bending         | 4.20            | 3.90               | 8.05 <sup>a</sup> | 7.59               |
| 2nd Fuel radial     | 5.90            | 5.59               | 5.72              | 5.51               |
| 4th Bending         | 4.50            | 6.36               | —                 | 10.47              |
| 2nd Fuel tangential | 6.67            | 6.77               | —                 | 6.54               |
| 2nd Lox radial      | —               | 7.75               | 7.60              | 7.77               |
| 5th Bending         | —               | 3.57               | —                 | —                  |
| Booster Cutoff      |                 |                    |                   |                    |
| 1st Bending         | 1.70            | 1.39               | 3.88              | 4.05               |
| 2nd Bending         | 2.60            | 2.38               | —                 | —                  |
| 3rd Bending         | 6.88            | 7.11               | —                 | —                  |
| 4th Bending         | —               | 10.45              | —                 | —                  |
| 1st Fuel radial     | 8.96            | 11.68              | 8.96              | 11.08              |

<sup>a</sup>Denotes mode coupled with outer tanks.

2. Dynamic crosscoupling measured on the test vehicle and not predicted by the model;

3. No provision by the model for slosh or engine modes.

Figures 18 and 19 show the lateral bending frequencies for the first and second bending modes obtained from the flight measurements and the full-scale testing of the AS-202 and AS-203 vehicles. These data are in good agreement, as depicted by the graphs. The small differences occurring in the plots could easily be attributed to (a) telemetry noise, (b) stiffness and mass distribution variances between the test vehicle and flight vehicle, and (c) steady-state excitation environment for the test vehicle as opposed to random and transient environment of the flight vehicle.

Vehicle AS-203 would be a prime target for argument relating to proper simulation of the flight vehicle by the test vehicle. Figure 20 depicts the dynamic test vehicle configuration compared with the flight vehicle configuration. The main difference is the absence of the nose cone on the test vehicle. The nose cone was not available at the time of testing, nor was a

substitute cone; however, a ring comprising part of the ground support equipment for the spacecraft lunar adapter (SLA) was placed in the upper (forward) end of the SLA to represent the nose cone stiffness characteristics. From all available information, this substitution was successful.

#### FULL-SCALE TEST UTILIZATION

Full-scale dynamic testing has served in two fundamental capacities since its beginning in the early 1960's:

1. It was first used primarily as the basis for all structural dynamic information necessary for control system design.

2. It was later used to substantiate and verify structural dynamics analyses used in designing the control system.

Obviously then its primary goal is always to provide assistance in the design of a reliable and capable control system. Inasmuch as the tests are primarily concerned with the control system, there are several items available from

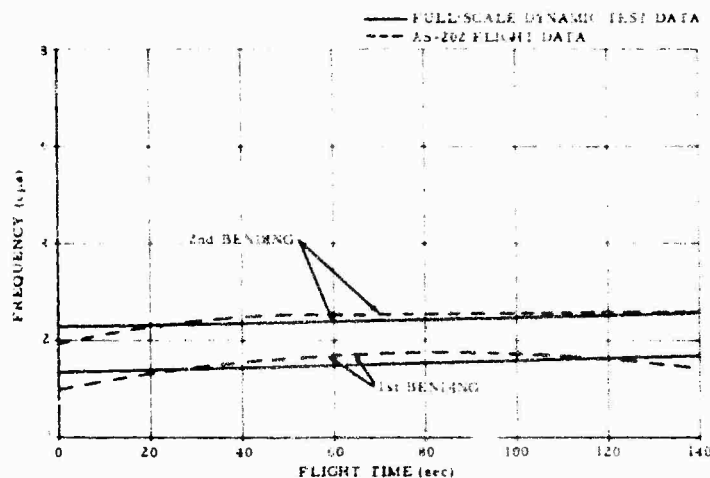


Fig. 18. Saturn IB vehicle AS-202 lateral bending frequencies from flight and test data (pitch)

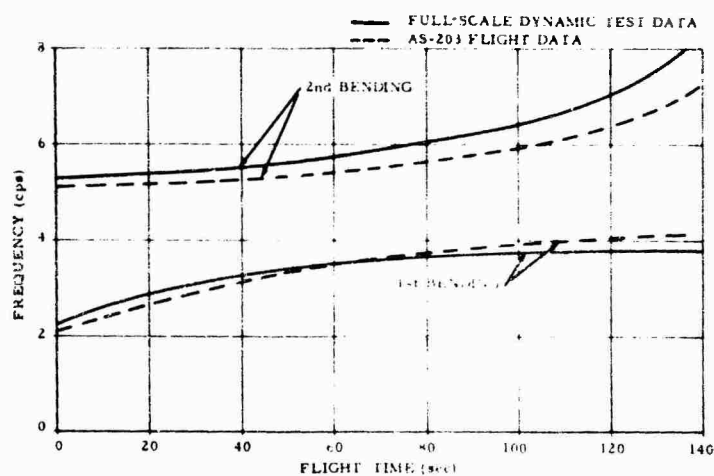


Fig. 19. Saturn IB vehicle AS-203 lateral bending frequencies from flight and test data (pitch)

the tests that are not readily obtainable (in some cases, not obtainable at all) from the theory. Some of these are (a) total integrated vehicle structural damping, (b) local response phenomena, (c) vehicle modes not encountered previously, and (d) dynamic crosscoupling not predicted by theory.

The change that has occurred in the basic uses of the dynamic test program is shown in two data flow lines of a chart for the design of the vehicle control system (Fig. 21): full-scale test inputs, and theoretical inputs. Figure 21 clearly shows that the total vehicle dynamics theory used in the design of the control system

depends upon the structural theory and the full-scale tests for its data input. In the early days of testing, when the structural theory based on a single-beam analysis was inadequate, the diagram would be drawn with a light line from structural theory and a heavy line from full-scale tests. As the theory improved and the multibeam analysis came into use, the weight of the lines would reverse; i.e., the full-scale tests inputs would be less and its line would become lighter.

As stated above, the total vehicle dynamics theory uses as its basic inputs the results from the structural theory and the dynamic tests.



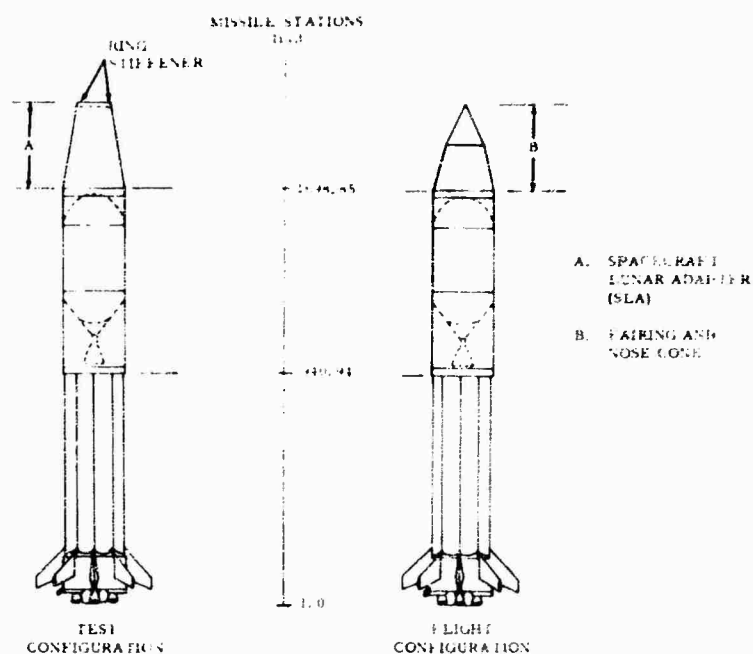


Fig. 20. Saturn IB vehicle AS-203 configuration comparison

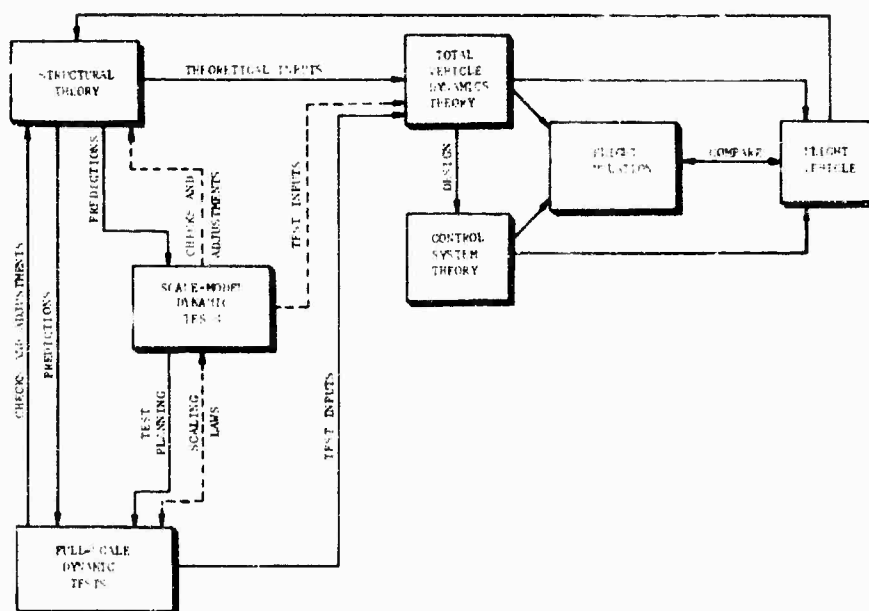


Fig. 21. Data flow chart for design of Saturn V vehicle control system

The theory provides natural frequencies and vehicle mode shapes. The full-scale tests verify this theory and supply additional data.

The control system is designed on the basis of total vehicle dynamics theory, which considers

not only the vehicle natural frequencies and response characteristics, but also the engine dynamics, propellant oscillations, and rigid-body characteristics. Most of this information is obtained from additional theory and other tests not discussed here. Following the control

system design, an analog simulation study is made of the combined vehicle and control system. Statistical evaluations are made to insure the adequacy of the control system design. Following the eventual flight (which might be considered as an additional dynamic test), flight data in the form of mode shape and frequency data are compared with the results of the structural theory. The schematic then shows the paths of checks and adjustments.

Referring again to Fig. 21, a block representing scale-model dynamic tests has been inserted to show the role these models will play in future full-scale test programs. Their main purpose would be to provide planning for performance of the proposed full-scale test program with minor direct inputs to the total vehicle dynamics theory. It seems safe to say that even if this is the present plan, it is certainly hoped that scale model testing could eventually replace the full-scale tests completely.

The idea of using scale models in planning the full-scale test programs has been tried with the Saturn I 1/5 scale model and the Saturn V 1/10 scale model. The attempt gained little with the Saturn I model, mainly for two reasons: (a) full-scale tests were completed prior to obtaining the results of the model tests; and (b) the model itself did not represent the full-scale vehicle to a sufficiently high degree of accuracy.

These two reasons should not be factors in the Saturn V model test series. This 1/10 scale model is a very accurate, geometrically scaled model of the flight vehicle, and its development reaped the benefits of the Saturn I model and full-scale tests. This model has been subjected to extensive tests at NASA's Langley Research Center. Figures 22 and 23 are photographs of the Saturn V 1/10 scale model. Note the detail and workmanship shown in Fig. 22.

With all the improvements in structural theory and with all the test data and experience that have been acquired, there is still a major problem whose answer has been found satisfactorily only from the tests: predicting the damping of a complex space vehicle from a direct analysis. In this respect, considerable emphasis is being placed on damping during the Saturn V model test series in an effort to use these results as an aid to analysis. The theoretical results will be compared with the full-scale Saturn V dynamic test results.

Full-scale testing has been invaluable, but it is extremely expensive, requiring the manufacture of a test vehicle, transportation, vast amounts of ground support equipment, huge towers, tremendous instrumentation and data acquisition capabilities, and a great number of test personnel. Of course, it is also extremely time consuming. These factors will only become more pronounced with larger and more

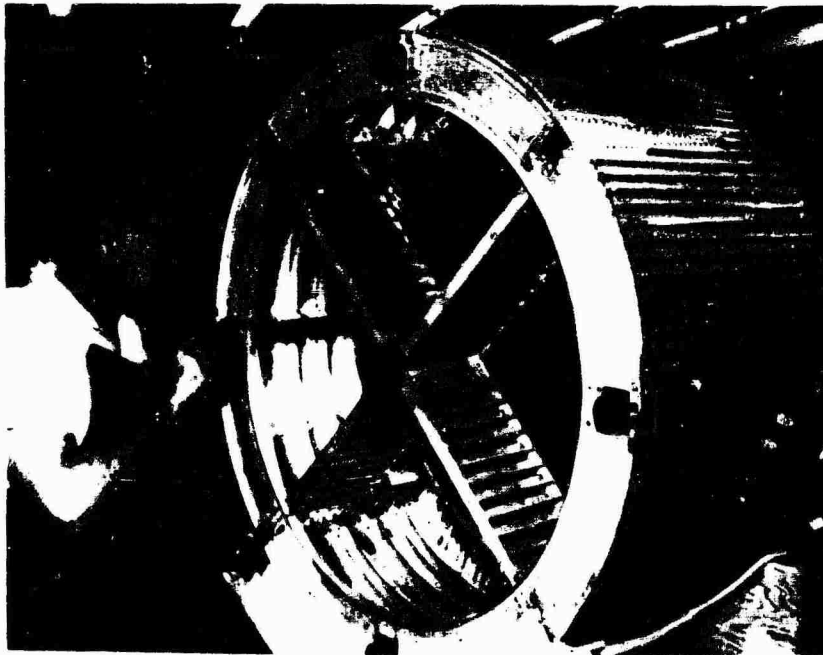


Fig. 22. Saturn V 1/10 scale model thrust structure fabrication



Fig. 23. Saturn V 1/10 scale model suspended in test position at Langley Research Center

complex launch vehicles; therefore, it seems logical to give consideration to the improvement of scaling laws and modeling techniques.

Properly scaled and used, geometrically scaled models should prove even more valuable than have the full-scale test programs. It is possible that the use of such models can be dramatic in information obtained; it is certain that their use will considerably lessen the expense and complexity involved in dynamic testing of space vehicles.

#### ACKNOWLEDGMENTS

The author expresses his gratitude to George F. McDonough, Larry Kiefling, and C. E. Watson of the Marshall Space Flight Center for their aid in making available much of the data and information presented in this report. Also, special thanks are due Charles White and his staff, of the Northrop-Nortronics Huntsville facility, for their efforts in illustration, typing, and photography.

#### REFERENCES

1. C. E. Watson and Kay W. Slayden, "Experimental Vibration Program on a Full Scale Saturn Space Vehicle," Marshall Space Flight Center, MTP-P&VE-S-62-3, Apr. 1962
2. J. S. Mixson, J. J. Catherine, and A. Aronson, "Investigation of the Lateral Vibration Characteristics of a 1/5 Scale Model Saturn Vehicle," NASA Langley Research Center, TN-D01593, Jan. 1963

3. B. R. Jacobs and N. L. Beard, "Ground Survey of SAD-8 and SAD-9," Chrysler Corp. Tech. Rept. HSM-R102, Feb. 1965
4. George F. McDonough, "Stability Problems in the Control of Saturn Launch Vehicles," paper presented at the International Conference on Dynamic Stability of Structures, Northwestern University, Oct. 1965
5. B. R. Jacobs, "Design of a Cable-Spring Suspension System for Dynamic Tests of a Saturn V Vehicle," Marshall Space Flight Center, R-P&VE-SED Tech. Memo., Mar. 1964
6. N. L. Beard, B. R. Jacobs, J. H. Durham, and C. H. Jones, "Final Report of Total Vehicle Testing of Saturn IB Dynamic Test Vehicle SA-200 D," Chrysler Corp. Tech. Rept. HSM-R856, Jan. 1966
7. J. Hord and E. Garza, "Saturn IB Dynamic Test Correlation," Chrysler Corp. Tech. Rept. TN-AP-66-148, Nov. 1966

#### DISCUSSION

Mr. Ungar (Bolt, Beranek & Newman): I am a little bit worried about your statement concerning the scaling of damping from a small model to a full-scale structure. Do you have any experience in that?

Mr. Jacobs: I don't think I made a statement relative to scaling the damping. If I did, I did not mean to. Right now that is a big problem. What I meant was that the model will be used extensively to understand these problems better. At the present time I believe that scaling factors are really not clearly understood as far as damping goes; we have not been able to predict damping theoretically. We have always had to measure it on the total integrated vehicle. This is one reason that the full-scale test program could not be eliminated.

Mr. Ungar: How did you excite the vehicle? I don't believe that was mentioned.

Mr. Jacobs: We had no unusual methods. We used electrodynamic shakers, sinusoidally.

Mr. Ungar: What about the attachment of a shaker to the vehicle? Did you have a big ring fixture around the bottom?

Mr. Jacobs: On the early Saturn I, Block I vehicles, before fins were attached, we punched a hole in the thrust structure, went right in, and attached to the "web." We did not use any rings. All of the shaker forces except for cantilever thrusts were introduced at the engine gimbal planes. On the vehicle with fins we attached directly to the fin. We used a 1500 lb shaker in lateral planes and a 500 lb shaker in roll planes. I might mention that we used water to simulate propellant and lox, and styrofoam balls for liquid hydrogen.

Dr. Morrow (LTV Research Center): I take it you measured force rather than acceleration.

Mr. Jacobs: Yes, we measured the force that the shaker introduces at that point. However, we did have accelerometers mounted on the vehicle itself. We used some 150 accelerometers on the I and IB and about six on the rate gyro packages, varying from two to three per package.

\* \* \*

## BUFFET RESPONSE MEASUREMENTS OF A SEVEN PERCENT AEROELASTICALLY SCALED MODEL OF VARIOUS TITAN III CONFIGURATIONS

Jerome T. Uchiyama and Frank W. Peters  
Martin-Marietta Corporation  
Denver, Colorado

Between January 1966 and May 1967, a 7 percent scale aeroelastic model of the Titan III with various payloads was tested in the 16-ft transonic propulsion wind tunnel at the Arnold Engineering Development Center, Tullahoma, Tennessee, to measure and determine ways to reduce buffet loads. Because of the variety and extraordinary shapes of some of the payloads tested, it is felt that the results are unique and will provide useful information to the aerospace industry.

Buffet loading for launch vehicles is associated with high turbulence occurring within the separated flow region surrounding the payload area. A major problem in analytically predicting buffet loading is that the loads are dependent on geometrical shape. Consequently, direct testing of the various configurations' buffet response was necessary.

There were three basic configurations tested: (a) single-body Titan IIIA; (b) three-body basic Titan III with 5-segment solid rocket motors; and (c) three-body Titan III with 7-1/2-segment solid rocket motors. Payload variations and "fixes" to reduce buffet loading applied to these basic configurations resulted in a total of 30 test configurations. Each configuration was tested over a Mach number range of 0.6 to 1.4 at nominal dynamic pressure. Response level changes resulting from angle of attack and dynamic pressure variations were also determined. (Acoustic sound level measurements were also taken, but these results are not presented.)

The model was constructed internally from thin aluminum tubing cut to simulate full-scale stiffness in the pitch and yaw planes. Thin segmented aluminum cylinders and balsa wood were used to obtain the external geometrical shape. The model was mounted on soft elastic springs located at or near the node points of the two free-free elastic modes to minimize the restraint effect of the springs. Measurements of bending moment were obtained with four-arm strain-gage bridges located along the model in the pitch and yaw planes. Buffet response data were recorded on tape and analyzed through digital computers to obtain power spectral densities.

Results from the test show that peak buffet response occurred at Mach numbers between 0.9 and 0.95. In all stable cases the peaks are pronounced and are about five times the off-peak buffet response. Results of dynamic pressure and angle of attack variation show no definite trend but are presented in the curves. The effect of the fixes in reducing buffet response are also presented. Methods and results of this test and its application to the full-scale vehicle are presented.

### INTRODUCTION

Knowledge of buffet phenomena is imperative during the design stages of space launch vehicles, especially from the standpoint of the additional loads it produces along the entire vehicle. Buffet is associated with high turbulence occurring within the separated flow regions surrounding space vehicle payload areas and substantially increases the total loading occurring on space vehicles. It is necessary to know the amount of buffet loading accurately to insure sufficient design strength and rigidity. Buffet loading levels are affected

by geometrical shape, and for this reason analytical prediction is difficult. Because of the many different geometrical payload shapes to be attached to the core of the Titan III family of three-body space launch vehicles, direct wind-tunnel testing of scale models to determine buffet loading levels that would occur on full-scale vehicles was required. The interaction of the unsteady aerodynamic forces with the elastic motion of the vehicle may cause excessive loads to occur and therefore required that an elastic model be tested. Reference [1] demonstrates that using judicious dimensional considerations in the design of scale models can

insure confidence in the prediction of full-scale buffet response.

This paper presents results of buffet response test measurements of 7 percent aerodynamically scaled models of three basic Titan III configurations with various payloads. These tests were conducted between January 1966 and May 1967 at the 16-ft transonic propulsion wind tunnel located at the Arnold Engineering Development Center, Tullahoma, Tennessee. The measurements taken were of the bending moment response to buffet at various locations along the vehicle over a Mach number range of 0.6 through 1.4. The effect of variation of pitch angle of attack  $\alpha$  and dynamic pressure  $q$  upon bending moment response was investigated.

## CONFIGURATIONS

Three basic configurations were tested.

1. The Titan IIIA is a 120-in.-diam three-stage single body with a 15-deg conical nose payload fairing (Figs. 1a, 2).

2. The Titan IIIC is a three-body configuration (Fig. 1b). The three bodies are a core that is identical to the Titan IIIA plus a 5-segment solid rocket motor (SRM) strapped to each side of the core. The third stage of the core of this configuration was either a transtage or a Centaur. The payloads had nose cone shapes like those shown in Figs. 1b, 1c, 3, 4, and 5.

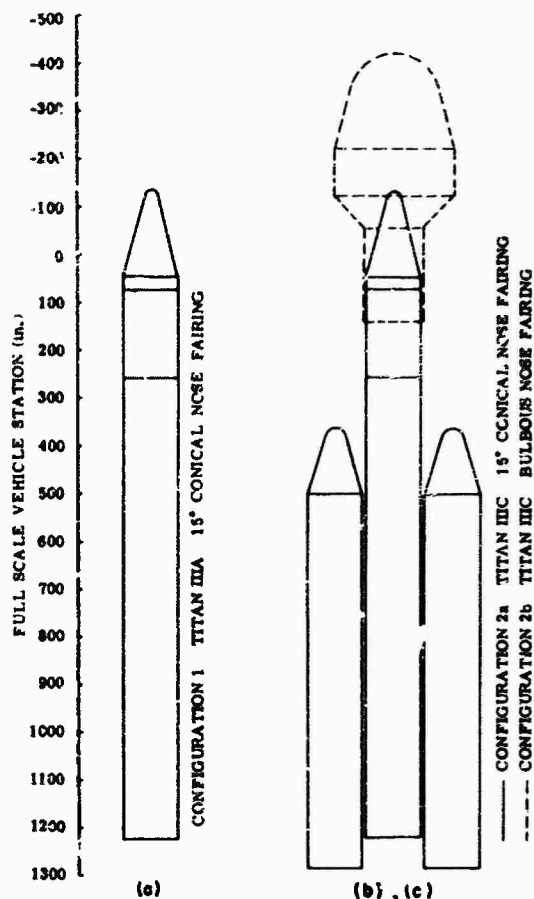


Fig. 1. Details of the Titan III booster

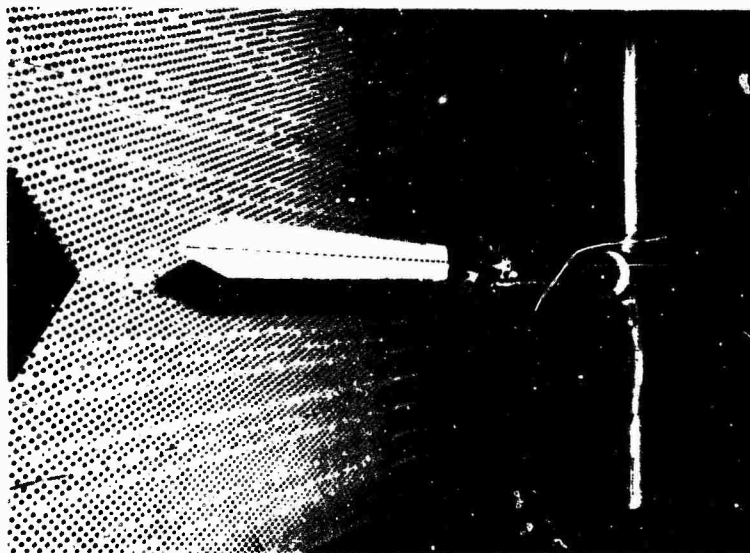


Fig. 2. Configuration 1, installed

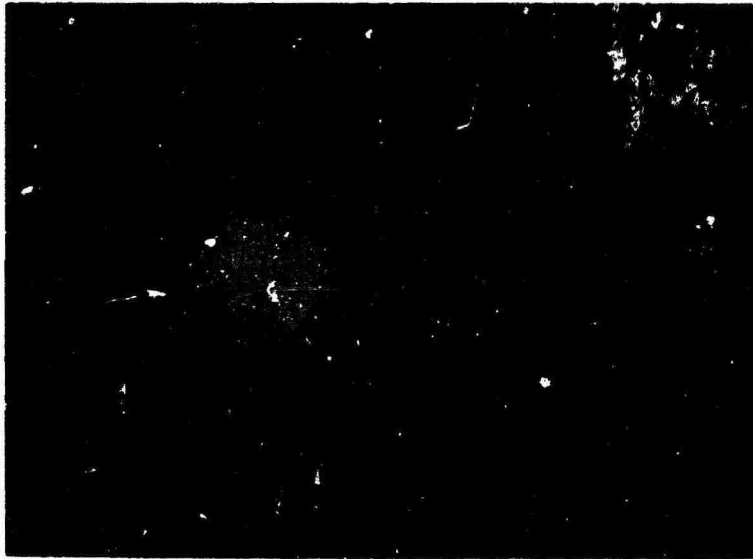


Fig. 3. Configuration 2b, Centaur-Voyager unshrouded



Fig. 4. Configuration 2b, Centaur-Voyager shrouded

3. The Titan IIC is the same as the second basic configuration, except that SRM's were 7-1/2 instead of 5 segments; the core was extended to incorporate Apollo, Gemini capsule, and other payloads (Figs. 6a, 6b, and 7).

#### TEST FACILITY

Tests were conducted in the transonic wind-tunnel circuit of the 16T propulsion wind tunnel

(PWT) at the Arnold Engineering Development Center (AEDC). The PWT is a continuous flow, closed-circuit wind tunnel capable of operation with stagnation pressure levels of 40 to 4000 psf. The test section measures 16 by 16 by 40 ft and is lined with perforated plates to allow continuous operation with minimum wall interference in the Mach number range of 0.5 to 1.6.

The test section used was a removable cart that becomes an integral part of the tunnel upon



Fig. 5. Complete model assembly, configuration 2a

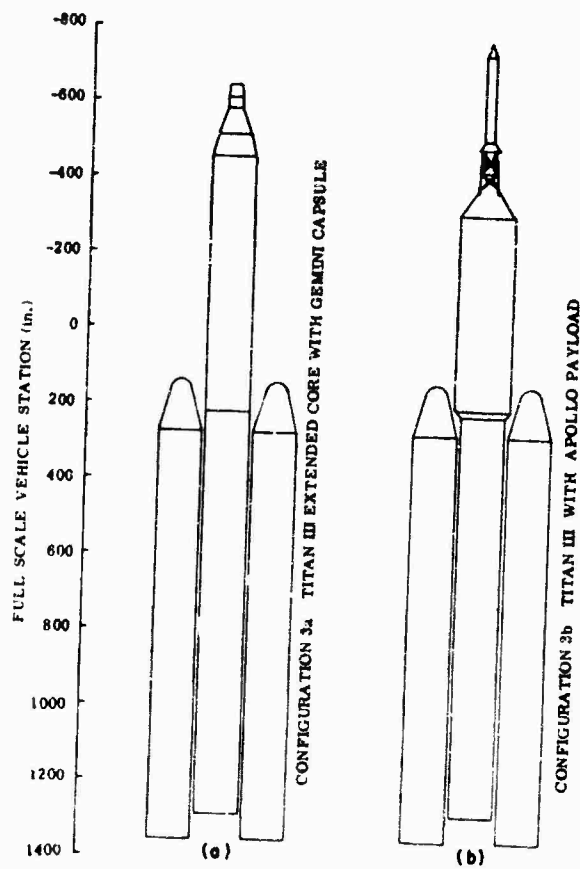


Fig. 6. Details of the Titan III booster



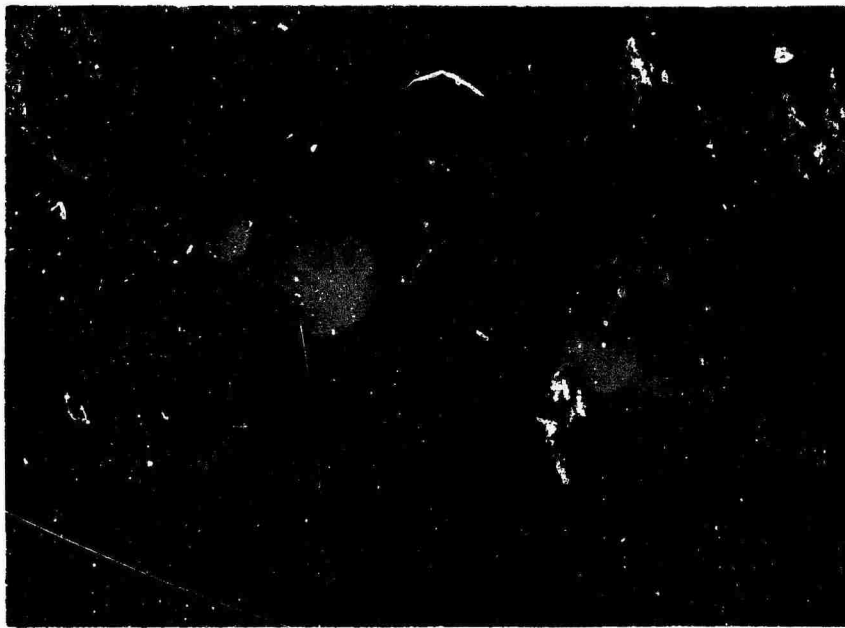


Fig. 7. Configuration 3b, installed

its insertion. The cart contained a sting support system with a pitch adjusting mechanism. A more detailed description of the wind tunnel is given in Ref. [2].

#### SCALING

A 7 percent aerodynamically scaled model was the maximum size allowed because of blockage limitations of the tunnel. Geometric and dynamic properties were scaled from the full-scale vehicle. A mismatch in Reynolds number and Froude number occurred because of linear scaling. The Reynolds number is the ratio of inertia to viscous forces in a flowing medium and is defined as  $Re = (\rho V D) / \mu$ ; the Froude number is the ratio of inertia to gravity forces and is defined as  $Fr = V^2 / (L g)$  where  $\rho$  = density,  $V$  = velocity,  $D$  = an equivalent diameter,  $\mu$  = absolute viscosity,  $L$  = a characteristic length,  $g$  = acceleration due to gravity. The test was conducted through a Reynolds number range of  $1.2 \times 10^6$  to  $3.7 \times 10^6$ , which was adequate to produce turbulent boundary layer at separation points. The Froude number accounts for the effect of gravity and, because of the 7 percent scale, was considered to have negligible effect upon the test results. The model was designed to simulate the weight conditions occurring at Mach 1.0. A more detailed summary of scaling and model properties is given in Ref. [3].

#### FABRICATION AND INSTALLATION

The core and SRM's were constructed from aluminum tubing machined to simulate full-scale stiffness in the pitch and yaw planes. Steel weights were clamped along the length of the tubing at locations required to meet the scaled weight and c.g. conditions of the Mach 1.0 flight condition. The payloads were designed to meet scaled mass and c.g. requirements but not stiffness. The payloads were constructed of balsa wood and/or aluminum covered with fiber-glass cloth. Thin segmented aluminum cylinders and balsa wood were used to obtain the external geometric shape. Spaces between each cylinder segment were filled with rubber base compound to provide smooth aerodynamic flow over the cylinders.

A single prong sting (for a single-body configuration) or a three-prong sting (for three-body configurations) was inserted into the model. The model was attached to the sting through soft elastic springs located at or near the nodepoints of the first two free-free elastic modes to minimize the restraint effect of the springs. The springs were designed so that the rigid body motion of the model on the soft springs would not interact with the structural elastic response of the model. Figures 5, 8, and 9 depict the installation sequence performed for each configuration.

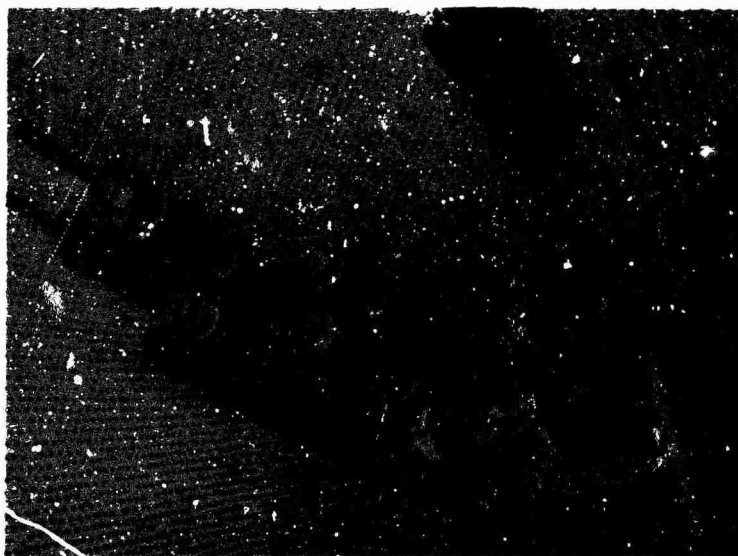


Fig. 8. Model sting support system

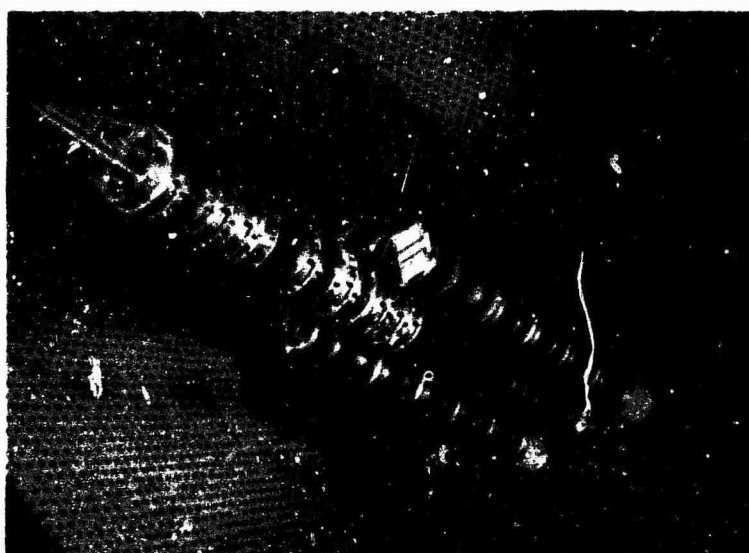


Fig. 9. Internal model structure

#### INSTRUMENTATION

The following transducers were installed on the model: strain gages, accelerometers, microphones, and deflection indicators. Lead wires from the transducers were routed through the model sting to the AEDC facility sting support boom.

Nine or 12 stations along the model core (depending on the configuration to be tested)

were allocated for strain gages to obtain measurements of bending moment in the pitch and yaw planes (see Table 1). Additional strain gages were arranged to determine the pitch and yaw deflection or load of the model support flexures tying the core and SRM's to the sting support system.

Microphones were flush mounted along the core and SRM's to measure sound pressure levels attained at various Mach numbers. Care

TABLE 1  
Bending Moment Strain Gage Locations

| Gage Number | Model Station (configurations 1, 2) | Model Station (configuration 3) |
|-------------|-------------------------------------|---------------------------------|
| 1           | 18.55                               | -13.84                          |
| 2           | 24.50                               | 6.86                            |
| 3           | 30.65                               | 20.16                           |
| 4           | 33.75                               | 21.41                           |
| 5           | 38.20                               | 23.16                           |
| 6           | 44.40                               | 33.73                           |
| 7           | 52.25                               | 35.48                           |
| 8           | 59.75                               | 51.98                           |
| 9           | 70.80                               | 53.98                           |
| 10          | —                                   | 55.36                           |
| 11          | —                                   | 69.41                           |
| 12          | —                                   | 70.73                           |

was taken that bulky lead wires and cathode followers associated with the microphone systems did not affect model damping, stiffness, and weight properties. These results are presented in Ref. [4].

To measure model angles of attack in pitch and yaw, deflection measuring potentiometers were mounted at the model support spring attach points. A dangleometer was installed just aft of the model on the sting support system to measure sting deflection.

## TEST CONDITIONS AND PROCEDURES

The tests were conducted through a Mach number range of 0.6 to 1.40, angles of attack of 0 to 4 deg, stagnation temperatures from 100° to 110°, dynamic pressures from 80 to 130 percent of nominal full-scale equivalent dynamic pressure shown in Fig. 10, and Reynolds numbers of  $1.2 \times 10^6$  through  $3.7 \times 10^6$ , also shown in Fig. 10.

Testing was conducted in two phases, wind off and wind on. During the wind-off phase, vibration data were obtained. This included obtaining mode shapes and frequencies, structural damping present in each mode, and the bending moment response in each mode along the vehicle length. This last step was done primarily to insure that the instrumentation was performing correctly, that there were, for example, no loose gages. During the wind-on phase, the buffet response at each sensor was recorded on tape for later digitization for use with digital computer programs, visually presented on oscillographs, and presented as rms values through on-line integrating circuits. Usually, a 50-sec integrating time was used. Bandpass filters were used to filter out response of the rigid body modes, to obtain the total response of the elastic modes, and to obtain the contribution of the first elastic mode to the total response.

Television cameras were used to observe the model during the wind-on phase. Standard

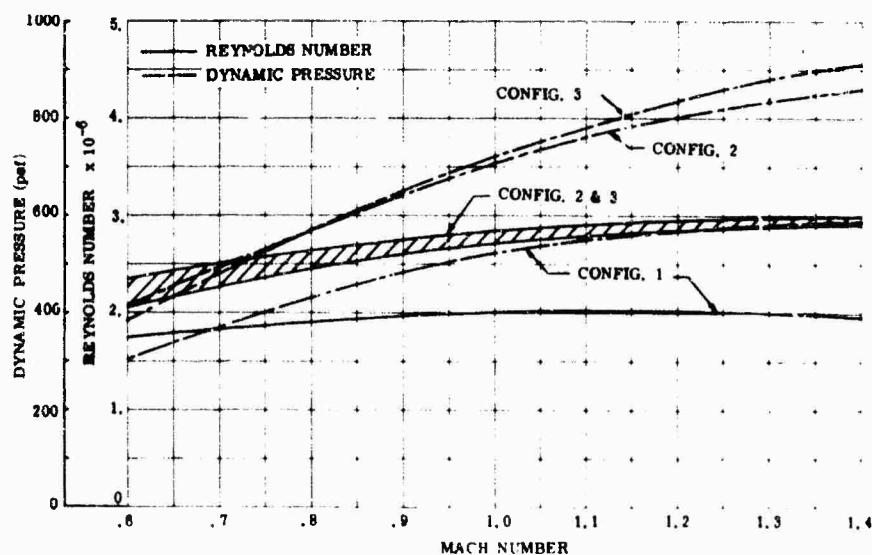


Fig. 10. Variation of Reynolds number and dynamic pressure with Mach number

motion picture cameras were used to photograph the general response of the vehicle. Schlieren cameras were used to obtain photographs of the flow pattern around the vehicle at each Mach number. Also, a brake was installed in the payload of each configuration to damp out any excessive vehicle response that might occur and thus prevent model damage.

## RESULTS

The analytical and experimental vibration data for the test configurations described here are presented in Fig. 11. These curves show that the model was slightly stiffer than the full-scale vehicle, but the mode shapes are in fairly good agreement and corrections for frequency differences were made.

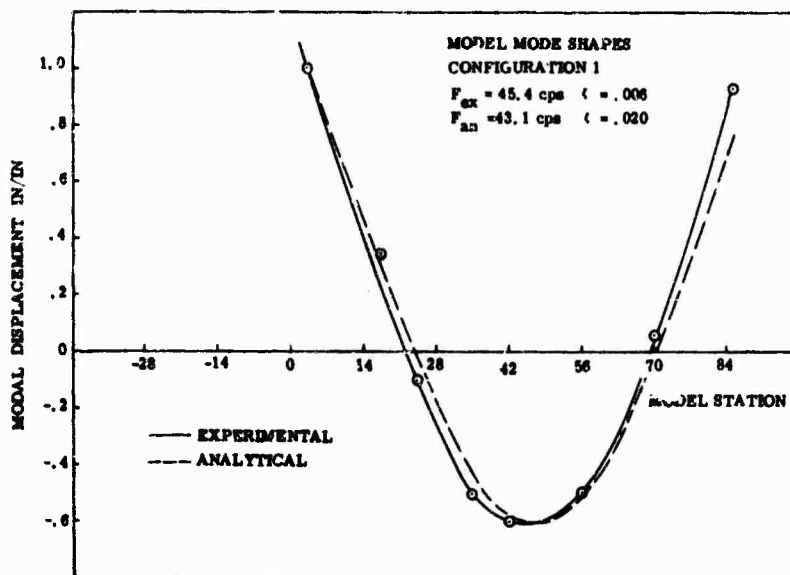


Fig. 11(a). First elastic model mode shapes

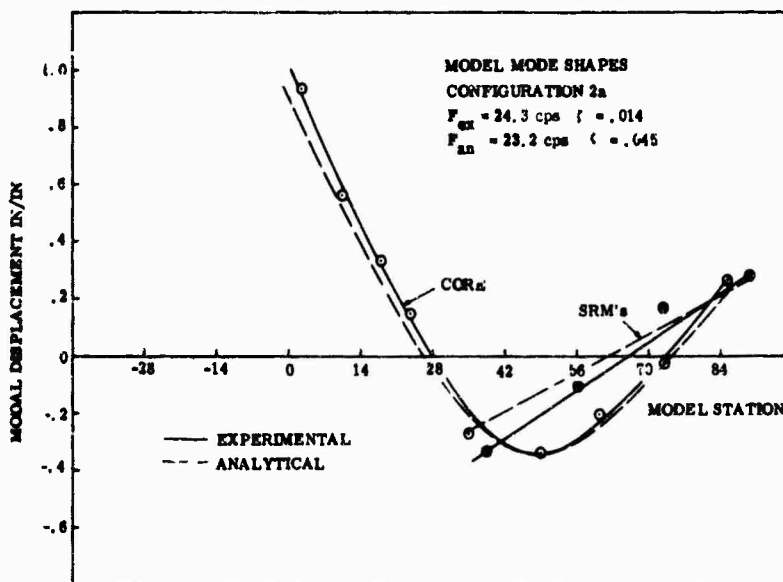


Fig. 11(b). First elastic model mode shapes

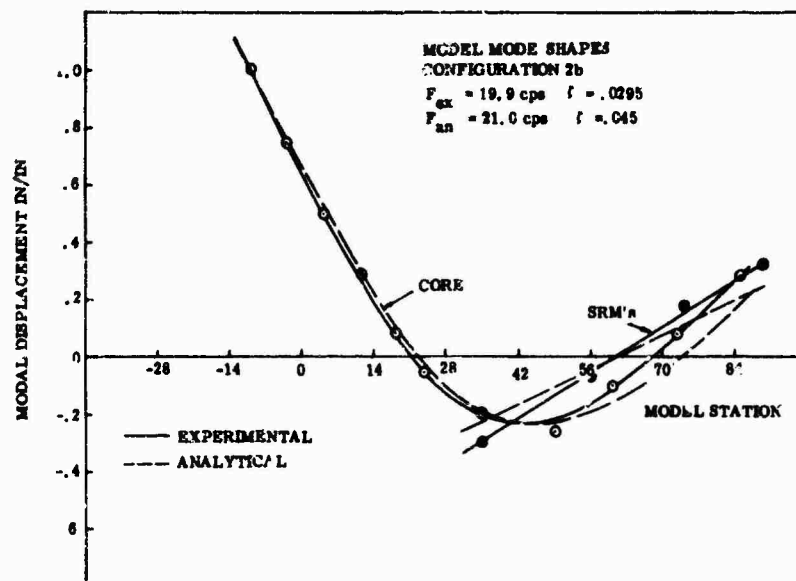


Fig. 11(c). First elastic model mode shapes

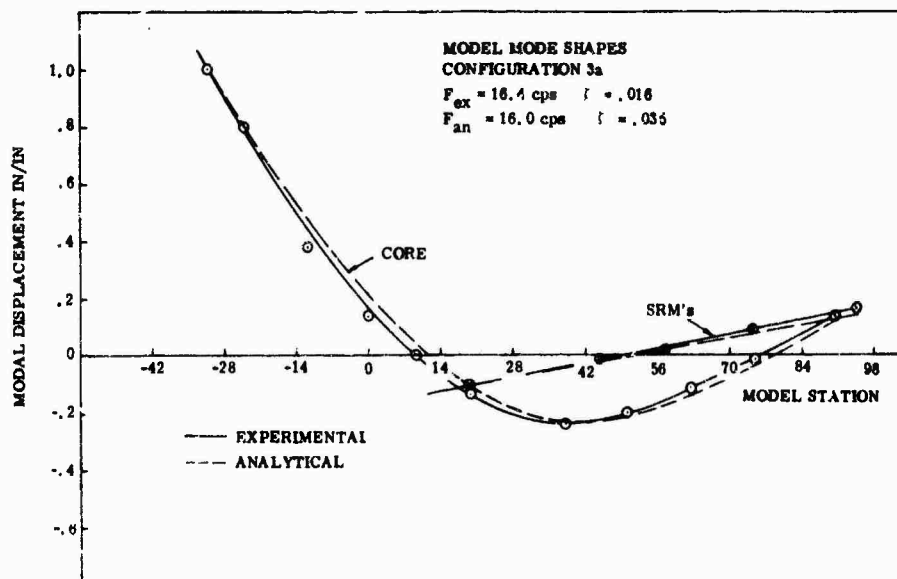


Fig. 11(d). First elastic model mode shapes

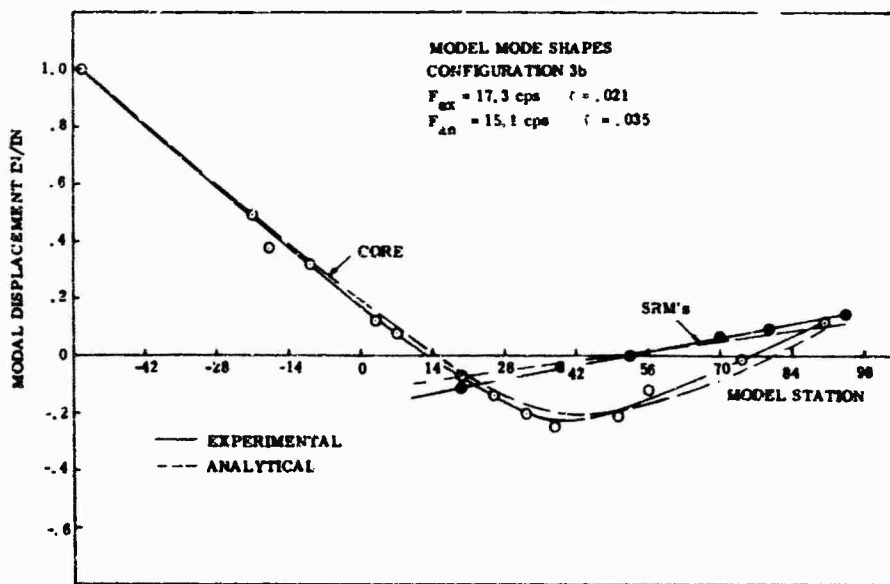


Fig. 11(e). First elastic model mode shapes

Assuming a free-free system, the bending moments were computed by summing the inertia loads and taking the first moment of the shear forces:

$$(\text{moment})_i = -\omega_i^2 [I] [M] (\phi_i)$$

where  $\omega_i$  is the frequency associated with the  $i$ th mode in radians per second,  $[I]$  is the distance between inertia loading points,  $[M]$  is the diagonal mass matrix,  $\phi_i$  is the experimental model deflection along the vehicle in the  $i$ th mode, and  $(\text{moment})_i$  is the bending moment in the  $i$ th mode. The first, second, and third elastic mode contributions ( $q_1$ ,  $q_2$ , and  $q_3$ , respectively) to the total elastic response were found at each vehicle station. (It was assumed that the total elastic vehicle mean squared response was the sum of the first three elastic mode mean squared responses.) In addition, damping per mode ( $C_1$ ,  $C_2$ ,  $C_3$ ) between the model and the full-scale vehicle was determined on the basis of the fact that a viscously damped system is proportional to the square of the stress or amplitude; therefore,

$$\text{bending moment} = \left( \frac{\text{model}}{\text{full scale}} \right)^{1/2} C_i$$

The mean squared bending moment per mode at each vehicle station was computed as

$$\left[ \text{mean squared bending moment per mode} \right] = \left[ \frac{[M]}{[I]} \right]^2 K$$

where

$$[K] = \frac{\text{measured mean squared bending moment in each mode at station X}}{\text{computed squared bending moment in each mode at station X}}$$

Each mode is then scaled to full-scale equivalence. The full-scale bending moment varies as  $n^{-3} \times$  model bending moment because of dimensional considerations;  $n$  is equal to length (model) divided by length (full scale). Also corrections for the mismatch in dynamic pressure ( $q$ ) and frequency ( $\omega$ ) were applied. With all factors considered, the full-scale modal bending moment becomes

$$\left[ \text{full-scale mean squared bending moment per mode} \right]$$

$$\left[ \text{mean squared bending moment per mode} \right] \left[ \left( \frac{M}{F} \right) \left( \frac{q_F}{q_M} \right)^2 \left( \frac{L_F}{L_M} \right)^6 \left( \frac{F}{\omega_M} \right) \right]$$

The total mean squared bending moment is obtained by adding the mean squared bending moment of the first, second, and third modes and taking the square root of their sum.

Buffet response data were obtained from the pitch and yaw planes, but only the peak pitch plane response data at one vehicle station are presented here. The pitch plane response was higher in most instances than the yaw plane response and presents a clearer picture of response variation over the Mach number range.

These results are presented in Figs. 12 through 16 as rms buffet response vs Mach number.

Figure 12 presents the data for peak response in the pitch plane of configuration 1 for nominal dynamic pressure (100 percent  $q$ ) and angles of attack of 0 and 4 deg at vehicle station

760. At 0-deg angle of attack, the peak bending moment occurred at Mach 1.1. At 4-deg angle of attack there were three definite Mach number peaks, with response levels generally lower than at 0-deg angle of attack. The loads induced by buffet forces were very low, in fact so low that the response was probably a result of wind tunnel

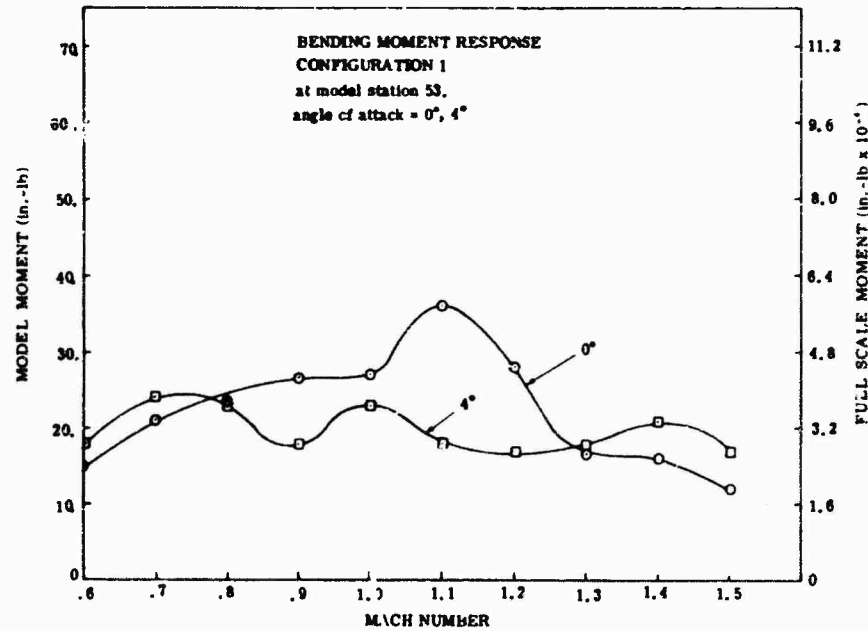


Fig. 12. Buffet bending moment response for configuration 1

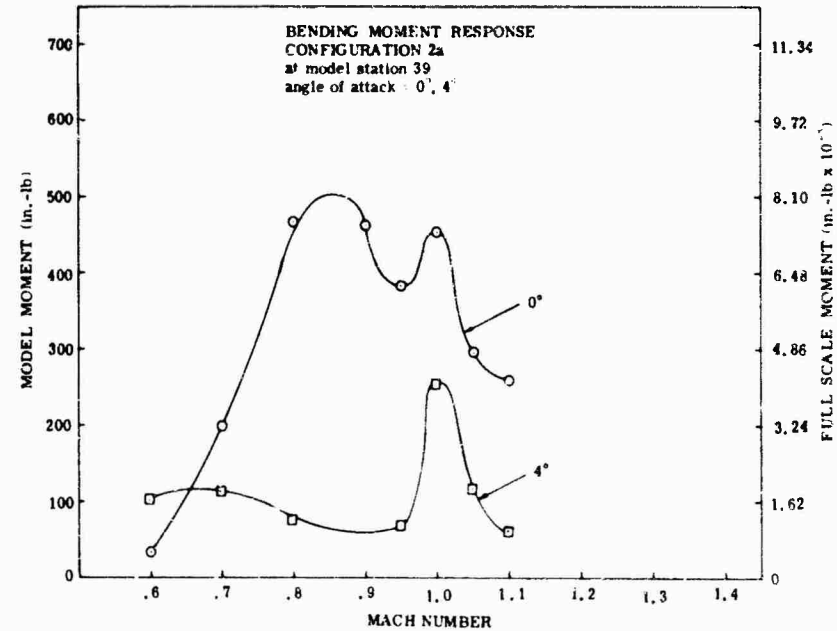


Fig. 13. Buffet bending moment response for configuration 2a

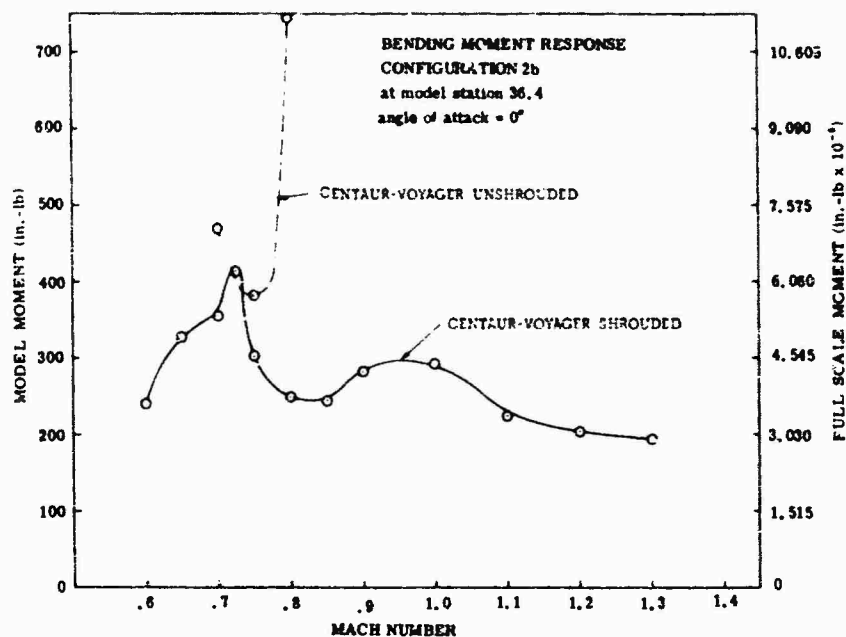


Fig. 14. Buffet bending moment response for configuration 2b

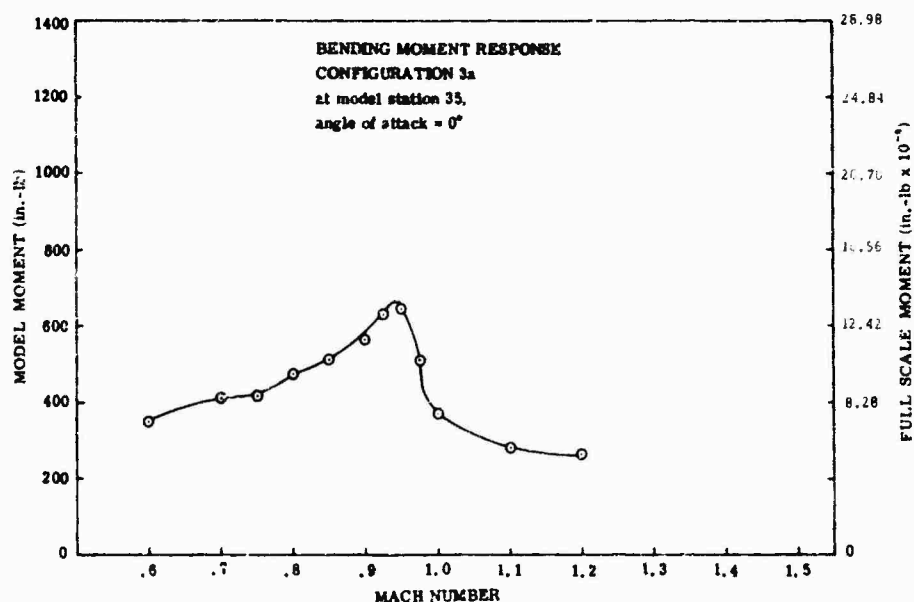


Fig. 15. Buffet bending moment response for configuration 3a

noise. Figures 13 and 17 present the peak pitch plane response for configuration 2a with conical nose payload fairing at vehicle station 560 for 100 percent  $q$  and 0- and 4-deg angle of attack. At 0-deg angle of attack a broad peak of 770,000 in.-lb occurred between Mach 0.8 and 0.9, dipped to 620,000 in.-lb at Mach 0.95, peaked again to 740,000 in.-lb at Mach 1.0, and then decreased

steadily at the higher Mach numbers. At 4-deg angle of attack, peak response occurred at Mach 1.0 with a value of 400,000 in.-lb, approximately one half of the response at 0-deg angle of attack. Figure 14 presents the peak pitch plane response for configuration 2b with a bulbous payload at vehicle station 500. This bulbous payload had a diameter of 260 in. and a length-to-diameter



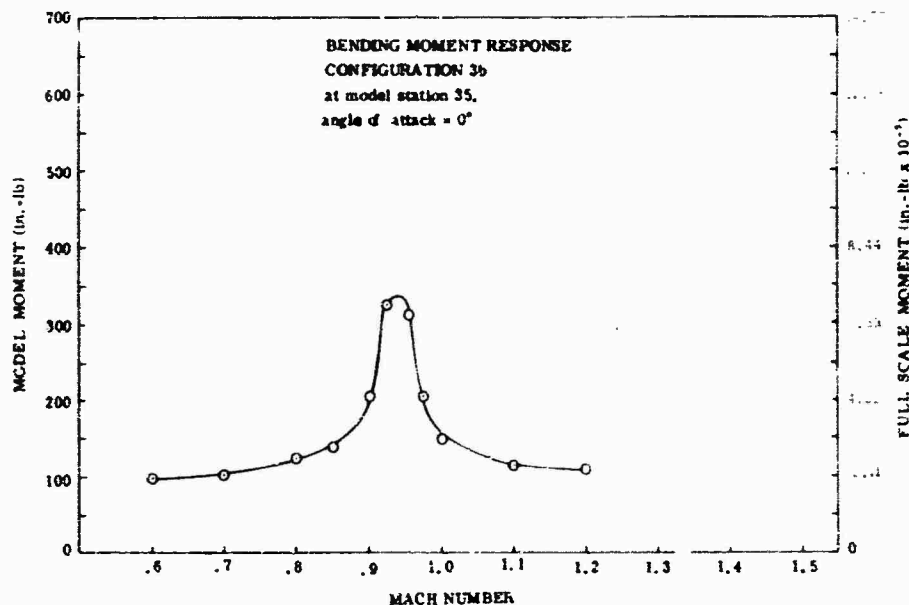


Fig. 16. Buffet bending moment response for configuration 3b

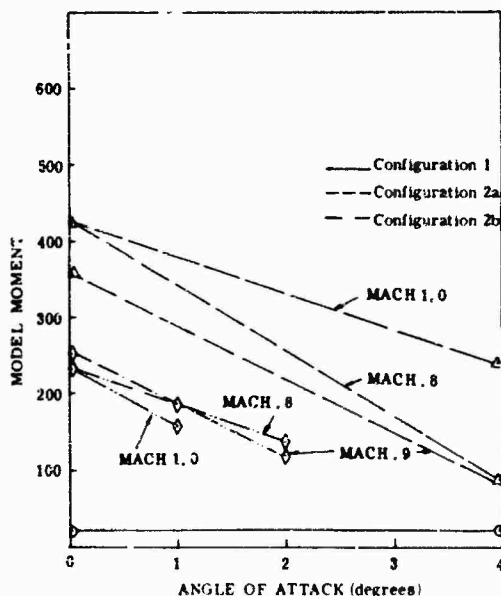


Fig. 17. Buffet response with variation of angle of attack

ratio (L/D) of 0.385. The data presented are for 100 percent  $q$  and 0-deg angle of attack. This configuration demonstrated unstable tendencies from the beginning of the wind tunnel run, so a close watch was kept on its response characteristics as each Mach number setting was attained. As demonstrated in Fig. 14, a sharp increase in response occurred at Mach 0.8; so

it was decided not to risk losing the model by trying to obtain data at higher Mach numbers. A value for bending moment of 1,930,000 in.-lb was obtained at Mach 0.8. Because of the expected high buffet loading for this configuration, several "fixes" had been designed. The effect of one of the fixes in reducing the buffet loading is also shown on Fig. 14. This fix was to add a cylindrical shroud of the same diameter as the payload until the L/D ratio exceeded a value of 1.0 (Fig. 18). The actual L/D ratio for this fix was 1.13. This fix reduced the buffet loading to acceptable levels. Peak pitch plane response occurred at vehicle station 520 at Mach 0.725 and 0 angle of attack with a response value of 620,000 in.-lb. This was a 68 percent reduction in buffet loading. Because of the success in reducing the loads, more parameter variations were conducted using this fix. Dynamic pressure ( $q$ ) variations with values of 90, 110, 130, and 150 percent of nominal were conducted. These results are shown in Fig. 19. Additional angle of attack values of 1 and 2 deg were conducted with 100 percent  $q$ . These results are shown in Fig. 17.

The Apollo with stiff launch escape system (LES) configuration results are shown in Fig. 16. The peak pitch plane response at vehicle station 507, 0-deg angle of attack, and 100 percent  $q$  occurred at Mach 0.95, with a bending moment value of 697,000 in.-lb. Figure 20 presents the effects of dynamic pressure variation at 80 and 120 percent of nominal  $q$  upon the buffet response for the Apollo configuration.

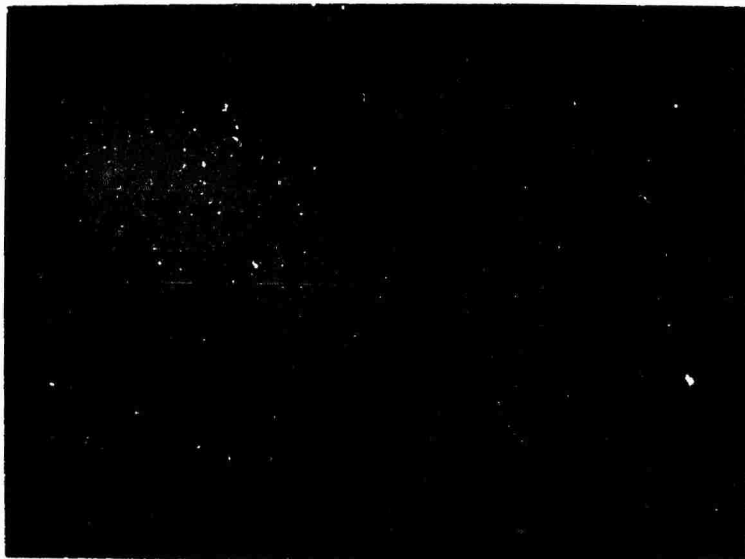


Fig. 18. Titan III C bulbous nose fairing with added shroud

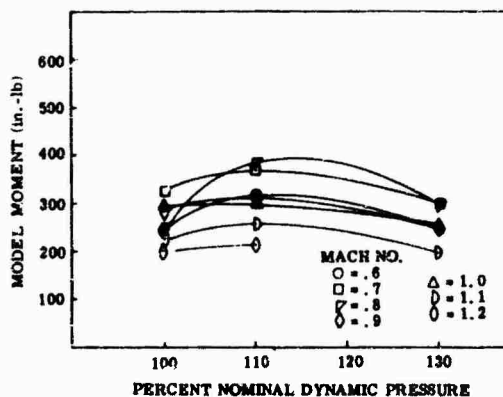


Fig. 19. Effect of dynamic pressure on buffet response for configuration 2b

Figure 20 depicts the results of linear and square root ratios of the actual dynamic pressure ( $q'$ ) to the nominal dynamic pressure ( $q$ ). These results show that the response varies linearly with dynamic pressure, indicating that the aerodynamic damping present in the system was small [5]. Reference [5] states that for the case where aerodynamic damping is large relative to structural damping, the rms bending moment varies with the square root of the dynamic pressure, and when the aerodynamic damping is small relative to structural damping the rms bending moment varies linearly with dynamic pressure. The equivalent viscous damping was less than 3 percent for this configuration.

The results of an extended core configuration with 7-1/2-segment SRM's and a Gemini capsule are shown in Fig. 15. The peak pitch plane response at vehicle station 507, 0-deg angle of attack, and 100 percent  $q$  occurred at Mach 0.95 with a bending moment value of 1,289,000 in.-lb. The flow patterns about the payloads are shown in Fig. 21. The Schlieren photographs show a large turbulent separated flow region at Mach numbers  $\geq 0.9$ . Figure 21 shows the flow and shock-wave patterns for Mach numbers 0.7, 0.8, 0.9, 0.95, 1.0, and 1.1 for configurations 3a and 3b.

There were many other configurations and fixes tested, but space limits their presentation and discussion here. References [5], [6], and [7] present these results.

## CONCLUSIONS

The primary conclusions drawn from the test results presented are:

1. Peak buffet response occurs at subsonic Mach numbers.
2. The Titan IIIA single-body configuration produces very low buffet loading.
3. Large-diameter bulbous payloads with blunt noses and  $L/D$  ratios less than 1.0 will produce excessive buffet loading (Voyager payload).

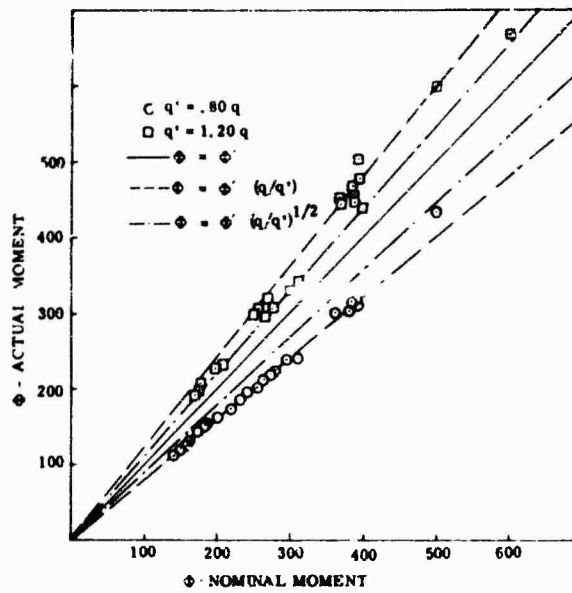


Fig. 20. Effect of dynamic pressure for configuration 5b

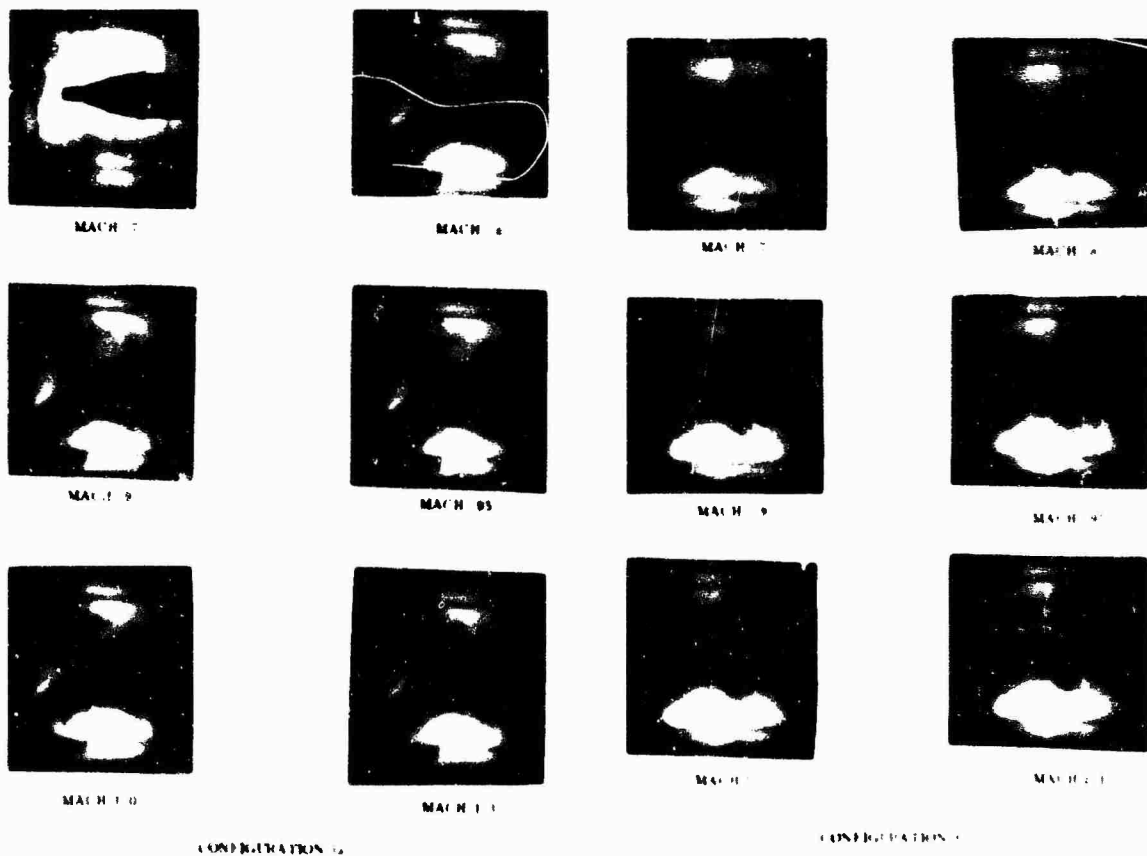


Fig. 21(a). Schlieren photographs of the flow about the payload

Fig. 21(b). Schlieren photographs of the flow about the payload

4. Excessive buffet loading obtained on the Voyager payload configuration can be reduced to reasonable levels by increasing the L/D ratio to greater than 1.0 by addition of a shroud with the same diameter as the payload.

5. Titan IIC configurations with 5-, 7-, or 7-1/2-segment SRM's and standard nose fairings do not produce excessive buffet loading.

6. There is a significant increase in buffet response in configuration 3 over configuration 2.

7. In general, a decrease in load occurs with angle of attack.

8. Buffet loads vary linearly with variations in  $q$  for Apollo payload.

#### REFERENCES

1. George W. Jones, Jr., and Jerome T. Foughner, Jr., "Investigation of Buffet Pressures on Models of Large Manned Launch Vehicle Configurations," NASA TND-163, May 1963
2. Arnold Engineering Development Center, Test Facilities Handbook (5th ed.) (Arnold Engineering Development Center, Tullahoma, Tenn.), 1963
3. "Pretest Report on 7 Percent Transonic Buffet Tests for Various Titan III Configurations," Martin Co., Denver, Colo., SSD-CR-65-257, Jan. 1966
4. John R. Baratonio, and F. A. Smith, "Scale-Model Wind Tunnel Acoustic Data," Shock and Vibration Bull. No. 37, Part 7, 1968
5. F. W. Peters, "Applications - Final Report on 7 Percent Transonic Buffet Model Test for Various Titan III Configurations, Martin Co., Denver, Colo., MCR-67-5, Feb. 1967
6. G. D. Bombardier, "Final Post Test Report on 7 Percent Transonic Buffet Model Test for Various Titan III Configurations," Martin Co., Denver, Colo., SSD-CR-66-563, Jan. 1967
7. J. E. Robertson and T. R. Brice, "Buffet Response of Aeroelastically Scaled Titan III Missile Configurations at Transonic Mach Numbers," AEDC-TR-67-33, Mar. 1967

#### DISCUSSION

Voice: What was the model constructed of, and what was its thickness?

Mr. Uchiyama: It was constructed from aluminum tubing. We did not use a uniform thickness. It was not a complete cylinder. The model we used simulated only the pitch and yaw planes; it was a skeleton-like fabrication. There is a picture in the report which shows how the model was cut out to simulate the full-scale system.

Voice: Did you use strain gages on the model?

Mr. Uchiyama: Yes.

Voice: Did you make any pressure measurements on the model itself?

Mr. Uchiyama: No.

Voice: I believe you have made some measurements on a five percent model. Have you tried correlating those?

Mr. Uchiyama: At this time they have not been correlated.

Voice: Did the loads correlate with your strain gage measurements?

Mr. Uchiyama: It would be a really good check to see if one could define the buffet forcing function and then force the model with that forcing function and see if the responses check with the actual test results.

Voice: Are you planning more tests, say with different configurations, more body sticking out, and this sort of thing?

Mr. Uchiyama: Not that I know of.

\* \* \*

## HIGH-FORCE VIBRATION TESTING OF THE SATURN S-IVB STAGE\*

L. G. Smith  
McDonnell Douglas Corporation  
Huntington Beach, California

In testing the Saturn I instrument unit, large strains induced by low-frequency modal behavior caused structural failures at points undetected during qualification testing of detail assemblies. To ensure the structural integrity of the Saturn V launch vehicle, NASA prime contractors performed high-force dynamic tests on subassemblies of their respective stages. High-force vibration testing by the Douglas Missile and Space Systems Division of two large subassemblies of the S-IVB stage is described. Included are program management, test specimens, test fixtures, test criteria, test control, test data system, and test results.

### INTRODUCTION

Vibration of major structural assemblies, referred to as high-force testing, for dynamic environmental simulation was initiated by the Marshall Space Flight Center in testing the Saturn I instrument unit. Large strains induced by low-frequency modal behavior caused structural failures at weak points which went undetected during qualification testing of detail assemblies. To ensure that low-frequency vibration would not impair the structural integrity of the Saturn V launch vehicle, NASA prime contractors were requested to perform high-force dynamic tests on structural subassemblies of their respective stages. This paper describes the testing accomplished by the Douglas Missile and Space Systems Division on two large subassemblies of the S-IVB stage.

### PROGRAM MANAGEMENT

To maintain cost and schedule control, a task force management team was created, and a team manager assigned. Team members included an assignee from each manufacturing, engineering, and laboratory function involved. Representatives of program management and contract departments were included to represent contractual aspects of the test, with regard

both to NASA and the testing vendor, Thiokol Corporation. A PERT representative was assigned to gather PERT program inputs and interpret program outputs. Figure 1 shows the team organization.

The team met weekly for the purpose of airing all problem areas and assigning corrective action to the specific responsible team member. Progress on all such items was reviewed weekly until the corrective action was completed. PERT outputs served as an adjunct to the basic problem-detection function of the team. After vendor selection, vendor inputs were included in the PERT program, and vendor status was verbally reported at the weekly meetings. To create an appropriate working atmosphere, the team meetings were informal and documentation was limited to a weekly agenda and action item summary.

The ultimate purpose of the team was to assure delivery of the correct specimens to the vendor's test site, and to assure that at that time the test was ready to proceed. Thus when delivery was accomplished, the team was dissolved and responsibility for test activity was mutually assigned to a test director representing development engineering, and a test conductor representing the engineering laboratories and the contracts department. The team manager was maintained to coordinate the required

\*Phases of work presented here were accomplished by the Douglas Aircraft Missile and Space Systems Division under the Saturn S-IVB contract NAS7-101 from NASA's Marshall Space Flight Center.

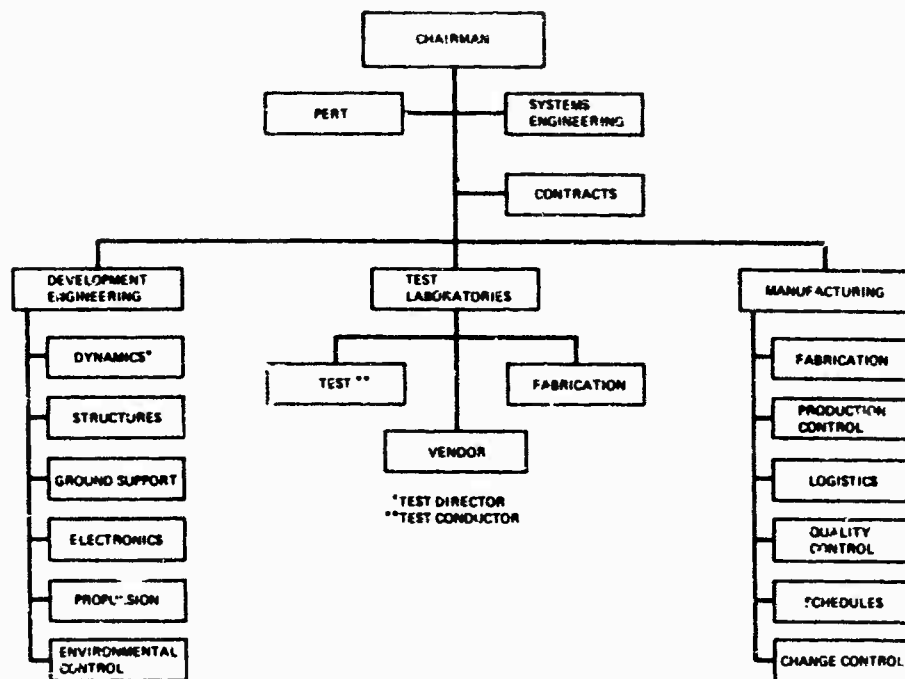


Fig. 1. Test task team organization

in-plant support, but primary control was maintained at the vendor site to preclude test delays. Fortunately, the difficulties arising during testing were sufficiently minor to allow on-site resolution, and delays were actually avoided. A valuable aid to this responsive type of program management was the assignment of NASA personnel to the test site, so that immediate approval of program implementation was possible.

#### TEST SPECIMENS

The test specimen included two 260-in.-diam structural subassemblies: the forward skirt and boattail specimens. Figure 2 shows these specimens as they relate to the S-IVB/V stage.

All specimen structure and bracketry was production configured and assembled by Douglas production departments. Large elastic members, such as propulsive system ducting, were also production configured. Smaller rigid items, such as electronic black box assemblies, were simulated in mass and center of gravity.

The thermal environmental control system in the forward skirt specimen was functionally operated and monitored during testing to study system dynamic behavior. This system

incorporates the electronic mounting panels as heat exchangers supplied by a fluid circulating manifold system.

#### TEST FIXTURES AND SETUP

The excellent test fixtures made a major contribution to the full accomplishment of this program. Special control methods are described; but it is emphasized that without adequate fixtures, even the most elaborate electronic control systems would probably be inadequate. For the design of the drive adapter fixtures, optimization formulas [1] were used to size fixture members after basic layout procedures were established.

After completion of layout and sizing, overall ring fixture modes were analytically determined using a digital computer adaptation of the Rayleigh-Ritz method; the frequency characteristics were found to be satisfactory. Fixtures are shown in Figs. 3, 4, and 5. The computer analysis gave quite different results from simple hand calculations because of large differences between the static and dynamic load distribution. The results of the computer analysis were in good agreement with the test results.

The combining of fixtures, shakers, and static stands into the overall test setup was

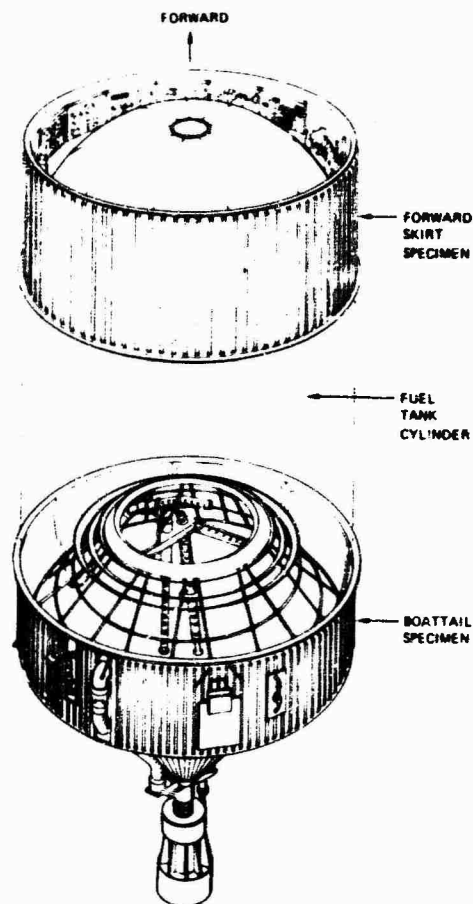


Fig. 2. High force specimens as related to the S-IVB stage

closely coordinated with the test vendor. Figures 6 and 7 show typical test setups. Because of an unusually detailed bid request and bid package, the contract scope was easily identified and the test setup design kept within this scope.

#### TEST CRITERIA

The opportunity to use the natural response of the large amount of available structure to achieve the test objectives was recognized early in the program, and special criteria methods were derived to allow such use. Control of the exciter systems was maintained at accelerometers located near the fixture-specimen interface (Fig. 3). Primary interest, however, was placed in internal specimen response at critical vehicle structural hard points. Envelopes of peak responses at these points were designated as "red-line parameters," and the control levels

specified at the control accelerometer locations were an estimate of the input required to induce the critical internal peak responses to reach, or approach, red-line parameter levels.

All full-level testing was preceded by half-level surveys to ascertain control level adequacy. If these levels proved unacceptable, they were adjusted and new levels tried. In most cases the original control levels were adequate to produce red-line parameter responses. Figures 8 and 9 show typical levels. The red-line parameters were based on a composite of known and expected static and flight vibration environments.

#### TEST CONTROL

Normal exciter control systems were used. Figures 10 and 11 show the control system block diagrams. The most unusual innovation was the

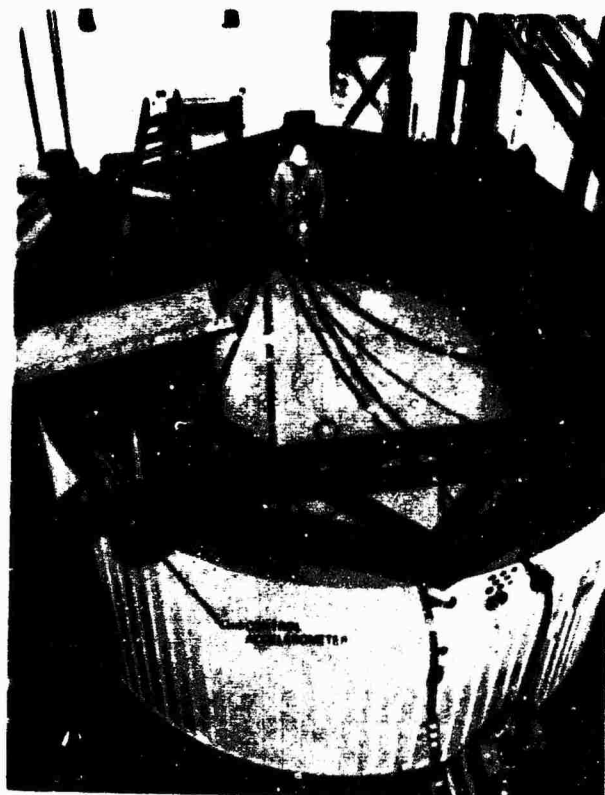


Fig. 3. Typical ring fixture -- upper forward skirt ring shown

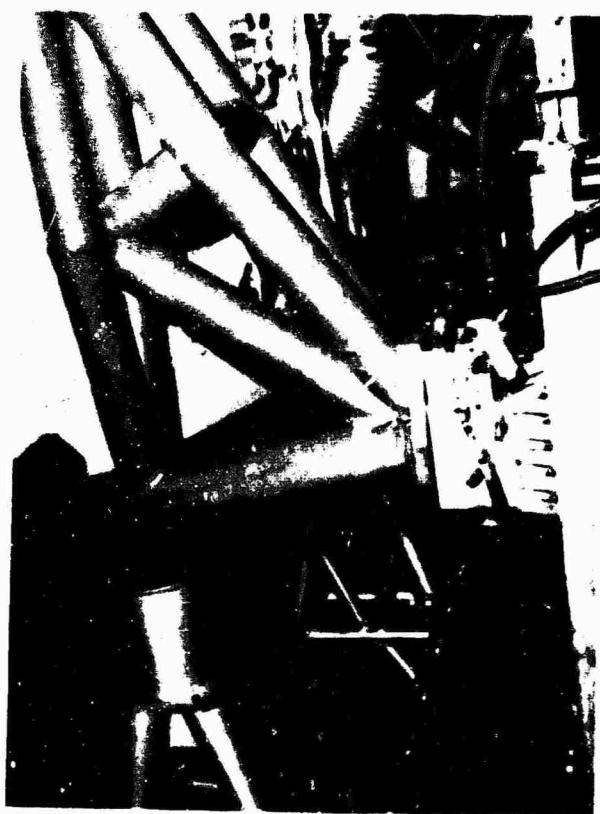


Fig. 4. Typical lateral drive adapter fixture -- boattail adapter shown



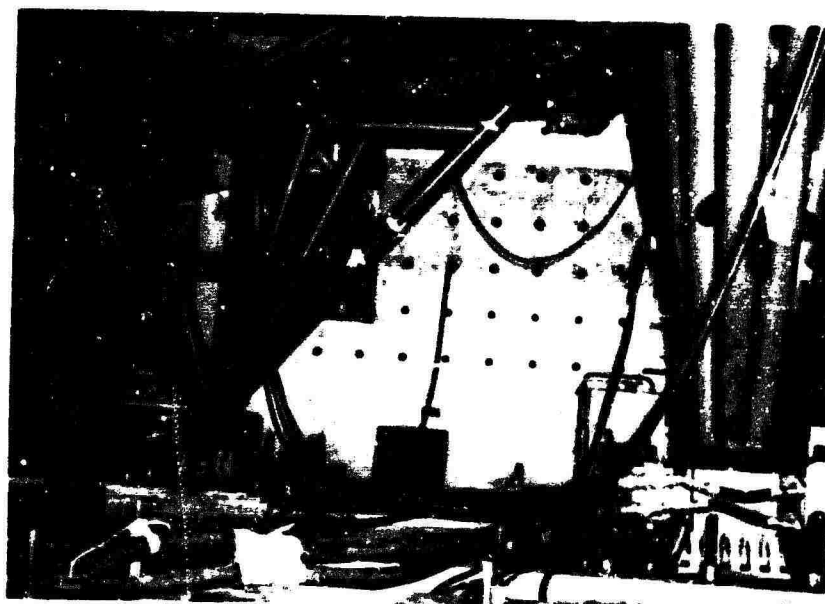


Fig. 5. Vertical drive adapter fixture

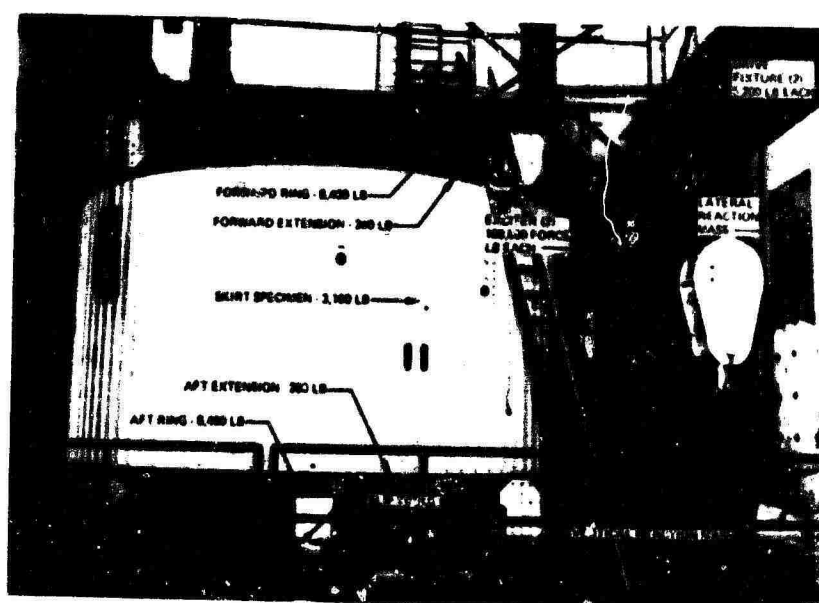


Fig. 6. Test setup -- forward skirt, lateral

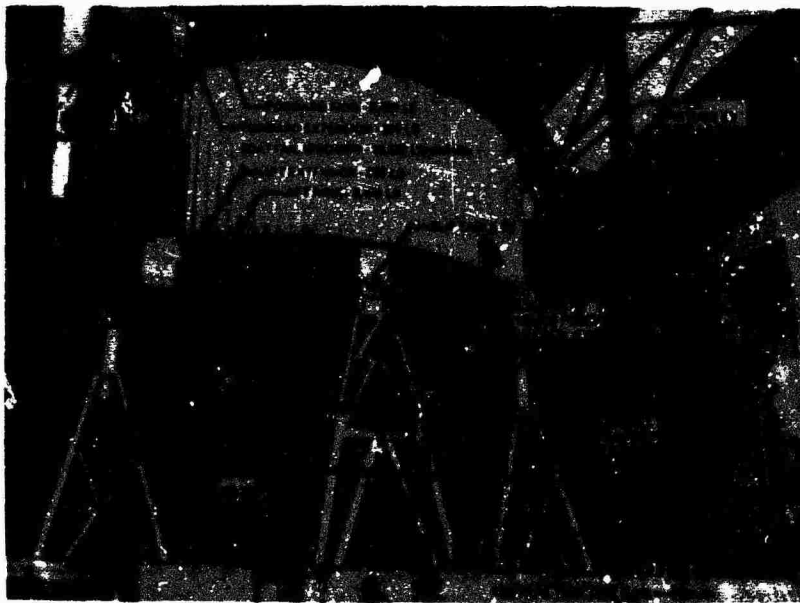


Fig. 7. Test setup -- boattail, lateral

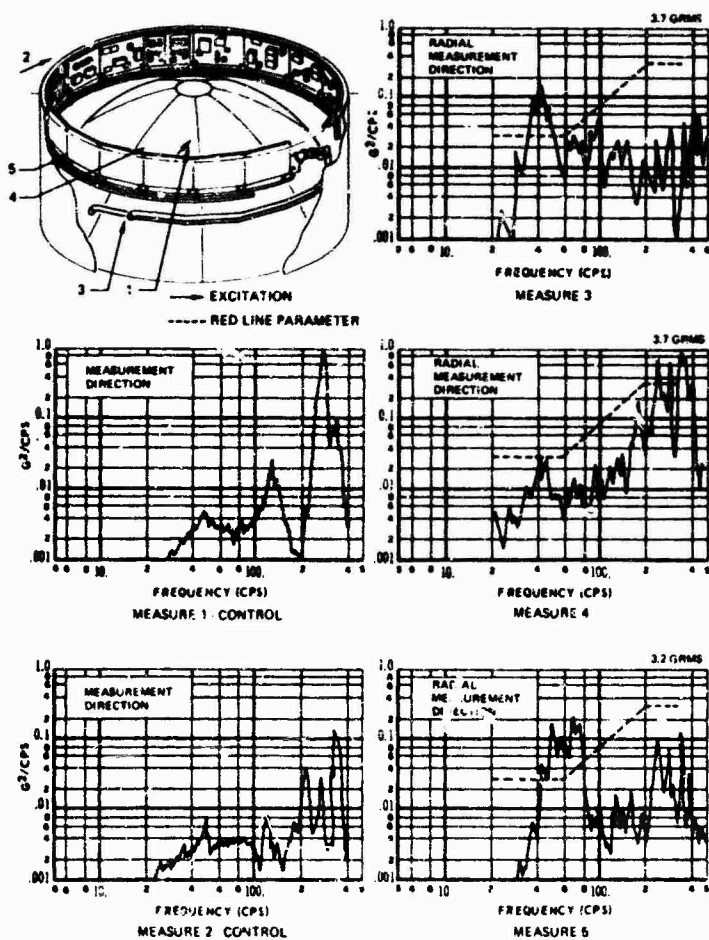


Fig. 8. Random levels -- forward skirt, lateral

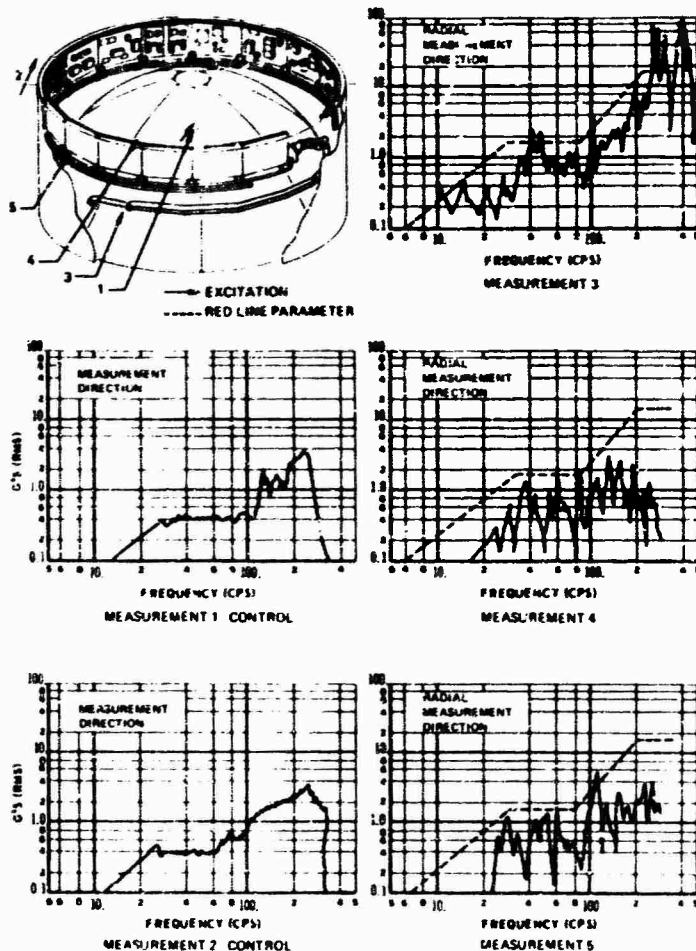


Fig. 9. Sinusoidal levels -- forward skirt, lateral

inclusion of time-multiplex-type random averaging. This averaging proved entirely adequate.

Even with averaging, random control on early test runs was unsatisfactory. The discrepancy seemed to be the type associated with subharmonic generation of high-frequency energy induced because of the great dynamic range of automatic equalizer servo loops. Since the test range was 20 to 300 Hz and equalizer range 20 to 2000 Hz, it was hoped that the servos from 300 to 2000 Hz, even though on the zero setting, were generating the unwanted energy. Resetting these channels to the manual mode did, in fact, solve the problem, and no further random control difficulty was experienced. It has been found to be almost always true that, unless some looseness exists, automatic equalization difficulties can be solved by finding the appropriate channels to put into the manual mode.

Sinusoidal phase control difficulty was experienced at low frequency. It was determined that control acceleration levels were too low to induce sufficient accelerometer voltage to drive properly the phase control system incorporated into the servo oscillator. Instead, the system tended to "wander," causing out-of-phasesness. The phase system was disabled over the frequency range of difficulty (5 to 25 Hz), and the intrinsic fixture stiffness in this range was relied upon for phase maintenance. Above 25 Hz, signal strength was sufficient for electronic control.

#### TEST DATA SYSTEM

Up to 120 channels of FM data were stored on a single tape for each test, eliminating the time correlation problem, and minimizing the time establishment and tape library problems.

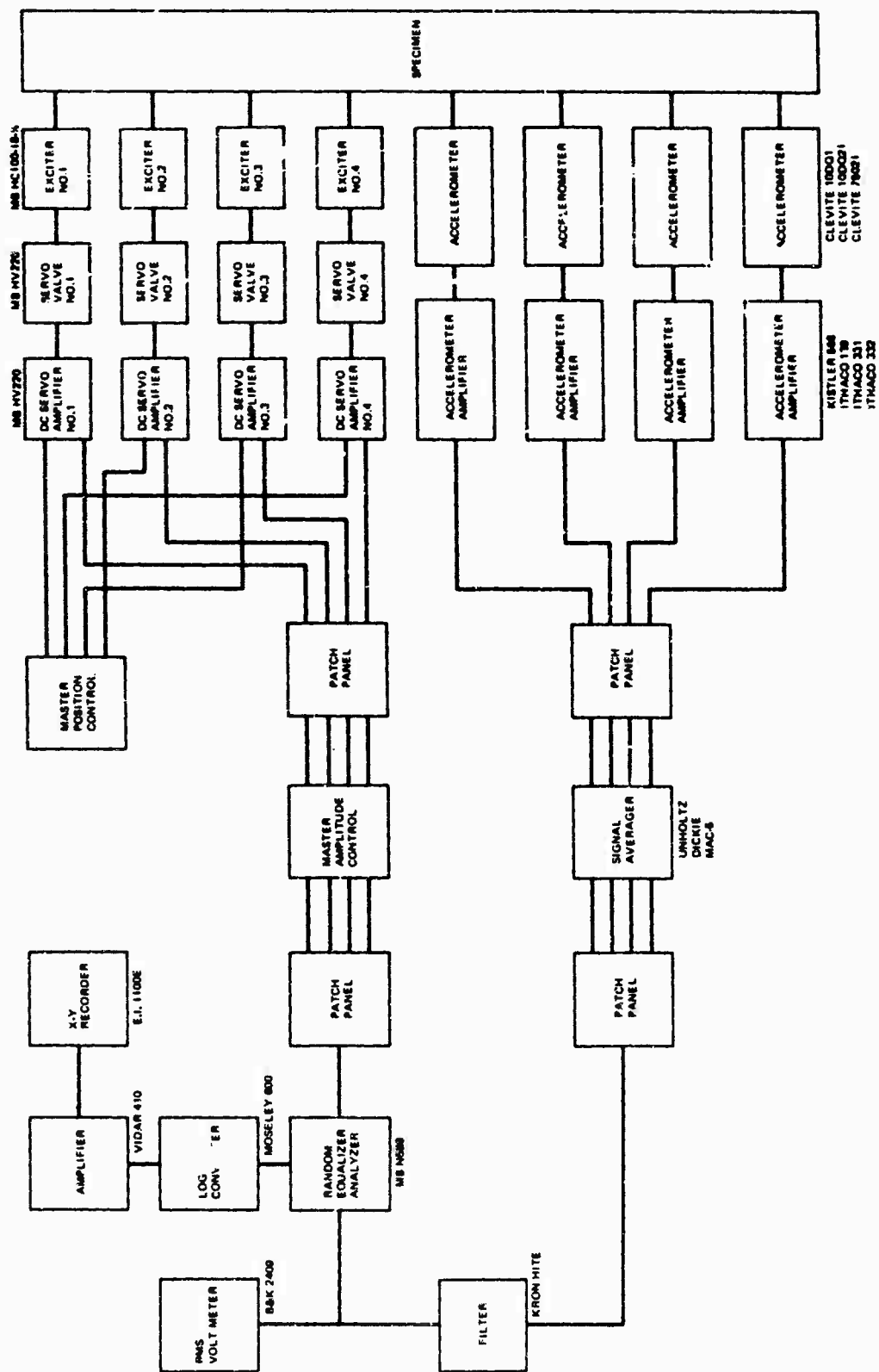


Fig. 10. Random control system

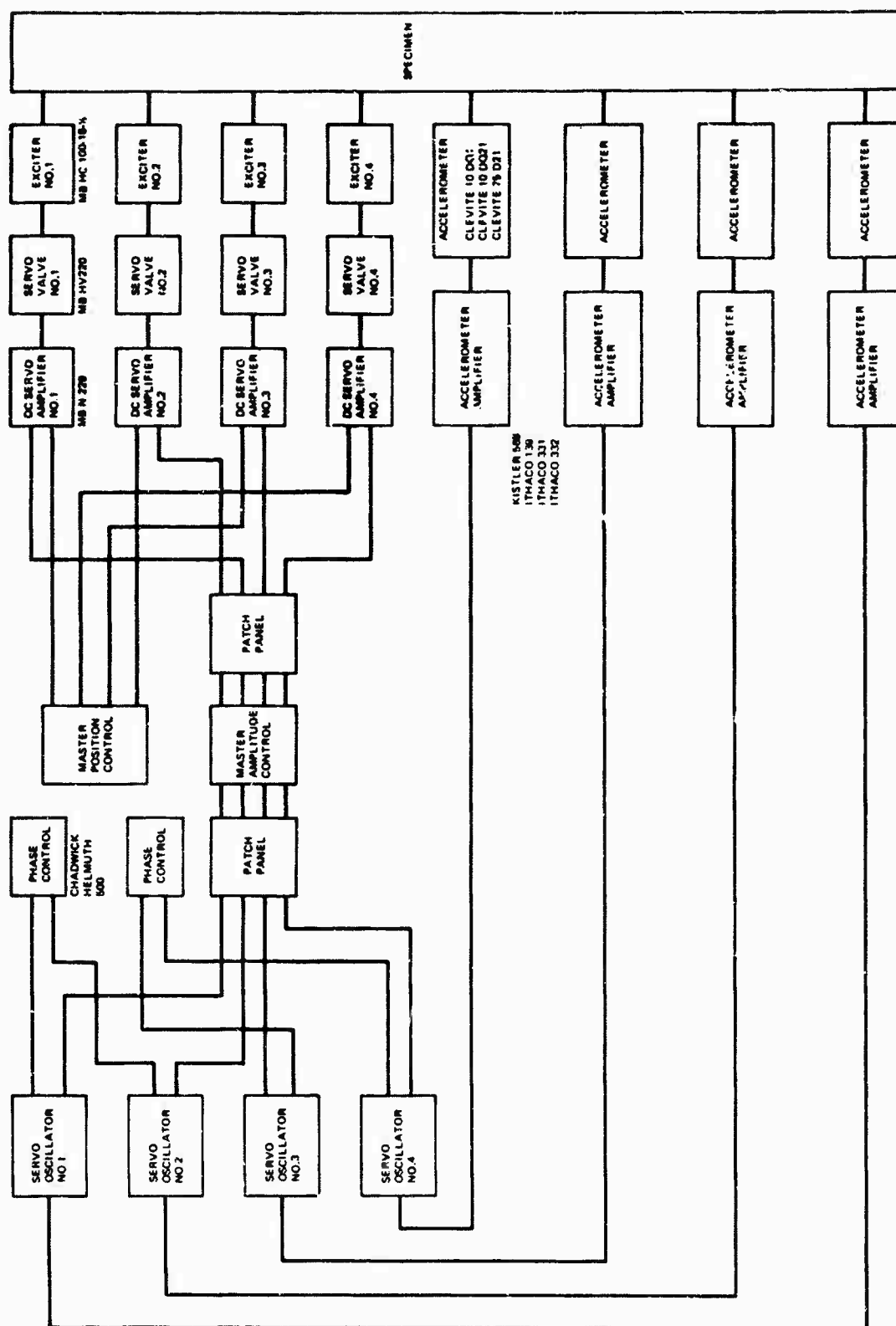


Fig. 11. Sinusoidal control system

To simplify channel identification, a separate document - which was a channel-by-channel cross reference of Douglas instrumentation drawing location and function designations, Thiokol location numbers, and Thiokol tape matrix locations - was prepared for each test setup.

The tape matrix refers to the system used to designate a single tape data channel by tape track and carrier frequency. The tapes contained 12 data tracks, each of which was frequency multiplexed into 12 constant-bandwidth channels associated with 16-kHz separated carriers between 32- and 208-kHz center frequency. The same predetermined data channel was recorded on the 32-kHz carrier of all tracks to facilitate reduction of transmissibility data. For a single sinusoidal test, transmissibility data consisted largely of plots referenced to the common data channel. Any channel on any track could, however, be referenced to any other channel on any other track. Data reduction output was  $g$ 's vs frequency, amplitude and phase transmissibility for sinusoidal tests, and power spectral density for random tests. Figures 12, 13, and 14 show the data reduction system block diagrams.

#### TEST RESULTS

The particular structures tested proved to have no basic low-frequency problems. The low-frequency response characteristics were of significance in attaining a better understanding of equipment dynamic behavior. Many equipment items are mounted to produce mounting-equipment spring-mass frequencies of 35 to 60 Hz. Qualification testing of these items verified the design mounting frequencies in most cases. At these frequencies, large-amplitude equipment

responses occurred while the specified structural input amplitude was maintained. During the high-force tests, these frequencies were generally characterized by a lowering of input, resulting in a much lower response than seen during qualification testing.

The latter type of dynamic behavior is characteristic of shell structure mounted equipment excited by either a force field uniformly distributed by a rigid fixture as in a high-force test, or an acoustic field as in space flight boost. In either case, high local forces, as required to sustain large-amplitude responses of the equipment masses, are not available. The possibility of exciting modes involving large amplitudes of both the local structure and equipment masses does, however, exist. Since such modes involve large accelerations of both structure and equipment, they are not characterized by high-amplification factors. The actual amplification factors associated with relatively high test responses were limited to a magnitude of 2.

#### ACKNOWLEDGMENTS

The contributions of the many members of the engineering department of Douglas Aircraft Missile and Space Systems Division to the successful accomplishment of the program are gratefully acknowledged.

#### REFERENCE

1. L. G. Smith, "Design of Large Vibration Fixtures for Saturn S-IV Stage Design Development and Qualification Program," Shock and Vibration Bull. No. 34, Part 5, p. 243, Feb. 1965

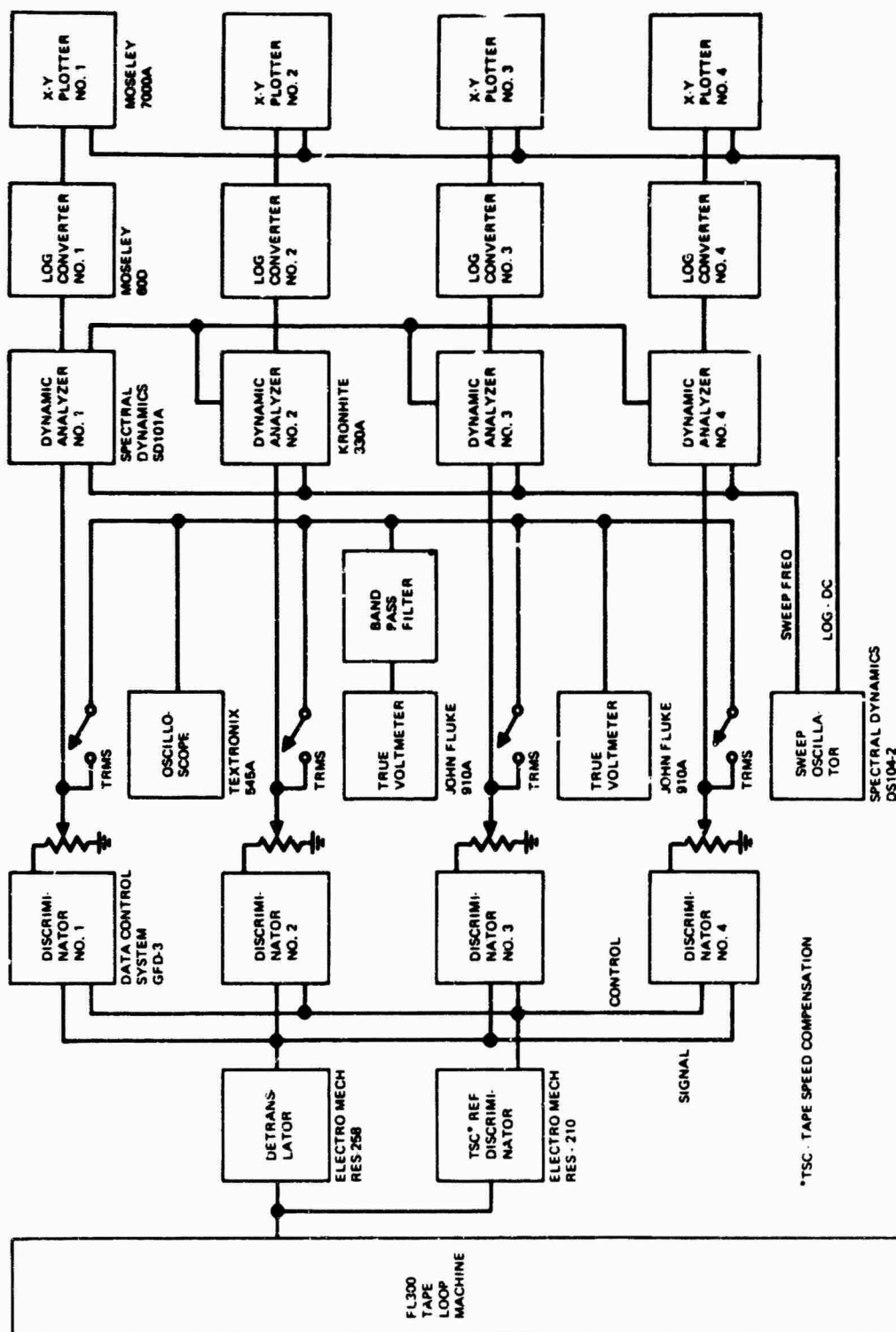


Fig. 12. Power spectral density reduction system

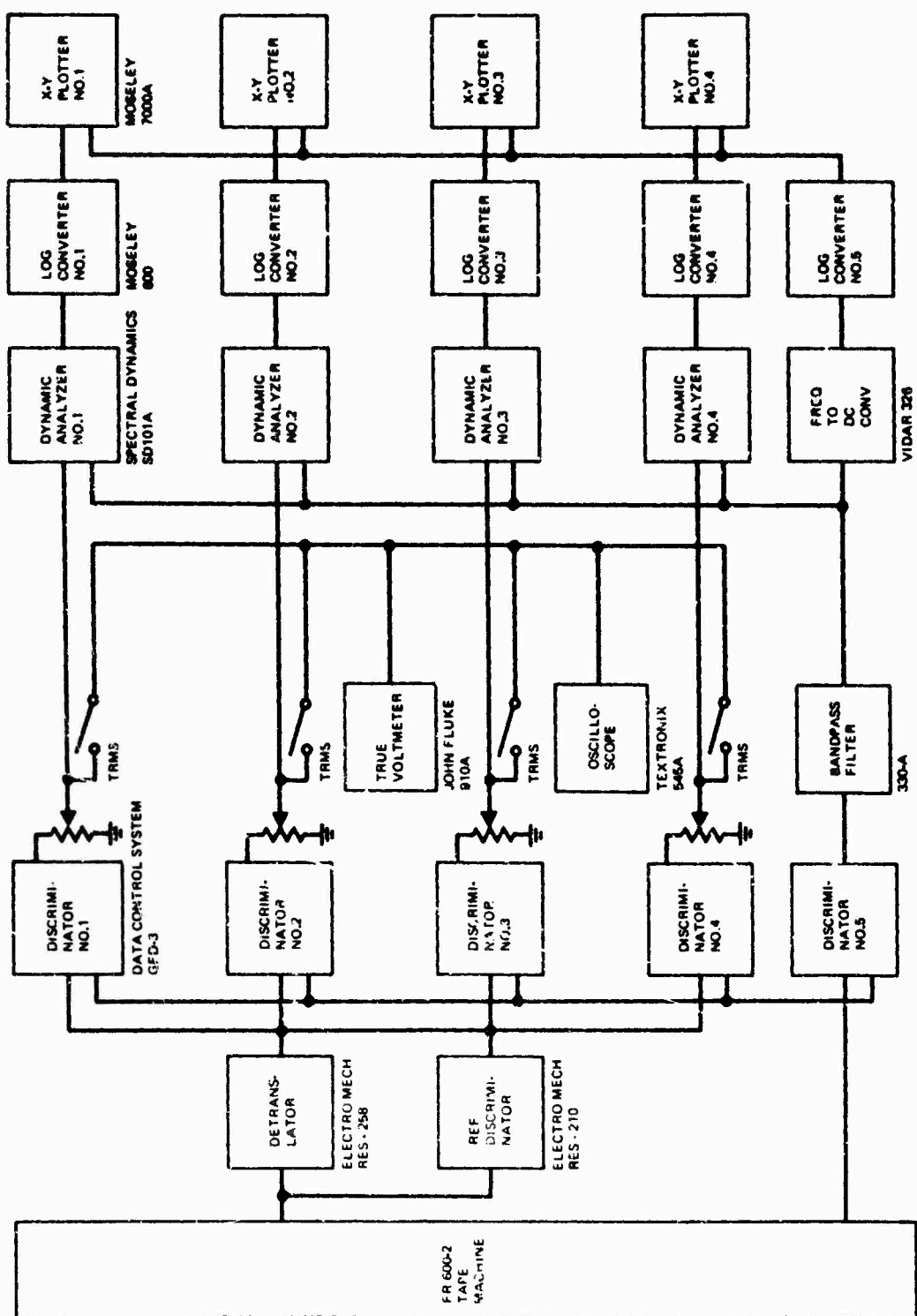


Fig. 13. Amplitude vs frequency reduction system



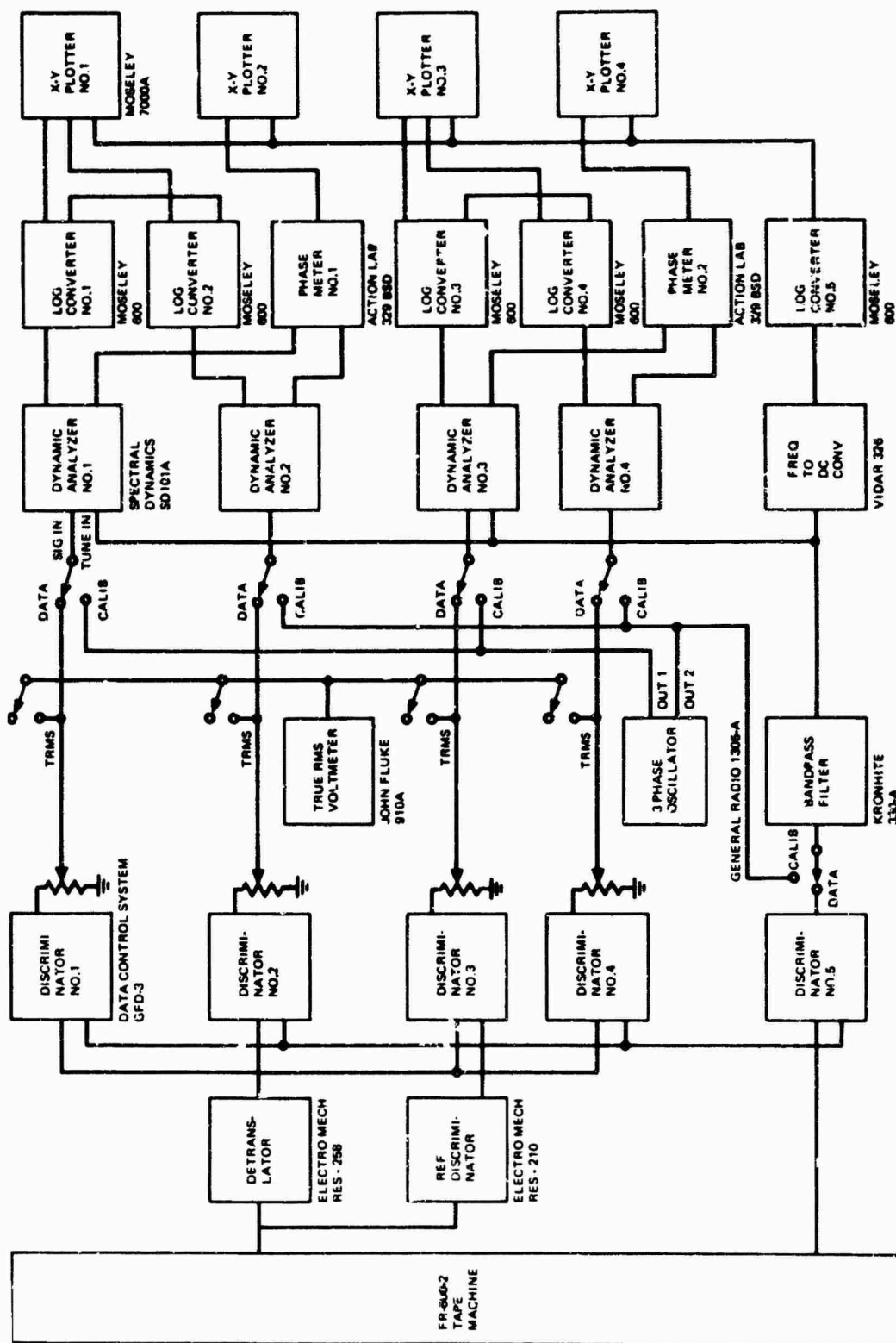


Fig. 14. Transmissibility reduction system

\* \* \*

## **SIMPLIFIED METHOD OF CONDUCTING A DUAL RANDOM-VIBRATION INTEGRATED SYSTEM TEST**

James G. Colt  
Radio Corporation of America  
Burlington, Massachusetts

Frequently a subsystem is not vibration tested as a complete subsystem because it is composed of assemblies that are mounted, for example, at various locations on a vehicle, making it necessary to generate different vibration inputs to test these subsystem components.

A simple subsystem of interest is a radar system in which an antenna assembly is mounted externally on the vehicle and an electronics assembly is mounted inside. Ordinarily an assembly of this nature is vibration tested at the assembly level and integrated for electrical performance test only after the dynamic tests.

A more realistic vibration test method is to conduct an integrated random-vibration/electrical-performance test. One way is to conduct, simultaneously, a random-vibration test on the antenna assembly to its expected random spectrum and a random-vibration test on the electronics assembly to its expected random spectrum.

This test can be accomplished easily with two vibration exciters and two random-vibration consoles. However, the problem is that many laboratories may have more than one vibration exciter but usually only one random-vibration console. The RCA Aerospace Systems Division ran the test successfully using two vibration exciters, one random console, and one magnetic tape recorder, with a prerecorded spectrum signal on tape replacing the second random console.

### **INTRODUCTION**

There are three basic assemblies in a rendezvous radar system: an antenna assembly, a rendezvous radar electronic assembly, and a transponder electronic assembly. Selected environmental tests were conducted individually on each assembly, with specific inputs applied according to the required assembly specification. During the environmental testing, each assembly was electrically and/or mechanically operated while undergoing the environmental exposure. Operationally, only during the electrical baseline tests are the three assemblies integrated and operated as one complete system. After the initial electrical baseline test is completed successfully, separation of the system takes place with each assembly thereafter environmentally tested with its respective check-out test unit. This procedure is followed throughout the entire qualification environmental test program until a final-system electrical performance test is completed.

Following the qualification test program, an electrical performance demonstration of the

integrated rendezvous radar antenna assembly and the rendezvous radar electronics assembly under simulated vibration conditions was required. Therefore, to demonstrate the performance of the rendezvous radar antenna and electronics assemblies during vibration, the assemblies were integrated electrically. Mechanically, the electronics and the antenna were mounted on separate shake tables. With only one random control console available, the problem was to vibrate both assemblies simultaneously utilizing separate shaped random inputs. A description of the facilities and procedure used to solve this problem is given below.

### **TEST FACILITY**

The dual vibration testing of the electronics and antenna was performed at the RCA Aerospace Systems Division plant, Environmental Laboratory, Burlington, Massachusetts. Two separate vibration systems were used: one to vibrate the antenna assembly at one random spectrum and the other to vibrate the electronics assembly at another random spectrum. Random

vibration of the antenna was accomplished using an MB C126 vibration exciter, MB T389 equalizer system, MB T130MC sine/random control console, and an MB 4200 power amplifier. This system is rated at 9000 lb peak sine force and 6500 lb rms force. It is completely automatic, incorporating 80 contiguous filters for equalization in random-vibration testing. Random vibration on the radar electronics was performed using the smaller vibration system comprising a Calidyne A174 vibration exciter, a CEC-type VR2800 tape recorder, and a Westinghouse FG-11 power amplifier. This system is rated at 1500 lb peak sine force and 1050 lb rms force.

The method employed to obtain a second random signal source (tape recorder) to drive a shaker system lacking an equalization system is explained best by briefly describing the function and characteristics of the equalization system and the recording instrumentation. Automatic equalization is accomplished utilizing a multiband random equalizer where the frequency spectrum is divided into 80 narrow bands of 12.5, 25, and 50 Hz. Attenuators are provided in each band, and the outputs of all bands are summed up.

Many contiguous narrow-bandpass filters are incorporated into this system where control of each increment of the spectrum is available. The controlled shaped spectrum is then amplified and introduced to the input of the power amplifier. This input to the power amplifier is recorded on tape (see Fig. 1); the tape recorder is later used as the second random signal source. Prior to the tape recording process, a check of the desired spectrum shape was made through the use of the parallel filter analyzer also incorporated into the equalizer system. This analyzer employs a series of parallel filters. Each filter samples a portion of the spectrum and the dc output of each filter is commutated and plotted on an x-y recorder. A graphical presentation of the required spectrum then becomes readily available prior to the recording process.

#### PRERECORDING THE SPECTRUM INPUT ON MAGNETIC TAPE

One of the most important factors for pre-recording the proper spectrum input on magnetic tape was use of the best representative mechanical model of the electronics assembly. Fortunately, a similar model of the radar electronics in this checkout procedure could be used to obtain the required shape of the input spectrum later to be applied to the actual test

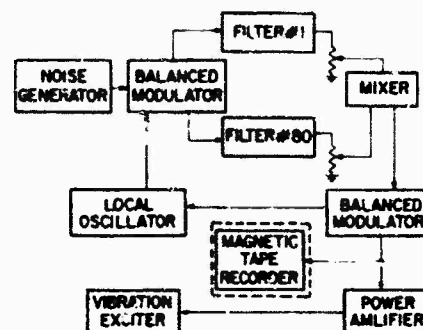


Fig. 1. Block diagram of equalization and recording system

item (electronic assembly) of the dual integrated test. The electronics and vibration fixture combination mounted in the most sensitive axis were secured to the small shaker armature with a driver, as shown in Fig. 2. Accelerometers were mounted at preselected points to control and monitor the input spectrum. Signal conditioning equipment in the form of charge amplifiers was used to obtain high signal levels and to obtain the optimum in signal-to-noise ratio. Voltage outputs from the charge amplifiers and the multiband equalizer were fed to a multichannel CEC-type VR2800 tape recorder. A specified random-vibration input spectrum (Fig. 3) was applied to the electronics mounting flange using the random console.

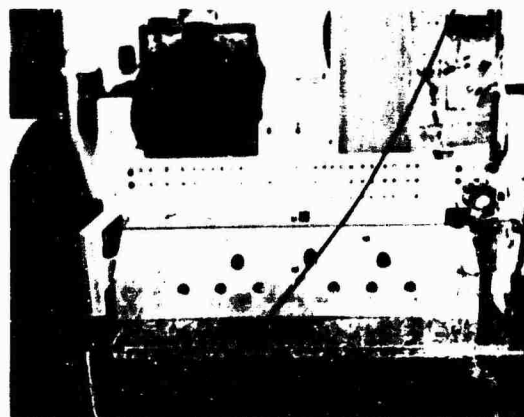


Fig. 2. Electronics vibration test arrangement

A playback of the input spectrum via the control accelerometer and charge amplifier through the console analyzer verified the input

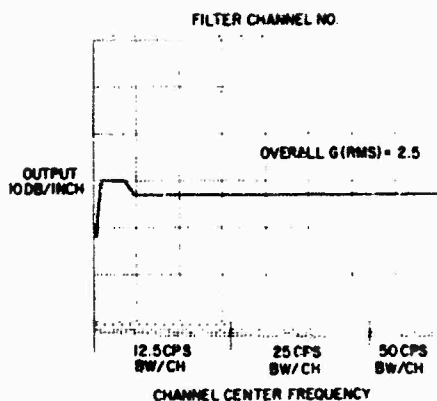


Fig. 3. Electronics random-vibration input spectrum

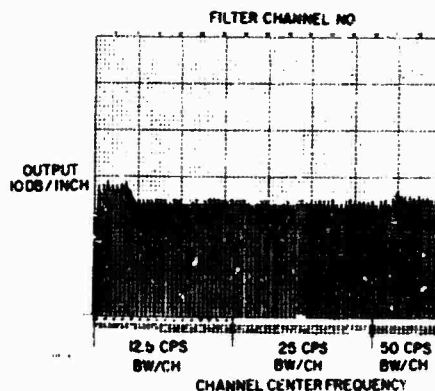


Fig. 5. Shaped spectrum utilizing tape recorder to drive shaker

spectrum shape, as shown in Fig. 4. The input to power amplifier (compensated by the equalizer) was recorded on tape. The tape recorder was then used as the second random driving source. A playback of the control accelerometer through the console analyzer verified the input spectrum shape obtained previously with the random console (Fig. 5). About 20 min of this recording was made for later testing. The tape recorder, in this case, replaced an entire equalization system. It provided the second driving source and a means to go ahead with vibration testing the electrically integrated assemblies simultaneously.

#### VIBRATION TESTING THE INTEGRATED SYSTEM

Testing the integrated system progressed with minimum problems once the second ran-

dom driving source was obtained on magnetic tape. The antenna and the electronics were electrically and mechanically set up, as shown in Fig. 6. The antenna was attached to the larger shaker in its most sensitive vibration direction, as shown in Fig. 7. All assemblies were electrically operated, and dur? random-vibration testing was conducted on the antenna electronic assemblies. Functionally, the integrated system worked well during the random-vibration exposure.

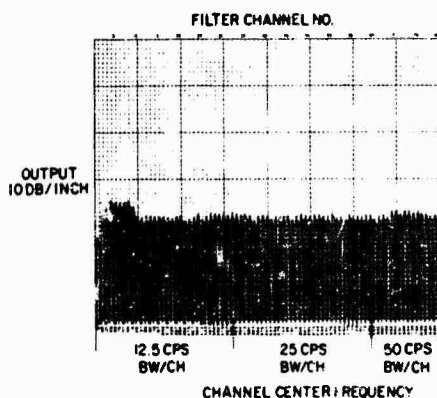


Fig. 4. Shaped spectrum utilizing vibration console to drive shaker

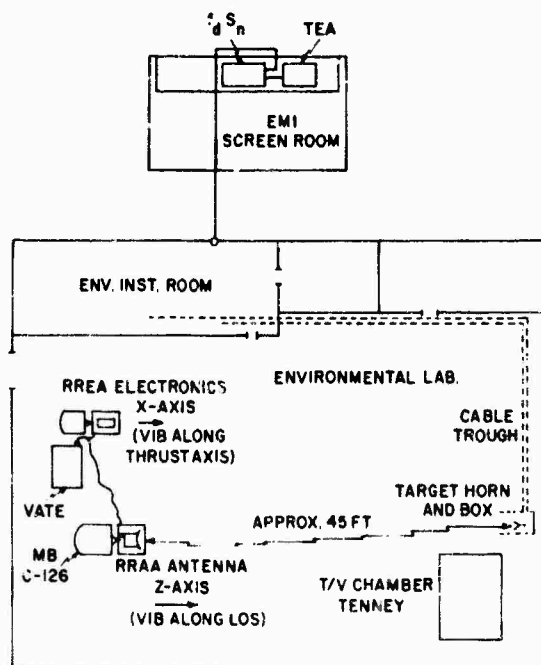


Fig. 6. Integrated mechanical and electrical test arrangement.

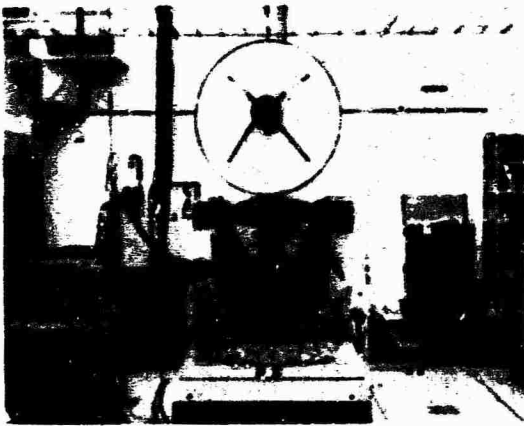


Fig. 7. Antenna vibration test arrangement

## CONCLUSION

Tape recordings of vibration levels induced by missile firings and the like are nothing new in the vibration field. What has been described above is one method that can be employed by the numerous environmental test laboratories in the country. In recent years, automatic equalization became the optimum method for vibration testing as compared to the time-consuming, peak-notch sine method of equalization. Once the automatic equalization is programmed and a very representative mechanical test specimen is used, it is necessary only to tape the voltage output from the automatic equalizer, thereby utilizing the tape as a control console.

# CONTROL STABILIZATION FOR MULTIPLE SHAKER TESTS\*

Norman F. Hunter, Jr.  
Sandia Corporation  
Albuquerque, New Mexico

and

James G. Helmuth  
Chadwick-Helmuth Company, Inc.  
Monrovia, California

Large test specimens often require multiple shaker excitation for realistic simulation of field vibration levels. At some frequencies, energy crossfeed between shakers causes control problems. Until recently no methods existed for controlling multiple shaker tests at frequencies where the specimen exhibited cross-coupling factors (CCF) in excess of about unity. A method for controlling any number of shakers with CCF  $> 1$  is described.

## INTRODUCTION

When more than one vibration exciter applies energy to a test specimen and it is desired to control this vibration input at each point of application (to conform with the expected final environment or a standard test procedure), a major difficulty will usually be encountered: at one or more frequencies the specimen will tend to vibrate in its natural mode shape in contradiction to the desired test levels and phase. Trouble will occur whenever the coupled vibration from one driven point to another exceeds the level desired at the second point, because "cause" and "effect" are no longer separate and contained within each shaker-servocontrol loop.

Consider the case of two exciters. When the cross-coupling factor (CCF) exceeds unity, switching the feedback vibration pickups (pickup "A" controls shaker B; "B" controls A) restores cause and effect and the system controls [1]. For more than two shakers, it is conceivable that causes and effects could be located and the pickups appropriately switched, but the practical difficulties become enormous. The approach taken here is to reduce effectively all CCF to less than unity.

## EQUATIONS FOR CROSS-COUPLING

A block diagram of a two-channel system with cross-coupling appears in Fig. 1. Here  $V_1$  and  $V_2$  are the responses at drive points 1 and 2, respectively. Cross-coupling occurs through the terms  $a_{12}$  and  $a_{21}$ . Note that the notation is: first subscript refers to effect, second subscript refers to cause. The steady-state equations

$$V_1 = a_{11}C_1 + a_{12}V_2 \quad (1a)$$

and

$$V_2 = a_{22}C_2 + a_{21}V_1 \quad (1b)$$

describe the system. Cross-coupling factor may be defined as:

$$\frac{\text{Response at point 2}}{\text{Response at point 1}} \bigg|_{\text{drive 2 shutdown}}$$

or

$$CCF_{21} = \frac{V_2}{V_1} \bigg|_{C_2=0} \quad (2)$$

Substituting Eq. (2) into Eq. (1b), it is apparent that  $CCF_{21} = a_{21}$ . Many cases of cross-coupling may occur, and the vector diagrams of Figs. 2 and 3 illustrate typical situations. Solving Eqs. (1a) and (1b) for  $V_1$  and  $V_2$  yields

\*This work was supported by the United States Atomic Energy Commission.

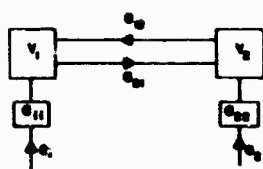


Fig. 1. Two-channel system with cross-coupling

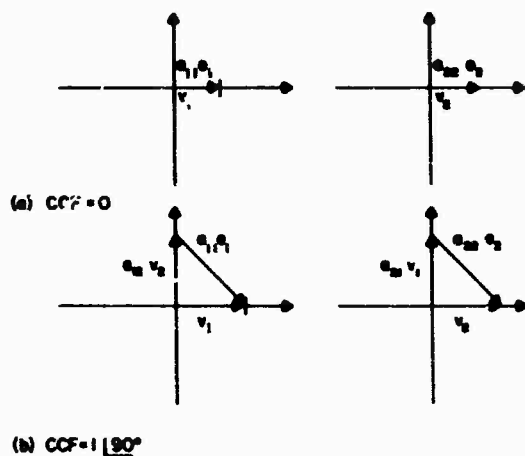


Fig. 2. Typical cross-coupling situations

$$V_1 = \frac{a_{11}e_1 + a_{12}a_{22}e_2}{1 - a_{12}a_{21}}$$

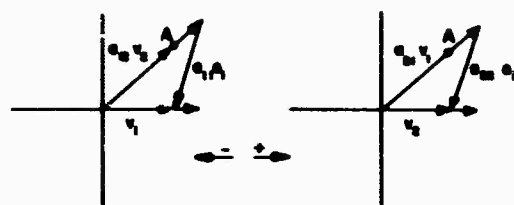
and

$$V_2 = \frac{a_{22}e_2 + a_{21}a_{11}e_1}{1 - a_{12}a_{21}}$$

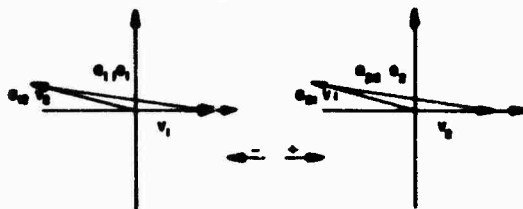
The dependence of  $V_1$  on both  $e_1$  and  $e_2$  illustrates the cross-coupling problem.

### SFRVO CONTROL PROBLEM

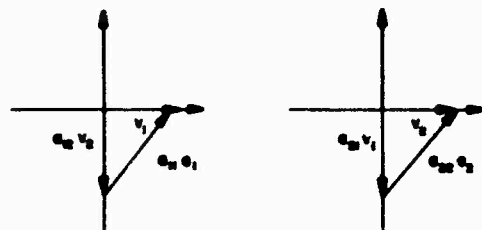
Three situations may create servo instabilities. The logic of the servo control at each shaker demands "sense" for amplitude and phase of produced vibration. Thus, an increase in  $e$  must result in an increase in  $V$ ; an increase in phase angle of  $e$  must result in an increase in phase angle of  $V$ . Consider the situation in Fig. 3a. If the cross-coupling vector  $a_{12}V_2$  is shorter than the indicated vector  $A$ , an increase in  $e_1$  will result in an increase in  $V_1$ . For  $a_{12}$  longer than  $A$ , however,  $a_{11}e_1$  points in the opposite direction to



(a) SELF VECTOR  $a_{11}e_1$  REVERSED IN DIRECTION



(b) SELF VECTOR MAGNITUDE INCREASED



(c) SELF VECTOR AT 90° TO DESIRED VIBRATION

Fig. 3. Unstable cross-coupling situation

$V_1$ , and an increase in  $e_1$  results in a decrease in  $V_1$ . This is an example of magnitude sense reversal.

As we enter the region of cross-coupling, the vector  $a_{11}e_1$  may become longer but retain the correct direction, as in Fig. 3b. Correct sense is retained, but a slight angular change in  $e_1$  results in a large change in the angle of  $V_1$ . The phase-servo-loop gain has been increased effectively, and the system, if previously optimized in gain for normal conditions, will now become unstable.

A third case occurs when the cross-coupling factor tends to be at 90 deg to the desired vibration (Fig. 3c). The difficulty now is that the effect of the amplitude and phase servos has been reversed. A change in phase angle of  $e$  will result in a change in amplitude of  $V_1$ , whereas a change in magnitude of  $A$  results in a change in angle of  $V$ . Control is again lost.

The net effect of these instabilities limits control to the region where the absolute value

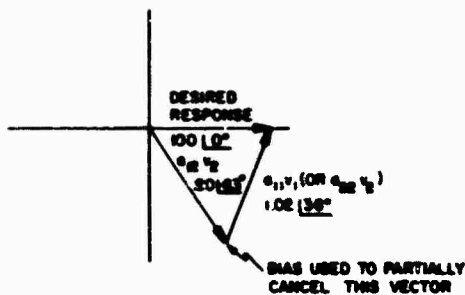


Fig. 4. Vector diagram for system control loss

of the cross-coupling vector is less than unity (Fig. 4).

### CROSS-COUPLING REMOVAL

If the electrical drive signal  $e$  at each shaker is crossed via transfer function  $k$  to every other shaker, the following equations result (for a two-channel system (Fig. 5)):

$$V_1 = e'_1 a_{11} + a_{12} V_2 \quad (3a)$$

and

$$V_2 = e'_2 a_{22} + a_{21} V_1 \quad (3b)$$

where

$$e'_1 = e_1 + k_{12} e_2 \quad (4a)$$

and

$$e'_2 = e_2 + k_{21} e_1 \quad (4b)$$

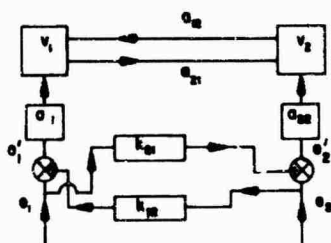


Fig. 5. Two-channel system with drive crossfeed

Substituting Eqs. (4a) and (4b) into Eqs. (3a) and (3b) and solving for  $V_1$  and  $V_2$  gives:

$$V_1 = \frac{e_1(a_{11} + a_{12}a_{22}k_{21}) + e_2(a_{12}a_{22} + a_{11}k_{12})}{1 - a_{12}a_{21}}$$

and

$$V_2 = \frac{e_1(a_{11}a_{21} + a_{22}k_{21}) + e_2(a_{22} + a_{11}a_{21}k_{12})}{1 - a_{12}a_{21}}$$

Now let

$$k_{12} = \frac{-a_{22}a_{12}}{a_{11}}$$

and

$$k_{21} = \frac{-a_{11}a_{22}}{a_{22}}$$

Then

$$V_1 = e_1 a_{11}$$

and

$$V_2 = e_2 a_{22}$$

From the standpoint of  $e'_1$  and  $e'_2$ , the cross-coupling has not changed, but for a linear system ( $a$  not affected by  $V$ ),  $e_1$  alone determines  $V_1$ , and  $e_2$  alone determines  $V_2$ ; the necessary cause-and-effect relationship has been re-stored. This method is expandable to an  $N$  channel system:

$$V_1 = e'_1 a_{11} + a_{12} V_2 + a_{13} V_3 + \dots + a_{1N} V_N$$

$$V_2 = a_{21} V_1 + e'_2 a_{22} + a_{23} V_3 + \dots + a_{2N} V_N \quad (5)$$

$$\vdots$$

$$V_N = a_{N1} V_1 + a_{N2} V_2 + \dots + a_{NN} e'_N$$

and

$$e'_1 = e_1 + k_{12} e_2 + k_{13} e_3 + \dots + k_{1N} e_N$$

$$e'_2 = k_{21} e_1 + e_2 + k_{23} e_3 + \dots + k_{2N} e_N \quad (6)$$

$$\vdots$$

$$e'_N = k_{N1} e_1 + k_{N2} e_2 + k_{N3} e_3 + \dots + e_N$$

To remove the cross-coupling vectors, write

$$k_{NM} = \frac{-a_{NM}}{a_{NN}} a_{NM} \quad (7)$$

Then,

$$V_1 = e_1 a_{11}$$

$$V_2 = e_2 a_{22} \quad (8)$$

$$\vdots$$

$$V_N = e_N a_{NN}$$



## PRACTICAL CONSIDERATIONS

In practice, it would be very difficult to generate electrical transfer functions  $k_{NM}$  that satisfy Eq. (7), especially if sweep operation is desired. However, the following factors relieve this situation:

1. Cross-coupling must be reduced to less than unity, but does not have to be totally eliminated; thus:

$$k_{NM} \approx - \frac{a_{NM}}{a_{NN}} a_{NM} \quad (9)$$

2. For some tests, the self-terms ( $a_{MM}$  and  $a_{NN}$ ) tend to be equal (similar exciters, symmetrical loads):

$$\frac{a_{MM}}{a_{NN}} \approx 1 \quad (10)$$

and therefore

$$k_{NM} \approx a_{NM} \quad (11)$$

3. For other tests in which the load is resonant but not symmetrical, as  $a_{NM}$  increases (e.g., node at M, antinode at N) and  $a_{MM}$  decreases,  $a_{NN}$  increases. Then, in Eq. (9),  $k_{NM}$  does not increase as fast as  $a_{NM}$ , thus:

$$|k_{NM}| < |a_{NM}| \quad (12)$$

4. Usually the most difficult control situations are high Q resonances when the structure seeks to vibrate in a "normal mode" state. At these frequencies, the cross-coupling terms tend to be either in phase or 180 deg out of phase. Then under condition 2,  $k$  is required to be simply a real transfer function and is much more easily generated than a complex function.

The determination of  $k$  can be simply done by a preliminary low-level test. At "trouble"

frequencies, each shaker is individually driven (with servo level control operating), and responses at all other points are reduced to less than unity by "knob twirling" the involved  $k$ 's. These settings are retained and, with a master gain control, used later when test frequency sweeps through the trouble regions.

## RESULTS OF ANALOG STUDY

Using the electrical "mobility" analog of a mechanical system, most multiple-shaker control problems may be simulated. Both beam and spring-mass analogs have been run. The analog circuit of Fig. 6 is particularly interesting where two shakers drive a 5-mass, 10-spring system. This system is reciprocal, i.e.,  $a_{12} = a_{21}$ , though not symmetrical ( $a_{11} \neq a_{22}$ ). The transfer functions  $a_{12}$ ,  $a_{11}$ , and  $a_{22}$  are shown in Figs. 7, 8, and 9. These polar plots show magnitude and phase of a vector quantity vs frequency. As would be expected, control is lost between 150 and 215 cps and between 853 and 887 cps, since these limits correspond approximately to those areas outside the unit circle in Fig. 7.

The system used for analog control is a two-channel Chadwick-Helmuth "A" system using B & K oscillator servos. When entering a region of instability during a frequency sweep, the phase and amplitude servos will begin to hunt. This hunting effect increases until control loss is complete. Usually one amplitude servo will shut off while the other remains active, although the case of both servos going to full drive may also be observed.

To stabilize control, the bias system of Fig. 5 is used. The functions  $k_{12}$  and  $k_{21}$  are adjusted to reduce the magnitude of  $a_{12}V_2$  and  $a_{21}V_1$  according to Eq. (7), and the control stabilizes. A master gain control sets the magnitude of  $k_{12}$  and  $k_{21}$  through each region of interaction. For this system only one bias is needed for each major region outside the unit circle, so a test with stable control from 20 to 2000 cps may be run simply.

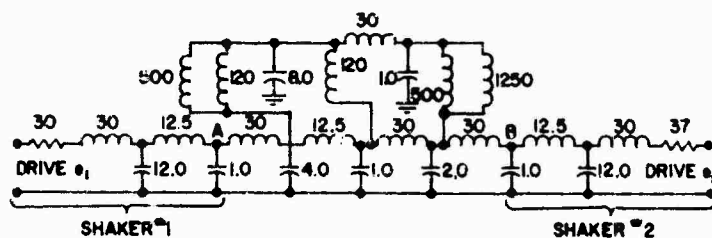


Fig. 6. Analog circuit for multiple-shaker control system

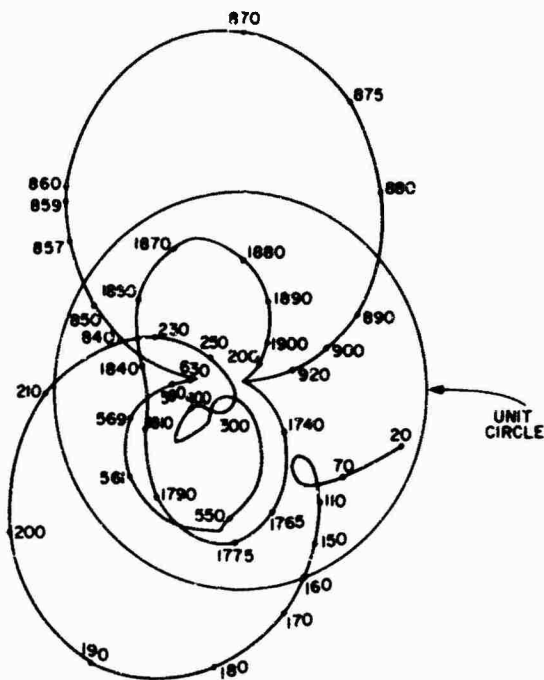


Fig. 7.  $a_{12}$  vs frequency for analog circuit ( $a_{12} = a_{21}$ )

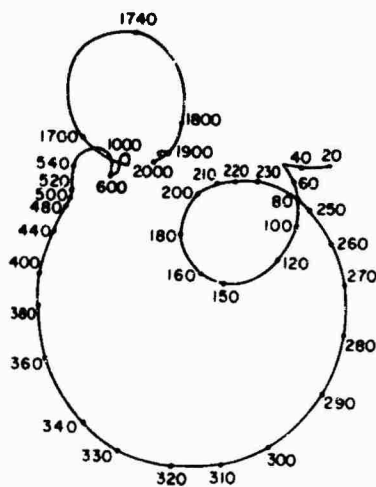


Fig. 8.  $a_{11}$  vs frequency for analog circuit

From the spring-mass system results, and from a similar study including an electrical beam analog, certain observations regarding the application of bias may be made:

1. The easiest way to adjust bias is to run one driver at a time and cancel the interaction.

2. If bias must be adjusted during a run, the sweep should be slowed and a hit-or-miss method of adjusting bias tried.

3. Approaches (1) and (2) could probably be automated, but for more than a two-channel system, the second approach appears quite impractical.

4. Generally the CCF must be less than unity for stable control without bias, as indicated in Fig. 10.

5. For a nonbilateral system ( $a_{12} \neq a_{21}$ ), a CCF as great as 2 without bias may sometimes be tolerated.

## TEST RESULTS

To verify the mathematical and analog system results, a test was run at MTS Systems Corporation on a 700-lb beam using two hydraulic shakers. To assure a large cross-coupling factor, the pickups were mounted away from the shaker heads, as shown in Figs. 11 and 12. Total system weight was 1255 lb. Shakers 1

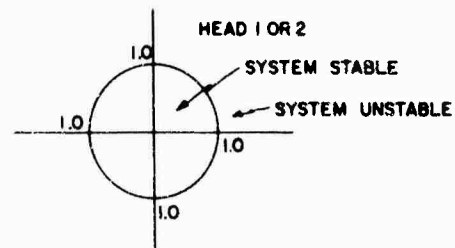


Fig. 10. Stable control region

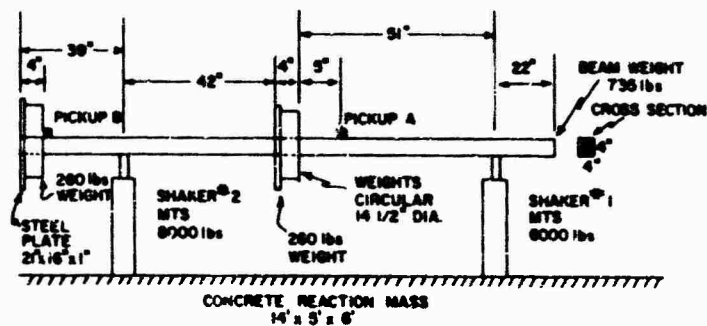


Fig. 11. Test setup for multiple control

and 2 were rated at 8000 and 6000 lb, respectively, and drive points are indicated in Fig. 11. Separate servo controls actuate each shaker; the servo controls are driven by a Chadwick-Helmuth amplitude and phase control system using Spectral Dynamics oscillators and amplitude servos (Fig. 12). The cross-coupling compensator system crossfeeds the drive voltages as indicated earlier. A front panel view of these controls (Fig. 13) shows that bias may be added to each channel individually and all

bias signals brought up together with a master gain control.

Each shaker was driven individually using displacement control, and the transfer function  $a_{12}$  and  $a_{21}$  of Table 1 was recorded. Unlike the analog tested, this system is not reciprocal ( $a_{12} \neq a_{21}$ ). Very large cross-coupling factors (80 at 16.3 cps) occur at the beam first mode.

Using the cross-coupling compensator (Fig. 13), bias was added to the undriven head

TABLE 1  
Interpickup Transfer Functions

| Frequency<br>(cps) | Pickup A<br>Displacement<br>(in.) <sup>a</sup> | Pickup B<br>Displacement<br>(in.) <sup>b</sup> | CCF <sup>c</sup> |
|--------------------|--|--|------------------|
| Driving Head 1     |  |  |                  |
| 5.0                | 0.05   | 0.05 at 180°                                   | 1.00 at 180°     |
| 10.5               | 0.05   | 0.10 at 180°                                   | 2.00 at 180°     |
| 14.5               | 0.05   | 0.20 at 180°                                   | 4.00 at 180°     |
| 15.5               | 0.05   | 0.40 at 180°                                   | 8.00 at 180°     |
| 15.9               | 0.05   | 0.80 at 180°                                   | 16.00 at 180°    |
| 16.3               | 0.05   | 4.00 at 90°                                    | 80.00 at 180°    |
| 16.5               | 0.05   | 1.20 at 30°                                    | 24.00 at 180°    |
| 17.2               | 0.05   | 0.35 at 10°                                    | 7.00 at 10°      |
| 19.8               | 0.05   | 0.095 at 0°                                    | 1.90 at 0°       |
| 32.5               | 0.05   | 0.15 at 0°                                     | 0.30 at 0°       |
| Driving Head 2     |  |  |                  |
| 5.0                | 0.015  | 0.05   | 0.30 at 0°       |
| 12.2               | 0.005  | 0.05   | 0.10 at 90°      |
| 14.0               | 0.010  | 0.05   | 0.20 at 160°     |
| 16.5               | 0.050  | 0.05   | 1.00 at 150°     |
| 19.2               | 0.080  | 0.05   | 1.60 at 90°      |
| 29.2               | 0.120  | 0.05   | 2.40 at 30°      |
| 38.0               | 0.100  | 0.05   | 2.00 at 0°       |

<sup>a</sup>At 0-deg angle for driving head 1.

<sup>b</sup>At 0-deg angle for driving head 2.

<sup>c</sup> $a_{21}$  for driving head 1;  $a_{12}$  for driving head 2.

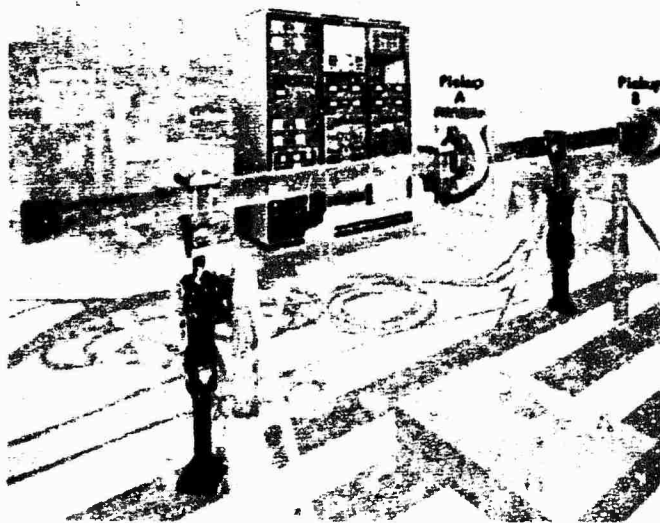


Fig. 12. Beam and multiple-shaker control system

until the CCF was reduced to less than unity. This bias addition was not as difficult as expected, and in fact addition at 0 deg and 180 deg sufficed at most frequencies. Absolute value of the biases,  $K$ , did not exceed 5, even when the  $CCF \approx 80$ , due to item (3) in Practical Considerations. One set of bias values was found which would allow control from 5 cps to above 20 cps, and a second set for control in the neighborhood of 30 cps.

After several test runs, the mechanical impedance of shaker A increased. This effectively

changed system restraints, resulting in a change in normal mode frequencies and shape. The preliminary run was redone, and again control could be achieved through the first mode with the addition of one bias set.

#### CONCLUSIONS

This method of cross-coupling compensation works well with the two-channel system tested. The required adjustments were easily made, and this procedure should be useful for



Fig. 13. Cross-coupling compensator

any general multiple exciter test where a preliminary run can be included in the program.

Expansion to any number of channels is now possible, but operational complexity will tend to increase as  $n(n-1)$ . Therefore, hardware is now being developed to determine, store, and then provide the electrical bias signals during a test more easily (automatically).

#### DISCUSSION

Mr. Angelopoulos (Lockheed Missile and Space Co.): Would you say that in the near future your system would be adaptable to multi-shaker control for random excitation, possibly by using any number of ASDE 80's and a random averager?

Mr. Helmuth: In its present form the system would not. It is only for sine wave testing. The servo controls for amplitude and for phase and the whole concept is based on sinusoidal motion, so we are not working in that direction, I am sorry to say.

Mr. Griffith (Bendix Corp.): In most of the tests where we supposedly have sinusoidal motion there are some other higher frequencies imposed on the sinusoid. It makes a very hashy

#### REFERENCE

1. J. G. Helmuth, "Control of Multiple Shakers," IES Proc., p. 493, 1965

#### BIBLIOGRAPHY

1. C. M. Harris and C. E. Crede, Shock and Vibration Handbook, Vol. 1, Chap. 10, McGraw-Hill, New York, 1961

record anyway. How do you propose to take care of all this high frequency noise? Does it affect you?

Mr. Helmuth: No, it does not because we detect the amplitude of vibration and the phase of vibration using an analog multiplier technique which is sort of like a crosscorrelator. We plug a pure sine wave into one input and then the signal to be measured into the other input, and only that part of it which is at shake frequency produces the error signal, you might say. It is essentially a tracking filter, but it does not have the time delays that a tracking filter would have. I emphasize that simply because this is a servo control system, and we have to watch it on time delays for stability reasons.

\* \* \*

## THE SHIM SPRING ISOLATOR

Leon Wallerstein, Jr.  
Lord Manufacturing Company  
Erie, Pennsylvania

The term "shim spring" identifies a new spring form which stores from three to nine times more energy -- per pound or per cubic inch -- than conventional metallic springs operating at the same stress. It requires no external damper and will operate continuously to at least 500°F. Externally, the shim spring resembles a metallic block having the unusual property that it will deflect readily in shear. It is made of thin, high-strength alloy shims arranged so that every element is in direct tension or direct compression, and it is this factor which accounts for the spring's high efficiency. Development toward commercial practice has centered on (a) protection of shim surfaces, which are in rubbing contact; (b) joints to transfer load efficiently between shims; and (c) analysis of the stiffness characteristics and of the damping associated with intershim friction. Progress has been such that the shim spring shows excellent performance as a vibration isolator with good fatigue resistance, and a prototype mounting is now being tested on an aircraft turbine. Design studies for heavy vehicle springing show large potential weight saving.

### INTRODUCTION

The term "shim spring" identifies a new spring form which is shown in elementary fashion in Fig. 1. It has several characteristics which may attract those interested in vibration isolators, suspension systems, and perhaps other uses of mechanical springs: (a) the shim spring has from three to nine times the energy storage capacity of conventional metallic springs, so that it can be made smaller and lighter; (b) it possesses inherent (and, to a degree, controllable) damping so that, unlike most conventional springs, it requires no external damper; (c) its all-metal construction gives it a high temperature capability (to at least 500°F) not possessed by elastomeric springs and isolators, and (d) it lends itself to nonlinear designs when that is required.

There are also substantial problems associated with the shim spring; this paper tells how (and to what extent) they have been overcome. Among these problems are: (a) protection of shim surfaces, which are in rubbing contact; (b) design and construction of joints to transfer load efficiently from each shim to its neighbor, and (c) methods for calculating stiffness and damping characteristics. There is also a problem in designing for the unsymmetrical nature of the shim spring. It has high capacity and readily controllable stiffness in the z direction (Fig. 1), less capacity and much

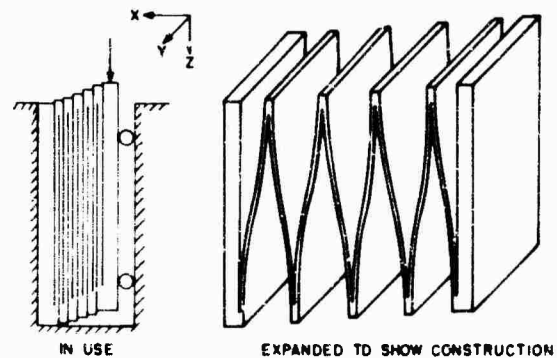


Fig. 1. Elementary shim spring

lower stiffness along y, and virtually infinite stiffness and capacity along x. There is capability for large angular deflection about x, and virtually none about y and z. We shall show through two quite different designs, an aircraft turbine mounting and a vehicular spring, how these characteristics may be combined in useful ways.

A force on the loading plate puts the first shim in tension, the next in compression (see Fig. 1); this alternation continues until the support is reached. The compression shims (shim thickness generally runs from about 0.010 to 0.030 in.) cannot buckle because they are confined. The extensions and compressions







combine to give large overall deflection, and load capacity is high because each shim is in a state of uniform tension or compression, i.e., there is no bending.

## SPRING EFFICIENCY

Comparing the energy stored by a linear spring per pound of material at a given maximum stress is a reasonable way to compare various designs [1]. Table 1 presents this comparison for several conventional springs, and shows that the shim spring has an efficiency ranging from about three times that of a torsion bar to nine times that of a simple cantilever. The tabular symbols are defined below, along with their numerical values. The stresses used are the elastic limits for a high-quality spring steel.

|                                       |                           |
|---------------------------------------|---------------------------|
| $S$ = Tensile (or compressive) stress | 205,000 psi               |
| $S_s$ = Shear stress                  | 115,000 psi               |
| $E$ = Young's modulus                 | $30 \times 10^6$ psi      |
| $G$ = Shear modulus                   | $11.5 \times 10^6$ psi    |
| $\rho$ = Density                      | 0.283 lb/in. <sup>3</sup> |
| $R$ = Wahl factor                     | 1.2 (Typical)             |

TABLE 1  
Spring Capacities

| SPRING FORM   | ENERGY STORAGE CAPACITY    |  |
|---|----------------------------|--|
|   | Expression                 | Typical Values<br>in-lb per pound weight |
|              | $\frac{S^2}{18E\rho}$      | 275                                      |
|              | $\frac{S^2}{18E\rho}$      | 275                                      |
|              | $\frac{S_s^2}{4G\rho R^2}$ | 610                                      |
|              | $\frac{S^2}{6E\rho}$       | 25                                       |
|              | $\frac{S_s^2}{4G\rho}$     | 885                                      |
|  Shim Spring | $\frac{S^2}{2E\rho}$       | 2500                                     |

In practical springs, the tabulated efficiencies are reduced by, for example, the inactive end coils in the case of a helical spring. In a shim spring, the connections between shims

have the same effect, and this points to a useful design practice: making the spring from relatively few, long shims rather than many short ones. We thereby reduce the number of joints and also invoke beneficial effects in terms of damping, which is discussed later.

## SPRING STIFFNESS: ELASTIC RESTRAINT ONLY

The longitudinal in-plane stiffness is given by

$$K = \frac{Ewt}{nL_e} \quad (1)$$

the crosswise, in-plane stiffness by

$$K_L = \frac{EGw^3t}{nL_e(Ew^2 + GL_e^2)} \quad (2)$$

and the rotational, in-plane stiffness by

$$K_r = \frac{Ew^3t}{12nL_e} \quad (3)$$

where

$E$  = Young's modulus

$G$  = Shear modulus

$w$  = Shim width

$t$  = Shim thickness

$L_e$  = Effective length of shim

$n$  = Number of shims.

If the shims were perfectly flat, the compression stiffness  $K_N$  of the stack would be that of a solid metal block. In practice, the initial value of  $K_N$  is less than we would expect, both because the shims are not perfect, and because there may be lubricating materials of measurable thickness between shims. Figure 2 shows the compression load-deflection curve for a spring having a longitudinal stiffness of 4000 lb/in. The initial compression stiffness is only about 8000 lb/in., but it increases to about 100,000 lb/in. very quickly. Because of this rapid stiffening and the fact that there is always normal load on the spring,  $K_N$  will usually run from 10 to 100 times the longitudinal stiffness  $K$ .

It is also worth noting from Fig. 3 that  $K_L$  cannot exceed about  $K/3$ , because the relation

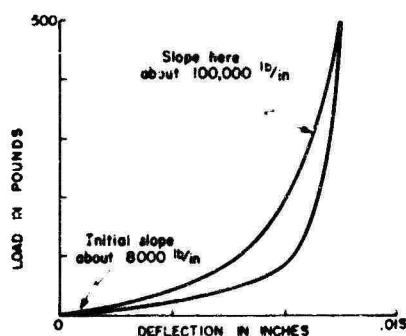


Fig. 2. Typical compression load-deflection curve

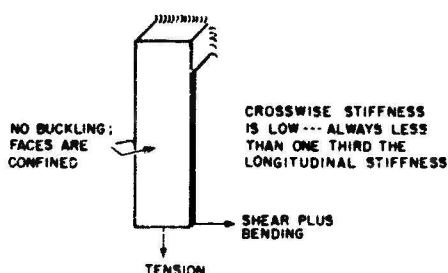


Fig. 3. Qualitative relation, cross-wise to longitudinal stiffness

is that of shear modulus to Young's modulus. The difference is much greater when the bending contribution is considered, which Eq. (2) of course, does.

### SPRING CAPACITY

The following simple relations determine the load-carrying capability of the working sections of the shims, that is, the uniform portions between the joined ends. Stresses in the joints are more complex and are considered separately:

$$\frac{P}{wt} \quad (4)$$

$$\frac{P_L}{wt} \quad (5)$$

$$\frac{6 P_L L_c}{wt^2} \quad (6)$$

where

= Normal stress

$P$  = Longitudinal load

= Shear stress

$P_L$  = Crosswise load.

### JOINT DESIGN

We can idealize the joint problem (Fig. 4a), and, recognizing that load must be transferred from one shim to the other by shear, ask what is the distribution of shear stress along the center plane about point O. The solution (Fig. 4b, from G. S. Healy) shows that the peak shear stress occurs very close to point O with a value equal numerically to the uniform tensile stress at a remote point in the shim. Since shear strength is only about half of the tensile strength, the joint in an elementary rectangular spring reduces its capacity proportionately. Rapid tailing off of the shear stress shows that making the joint longer above O will do very little to reduce the peak. We therefore adopted the form shown in Fig. 5 in which the joint is made approximately twice as wide as the working section. Again, the virtue of long shims is apparent; the relatively inefficient joints become a small portion of the total length.

Spot welding has proved to be an effective means for joining shims, and is employed in parts now undergoing field tests. The welds can be made with high reliability, and by fatigue testing a number of patterns we achieved joints equal in strength to the shim working sections. Figure 5 shows three of these patterns, including the one which was adopted. Current development, based on a simultaneous braze and heat treat cycle, looks promising for further improvement.

One other aspect of joint configuration is illustrated by Fig. 6. There is bending as well as shear across each joint, and a tendency to "curl over" where clearances accumulate as in Fig. 6a. Extension of the joined section (Fig. 6b) provides rigidity against such deformation.

### DAMPING

The damping of shim springs results from intershim friction, and two factors are at work to produce it: initial precompression, which causes a constant friction force, and reaction to shear loading, which causes a friction force increasing with displacement. If one assumes



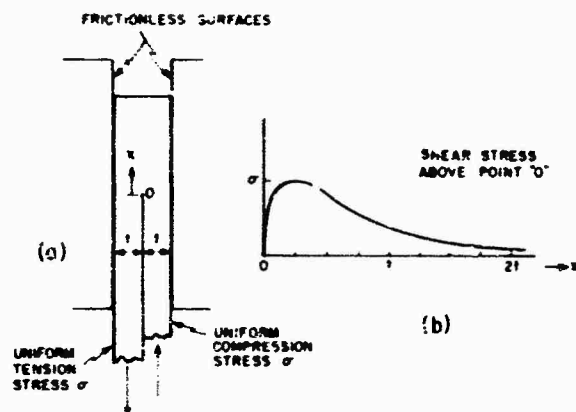


Fig. 4. Shear stress in joint

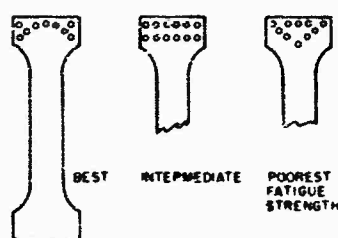


Fig. 5. Shim form and some spot-weld patterns

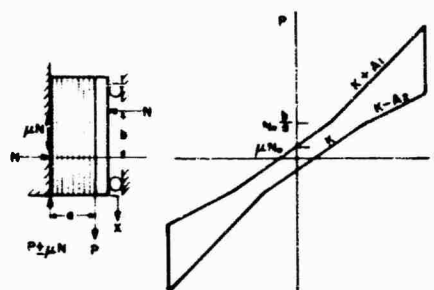


Fig. 7. Free body diagram and idealized force-deflection curve

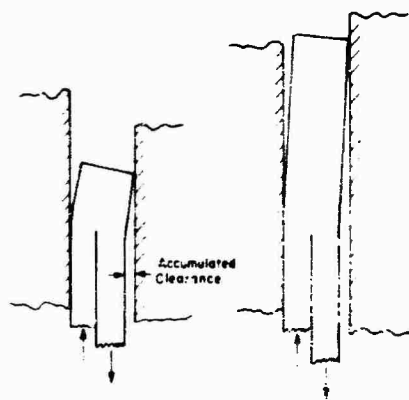


Fig. 6. Extension of joint to reduce bending

the relation to be a direct proportion, we can define friction gradients which have the same dimensions, e.g., pounds per inch, as an elastic gradient or stiffness, and which correlate satisfactorily with experimental results. Figure 7 which shows the balance of forces on a shim spring as a free body.

Let

$N$  = Normal force (resultant of the roller reactions)

$N_0$  = Initial value of  $N$  (i.e., the compression preload)

$N' = P(a/b) =$  "Self-generated" normal force due to external force

$\mu$  = Coefficient of friction

$b$  = Distance between normal forces, which depends on some undefined pressure distribution on the shim faces. It will generally be less than  $1/3 L$ , corresponding to a triangular distribution

$K$  = Elastic spring rate or gradient

$A_1$  and  $A_2$  = Friction gradients for  $x$  and  $\dot{x}$  of like and of opposite sign, respectively

$\dot{x}$  = A change in displacement

$\dot{P}$  = The corresponding change in P because of changes in both elastic and friction forces

$\dot{N} = \dot{P}(a/b)$  = Change in normal force.

Then  $\dot{P} = K\dot{x} + \dot{P}(a/b)$ , for  $x$  and  $\dot{x}$  of like sign, giving

$$\dot{P} = \frac{K\dot{x}}{1 - \frac{a}{b}}$$

and

$$\dot{N} = \frac{K\dot{x} \frac{a}{b}}{1 - \frac{a}{b}}$$

By definition,

$$A_1 = \frac{\dot{N}}{\dot{x}}$$

$$A_1 = \frac{K(a/b)}{1 - (a/b)} \quad (7)$$

for  $x$  and  $\dot{x}$  of like sign, and

$$A_2 = \frac{-K(a/b)}{1 + (a/b)} \quad (8)$$

for  $x$  and  $\dot{x}$  of opposite sign.

We can now construct an idealized force-deflection curve for the spring (Fig. 7) if we note that:

1. The "self-generated" normal force  $N'$  has no effect on friction until it exceeds the compression preload  $N_0$ , i.e., friction force is constant ( $=N_0$ ) for  $P \leq N_0(b/a)$

2. As long as the friction force is constant, the slope of the force-deflection curve is the elastic spring rate  $K$ .

3. The intercept of the force-deflection curve on the force axis is  $P = N_0$  when  $\dot{x}$  is positive and  $P = -N_0$  when  $\dot{x}$  is negative.

4. When the self-generated force  $N'$  exceeds the precompression  $N_0$ , i.e., when  $P > N_0(b/a)$ , the friction force varies directly with deflection according to the gradients  $A_1$  and  $A_2$ , and the curve slopes become:  $K + A_1$  for  $x$  and  $\dot{x}$  of like sign,  $K + A_2$  for  $x$  and  $\dot{x}$  of opposite sign.

5. The  $K + A_1$  and  $K + A_2$  portions, projected, pass through the origin.

Frictional characteristics discussed in this section are another reason for making long thin shim springs (Fig. 8): if anything, there is too much rather than too little damping. Making  $a/b$  small (which is the case for a long spring) is a simple way to limit damping, as Eq. (7) and (8) show.

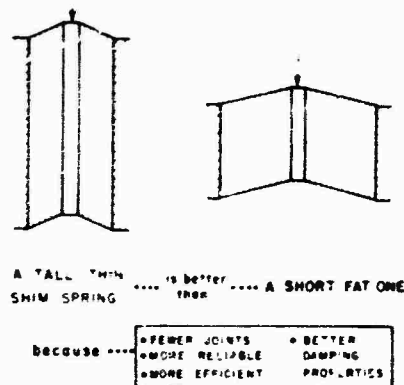


Fig. 8. Shim springs. Tall vs short

## RESONANCE TRANSMISSIBILITY

For a centered spring (Fig. 9a), we can predict resonance transmissibility ( $T_{res}$ ) with assurance, using the following expression from Ref. [2]:

$$T_{res} = \frac{1}{2(A + K)} \quad (9)$$

where we can take  $A = (A_1 + A_2)/2$  with very little error. Although the damping is frictional,  $T_{res}$  is always finite, depending only on  $A + K$ . Infinite resonance, possible when conventional friction dampers are used beyond a critical input [3,4], cannot occur in this case.

When there is static displacement as in Fig. 9b (and this is more often the case), we do not yet have a good analytical procedure for calculating  $T_{res}$ . This is one of the substantial problems referred to early in this paper. Experimentally, very favorable damping characteristics have been shown. Figure 10, for example, shows transmissibility data from tests on a prototype aircraft turbine isolator. At resonance, transmissibility is low, about 2.5, and it decreases rapidly with increasing frequency, at about 12 db/octave for constant displacement input and 6 db/octave for constant

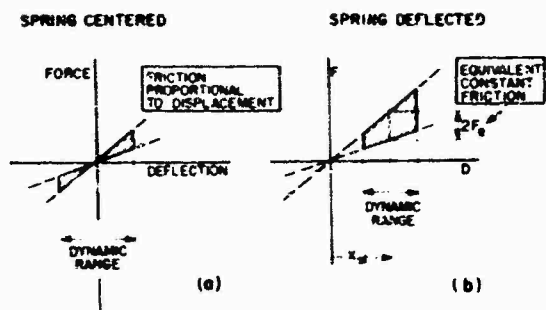


Fig. 9. Effect of static displacement on damping characteristic

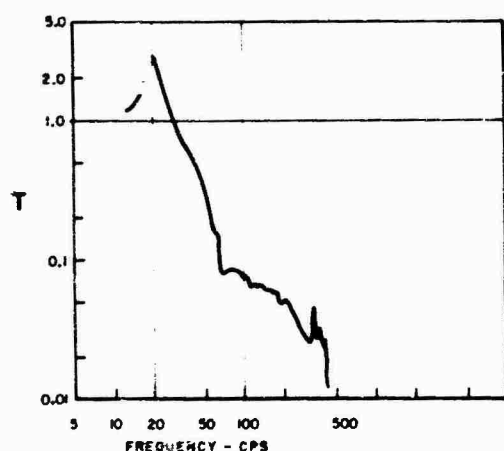


Fig. 10. Transmissibility: Shim spring isolator for aircraft turbine

acceleration. Performance as an isolator is, therefore, as good as or better than that of a classical, viscous damped spring; it is much better than that of springs combined with conventional friction dampers. The latter, under constant input acceleration, displays constant rather than decreasing transmissibility [4]. In attempting to explain the above performance, we run into the problem that the shim spring, with a static displacement, should appear to have conventional friction damping of equivalent force  $F_c$  (Fig. 9b). A sudden jump in  $T_{res}$  with increasing input should therefore be expected, with finite limitation as displacement-proportioned damping begins to dominate. So far, this postulated characteristic has not been identified.

## PROTECTION OF SHIM SURFACES

As each shim is in intimate, oscillatory contact with its neighbor, protection from fretting corrosion is essential for maintaining a uniform coefficient of friction during the life of the spring. A variety of treatments was tested using small flat coupons under conditions simulating aircraft turbine operation: 1000-psi surface pressure, 500° F temperature, 0.005-in. double amplitude relative motion, and 100-cps frequency.

Films of solid lubricants such as graphite and molybdenum disulfide proved completely inadequate, whether applied by simple burnishing or in bound coatings. In general, they were so thin that they wore through at high spots, and fretting corrosion occurred in a few hours at most. These materials work excellently in bearings with closely machined surfaces, but not on rolled shims which have a relatively irregular surface. Lubricating tapes of reinforced Teflon, on the other hand, performed excellently. They were thick enough (about 0.010 in.) to accommodate minor irregularities, showed very little flow or wear after several hundred hours of testing, and maintained a uniform coefficient of friction.

## FATIGUE

Much remains to be done in establishing the fatigue life of shim springs in a broad sense, but for the particular case of an aircraft turbine, considerable information has been acquired.

### Low-Stress, Long-Duration Testing

Durability for long-term, relatively low-stress operation, corresponding to cruise conditions, was demonstrated by a spot-welded spring assembly composed of 31 shims. Tested at 500° F, the spring experienced a mean stress of 32,000 psi with oscillatory motion of 0.005-in. double amplitude at a frequency of 150 cps. The corresponding stress oscillation, about  $\pm 2000$  psi, was monitored and showed little change during the course of the test, which was terminated at 1000 hr. Static stiffness was not measurably changed. Deterioration of the lubricating tape adhesive was apparent, and improvement is needed. The tapes were, however, not displaced, and their wear was nil. This spring was made of 410 stainless steel; a change to 17-7PH

stainless has been made since then for better mechanical properties, weldability, and environmental resistance, and for heat treatment which is more compatible with our fabricating procedure.

#### Tests at High Stress Levels

Occasional abnormal loads (limit loads) occur in aircraft due to hard landings, severe maneuvers, or other conditions, for a total of about 5000 such loads during an engine overhaul period. This number represents minimum acceptable life for an isolator, and fatigue tests to limit loads were run both for development purposes and to assure performance of 5000 limit load cycles with a high degree of certainty.

Two types of tests were performed. One was to determine a safe cyclic stress for various materials in the thin gages characteristic of shim springs, 0.010 in. and 0.018 in. in our prototype. The second was to determine a safe cyclic stress for the welded assembly, or elements of it, in which joint design and fabrication are major elements.

The results of material testing on 17-7PH stainless are presented in Table 2, which also shows the specimen. The data were badly skewed to the right, and were analyzed by the Weibull distribution function [5] which provides an estimate of minimum fatigue life (column 3). No failures are to be expected below this figure. Another analysis was made, based on the log of cyclic life, which made the distribution more nearly normal. Based on this, the last column gives expected life, assuming we will accept the risk (i.e., probability) of 0.00135 that failure will occur earlier. This applies to the testing of single specimens, and is a probability level corresponding to three standard deviations. In the critical section of our prototype there are 21 shims in series, and the probability of failure in that case (0.028) comes from:

$$a_n = 1 - (1 - a)^n \quad (10)$$

where  $a_n$  = probability of failure for a spring of  $n$  shims, and  $a$  = probability of failure of a single shim.

From the tabulated results, we can expect about 10,000-15,000 cycles of operation at a peak stress of 140,000 psi. Our prototype is designed to a peak stress of only 90,000 psi. As far as material capability is concerned, the design is therefore entirely safe.

The results of tests on welded specimens are shown in Fig. 11. Each specimen consisted of three shims and therefore two joints, a so-called N specimen, and the design proved to be most convenient. It is easy to install in the test fixture, and it represents minimum construction time for given data acquisition; specimens with more shims would add very little information since only the first shim or joint to break provides a data point.

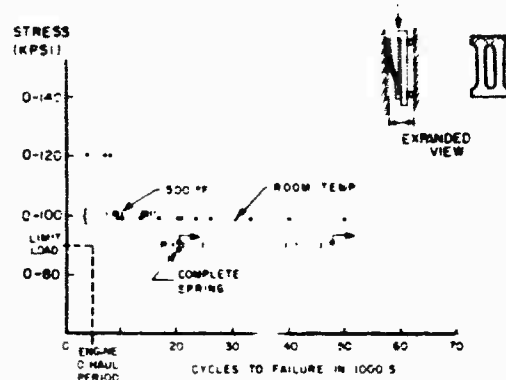


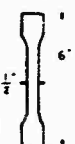
Fig. 11. Fatigue test, spot-welded springs

The most complete data, for room temperature tests at 100,000 psi, is again badly skewed to the right, resulting in pessimistic interpretation of life expectancy. In a qualitative way, Fig. 11 shows that we can reasonably expect life of at least one engine overhaul period. Tests on four complete prototype springs, also plotted, bear out this expectation. Quantitatively, analysis shows 0.006 probability of failure at 5000 cycles at 100,000 psi for the N specimens. Because each has two joints, we estimated reliability of our 21-joint isolator by substituting  $a = 0.006$  and  $n = 21/2$  in Eq. (10). A rather high failure probability of 0.065 at 5000 cycles at 100,000 psi results. A limit-load stress of 90,000 psi was therefore established, and the resulting performance of four complete springs has already been noted.

#### AIRCRAFT TURBINE MOUNTING

Figure 12 is a good example of how one can devise a shim spring assembly to provide characteristics which differ substantially from those of the springs themselves. Rigidity of the individual elements parallel to the y axis is high.

TABLE 2  
Tensile Fatigue Tests 17-7PH Stainless Steel (0.018-in. Thick)

| CONDITION (HEAT TREATMENT) | STRESS CYCLE (PSI) | MINIMUM LIFE (CYCLES) BY WEIBULL DISTRIBUTION FUNCTION | LIFE (CYCLES) BASED ON NORMAL DISTRIBUTION FUNCTION and $-3\sigma$ DEVIATION <sup>a</sup> FAILURE PROBABILITY | TEST SPECIMEN  |
|----------------------------|--------------------|--|---|--|
| RH 950 <sup>b</sup>        | 0-140,000          | 14,000   | 11,500  |  |
| RH 950 <sup>b</sup>        | 0-140,000          | 10,300   | 8,800   |  |
| TN 1050                    | 0-140,000          | 12,200   | 9,200   |  |
| TN 1050                    | 0-100,000          | 60,000   | 11,400  |  |
| TN 1050 <sup>b,c</sup>     | 0-140,000          | 28,000   | 14,000  |  |
| TN 1050 <sup>b,c</sup>     | 0-140,000          | 21,000   | 19,600  |  |
| TN 1050 <sup>c</sup>       | 0-120,000          | 18,400   | 40,200  |  |

<sup>a</sup> FAILURE PROBABILITY = 0.00135 FOR 1 SHIM, 0.028 FOR 21 SHIM SPRING

<sup>b</sup> DIFFERENT LOTS

<sup>c</sup> SHOT PEENED

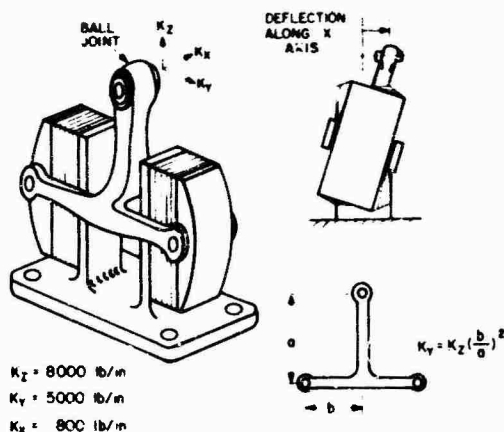


Fig. 12. Schematic of aircraft turbine mounting

However, at the engine attachment point (the ball joint) deflection along  $y$  is converted into shear of each spring, and the ratio of  $K_y$  to  $K_z$  is controlled by the geometric ratio  $b/a$ . The fore-and-aft stiffness  $K_x$  is a function of cross-wise stiffness  $K_L$  and rotational, in-plane stiffness  $K_r$  of the individual springs, and of dimension  $a$ . A balance of these factors produced excellent compliance with suspension requirements. Figure 13 is a photograph of the prototype isolator now under test.

Not apparent from either figure is that the springs are bilinear, having increased stiffness above the normal load range. Figure 14 shows schematically how this is done, and is self-explanatory. Not so obvious is the weight and

space saved; stage 1 bottoms before maximum load on the assembly is reached and can, therefore, be made from thinner shims than stage 2. In the prototype, for example, the two stages have equal spring rates, but a two-to-one difference in weight and thickness.

## TRUCK SUSPENSION SPRINGS

Figure 15 depicts a case where the compressional rigidity of a shim spring is put to good use: it transmits driving and braking forces from axle to chassis, making radius rods unnecessary. In-plane rotation of the springs accommodates tilting of the axle when one wheel rises or falls, and the truck weight is carried in the lengthwise direction of the spring, the direction in which its high efficiency can be realized. We do not know yet whether shim damping can eliminate the use of conventional shock absorbers.

The really attractive feature of shim spring suspension to the vehicle operator is weight saving, roughly 50 percent over conventional springs. The vehicular shim spring is also a lot more expensive, and this factor has so far kept it in the laboratory stage.

## FUTURE DEVELOPMENT

The weight of any spring varies inversely as the square of allowable stress, and means to utilize materials closer to their maximum capabilities are of great importance. Our present maximum level of about 90,000 psi for  $10^4$ - $10^5$  cycles leaves room for improvement. Some steps which will lead to this are:

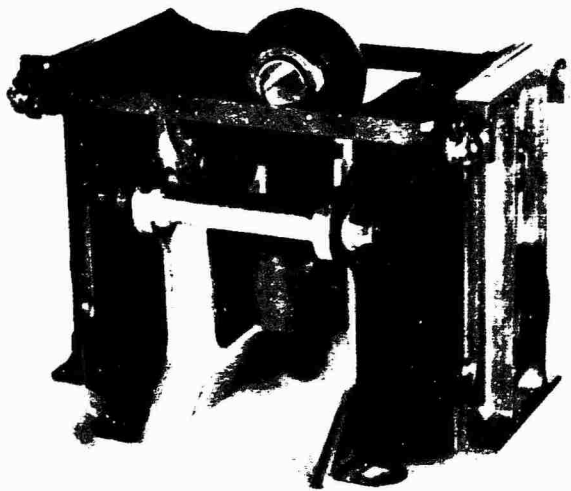


Fig. 13. Aircraft turbine mounting prototype

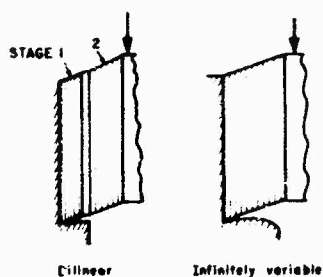


Fig. 14 Nonlinear shim springs

1. More comprehensive fatigue tests to establish endurance limits of various materials in thin gages;

2. Improvement in joint design, fabrication, or both to enable more efficient transfer of load from shim to shim;

3. Investigation of special surface finishes, shot peening (difficult on very thin materials), and other refinements to improve fatigue life.

4. Lubrication studies: a number of greases and other lubricating materials have shown potential as a replacement for lubricating tapes, especially at normal temperatures, and at a much lower cost.

#### SUMMARY

The shim spring conception and its advantages have been described; its characteristics have been identified qualitatively and by design formulas, and some of the problems associated with its use have been stated. There is a re-counting of the degree to which they have been overcome, and two practical applications, one now undergoing field test, have been described. Steps for further development have been noted.

#### ACKNOWLEDGMENTS

I am most grateful to Gene D. Garn, senior technician, for the fabrication and testing of the specimens, and for his numerous valuable suggestions. Thanks also go to L. J. Bindseil, G. S. Healy, and David G. Gardner, and to Mrs. William Mellow for preparation of the drawings.

#### REFERENCES

1. J. T. Gwinn, "Storing Energy in Springs," *Machine Design*, Vol. 36, No. 8, pp. 166-172, March 1964
2. L. Wallerstein, Jr., "Dry Friction Damping with Force Proportional to Displacement," *Shock and Vibration Bull.* No. 35, Part 5, pp. 179-185, Jan. 1966
3. J. P. Den Hartog, *Mechanical Vibrations* (4th ed.) (McGraw-Hill, New York), 1956, pp. 373-377.

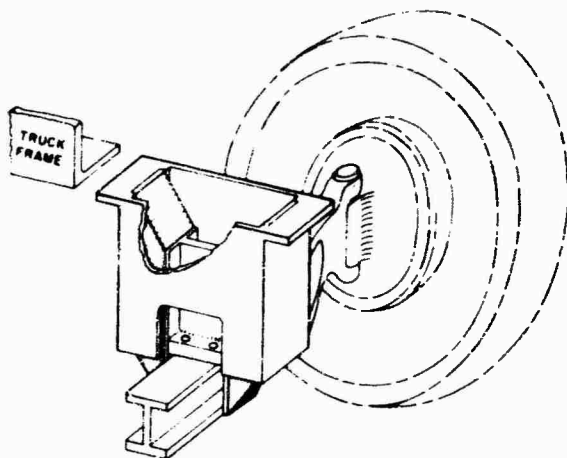


Fig. 15. Truck suspension spring

4. G. W. Painter, "Dry Friction Damped Isolators," *Product Eng.*, Vol. 30, No. 31, pp. 48-51, Aug. 1959

5. "The Weibull Distribution Function for Fatigue Life," *Proposed ASTM Materials Res. and Stand.*, Vol. 2, No. 5, May 1962, pp. 405-411

#### DISCUSSION

Mr. Kunica (Perkin-Elmer Corp.): Could you please comment from the practical point of view on the problem associated with controlling the dimension B or the parameter B which of course in turn controls the damping?

Mr. Wallerstein: That dimension is a function of the pressure distribution between shims, or between the shims and the restraining faces.

Mr. Kunica: But it would seem that from a production point of view it may be difficult to maintain, quality-control-wise.

Mr. Wallerstein: It is not difficult to do it in a uniform fashion from one spring to another. They operate very uniformly. Our trouble is, how do we calculate it. Once you build a spring and duplicate it, the performance is quite uniform from one to the next.

Mr. Kunica: Could you comment further on the fatigue life problem? This is something which is being worked on I assume.

Mr. Wallerstein: Yes. We have done quite a bit of work on fatigue. We are at a level now where, with a high level of confidence, we can expect to get at least one engine overhaul on a conventional turbine aircraft turbine. We do

not look on this as being the ultimate by any means, but we have reached that level of operation now. The paper which will be printed has quite a bit of detail on fatigue testing.

Mr. Berkman (Litton Data Systems): What is the smallest practical size in which this could be built? — the smallest load which it might be able to carry?

Mr. Wallerstein: In initial studies we looked at everything from instrument mountings of just a few pounds capacity up to things to carry trucks. I think the limitation on small size will come in the ability to weld very very thin shims together in a satisfactory manner. Right now I would hesitate to say that a spring could be made in the range of a very light instrument mounting.

Mr. Verga (Hazeltine Corp.): I think that the design is very clever. You spoke about damping, and certainly when you have components that slide against each other with a normal force applied there will be damping. But the thing that bothers me about this design is that it is being used as an isolator, and as an isolator it has to have flexibility, deflectionability, so that it can resonate, and then isolate. An isolator does not necessarily have to have damping, although most of the time it is desired to have

damping in an isolator. In the axial direction there is no question that this device does not perform as an isolator. However, in the other two directions you have stated that the elements are loaded in tension and compression with virtually no buckling. Are you going to be able to get deflectionability? If you have pure tension and compression it is inconceivable to me to think that you will be able to get enough deflection to get a resonance such as 20 or 12.

In that first chart you plotted energy stored per pound, and you showed the shim isolator as a very high one. However, if I would plot the same thing for a little block of steel, say, wouldn't I expect it to be still higher?

Mr. Wallerstein: No. It should be exactly the same. A block of steel, if you assume pure compression or pure tension, you would get the same thing.

\* \* \*



## TEST FACILITIES

### ADVANCED COMBINED ENVIRONMENTAL TEST FACILITY

Edward J. Kirchman and Charles J. Arcilesi  
NASA Goddard Space Flight Center  
Greenbelt, Maryland

A new spacecraft test facility, the launch phase simulator (LPS), is now operational at the Goddard Space Flight Center in Greenbelt, Maryland. This facility can reproduce the combined launch environmental conditions of steady or sustained acceleration, acoustic noise, pressure profile, and mechanical vibration. These environmental capabilities are:

1. Steady acceleration -- 30 g maximum with capability of simulating acceleration and deceleration rates of the Delta, Agena, and larger classes of liquid engine boosters.
2. Acoustic noise -- 150-db rms overall SPL exterior to the shroud-enclosed spacecraft. This spectrum is flat from 100 to 700 Hz, with 6 db/octave roll-off from 700 to 12,000 Hz.
3. Pressure -- programmed to follow the launch pressure profile from 760 torr to  $3 \cdot 10^{-1}$  torr, i.e., up to an altitude of approximately 190,000 ft.
4. Mechanical vibration -- three degrees of freedom (longitudinal, lateral, and pitch) from 0.5 to 200 Hz with both sinusoidal and random capability. Multiaxis motion with this system may be either independent or simultaneous. (This system is capable of operation on the centrifuge arm or in an offboard condition mounted on a seismic reaction mass.)

Each of these systems can simulate the actual environmental conditions in real time and can be operated in either the automatic or manual mode.

Physically, the facility is a large centrifuge (60-ft radius to payload c.g.) which weighs approximately 500,000 lb and has a cylindrical test chamber (12 ft in diameter and 22 ft long) mounted on the end of the centrifuge arm. The chamber houses the acoustic, vacuum, and vibration systems, and can accommodate a payload or spacecraft configuration that weighs up to 5000 lb and can be defined in an envelope 10 ft in diameter and 15 ft long. The centrifuge is located in an enclosure or rotunda which is 157 ft in diameter and 27 ft high.

A description of the environmental capabilities of the LPS is presented, with a detailed explanation of the facility and its various subsystems. In addition, operational philosophies and procedures are explained, and spacecraft and component tests conducted to date are summarized. These tests consisted of the simulation of single and combined environments involving the vacuum, acoustic, and steady acceleration systems. Design investigations and research programs used as engineering tools in the design and development of the facility are also discussed. Finally, future applications and growth potential of the facility are discussed with respect to third generation or advanced mission satellite programs such as the Voyager.

#### INTRODUCTION

The environmental exposures can, in general, be divided into three broad categories: the prelaunch or ground handling environment, the launch environment, and the orbital environment. In particular, during the launch environment the environment loading conditions usually occur simultaneously, and in the past reproduction of this environment has not been attempted because of the lag in simulation techniques between the design engineer and the

environmental tester. In fact, design philosophies have often resulted in hardware tailored to the simulated test condition rather than the actual environment. Thus, the practice in launch environmental testing has been to conduct a series of individual tests usually consisting of single environmental conditions or, at best, simple combinations of such conditions.

During launch of a space vehicle, the severity of noise-induced vibration is at its greatest; at the same time the liftoff accelerations

are of an appreciable magnitude, not to mention other effects such as pressure and temperature variations. The combination of merely mechanical vibration and sustained (or steady) acceleration in a laboratory test is especially difficult and, until recently, has been avoided because of the inherently complex nature of the facility required. However, we are rapidly approaching a sophistication in the design of spacecraft and vehicles where the specific effects of combining sustained acceleration, mechanical and acoustic vibration, and pressure can no longer be ignored in evolving efficient and reliable designs for spacecraft structure, systems, subsystems, and components. Significant effects can be produced by a combination of stresses resulting from such factors as steady-state structural deformations which modify vibration response characteristics, binding or friction in mechanism causing erratic responses under vibration, and additive steady-state and vibratory accelerations overstressing both structure and components. To complicate matters further, additional combinations of environmental stresses such as temperature and pressure can multiply the physical effects that must now be considered in simulating the launch environmental conditions.

Since the goal in environmental testing at Goddard Space Flight Center is to test in a manner which will most accurately simulate the actual environment, a task team effort was initially established to determine the feasibility of designing and building a large facility which could simulate the combinations of the launch environmental conditions. From this small task team emanated an advanced combined

environmental test facility designated as the launch phase simulator (LPS) [1], which is now operational at the Goddard Space Flight Center in Greenbelt, Maryland.

Presented here is a detailed treatment of the environmental capabilities of the facility, with a complete description of the operational conceptions. In addition, spacecraft and components tests conducted to date are summarized. Finally, design investigations and research programs used as engineering tools in the development of the LPS are discussed.

#### CAPABILITIES OF FACILITY

The LPS, shown in Fig. 1, is capable of reproducing the combined major launch environmental conditions, i.e., steady or sustained acceleration, acoustic noise, pressure profile, and mechanical vibration. (Thermal heating simulation was not included in the environmental capabilities, because in the launch phase this effect is of short duration and confined to the shroud which is jettisoned before much transfer to the spacecraft takes place.) Figure 2 presents a general representation of the combined-environment parameters available on the LPS. Specifically, the environmental capabilities are:

1. Steady acceleration of 30 g maximum, with capability of simulating acceleration and deceleration rates of the Delta, Agena, and larger classes of liquid engine boosters. Figure 3 presents the thrust onset capability in

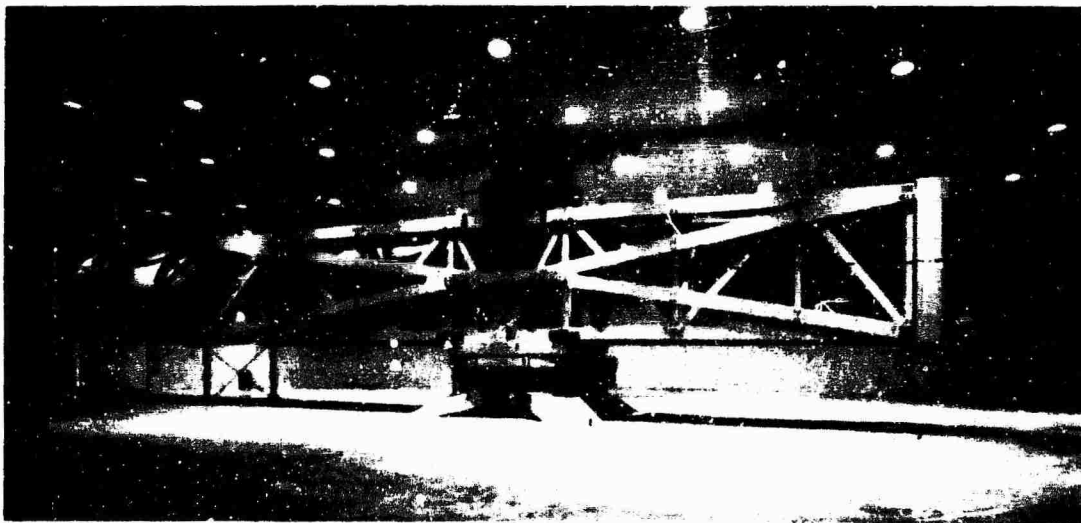


Fig. 1. LPS located in building enclosure

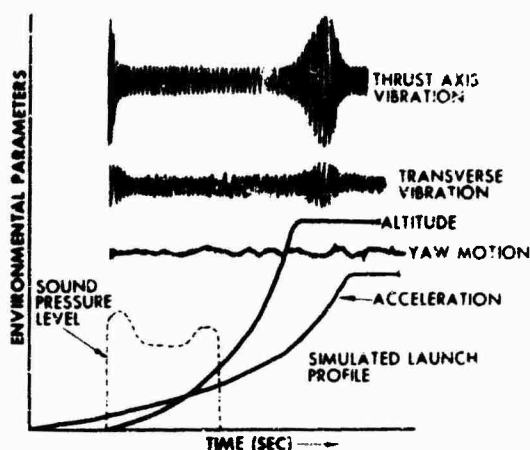


Fig. 2. Available parameters of the LPS

comparison with the data from a Delta S-3 launch and an Atlas-Agena B launch [2]. The former vehicle carried an 85-lb payload, whereas the latter carried a 1000-lb payload (EGO).

2. Acoustic noise of 150-db rms overall SPL exterior to the shroud-enclosed spacecraft. This spectrum is flat from 100 to 700 Hz, with 6 db/octave roll-off from 700 to 12,000 Hz. Figure 4 illustrates the capability of the LPS acoustic system, with both OGO-C launch measurement data and test data from an acoustic test

performed at Langley Research Center in March 1964 [3]. The LPS acoustic data shown in Fig. 4 present a typical spectrum and not one that attempted to reproduce the flight measurements or the OGO-C test. This is the reason for the difference in levels at the lower frequencies. Actual simulation with the LPS acoustic system very closely approximates the launch measurement data.

3. Pressure programmed to follow the launch pressure profile from 760 torr to  $3 \times 10^{-1}$  torr, i.e., up to an altitude of approximately 190,000 ft. In general, this system can simulate the launch pressure profile for Delta, Agena, and Atlas-Centaur launched spacecraft. This is illustrated in Fig. 5, where the LPS dp/dt capability is presented with profiles for actual Delta, Atlas-Agena, Atlas-Centaur, and Aerobee 350 launch data. Simulation down to 10 torr is extremely good, with some deviation for the Delta launches below this level. The Aerobee 350 is a solid propellant rocket; the pressure profile for this vehicle is presented for comparison purposes.

4. Mechanical vibration having three degrees of freedom (longitudinal or thrust, lateral, and pitch) from 0.5 to 200 Hz with both sinusoidal and random capability. Multiaxis motion with this system may be either independent or simultaneous. (This system is capable of operation on the centrifuge arm or in an offboard condition mounted on a seismic reaction mass.

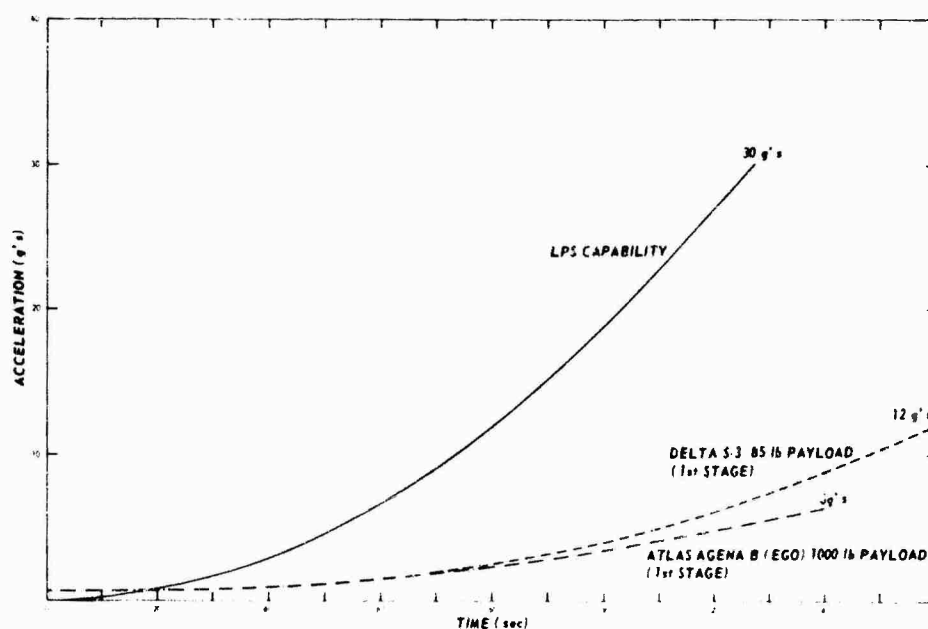


Fig. 3. Comparison of flight acceleration data with LPS capability

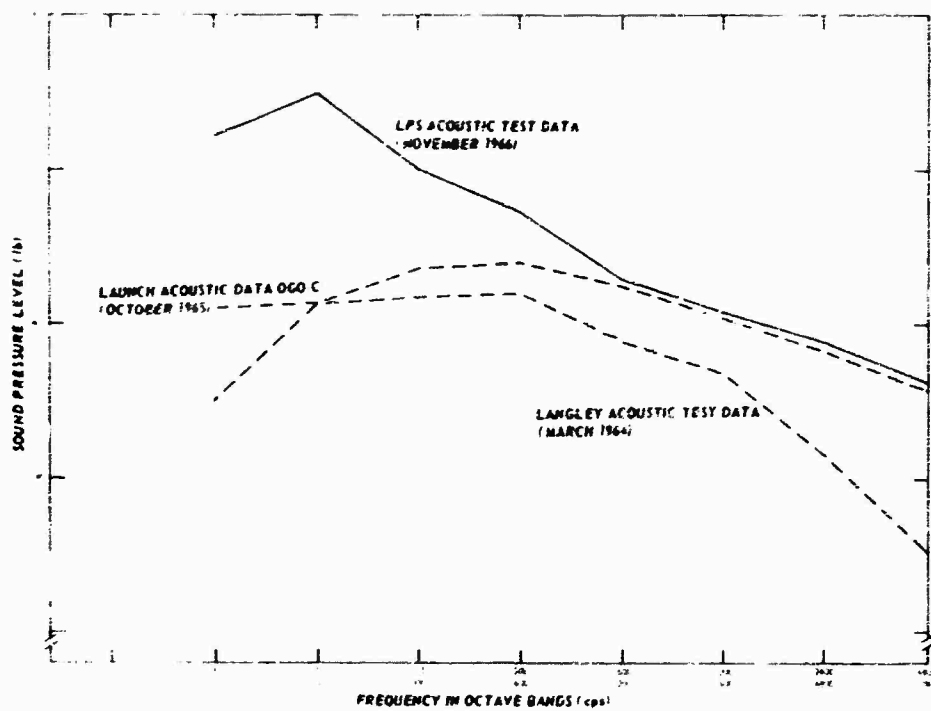


Fig. 4. Comparison of acoustic test data

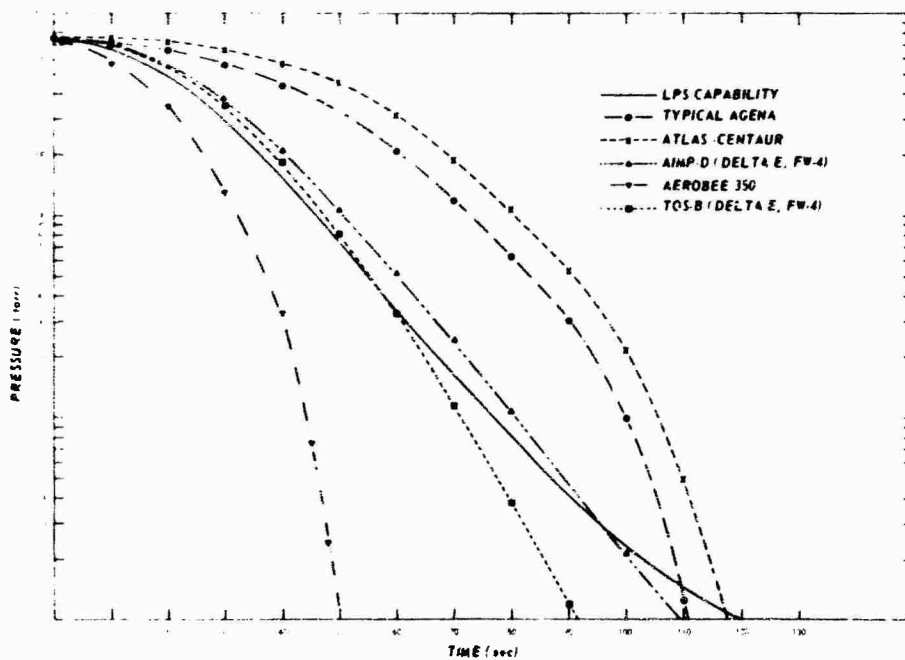


Fig. 5. Comparison of flight vacuum profiles with LPS capability

At present, the system is operational in the off-board condition. Completion of the system to permit operation on the centrifuge arm is scheduled for December 1967.) The sinusoidal and random vibration schedules for this system are as follows:

#### Sinusoidal Vibration

Longitudinal or thrust:  $\pm 4$  g, 1-in. double amplitude motion

Lateral:  $\pm 2$  g, 1-in. double amplitude motion

Pitch:  $\pm 10$  rad/sec<sup>2</sup> angular acceleration, 0.015-rad double amplitude motion

#### Random Vibration

Longitudinal or thrust: 2.8 g rms (8.4 g peak), 1-in. double amplitude motion

Lateral: 1.4 g rms (4.2 g peak), 1-in. double amplitude motion

Pitch: 7 rad/sec<sup>2</sup> rms angular acceleration, 0.015-rad double amplitude motion.

(Operational capabilities of the vibration system when mounted on the seismic reaction mass or on the centrifuge arm are identical except the

frequency range which is 1/2-200 Hz for the former condition and 5-100 Hz for the latter condition.) Each of these systems can simulate the actual environmental conditions in real time and can be operated in either an automatic or manual mode.

The facility can accommodate a payload or spacecraft configuration that weighs up to 5000 lb and is defined in an envelope 10 ft in diameter and 15 ft long. This spacecraft size was based on the second generation or observatory class of spacecraft. The mode of operation for combined-environment testing on this facility is to test the spacecraft in the flight shroud hardware for most realistic simulation.

#### FACILITY

The facility (Fig. 1) is a large centrifuge (60-ft radius to payload c.g.) which weighs approximately 500,000 lb and is made of a truss structure with a cylindrical test chamber mounted on the end of the arm. The centrifuge as shown in Fig. 6 is located in a circular enclosure or rotunda 157 ft in diameter and 27 ft high. For purposes of discussion, the facility is broken down into (a) five major components—the rotating structure and support pedestal assembly, the drive system, the test chamber,

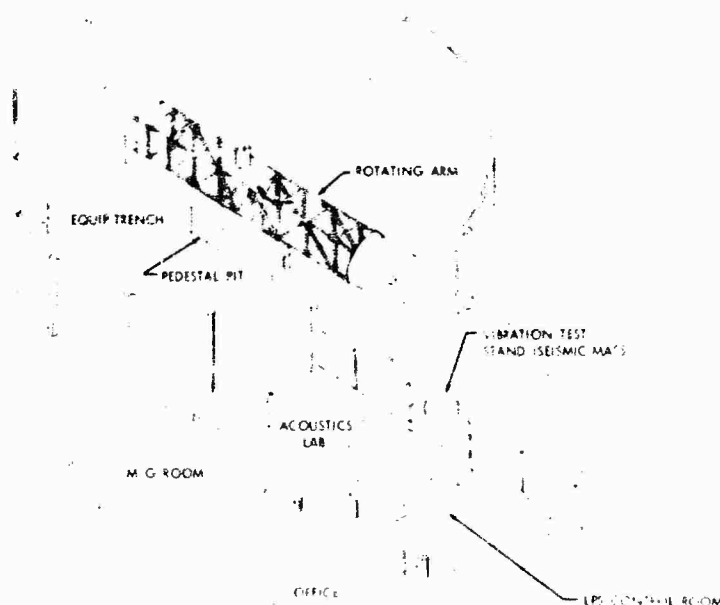


Fig. 6. LPS facility including overall building arrangement

the building, and the controls and instrumentation system for the components — and (b) the four environmental systems — the sustained acceleration system, the vacuum (pressure profile) system, the acoustic noise system, and the mechanical vibration system.

### Rotating Structure and Pedestal Assembly

The main components of the rotating structure and pedestal assembly (Fig. 7) are:

1. Arm structure and counterweight
2. Support pedestal
3. Aximuth bearing
4. Drive gear
5. Brake system
6. Rotary joint
7. Power and instrumentation slip rings
8. Load balance system

The arm structure and counterweight system are fabricated of ASTM A441 steel; the four main members are 14WF219 sections approximately 85 ft long. (Radial distance from the center of rotation to the tip of the rotating structure is 72.5 ft.) The support pedestal, which supports the entire rotating structure, is cruciform in shape and is supported by a massive concrete base and some 50 piles each driven approximately 60 ft into the supporting soil. The aximuth bearing and drive (or bull) gear are a composite assembly, with the stationary portion of the bearing mounted on the pedestal.

The bearing is a 1/1 configuration X-type roller bearing and is approximately 13 ft in diameter. The bull gear, which is exterior to the bearing, meshes with two pinion gears oriented 180 deg apart. These pinions are coupled to drive motors at these locations. Regenerative braking is employed for deceleration of the rotating arm from any speed down to 5 rpm, at which point mechanical braking is employed. The rotary joint at the center of rotation is both a hydraulic and vacuum rotary joint. The slip rings are made up of some 150 power rings and 650 instrumentation slip rings. The load balance system is capable of sensing a static unbalance (and the associated dynamic unbalance) of 500 lb at the 60-ft radial station (typical c.g. of spacecraft).

### Drive System

The drive system is composed of two 1250-hp dc motors operated in conjunction with a motor generator set. The drive motors are located around the support pedestal 180 deg apart and mate to the pinions through large couplings. The motor generator set is located in a separate room in the building, as shown in Fig. 6. The total drive horsepower is 2500, with overload ratings of 40 percent and 100 percent for 30 min and 5 min, respectively. This overload rating may be used for either higher sustained speed or increased (onset) acceleration and deceleration rates. The speed control for the operation of the drive system is 0.5 percent of

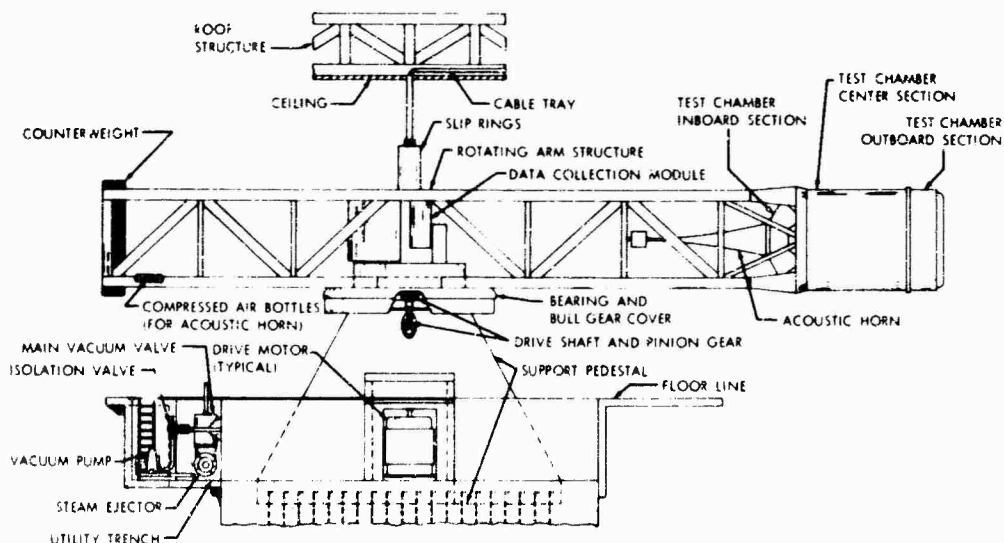


Fig. 7. General arrangement of LPS showing rotating structure, pedestal, and vacuum trench

rated speed of 38.3 rpm (speed corresponding to 30 g at 60-ft test radius).

### Test Chamber

The test chamber, which is a cylinder approximately 12 ft in diameter and 22 ft long, is a vacuum chamber and houses both the acoustic and vibration systems. As depicted in Fig. 8, it has three sections: inboard or dome-type section, center section, and outboard section or end cap. The outboard section (or end cap) is removable and has a support table which functions as a mounting (attachment) surface for the particular spacecraft undergoing test. The test chamber weighs approximately 80,000 lb without spacecraft; the end cap which houses the vibration system weighs about 32,000 lb. For growth

capability, the complete test chamber can be removed from the arm structure at the splice section shown in Fig. 7. This permits the replacement of this chamber with a larger one to accommodate larger, third generation spacecraft of the Voyager class.

### Vacuum System

Actually, the vacuum system is two systems, a primary (main) and a secondary. The main vacuum (pressure profile) system operates off of a multistage steam-operated air ejector system. This system operates on power plant steam and, as an example, requires 60,000 lb/hr of steam consumption at 115 psig to match a typical launch profile of 760 torr to  $3 \times 10^{-1}$  torr in 110 sec. Figure 9 shows the exhaust from the

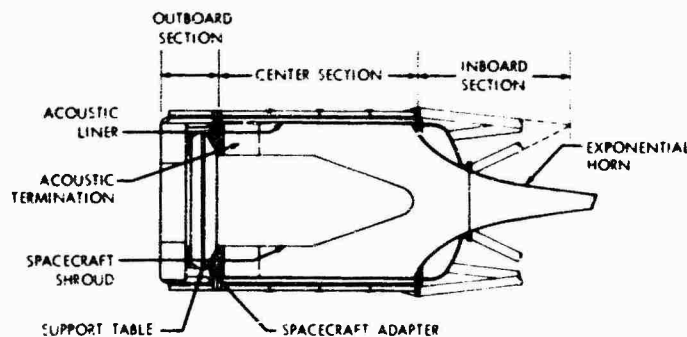


Fig. 8. Cross section of test chamber

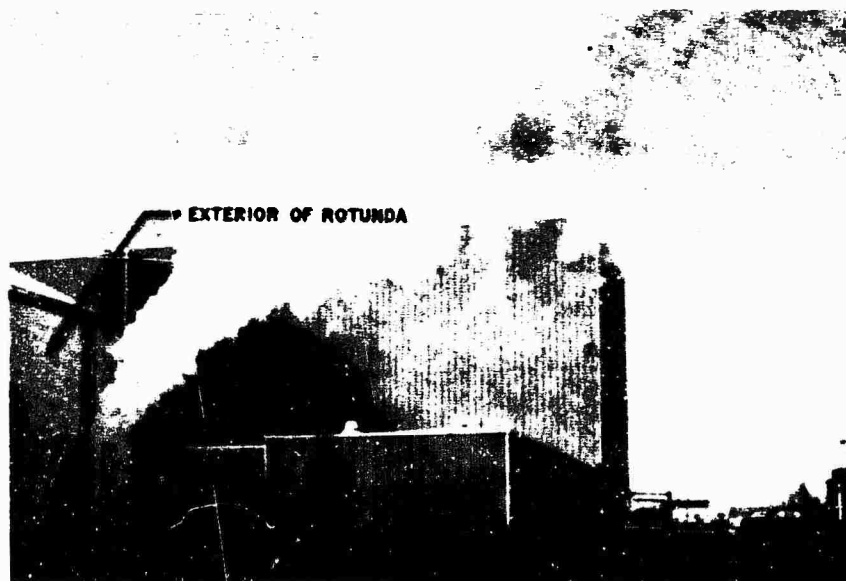


Fig. 9. Steam exhaust during an operational vacuum (pressure profile) test

steam during a typical profile simulation. The secondary vacuum system consists of a mechanical holding pump which permits the vacuum in the test chamber to be maintained at any level down to  $3 \times 10^{-1}$  torr for an extended period of time. The steam ejector system is located in the utility trench shown in Fig. 7 with the main vacuum valve which connects to a 24-in.-diam line. This line is routed through a vacuum rotary joint at the center of rotation and runs out the arm to the inboard section of the test chamber. Total system volume is 3400 cu ft. This does not include the end cap volume, which is evacuated with the secondary vacuum system. The end cap, which houses the vibration system, is isolated from the center section of the test chamber by a flexible seal (boot) because of the presence of hydraulic fluid and other spacecraft contaminants present in the vibration system. The operation of both of these vacuum systems is controlled from a central control complex adjacent to the rotunda, as shown in Fig. 6. Curve-following programmers with control transducers located in both the test chamber and end cap are used for the control of the profiles in the automatic mode of operation.

#### Acoustic System

The acoustic system consists of a noise generator, an impedance matching (exponential)

horn, and an acoustic liner and termination section which are located in the interior of the test chamber (Figs. 7 and 8). The electrohydraulically actuated noise generator can produce an overall SPL of 150 db rms (re: 0.0002  $\mu$ bar) at 760 torr interior to liner at the specimen c.g. The system outputs a continuous spectrum from 100 to 12,000 Hz, which is flat from 100 to 700 Hz with a roll-off of 6 db/octave above 200 Hz. The acoustic liner is sized and shaped to produce the required SPL distribution for a particular spacecraft-shroud configuration. Delta-launched spacecraft require a liner different from that for Agena-launched spacecraft. Figure 10 illustrates a view looking into the test chamber (with end cap removed) depicting the liner used for acoustic testing of Agena-launched spacecraft. This view does not show the termination section because it is attached to the support table located in the end cap. The spectrum is controlled by microphones located inside the test chamber responding to a pre-plotted noise level distribution in the control room complex. The electrohydraulic actuator operates from hydraulic power supplied by a system located in the pedestal pit.

#### Mechanical Vibration System

The vibration system consists of a configuration of five electrohydraulic actuators



Fig. 10. End view of LPS showing interior of test chamber and acoustic liner



interconnected with two structural tables, which permits the three-degree-of-freedom motion. This system is completely housed in the end cap structure, except for the hydraulic power supply which is located in the pedestal pit. Hydraulic power requirements for maximum force output with simultaneous motion of the three degrees of freedom is 105 gpm at 3000 psi. This hydraulic power supply is required for operation of both this system and the acoustic noise system; however, hydraulic power requirement for the latter is only 20 gpm at 3000 psi. The hydraulic fluid is transferred from the power supply to each of these systems through the hydraulic rotary valve at the center of rotation and out the arm through piping to the respective systems.

The vibrators can be operated either on the centrifuge arm together with the other environmental systems or by itself on the seismic mass, as shown in Fig. 6. The degrees of freedom (longitudinal, lateral, and pitch) can be obtained with this system in either orientation; the only difference is that on the centrifuge arm all motion is in the horizontal plane, whereas on the seismic mass all motion is in the vertical plane.

From Fig. 10, the multiaxis motion of this system on the centrifuge arm is as follows: (a) longitudinal is motion along the x axis or thrust axis (longitudinal axis of test chamber); (b) lateral is rectilinear motion along the z axis; and

(c) pitch is rotary motion in the horizontal (x-z) plane about the vertical (y) axis. The motions for the system when oriented on the seismic mass are identical except that they are in the vertical plane rather than the horizontal plane. Explanation of the motion capability requires a description of the shake table arrangements: four actuators are mounted 90 deg apart on the periphery of the interior of the end cap structure. A table designated as the lower vibration table is attached to the moving elements (pistons) of these actuators. When these four actuators are operating in phase, longitudinal or thrusting motion is produced. When the two primary actuators of this system are operating 180 deg out of phase, pitching motion is produced. An upper vibration table structure is mounted to the lower vibration table through a series of hydrostatic bearings and moves relative to the lower table by virtue of imposed motion from the fifth actuator located in the lower table structure. Figure 11 depicts the end cap (on the seismic mass) with the lower vibration table being lowered into place and shows coordinate system with x axis vertical for this orientation. Shown in Fig. 12 is the end cap with lower vibration removed and upper vibration table adjacent to end cap. Note the vacuum seal (or boot) attached to the upper table structure. The vibration system can be operated either manually or automatically from the control room complex. Automatic operation is controlled by magnetic tape signals.

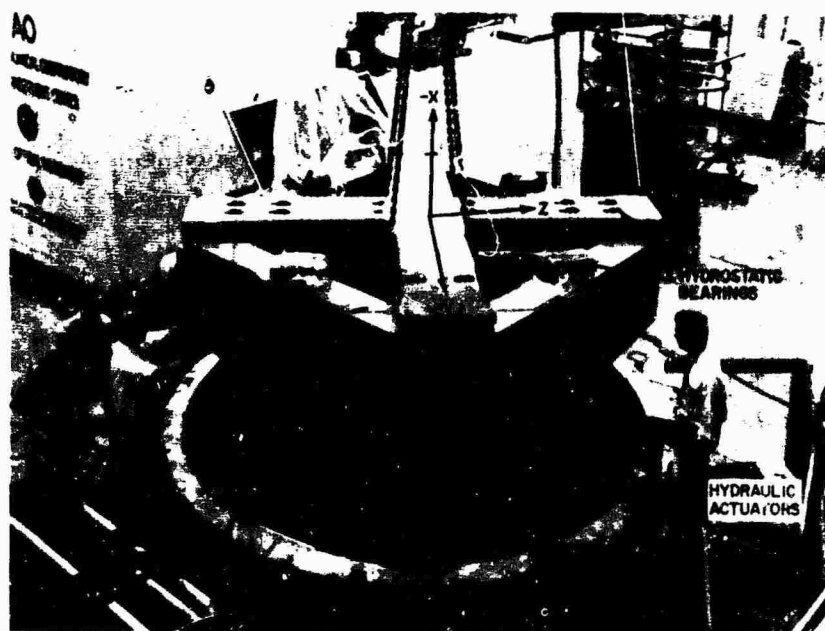


Fig. 11. End cap on seismic mass showing lower vibration table during assembly

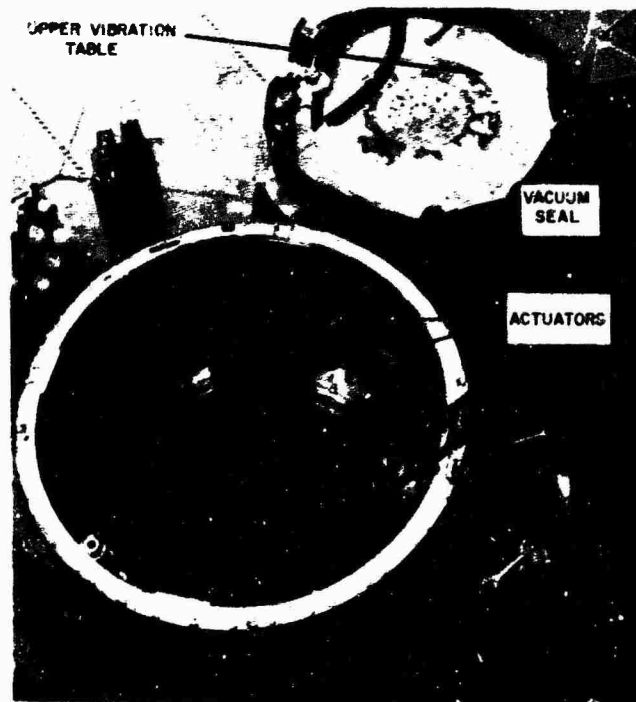


Fig. 12. View looking down on end cap with table removed

#### Controls and Instrumentation

The operation of the LPS facility and all its subsystems is completely controlled from a central complex designated as the control room in Fig. 6. During a combined-environment test, each of the environmental systems is manned by an operator. The control conception includes a master control programming console (MCPC) which permits the test to be under the cognizance of one individual, who can override the control of any of the environmental systems at any time during a test. Figure 13 presents the LPS control conception for a typical test. The status display board, which is illustrated in Fig. 14 in an overall view of the control room, provides a visual indication of both system and equipment status prior to and during all tests. The spacecraft monitor shown in Fig. 13 monitors the response of the spacecraft during the complete test operation. He has a direct link to the master control operator and can abort the test (through this operator) at any time. Audio communication is employed between the control stations represented in Fig. 13 and any other areas deemed necessary for a particular test. For visual monitoring during a test, there is a video system consisting of four closed-circuit TV cameras and two TV monitors. The cameras are strategically located to monitor both the

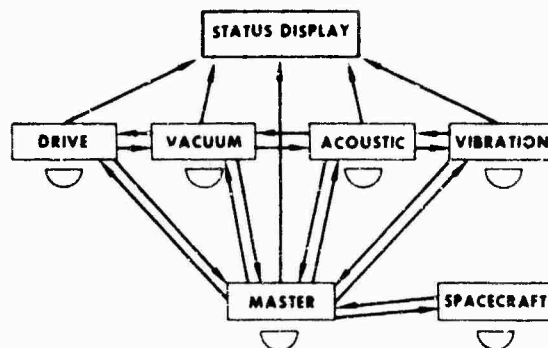


Fig. 13. LPS control conception

LPS system and also the spacecraft which is located in the test chamber. Figure 14 shows the TV monitors on the MCPC, which are monitored continuously during a test. Safety interlocks for both personnel and equipment are provided in the control conception and will not permit any system and/or component operation if condition is not "go." For example, if one of the personnel doors to the rotunda is not locked, the controls for the drive system cannot be operated. Similarly, if someone is inadvertently left in the equipment trench, pit, or rotunda



Fig. 14. LPS control room complex during operational test

during a test, "panic" buttons located in these areas will halt all operations when depressed.

Any facility as sophisticated and complex as the LPS is of little or no value if not provided with an adequate data monitoring or instrumentation system. Therefore, plans were initiated early in the program to procure an instrumentation system which would complement the facility operation. The LPS instrumentation system [4] provides for the acquisition and recording of 24 channels of static data and 56 channels of dynamic data with growth capability of static instrumentation to 48 channels. These data may be recorded on either oscillograph or magnetic tape for permanent record. This system operates in conjunction with slip ring modules at the center of rotation (of the centrifuge arm) which number 650 instrumentation rings and 150 control rings. During an operational test, data are recorded on the rotating structure (generally inside test chamber) and then amplified by conditioning equipment located at the center of rotation. From here, the signals are transmitted through the slip rings to the recording equipment located in the control room, shown in Fig. 14. Instrumentation access to the vacuum-tight test chamber is made possible by instrumentation penetration plates fitted with electrical connectors. These connectors mate the cables on the exterior of the chamber to the cables inside

the chamber, which are routed to transducers, strain gages, thermocouples, etc. Figure 15 shows the cables and penetration plates in a closeup view of the test chamber.

#### OPERATIONAL PROCEDURE

The operation of the facility during a test has been given something of a cursory treatment above. Some very important factors in the overall operational conception were not discussed. These items include handling and loading procedures and safety precautions, just to mention a few. To explain the entire operation, an explanation of the sequence of events for both preparing and conducting the test is necessary.

The spacecraft or specimen is delivered to the high bay area of the building complex and mounted on the end cap, which is resting on the seismic mass. (Reference should be made to Fig. 6 for complete understanding of this operation.) The spacecraft is then instrumented and prepared for the sequence of testing. At this point, the end-cap-spacecraft assembly is transported from the seismic mass in the high bay area into the rotunda and mounted to the test chamber structure. This transportation operation is accomplished with the LPS loading vehicle, which is shown in Fig. 16 approaching

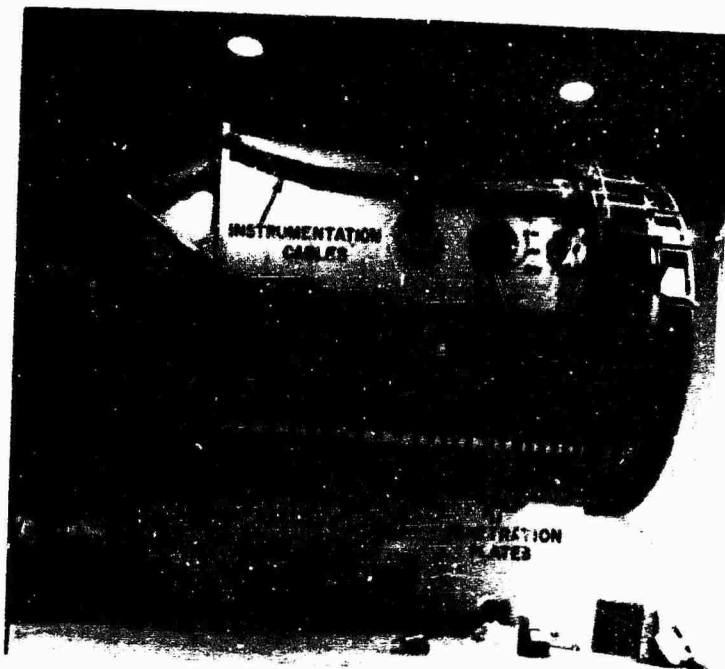


Fig. 15. Closeup of test chamber with end cap removed



Fig. 16. ATS-A prototype spacecraft during loading vehicle pitching operation

the test chamber with a prototype model of the Applications Technology Satellite (ATS). The vehicle, fascinating system in itself, is self-propelled and has six-degree-of-freedom capability, i.e., three translational and three rotational modes of motion. Mounting plates on the vehicle are used to attach to the end cap; the end cap is then lifted and pitched from the vertical to the horizontal position. Figure 16 illustrates the pitching operation. Once the end-cap-spacecraft assembly is in the horizontal position, the vehicle is then driven into the rotunda for the mating operation of the end cap to the test chamber. Figure 17 shows the ATS prototype spacecraft during the final phase of the loading operation. After the end cap has been secured to the test chamber, all systems are readied for the operational test(s).

The actual conducting of the tests was covered, in general, under the preceding section. For all tests, including the sustained acceleration environment, the loading vehicle is detached from the end cap, and the rotunda doors are

closed and pneumatic seals are activated to prevent loss of air from the rotunda during centrifuge rotation. This procedure is followed for both personnel and equipment safety and also for aerodynamic drag reasons. In addition, for all tests, the rotunda and the high bay area (Fig. 6) are restricted areas, and, in most cases, personnel access is prohibited. All operations are performed from the control room where visual observation of the facility and spacecraft is available through the closed-circuit TV system. As a rule, all tests are conducted in the programmed or automatic mode because of the sequence of events of the combinations of environments and also the short duration of the test, i.e., real-time simulation. After completion of a test, the reverse procedure for removal of the end cap from the test chamber is used. In other words, the vehicle is attached to the end cap, which is then removed from the test chamber structure. The end-cap-spacecraft assembly is then transported into the high bay area, pitched into the vertical position, and then placed on the seismic mass.

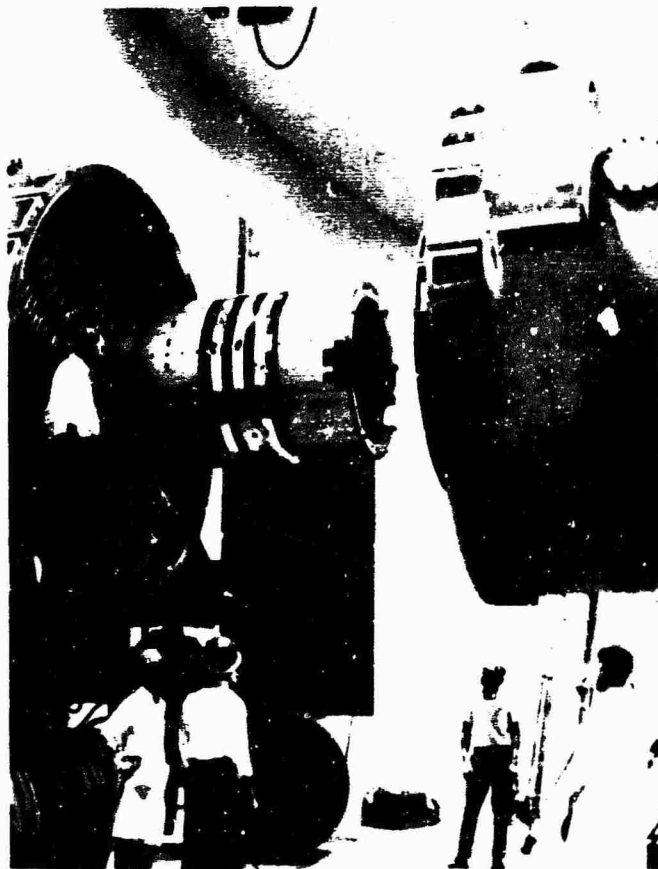


Fig. 17. Placement of ATS-A prototype spacecraft into test chamber

## SPACECRAFT TESTS

The LPS has been an operational test facility for only about one year. However, in this time, the usage rate has been quite high. Table 1 presents a summary of the tests conducted to date. All of the tests listed were made in support of flight program projects, except for the Agena shroud testing, which was conducted under a research task. The combined environmental tests to date have been combinations of vacuum (pressure profile) and acoustics; however, the combination of these together with profiled acceleration have been conducted on nonflight-program-type hardware. Prior to completion of the LPS, it was anticipated that the sustained acceleration (centrifuge) environment would be used more frequently than the other environmental systems. This is verified to some extent in Table 1. As a result, plans were developed early in the design phase of the facility to design and fabricate an end cap which could be used for acceleration testing only. Logistical advantages are:

1. The combined environment end cap could be used for vibration testing on the seismic mass during the same time that the acceleration end cap was being employed for centrifuge testing.

2. Spacecraft preparation could be performed on the combined environment end cap while the acceleration end cap was in use.

Figure 18 shows the acceleration end cap during loading operations for acceleration testing of an engineering model of the International Satellite for Ionospheric Studies (ISIS).

The first combined-environment flight program test was performed on the ATS prototype spacecraft [5], which is shown in Figs. 16 and 17 during the loading operation prior to the test. This test was a combined acoustic-vacuum test conducted in real time to evaluate spacecraft response to the launch conditions for these environments. Figure 19 presents the test specification levels with the actual test chamber conditions monitored during the test. In general, the simulated environments closely approximated the launch environmental specifications. Other combined acoustic-vacuum tests are described in Table 1. Figure 20 illustrates the Goddard Experiment Package (GEP) prototype model during preparation for a pressure profile test. This experiment is a large telescope package for the Orbiting Astronomical Observatory (OAO) spacecraft. It was tested under the dp/dt launch pressure profile conditions primarily to ascertain the venting characteristics

TABLE 1  
Launch Phase Simulator Tests

| Item                           | Test                | Acceleration Level (g) | Test Date                     |
|--------------------------------|---------------------|------------------------|-------------------------------|
| A-IMP-E engineering spacecraft | Acceleration        | 29.0                   | Nov. 16, 1966<br>Mar. 3, 1967 |
| ISIS-A engineering spacecraft  | Acceleration        | 17.0                   | Dec. 13, 1966                 |
| IMP-F prototype spacecraft     | Acceleration        | 36.5                   | Feb. 1, 1967                  |
| OSO-E pointed experiment       | Acceleration        | 21.0                   | Feb. 8, 1967                  |
| Agena shroud                   | Acoustic            | —                      | Feb. 17, 1967                 |
| ATS-A prototype spacecraft     | Vacuum and Acoustic | —                      | Mar. 16, 1967                 |
| OAO 3-bay model                | Vacuum              | —                      | Mar. 30, 1967                 |
| SAO telescope assembly         | Acceleration        | 11.5 & 3.8             | May 3, 1967                   |
| RAE spacecraft E.T.U.          | Vacuum and Acoustic | —                      | July 25, 1967                 |
| OAO-GEP prototype experiment   | Vacuum              | —                      | July 29, 1967                 |
| Nimbus-D prototype experiment  | Acceleration        | 30.0                   | Aug. 7, 1967                  |
| ATS structural model           | Acceleration        | 10.6                   | Oct. 5, 1967                  |

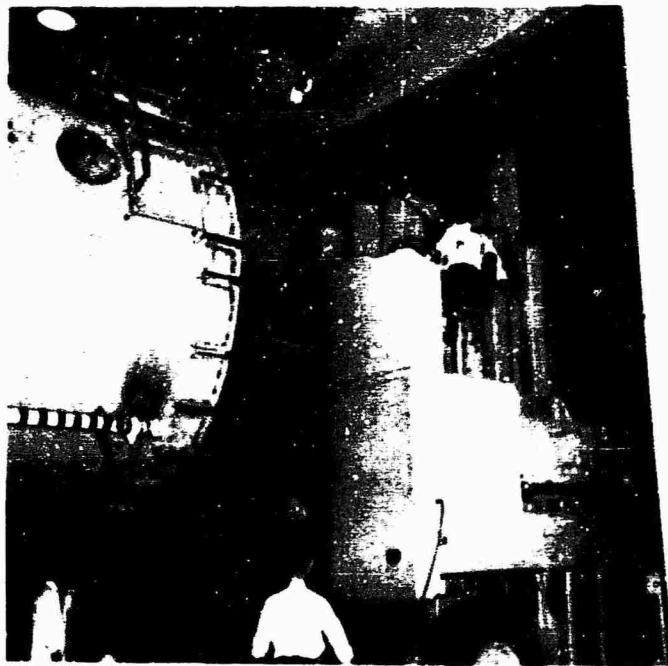


Fig. 18. ISIS-A structural model during loading operation

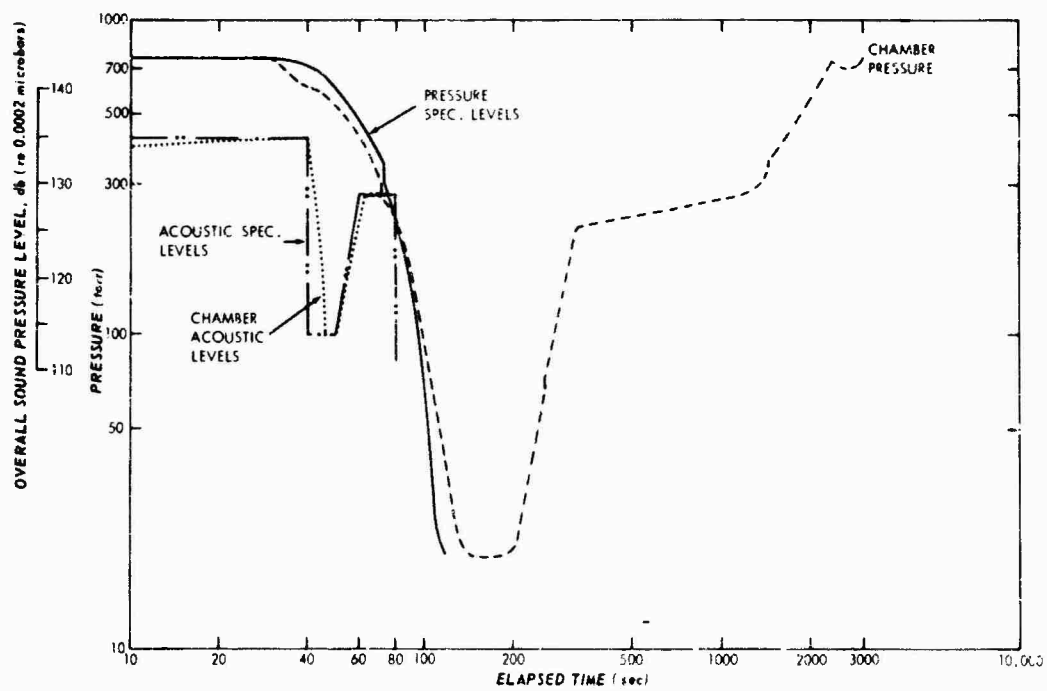


Fig. 19. Acoustic-venting data for ATS-A prototype spacecraft



Fig. 20. OAO-GEP prototype in vertical position during loading operation

of insulation-type blankets and material. The other tests listed in Table 1 were similar in nature to the ones covered here and, consequently, are not discussed any further.

#### DESIGN PHILOSOPHY AND BACKGROUND RESEARCH

The basic philosophy adopted during the design and development of the LPS was that of providing an advanced combined-environment facility that could readily lend itself to future growth capability. Of course, this philosophy is quite obvious since experience has shown that many facilities were usually obsolete a relatively short time after they became operational. Specifically, some of the components or subsystems which may be added or modified to permit increased environmental capabilities for the LPS are described.

1. The test chamber, which was sized for the OAO (or second generation) class spacecraft, can be removed at the attachment to the truss structure and replaced by a larger chamber that can accommodate the Voyager (or third generation) class.

2. An additional two dc drive motors can be added to the present two to increase not only sustained acceleration capabilities, but also onset (acceleration) and deceleration rates.

3. The complete rotating structure was designed with a factor of safety of 2.5 based on material yield points for all loading conditions encountered under normal operation of all systems described here. However, the centrifuge was designed to operate alone at 48 rpm (50 g at spacecraft c.g.) with a factor of safety of 1.5. Use of this capability has already been made, as verified by the sustained acceleration test at 36.5 g of the prototype model of the Inter-Planetary Monitoring Platform (IMP) spacecraft (see Table 1).

4. The data acquisition and recording system was designed with growth capability for additional channels of both static and dynamic data. In conjunction with this, the 650 instrumentation slip rings are more than enough for increased future instrumentation requirements.

Considerable experimental and theoretical research was carried out in support of the design of the LPS. Some of the more significant programs were:



1. Aerodynamic model studies
2. Dynamic model studies
3. Hydraulic shaker development
4. Theoretical dynamics analyses

The aerodynamic model studies [6] were conducted early in the program to determine torque requirements for sizing the drive motors and also to aid in determining the size and shape of the simulator enclosure. The dynamic model investigations [7] served as a tool in the design of the facility and provided such data as natural frequencies, mode shapes, transmissibilities, and damping coefficients for the major modes of vibration. In particular, detailed investigations were made in regard to possible flutter and oscillating conditions induced by a combination of loads resulting from centrifuge arm rotation and vibration system operation at the same time. Much effort was devoted to developing a small combined environmental facility [8] consisting of a 5000-lb electrohydraulic shaker operating on a 20-ft-diam centrifuge. Results and experience from this program, together with research effort in a two-degree-of-freedom hydraulic shaker system, aided to a great extent the development and design of the LPS three-degree-of-freedom vibration system. Of course, numerous theoretical and analytical studies were conducted in the program. A complete systems loads and response analysis was conducted in conjunction with the experimental dynamic model program, and the respective results were in very close agreement. Also, extensive theoretical studies were conducted in the design of the X-type azimuth bearing. These investigations were also performed in conjunction with the dynamic model program.

## CONCLUSIONS

The LPS completely covers in a single exposure the major launch environmental conditions, i.e., steady or sustained acceleration, acoustic noise, altitude variation (pressure), and mechanical vibration. These systems can reproduce the actual launch environment conditions in real time and can be operated in the programmed (automatic) or manual mode. The facility can accommodate the observatory or second generation class of spacecraft that weighs up to 5000 lb and can be defined in a cylindrical envelope 10 ft in diameter and 15 ft long.

Test experience with the LPS has verified to some degree the advantages of combined-environment testing over a combination of single environment tests. These advantages can be summarized in two general categories: (a) This improved simulation permits more thorough evaluation of design features necessary to insure reliability of spacecraft under launch conditions; it also aids in reducing overdesign for ruggedness at the expense of effective spacecraft weight without increasing the risk of underdesign and resultant failure. (b) The LPS serves as a valuable research tool, long desired by the environmental engineer, as a replacement for the cumbersome and costly launch simulations such as sled track or flight test. A considerable time savings for test support is also realized. In other words, only one test setup has to be made for testing on the LPS, whereas separate preparations are required when testing under individual environments.

Of course, facilities like the LPS will not make the present single environment tests obsolete; however, they should help put environmental testing on a more scientific basis and thus help to increase spacecraft reliability and efficiency of design.

## REFERENCES

1. E. J. Kirchman "Launch Phase Simulator," AIAA Publ. CP-11, Nov. 1964
2. W. J. Neff and R. A. Montes de Oca, "Launch Environment Profiles for Sounding Rockets and Spacecraft," NASA TN D-1916, Jan. 1964
3. P. J. Alfonsi, "The Vibration Response of an Orbiting Geophysical Observatory Spacecraft Full-Scale Structural Model to a Simulated Launch Acoustic Environment," NASA-GSFC Rept. X-320-66-353, Aug. 1966
4. H. D. Cyphers and F. J. Holley, "Automatic Calibration and Environmental Measurement System for Launch Phase Simulator," Shock and Vibration Bull. No. 36, Part 6, pp. 207-214, Feb. 1967
5. L. J. Demas, "Real-Time Combined Acoustic-Vacuum Testing of Spacecraft," Shock and Vibration Bull. No. 37, Part 5, 1968
6. R. I. Windsor, "Launch Phase Simulator Aerodynamic Model Study," NASA-GSFC Rept. X-321-63-268, Jan. 1964
7. C. J. Arcilesi and L. R. Bruck, "Investigation of Dynamic Characteristics of a 1/20th

Scale Model of the Launch Phase Simulator," Shock and Vibration Bull. No. 35, Part 3, pp. 207-225, 1966

8. E. J. Skolka, "Hydraulic Exciter Combined Environment Tests," Shock and Vibration Bull. No. 36, Part 3, pp. 119-138, Jan. 1967

\* \* \*

## DEVELOPMENT OF SIMULATED AIRCRAFT DELIVERY USING A ROCKET SLED\*

William R. Kampfe and K. M. Timmerman  
Sandia Corporation  
Albuquerque, New Mexico

At Sandia Corporation's rocket sled test track facility, tests are being conducted that simulate aircraft delivery of a wide variety of systems. The device being tested is attached to a rocket sled and accelerated to the test velocity, where it is then ejected from the rocket sled into a ballistic trajectory that results in the simulated aircraft delivery. This simulated aircraft delivery testing technique has been developed in essentially three stages using four different sled designs over the past five years. Having begun with aircraft-type ejection racks on tower sleds, the technique has been continuously improved to meet the ever-changing requirements for aircraft-delivered systems. Present ejector sleds have built-in air actuators for ballistic trajectory capabilities well beyond the earlier tower sleds.

Simulating aircraft delivery by rocket sleds has numerous advantages: (a) a high degree of ballistic accuracy and repeatability, achievable under the controlled semilaboratory conditions of the rocket sled track; (b) excellent photographic and ballistic data, obtainable because of the accuracy; (c) temperature preconditioning of test units until immediately prior to launch; (d) ease of scheduling, as track time is more readily available than aircraft time; (e) lower cost.

Development of this technique, present capabilities, and plans for improved trajectory instrumentation are discussed. A photometric ballistic range was installed in conjunction with the rocket sled track for recording trajectory data. In the near future, a laser tracking system, now under development by Sylvania, will replace this ballistic range for more flexible and automated trajectory data gathering.

### INTRODUCTION

At Sandia Corporation's rocket sled test track facility, tests are being conducted that simulate aircraft delivery of a variety of systems. The device being tested is attached to a rocket sled and accelerated to the test velocity, where it is then ejected from the rocket sled into a ballistic trajectory that results in the simulated aircraft delivery.

The development of this technique grew out of an original requirement that called for the impacting of a weapon system at a low angle onto a horizontal target under closely controlled conditions to permit detailed high-speed motion picture photography of the resultant weapon response. Actual delivery by aircraft was considered; however, aircraft are not capable of the extremely accurate deliveries that are required for the placing of a weapon in the immediate field of view for close-up, detailed motion pictures. In addition, aircraft delivery is an

expensive way to conduct this type of study. Other available test facilities were screened, but the desired impact velocity conditions were beyond their capabilities.

Rocket sleds have been used, for some time, for impact testing at high velocities. Up to this time, however, rocket sleds have had only the capability of generating a horizontal component of velocity. These lay-down impact test requirements called for the weapon to have a vertical component of velocity also.

### TOWER ROCKET SLED WITH EJECTION RACK

Since this test series called for only a limited number of tests at the same conditions, a simple solution was sought using a rocket sled. A 10-foot-high tower rocket sled was designed to carry the weapon. The sled was constructed of steel tubing in an A-frame design to allow the

\*This work was supported by the United States Atomic Energy Commission.

weapon to be suspended from the top of the frame in an Aero 7A aircraft ejection rack (Fig. 1). Since this rack was designed for use on aircraft, it only had 7500 ft-lb of ejection energy. The combined velocity resulting from the 10-ft sled drop height and the downward ejection velocity still did not provide the necessary component of vertical velocity. A 15-ft pit, dug immediately off of the end of the track, provided the necessary additional drop height for generating the required vertical velocity component. The sled was launched to the desired horizontal velocity, at which time the unit was ejected downward through the sled frame. The ejection point was selected to allow the sled to be stopped on the track, but still permit the unit to clear the end of the track and continue into the target pit.

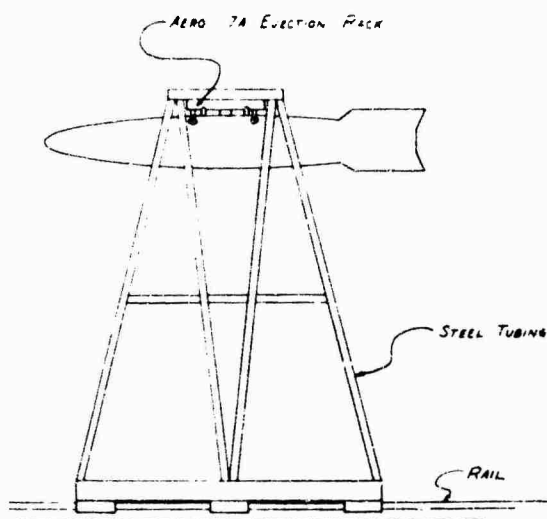


Fig. 1. Ten-foot steel tower sled with Aero 7A ejection rack in downward position

This original technique proved very successful from the standpoint of accuracy. The impact point was highly predictable and the desired conditions readily obtainable. Therefore, after an original series of eight tests, there was a considerable amount of interest in investigating the further potential of this system.

The original tests had been conducted on a parachute-retarded weapon system. For this original series, however, the parachute was left out of the weapon and the impact velocities were controlled to match the conditions resulting from the use of the parachute. A more desirable test would be one that allowed for including

the effects of the parachute. It would require a higher sled velocity and a longer time of flight to deploy the parachute completely. The additional delivery velocity would be necessary to overcome the effects of the parachute on the ballistic trajectory, as the resultant impact velocity had to be the same as on the earlier tests where the parachute had been neglected.

The increased velocity could be achieved solely by increasing the sled velocity, since the test trajectory was predominantly flat. The increased flight time was achieved by mounting the Aero 7A ejection rack inverted on the sled and ejecting the weapon upward (Fig. 2). Although the resultant vertical velocity would be the same as in the first case, when the unit was ejected down, the ballistic trajectory was lengthened by imparting the ejection energy upward, thereby allowing for enough time to deploy the parachute completely. The effect of the parachute upon the vertical velocity was slight because of the flatness of the trajectory.

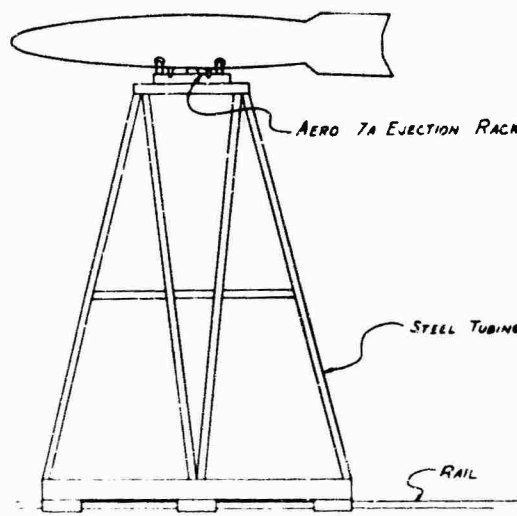


Fig. 2. Ten-foot steel tower sled with Aero 7A ejection rack in upward position

#### AIR-POWERED EJECTOR SLED

The original tests conducted using this technique were concentrated within a narrow band of requirements for structural evaluations only. As the number of tests increased, however, the advantages of conducting aircraft simulated tests from rocket sleds under semi-laboratory conditions became more apparent. As a result, the test requirements increased,

requiring an increase in the capabilities of the rocket sleds. Air-powered ejection systems replaced the aircraft ejection racks to provide greater ejection energy. The rocket sled velocity was continually increased until it reached the maximum capabilities of existing equipment.

Up to this point, the rocket sled aircraft simulation technique had developed by a process of evolution to meet new requirements as they occurred. Continued interest in this type of testing prompted the development of a new testing capability to meet the complete range of conditions associated with aircraft-delivered systems. This required the development of a new sled system capable of delivery velocities up to Mach 1.6. This provided the necessary range of dynamic pressures that were required to make aerodynamic studies as well as studies associated strictly with the structural response of a weapon impacting a target.

The new sled was designed and built to incorporate a complete air actuator. The actuator cylinder, the high pressure reservoir for powering the actuator piston, and the cushion reservoir for stopping the actuator piston after the power stroke were all built into the sled's structural members (Fig. 3). The actuator cylinder has a 5.5-in. I.D. and is capable of generating 120,000 ft-lb of energy. It is sandwiched between the water brake scoop and the rocket thrust plate, acting as the structural support member for both the rocket thrust and water brake sled recovery forces (Fig. 4). The four lower members that meet at the base of the actuator cylinder, along with the member running laterally across the sled between the front shoes, are connected through manifolds and make up the high pressure reservoir for the fire pressure (Fig. 3). They can be pressurized to a safe working pressure of 2500 psi through the filler valve on the left front of the sled (Fig. 3). The two front smaller tubes extending from the front shoes up to the top of the cylinder, along with the volume above the piston in the cylinder, serve as a cushion reservoir for stopping the piston after the test item has been ejected (Fig. 3). This cushion volume has a maximum safe working pressure of 3000 psi. The piston is designed so that the fire pressure is originally acting only on the circumferential area of the piston and there is no fire pressure acting on its base (Fig. 5) until after the explosive valve (Fig. 4) is triggered. The explosive valve is initiated by a 28-v electrical pulse that is picked up at the desired point of ejection from a trackside power source by the two knife blades shown in Fig. 3. Triggering the explosive valve allows the fire pressure to act on the base of the piston through the trigger line

inlet, causing an unbalance of pressure and forcing the piston to move upward releasing the lower O-ring seal (Fig. 5). When the lower O-ring seal is broken, the entire volume of fire pressure acts on the base of the piston. For safety reasons, the trigger line has a 1/16-in.-diam hole drilled into it so that if, for some reason, the lower O-ring on the piston has a small leak, pressure could not build up in this line and cause the actuator to fire prematurely. The same air pressure that triggers the actuator piston through the explosive valve is supplied to the two pneumatically actuated lug latches shown in Fig. 4. By this means, the test item is released and ejected from the sled simultaneously, using only one explosive valve. This valve can be reused by the installation of a replacement kit.

## PRESENT CAPABILITIES

The pneumatically actuated lug latches are spaced 30 in. apart to accommodate most test items and have adjustments of  $\pm 0.25$  in. so that the test item c.g. can be placed directly over the ejector or actuator thrust column. Because every effort was made to make multiple use of the sled's structural members and the sled height was kept to 2.5 ft above the rail, this sled only weighs 730 lb. This sled can accommodate 10 5-in.-diam rocket motors. The number of rocket motors is varied to give the required sled velocity. The sled is recovered with the water brake, which is a combination probe and vertical momentum exchange brake, capable of developing in excess of 100,000 lb of braking force. This sled has been successfully stopped from a velocity of 1750 fps in less than 700 ft of track.

To date, this sled has been used for approximately 150 tests; one of its greatest accomplishments has been to accelerate a 2000-lb test item to 1240 fps and then eject it 60 ft vertically. Also, 600-lb test items have been accelerated to 1650 fps and then ejected 75 ft vertically.

In August 1966, Sandia's new 5000-ft track was completed. Since the gage of the new track is 22 in. as compared to 56.5 in. for the old track, a new ejector sled, which is essentially the same as the preceding ejector sled with only minor changes (Fig. 6), was designed and built. The fire reservoir volume was doubled; and the ejector cylinder is removable so that cylinders of different diameters can be used. With the added fire volume, 160,000 ft-lb of ejection energy can be developed. The pneumatic lug latches are adjustable to any position atop the

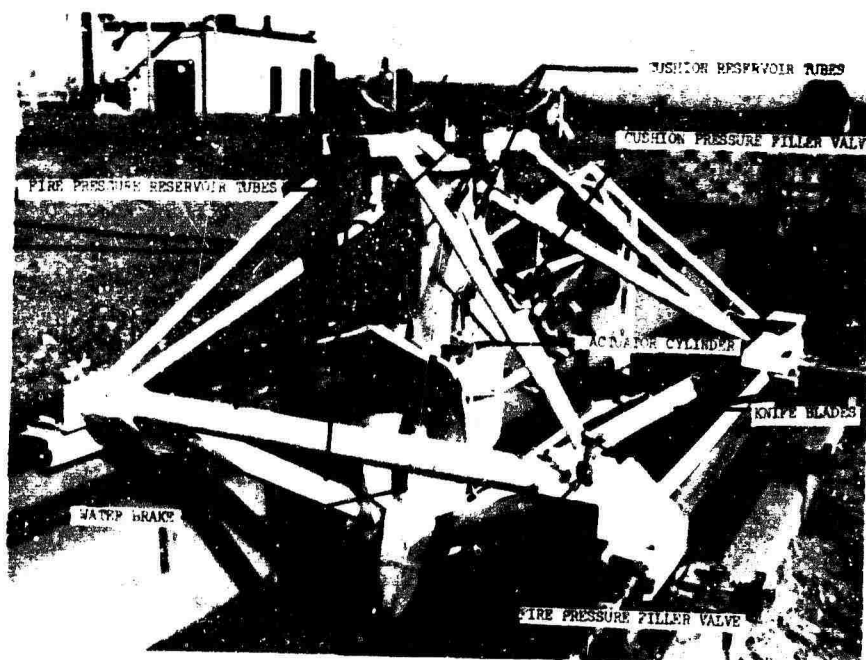


Fig. 3. Ejector sled with built-in actuator

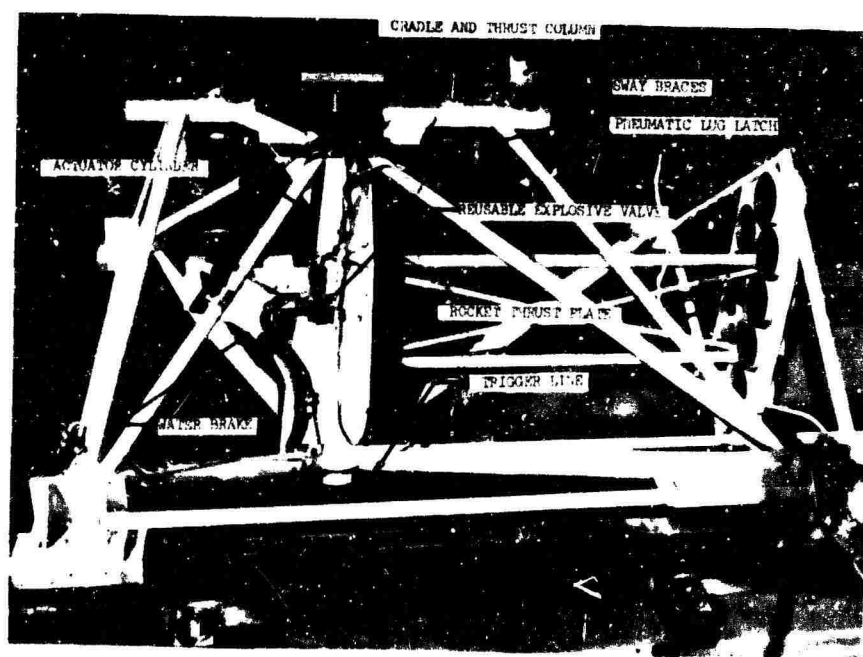


Fig. 4. Ejector sled with built-in actuator

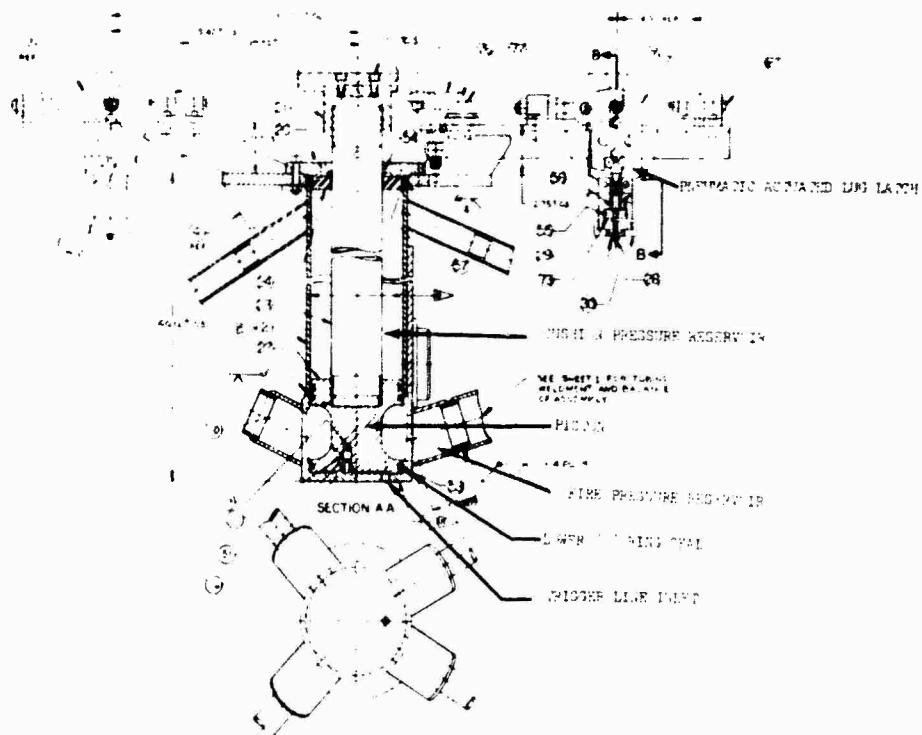


Fig. 5. Schematic of built in actuator

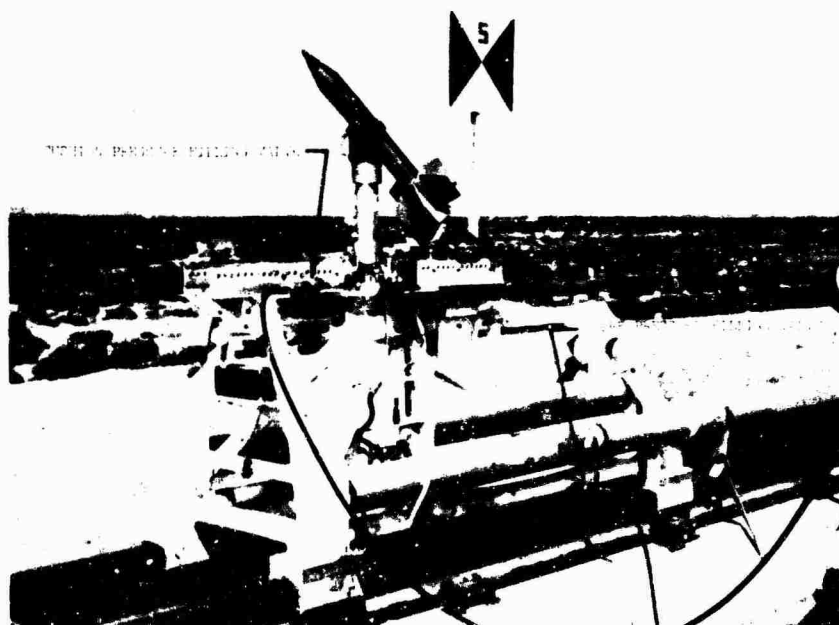


Fig. 6. New 22-m. ejector sled for 5000-ft track

sled, giving more flexibility for attaching test items which may have lug spacing different from the standard 30 in. This additional lug adjustability also allows for last-minute adjustment of the lug latches to move the c.g. over the thrust column if the c.g. of the test item is not where expected. With this new ejector sled on the new track, a 2000-lb test item can be accelerated to 1620 fps and then ejected 80 ft vertically.

Along with the new requirements that prompted the building of the new ejector sleds, temperature preconditioning requirements from  $-65^{\circ}\text{F}$  to  $+275^{\circ}\text{F}$  had to be met. These preconditioning requirements are achieved while the units are on the sled by using either a cold chamber for cold soaking the units with  $\text{CO}_2$ , or a heating array that can hot soak the units either with heated air or radiant heat from quartz heat lamps (Fig. 7). These chambers are built in a clamshell configuration that surrounds the units on board the sleds. The chambers are remotely opened and raised free of the test unit just seconds before sled launch.

A new concrete horizontal target 120 ft wide, 400 ft long, and 12 in. thick was placed from 650 to 1050 ft off the end of the track. With the target 120 ft wide, tests can be conducted with cross winds up to 35 knots without



Fig. 7. Clamshell heating array

danger of the unit drifting far enough to miss the target. Four rows of vertical targets 15 ft high and 80 ft wide can be placed on the horizontal target. Each row consists of four individual targets 15 ft high, 20 ft wide, and 1 ft thick, which are supported by concrete gussets 15 ft high and 18 in. thick. These targets are portable so that they can be put up and taken down in less than a week (Fig. 8).



Fig. 8. Portable vertical targets



The following equations describe the theoretical behavior of the ejector:

$$E_0 = \left[ 540 - \frac{635}{(1.5 + 0.165x_0)^{0.4}} \right] P_{1f} + \left[ 119 - \frac{76.3}{(0.330 - 0.116x_0)^{0.4}} \right] P_{1c} \quad (1)$$

$$x_0 = \frac{0.330 - 0.256\beta}{0.116 + 0.028\beta} \quad (2)$$

$$\beta = \left[ \frac{P_{1c}}{P_{1f}} \right]^{0.714} \quad (P \text{ in psi}) \quad (3)$$

where  $E_0$  is the total energy delivered to the payload and thrust column prior to ejection which occurs when the payload separates from the thrust column;  $x_0$  is the length of the power stroke to ejection;  $P_{1c}$  is the initial cushion pressure and  $P_{1f}$  is the initial fire pressure, with  $\beta$  an arbitrary coefficient expressing the relationship between  $P_{1c}$  and  $P_{1f}$ .

The maximum allowable final cushion pressure,  $P_{2c}$ , has been set at 3000 psi. This value can be substituted along with the initial cushion pressure  $P_{1c}$  into the following equation for the total length of stroke:

$$x_2 = 2.85 \left[ 1 - \left( \frac{P_{1c}}{P_{2c}} \right)^{0.714} \right] \quad (4)$$

which, when substituted in

$$E_{min} = \left\{ \left[ 3.75 - \frac{4.41}{(1.5 + 0.165x_2)^{0.4}} \right] P_{1f} + \left[ 0.285 - \frac{0.530}{(0.330 - 0.116x_2)^{0.4}} \right] P_{1c} \right\} \cdot 144. \quad (5)$$

gives the value of ejection energy carried away by the test item.

A computer program which has been written for these equations solves the equations as functions of the initial fire and cushion pressures  $P_{1f}$  and  $P_{1c}$ . The resultant solutions are printed out in tables from which the appropriate solutions can be selected for each particular case.

Test requirements are usually given in terms of test item weight  $w_b$  and the maximum unit height  $h$  after ejection. Knowing the weight of the thrust column  $w_c$ , the energy at ejection

required to attain  $h$  can be calculated from the equation

$$E_0 = (w_b + w_c)h \quad (6)$$

where  $\eta$  is a constant representing the efficiency of the thermodynamic behavior of the particular sled and is arrived at by empirical means; for the present systems  $\eta$  is 0.85.

As an example, take the case of a 700-lb unit which is to be ejected to an apogee of 25 ft; the thrust column weight is 21 lb. Substituting into Eq. (6) gives

$$0.85 E_0 = (700 + 21)25$$

$$E_0 = \frac{18,025}{0.85} = 21,200 \text{ ft} \cdot \text{lb.}$$

Referring to Table 1, where  $P_{1c}$  is 50 psi, the value of  $P_{1f}$  that gives the approximate value for  $E_0$  of 21,200 is a  $P_{1f}$  of 575. The  $E_{min}$  is 17,208, which compares with the resultant potential energy change

$$P.E. = w_b h = 700 \cdot 25 = 17,500.$$

If the maximum thrust-column force  $F_1$  in Table 1 is excessive, a different initial cushion pressure, and thus a different table, should be selected where the  $F_1$  is acceptable.

## INSTRUMENTATION

Instrumentation for the first tests consisted mainly of motion picture photography, as the original tests were run with the express purpose of obtaining detailed motion pictures. When the test parameters were expanded, telemetry systems were added to the test system for transmitting environmental and functional data that occurred during the test. A photometric ballistic range was permanently installed at the end of the track. The output from this photometric ballistic range is 70-mm film, which, when read, provides raw data for insertion into a ballistic trajectory computer program giving three-dimensional position and velocity.

A mobile, automatic motion data system (laser tracker) now under development by Sylvania for Sandia Corporation, is scheduled to arrive at Sandia in January 1968 for final checkout. This laser tracker will replace the original photometric ballistic range. The system uses a servo-controlled mirror to direct a modulated CW laser beam at the target which

TABLE 1  
Ejection Calculations for 22-inch Ejection Sled at PIC = 50

| P1F        | X 0     | E 0         | X 2     | E MIN       | F 1         |
|------------|---------|-------------|---------|-------------|-------------|
| 100.00000  | 1.30710 | 1164.03689  | 2.69680 | -8122.30446 | 1545.00000  |
| 125.00000  | 1.50933 | 1920.91194  | 2.69680 | -6789.08506 | 2140.00000  |
| 150.00000  | 1.65527 | 2760.51051  | 2.69680 | -5455.86566 | 2735.00000  |
| 175.00000  | 1.76812 | 3660.85432  | 2.69680 | -4122.64626 | 3330.00000  |
| 200.00000  | 1.85797 | 4608.00247  | 2.69680 | -2789.42686 | 3925.00000  |
| 225.00000  | 1.93150 | 5592.49732  | 2.69680 | -1456.20746 | 4520.00000  |
| 250.00000  | 1.99299 | 6607.59640  | 2.69680 | -122.93805  | 5115.00000  |
| 275.00000  | 2.04529 | 7648.30574  | 2.69680 | 1210.23135  | 5710.00000  |
| 300.00000  | 2.09042 | 8710.81247  | 2.69680 | 2543.45075  | 6305.00000  |
| 325.00000  | 2.12983 | 9792.13256  | 2.69680 | 3876.67015  | 6900.00000  |
| 350.00000  | 2.16458 | 10889.88226 | 2.69680 | 5209.88955  | 7495.00000  |
| 375.00000  | 2.19551 | 12002.12399 | 2.69680 | 6543.10895  | 8090.00000  |
| 400.00000  | 2.22324 | 13127.25932 | 2.69680 | 7876.32836  | 8685.00000  |
| 425.00000  | 2.24826 | 14263.95253 | 2.69680 | 9209.54776  | 9280.00000  |
| 450.00000  | 2.27097 | 15411.07486 | 2.69680 | 10542.76716 | 9875.00000  |
| 475.00000  | 2.29170 | 16567.66294 | 2.69680 | 11875.98656 | 10470.00000 |
| 500.00000  | 2.31071 | 17732.88730 | 2.69680 | 13209.20596 | 11065.00000 |
| 525.00000  | 2.32820 | 18906.02810 | 2.69680 | 14542.42536 | 11660.00000 |
| 550.00000  | 2.34438 | 20086.45625 | 2.69680 | 15875.64476 | 12255.00000 |
| 575.00000  | 2.35938 | 21273.61835 | 2.69680 | 17208.86417 | 12850.00000 |
| 600.00000  | 2.37334 | 22467.02486 | 2.69680 | 18542.08357 | 13445.00000 |
| 625.00000  | 2.38636 | 23666.24033 | 2.69680 | 19875.30297 | 14040.00000 |
| 650.00000  | 2.39855 | 24870.87556 | 2.69680 | 21208.52237 | 14635.00000 |
| 675.00000  | 2.40999 | 26080.58115 | 2.69680 | 22541.74177 | 15230.00000 |
| 700.00000  | 2.42074 | 27295.04209 | 2.69680 | 23874.96117 | 15825.00000 |
| 725.00000  | 2.43087 | 28513.97331 | 2.69680 | 25208.18058 | 16420.00000 |
| 750.00000  | 2.44044 | 29737.11592 | 2.69680 | 26541.39998 | 17015.00000 |
| 775.00000  | 2.44948 | 30964.23399 | 2.69680 | 27874.61938 | 17610.00000 |
| 800.00000  | 2.45806 | 32195.11195 | 2.69680 | 29207.83878 | 18205.00000 |
| 825.00000  | 2.46620 | 33429.55206 | 2.69680 | 30541.05818 | 18800.00000 |
| 850.00000  | 2.47394 | 34667.37274 | 2.69680 | 31874.27758 | 19395.00000 |
| 875.00000  | 2.48130 | 35908.40646 | 2.69680 | 33207.49699 | 19990.00000 |
| 900.00000  | 2.48833 | 37152.49864 | 2.69680 | 34540.71639 | 20585.00000 |
| 925.00000  | 2.49503 | 38399.50608 | 2.69680 | 35873.93579 | 21180.00000 |
| 950.00000  | 2.50144 | 39649.29596 | 2.69680 | 37207.15519 | 21775.00000 |
| 975.00000  | 2.50757 | 40901.74477 | 2.69680 | 38540.37459 | 22370.00000 |
| 1000.00000 | 2.51345 | 42156.73749 | 2.69680 | 39873.59399 | 22965.00000 |
| 1025.00000 | 2.51908 | 43414.16677 | 2.69680 | 41206.81339 | 23560.00000 |
| 1050.00000 | 2.52449 | 44673.93231 | 2.69680 | 42540.03279 | 24155.00000 |
| 1075.00000 | 2.52969 | 45935.94012 | 2.69680 | 43873.25220 | 24750.00000 |
| 1100.00000 | 2.53468 | 47200.10213 | 2.69680 | 45206.47160 | 25345.00000 |
| 1125.00000 | 2.53950 | 48466.33567 | 2.69680 | 46539.69100 | 25940.00000 |
| 1150.00000 | 2.54413 | 49734.56284 | 2.69680 | 47872.91040 | 26535.00000 |
| 1175.00000 | 2.54860 | 51004.71040 | 2.69680 | 49206.12980 | 27130.00000 |
| 1200.00000 | 2.55291 | 52276.70930 | 2.69680 | 50539.34921 | 27725.00000 |
| 1225.00000 | 2.55708 | 53550.49422 | 2.69680 | 51872.56861 | 28320.00000 |
| 1250.00000 | 2.56110 | 54826.00354 | 2.69680 | 53205.78801 | 28915.00000 |
| 1275.00000 | 2.56499 | 56103.17888 | 2.69680 | 54539.00741 | 29510.00000 |
| 1300.00000 | 2.56875 | 57381.96497 | 2.69680 | 55872.22681 | 30105.00000 |
| 1325.00000 | 2.57240 | 58662.30935 | 2.69680 | 57205.44621 | 30700.00000 |

carries a cooperating retroreflector. The reflected signal is redirected by the same mirror to the receiver. Angular encoders with digital outputs are attached to the mirror and tracking mount shafts. The output from this system will be in a digital format compatible with available computers; therefore, complete ballistic trajectory data can be available in a matter of hours. This will provide a distinct advantage over the photometric system, the data from which had to be hand read from data film and punched onto data cards prior to insertion into the computer. Also, the automatic tracking feature of the laser tracker will provide motion picture and TV monitoring of the test.

### CONCLUSIONS

The advantages of simulating aircraft delivery using a rocket sled are:

1. A high degree of ballistic accuracy and repeatability, achievable under the controlled semilaboratory conditions of the rocket sled track (release velocity can be controlled to  $\pm 0.5$  percent, release point is physically predetermined, thus giving high accuracy upon point of impact);

2. Excellent photographic and ballistic data, obtainable because of the accuracy;

3. Temperature preconditioning of test units until immediately prior to launch;

4. Ease of scheduling, as track time is more readily available than aircraft time;

5. Lower cost.

### DISCUSSION

Voice: What acceleration levels on ejection did you have on the piston? — on the sled?

Mr. Kampfe: These can go as high as 100 g. It is a function of the test item being ejected.

When we stop the piston in the sled a higher fire pressure is required. This sometimes exceeds the acceleration loads that the units can take. That is why we allow it to go out the top.

\* \* \*

## AERODYNAMIC NOISE INVESTIGATION IN A SHORT-DURATION SHOCK TUNNEL

David H. Ross  
Aerospace Corporation  
El Segundo, California

The Aerospace Corporation low speed shock tunnel was used to determine fluctuating pressure levels on the surface of Titan III models. This novel employment of the shock tunnel permits rapid and cheap model testing, thus assisting in the prediction of booster-vehicle acoustic environment. The configurations tested were 1:30 scale models of the Titan IIIA (cone-cylinder-core only) and the Titan IIIC with both 120-in.-diam and 156-in.-diam solid rocket motor boosters attached to the core.

The electrical signals from the high-frequency, flush-mounted pressure transducers were digitized and then spectrally analyzed by digital computer. These model spectra were scaled for comparison with flight data on the basis of dynamic pressure  $q$  and Strouhal frequency  $fD/U$ .

The model and full-scale data compared favorably for the one station available from a Titan IIIA flight (core only) and Titan IIIC flight (core plus 120-in. solids). Spectral distributions were similar and the overall and 1/3-octave-band sound pressure levels were within 2 db for both the model and full-scale results, when scaled as above. The values for the 156-in. solid configuration were slightly higher at a given position than those for the 120-in. solid configuration; the difference was 0 to 3 db. Those positions on the core body in the plane of the solid booster (i.e., under the motor body) produced fluctuation about 8 to 10 db higher than the positions 90 deg from that plane (away from the direct influence of the boosters).

### INTRODUCTION

This study investigated simulation of the aerodynamic noise environment of a booster-rocket launch vehicle during the transonic portion of a launch trajectory. The usual method of providing this simulation is to mount a scale model of the vehicle in a fairly large continuous-flow wind tunnel. This report, however, describes the use of a short-duration shock tunnel for this purpose.

The aerodynamic noise environment is produced by the surface pressure fluctuations induced by the turbulent boundary layer and by interactions of the boundary-layer flow with shock waves, surface discontinuities, and other disturbances. The most common measurements of these fluctuations for engineering purposes are the total variance or rms fluctuation level and the power spectral density (or its related forms integrated over fixed bandwidths, the 1/3-octave-band or octave-band spectra).

The parameters which must be reproduced or accounted for in the simulated model flow are the Mach number, Reynolds number, and

dynamic head of the flow, as well as the dimensionless fluctuation frequency or Strouhal number  $fD/U$ . The flow Mach number should be reproduced as nearly as possible since shock wave locations and shock-wave/boundary layer interaction will be a strong function of this parameter. On the other hand, the major requirement for the Reynolds number is that it be high enough to ensure a well-developed turbulent boundary layer in the region of interest. There is some evidence of Reynolds number effects, but these seem to be in the nature of slow trends rather than strong functions of Reynolds number. Since it is very difficult to realize the very high dynamic pressures found in free flight within a wind tunnel (because of high pressure and high power requirements), it is customary to rely upon the frequently demonstrated experimental result that the surface pressure fluctuations are at least approximately proportional to the dynamic pressure  $q$ . While it is clear that the fluctuation frequencies must scale with a Strouhal number, selection of the appropriate length scale or scales presents a problem for adequate model-to-full-size scaling. This point is discussed later in this report.

The investigation described here represents a scale-model simulation of the aerodynamic noise values for selected points on three configurations of the Titan III launch booster vehicle. The transducer locations were selected with a view toward obtaining information on the role of the bow shocks from the strap-on solid rocket motor casings on the Titan IIIC vehicle.

The remainder of this report presents the experimental methods and results of a novel approach to the aerodynamic noise simulation environment for the scale models mentioned above. This approach employs a short-duration shock tunnel to achieve a few milliseconds of test time at the desired Mach number. The test conditions were calculated to yield a turbulent boundary layer on the model surface in the regions of interest.

This unconventional use of a shock tunnel to obtain unsteady aerodynamic data has good and bad features when compared with the usual continuous-flow facility.

The shock tunnel permits relatively inexpensive and rapid tests to be made. A relatively high Reynolds number per foot of model is available during the test time without the expenditure of the large amounts of power required by continuous-flow tunnels. In addition, the relatively brief period of flow means that the pressure transducers are not subjected to appreciable heating and permits the use of rapid-response piezoelectric crystal transducers.

However, the brief running times available do pose certain problems, four of which are discussed below. Of these, two are of a fundamental nature and two concern data acquisition and analysis.

The first fundamental problem concerns the time required to establish a reasonably uniform and steady mean flow about the model, and for the boundary layer to grow to an equilibrium condition. Consideration of the pressure traces from these tests and of the results from the simplified Rayleigh boundary-layer growth problem suggests that the flow establishment time is substantially less than the test time for the applicable conditions.

A fundamental limitation to the lowest significant frequencies that can be determined is provided by the brief test time. Both intuition and consideration of stochastic process theory indicate that there can be virtually no information yield for frequencies less than the reciprocal of the test time. In fact, sampling,

signal-to-noise, and statistical considerations indicate that the lower frequency limit should be considered to be 2 to 10 times that mentioned above.

In addition, the brief test time and the high frequencies make stringent demands upon the frequency response and resolution of the pressure transducers, the electronic instrumentation, and the data analysis system. The brief test period requires digital computer correlation function and spectral analysis programs for proper data reduction.

This report discusses how the short-duration test technique was employed to advantage and how the problems affected the results or how they were circumvented.

## TEST FACILITY AND MODEL

The tests were conducted in the Aerospace Corporation Aerodynamics and Propulsion Research Laboratory low speed shock tunnel facility. Figure 1 is a sketch of the tunnel. Since a detailed description of this facility and its operating characteristics are contained in a report by Varwig and Rosenman [1], only a brief discussion is presented here. A sting-mounted model is contained in a large, evacuated test chamber; a high-pressure driver-gas chamber is attached to one end of the test chamber, isolated from it by a diaphragm. A test is initiated by bursting the diaphragm and producing a shock wave, which propagates down the test chamber and passes over the model. The gas in the test chamber is compressed and accelerated by the shock wave and flows past the model at a predetermined Mach number;  $M = 1.1$  in the tests discussed here. The test time was about 3 msec for this condition.

The model employed was a 1:30 scale model of the Titan III. Three configurations were tested: (a) the Titan IIIA, which is the core of the Titan IIIC and is essentially a cone-cylinder body; (b) the Titan IIIC with the standard 120-in.-diam solid rocket motor (SRM) booster bodies strapped onto the core body; and (c) the Titan IIIC with 156-in.-diam SRM bodies. Drawings of these models are shown in Fig. 2, where the six pressure transducer locations are noted. Figures 3 and 4 are photographs of the model mounted in the tunnel.

The models differed from the full-scale vehicle in one important respect: the cylinder of the core body was extended forward in order to ensure a fully developed turbulent boundary layer in the region where the pressure

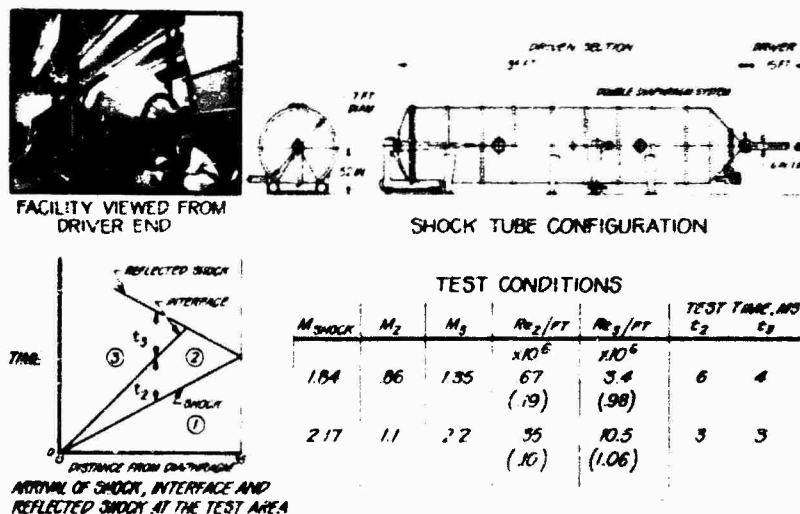


Fig. 1. Diagram and photograph of the Aerospace Corporation low speed shock tunnel (table shows typical operating conditions)

transducers were located. In addition, two boundary-layer trips of the "Hama" type were used [2]. These trips consisted of circumferential rings of forward-facing triangular points which induce secondary vorticity within the boundary layer and thus promote transition.

The pressure transducers employed are of a special rapid-response (high-frequency

capability), ceramic piezoelectric type developed in this laboratory by L. Rosenman. They were installed flush with the outer surface of the model in vibration-isolating mountings.

The pressure transducer output signals are recorded as oscilloscope traces and photographed. The preamplifiers and a few of the array of oscilloscopes used to record the data

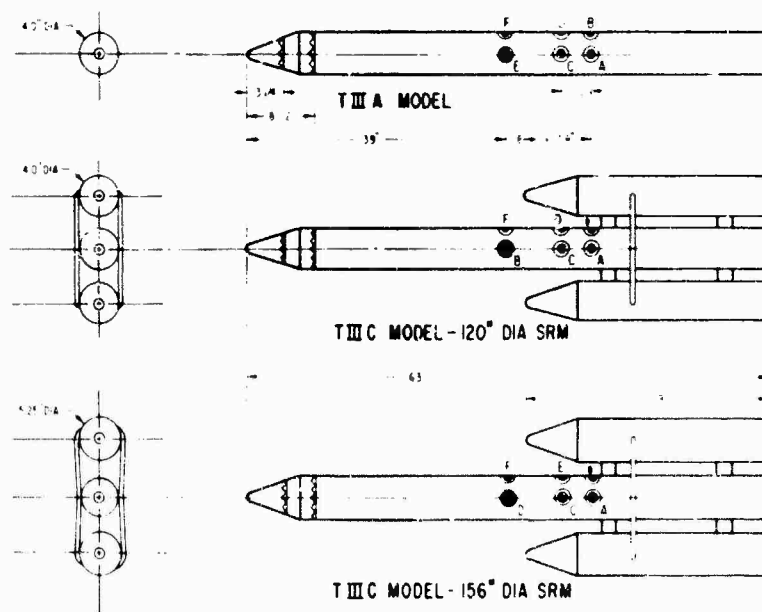


Fig. 2. Three Titan III vehicle configurations tested



Fig. 3. Titan III model mounted in tunnel (note pressure transducers located near middle of core body)



Fig. 4. Titan III model mounted on sting; boundary-layer trips attached to the nose

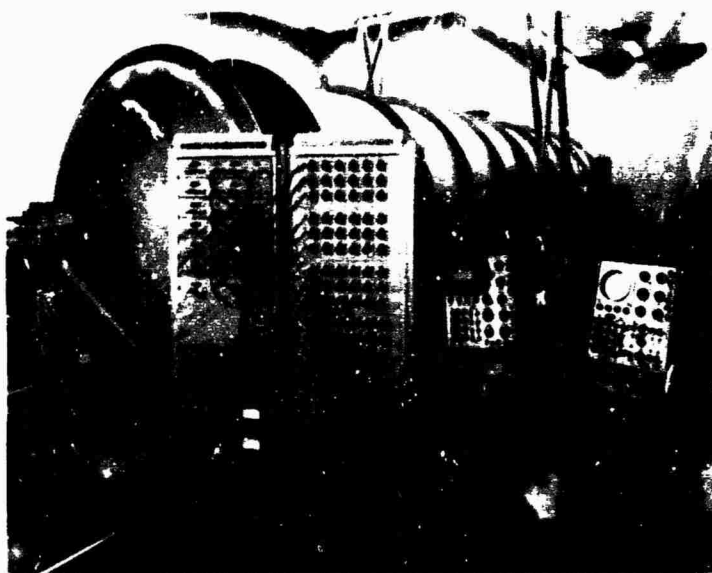


Fig. 5. Tunnel instrumentation, including pre-amplifiers, with test chamber in background

during these tests are shown in Fig. 5. One scope records the signals from two pressure transducers mounted a known axial distance apart on the inside surface of the test section. The resulting signal is used to trigger the remaining scopes at predetermined intervals, and the signal is displayed on an oscilloscope and photographed to determine shock Mach number.

#### TEST PROCEDURE

This investigation consisted of measurement of the surface pressure fluctuation at six transducer stations on the three Titan III configurations. All tests were conducted at the single Mach number,  $M = 1.1$ , and at 0-deg angle of attack and 0-deg yaw.

As each model configuration was mounted on the sting, an in-place calibration of the entire pressure transducer and readout electronics chain was accomplished with the aid of a pressure-pulse apparatus.

The electrical output signals from the pressure transducers were recorded on oscilloscopes and photographed. Two of the transducers were monitored on a single scope over the entire test period (Fig. 6). The actual data were obtained from two expanded scale traces, sequentially triggered on two scopes to give a total data period of 1 msec during the most stationary part of the 3-msec test time. In

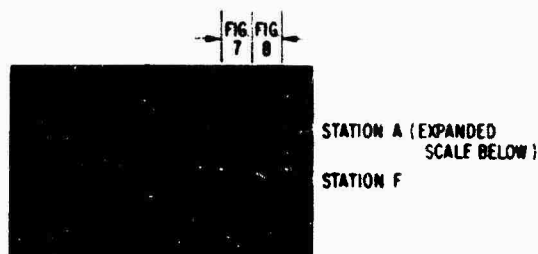


Fig. 6. Oscilloscope traces showing overall pressure-time history for two gauges

addition, these expanded data traces were high-pass filtered at 1 kHz. The expanded scale traces corresponding to the upper trace in Fig. 6 are presented in Figs. 7 and 8. The corresponding noise trace for no flow is shown in Fig. 9.

The position of the "steady" detached shock wave ahead of the solid boosters during the test time was determined by separate shots during which schlieren photographs were obtained for both the 120-in.-diam and 156-in.-diam SRM bodies. The 120-in.-diam case appears in Fig. 10.

The standard tunnel operating conditions for this test series were: driver-gas pressure, 650 psig; test chamber initial pressure, 2 mm



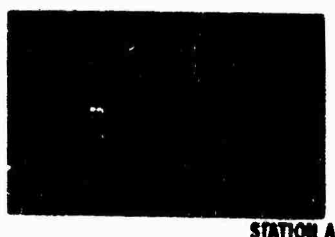


Fig. 7. Amplified signal from portion of Fig. 6 (first section)



Fig. 8. Amplified signal from portion of Fig. 6 (differentially triggered second section)

Hg abs.; flow Mach number, 1.1; model Reynolds number per foot,  $1.2 \times 10^5$ ; and free-stream dynamic pressure,  $q = 31$  psf.

#### DATA ANALYSIS

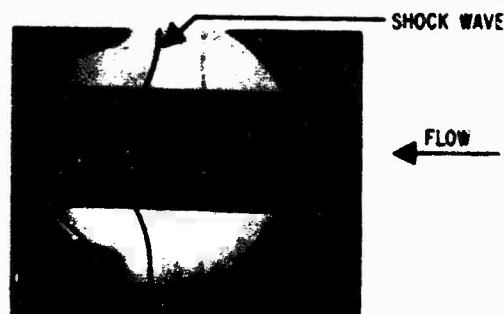
The data analysis procedure was based upon analog-to-digital conversion of the oscilloscope traces and subsequent digital processing and spectral analysis on the IBM 7094 computer. (An outline of the major steps appears in the Appendix.)

The pressure transducer output (in terms of volts vs time) is recorded on two oscilloscope trace photos, each of 0.5-msec duration. These Polaroid prints are photographically copied, and enlarged 11-in. by 14-in. prints are produced. The enlargements are then read with the aid of a Benson-Lehner OSCAR machine, a crosshair follower device which performs an analog-to-digital conversion. The machine operator samples the data at a sampling density equivalent to a 2-MHz sampling rate. The OSCAR machine records the  $x$  and  $y$  displacements of the sample point upon the IBM card, thereby converting the analog trace into a deck of digital input cards.



NOISE TRACE WITH NO FLOW

Fig. 9. Noise trace corresponding to conditions of Figs. 7 and 8



SCHLIEREN PHOTOGRAPH OF T IIC MODEL WITH 120° SOLIDS

Fig. 10. Schlieren photograph of SRM bow shock impinging on core body

The deck of cards is then used as input data for a digital computer calibration and trend-removal program. The calibration portion of the program converts the arbitrary "counts" of the OSCAR to physical pressure and time units through the use of the OSCAR calibration, the preamplifier and scope setting data, and the individual pressure transducer calibration. The trend removal consists of suppressing the effects of a trending mean (caused by small changes in the mean flow as a function of time, finite electrical bandwidth effects upon the step-function mean-flow signal, etc.) by a least-squares polynomial curve fit. The residue, or variation about the polynomial, is printed and also plotted by Calcomp plotter as pressure in pounds per square foot as a function of time. The rms value of this residual pressure fluctuation is also an output of the program and is taken as the mean value of the surface pressure fluctuations  $\bar{p}'$ . In addition, any wild points or breaks in the data introduced

by human error or OSCAR machine troubles can be detected by visual inspection of the output plot.

Spectral analysis of the time-varying pressure  $p'(t)$  was accomplished by processing the output of the calibration program by means of the Aerospace Data Processing Center digital-computer wave analyzer program [3]. This program is based upon some of the well-known properties of sampled stationary random functions. Therefore, any substantial departure from stationary behavior displayed by  $p'(t)$  would introduce doubt as to the applicability of the method and the accuracy of the results (stationary implies that the process, or at least its relevant statistical properties, depends only on time differences and is invariant to displacement on the time scale). The trend-removal program is an important factor in meeting the requirement of at least a process with a stationary increment by removing any nonstationary mean values and allowing a visual check on any radically nonstationary variance by inspection of the Calcomp plot.

The wave analyzer program is a digital computer approach to random data analysis and is based upon the theory of random or stochastic processes. The general approach can be found in Bendat and Fiersol [4] and the details of the Aerospace procedure in Holtz and Morris [3]. In terms of the continuous stationary function of time  $p'(t)$ , there exists an autocorrelation function  $R(\tau)$ , defined as follows (see Appendix for nomenclature):

$$R(\tau) = \lim_{T \rightarrow \infty} \frac{1}{T} \int_0^T p'(t) p'(t + \tau) dt$$

The Wiener-Khinchine theorem for stationary functions shows that the autocorrelation function and the power spectral density function

$$G(f) = \lim_{T \rightarrow \infty} \lim_{\Delta f \rightarrow 0} \left( \frac{1}{\Delta f T} \int_0^T [(p')^2(t, \tau, f, f)] dt \right)$$

are Fourier transform pairs:

$$G(f) = 2 \int_{-\infty}^{\infty} r(\tau) e^{-2\pi i f \tau} d\tau$$

The digital program operates in a similar way upon the discrete sample set  $p'(t_i)$  obtained from the continuous  $p'(t)$ : computing the autocorrelation function  $r(\tau)$  and taking its Fourier transform to obtain the power spectral density function  $G(f)$ . The power spectral density, as

implied by the name, gives the density distribution in frequency space of the pressure fluctuation squared  $[(psf)^2 \text{ per hertz in our case}]$ .

To compare the model test results to the full-scale flight test results, it is necessary to convert the power spectral density  $G(f)$  to an integrated spectrum  $E(f_1, f_2)$ , which can be specified in a manner equivalent to the acousticians' standard sound power level (SPL) in 1/3-octave-bandwidth increments. We define the integrated spectrum function  $E(f_1, f_2)$  as follows:

$$E(f_1, f_2) = \int_{f_1 - \frac{1}{2} \Delta f}^{f_1 + \frac{1}{2} \Delta f} G(f) df \quad \text{SPL}$$

where the  $f_1$  are the specified integration bandwidth center frequencies and the  $\Delta f$  are the integration bandwidths. In our case, the  $f_1$  and  $\Delta f$  are prescribed numbers, being the standard USA Standards Institute acoustic center frequencies and proportional bandwidths corresponding to the 1/3-octave-band values. Since an integrator subroutine to the wave analyzer program was not available at the time the work reported here was carried out, the transformation from  $G$  to  $E$  was computed by hand.

The analog-to-digital conversion of  $p'(t)$  to  $p'(t_i)$  and subsequent spectral analysis raises the question of "aliasing" or folding of high-frequency content in the true spectrum back into the lower-frequency range of the digitally computed spectrum and thereby falsely reporting the frequency of this energy. The remedy for this behavior is to sample the data at a frequency at least twice that of the highest frequency where a substantial energy content is present. For a number of reasons (including the finite-size pressure transducer placing a limit upon the upper frequency obtained from the convected fluctuating flow field), the electrical signal was low-pass filtered at 40 kHz (-3 dB). The sampling frequency of 2 MHz was well beyond the 80-100 kHz that would be required on the basis of the Nyquist sampling criterion.

The model data were scaled to full-scale flight test basis for comparison with the available examples of the latter. Additional comments on scaling appear in the Appendix; consideration will be given here only to how the scaling laws used influenced the numerical results. The amplitude of the pressure fluctuations was scaled on the basis of free-stream dynamic pressure  $q$ .

$$\frac{\overline{p_m}}{q_m} = \frac{\overline{p_f}}{q_f}$$

In terms of the sound power level (SPL) in db units, the scaling can be expressed as follows:

$$\text{SPL}_{\text{simulated full scale}} = \text{SPL}_{\text{model}} + 20 \log_{10} \frac{q_f}{q_m}$$

The following typical  $q_f$  values were employed, based on the flight profiles of Reids 5 and 6: For the Titan IIIA flights (core only),  $q = 550$  psf; for the Titan IIIC flight,  $q = 600$  psf. The frequencies at which the amplitudes were reported resulted from the application of Strouhal scaling to the model data. A Strouhal number based upon body diameter  $D$  and free-stream velocity  $U$  was employed. Since  $U_m/U_f = D_m/D_f = 1/30$ , application of Strouhal scaling on this basis results in:

$$\frac{f_m D_m}{U_m} = \frac{f_f D_f}{U_f}$$

or

$$f_f = 1/30 f_m$$

## RESULTS AND DISCUSSION

All the model results in this report have been scaled to the flight basis as described.

The overall sound pressure level values are summarized in Table 1. Different values for a given gage position and test condition indicate independent determinations. An example of the autocorrelation function  $R(\tau)$  is plotted in Fig. 11. A typical power spectral density plot for the same case appears in Fig. 12. Selected comparisons between the available flight data and the model results appear in Figs. 13 and 14; Fig. 13 depicts the comparison between the core-only Titan IIIA model and the Titan IIIA configuration -03 flight [5]. Figure 14 represents a similar comparison for the same Station 567, open-side or target-side position, between the Titan IIIC configuration -07 flight and the model results for Titan IIIC models consisting of core plus 120-in. solids and 156-in. solids. The typical effects of model location are demonstrated by Fig. 15, where the 1/3-octave-band spectra for various stations are compared.

In general, the overall sound pressure levels determined by this investigation agree quite well with both the general estimates based upon various experiments [7,8] and the flight test results for the single Station 567 target-side measurement point available at this time. In the latter case, the agreement is good between both model and full-scale 1/3-octave-band energy spectra.

Figure 13 shows the closeness of the sound pressure level spectra for the core-only A

TABLE 1  
Overall Sound Pressure Levels

| Case | Measurement Station |     |     |     |     |     | Configuration |         |         |
|------|---------------------|-----|-----|-----|-----|-----|---------------|---------|---------|
|      | A                   | B   | C   | D   | E   | F   | "A"           | "C" 120 | "C" 156 |
| 196  | 145                 |     |     |     |     |     | X             |         |         |
| 203  | 144                 |     |     |     |     |     | X             |         |         |
| 205  | 143                 |     |     |     |     |     | X             |         |         |
| 206  | 144                 |     |     |     |     |     | X             |         |         |
| 207  | 148                 | 153 |     | 155 |     | 156 |               | X       |         |
| 208  | 146                 | 154 |     | 150 | 152 |     |               | X       |         |
| 209  | 151                 | 151 | 150 | 155 |     |     |               | X       |         |
| 210  | 148                 |     | 152 |     | 152 |     |               |         | X       |
| 212  | 149                 |     |     | 158 | 154 | 156 |               |         | X       |
| 213  |                     | 151 |     |     |     | 153 |               |         | X       |

Note. — Unit is decibels referenced to 0.0002 bar, scaled on the basis of  $q = 550$  psf for "A" configurations and  $q = 700$  psf for 120-in. and 156-in. "C" configurations.

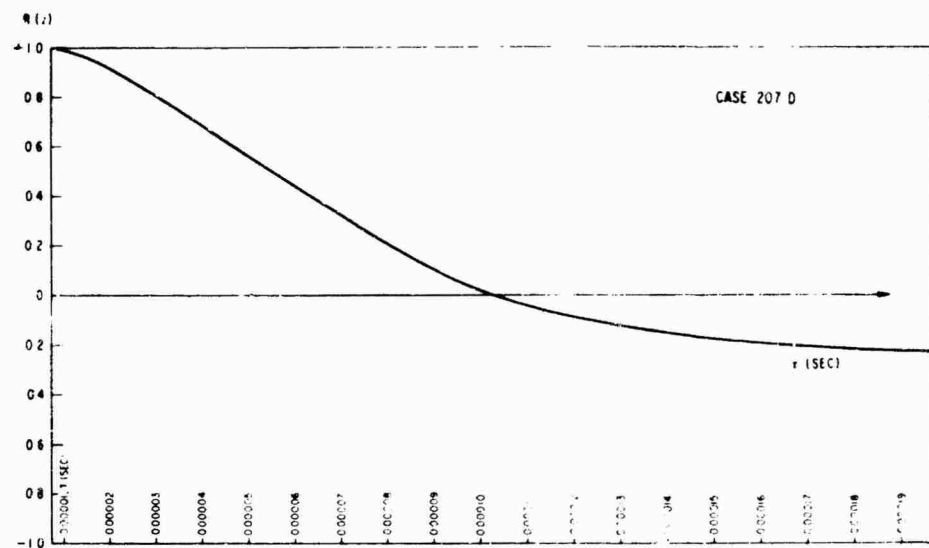


Fig. 11. Typical autocorrelation function



Fig. 12. Typical power spectral density

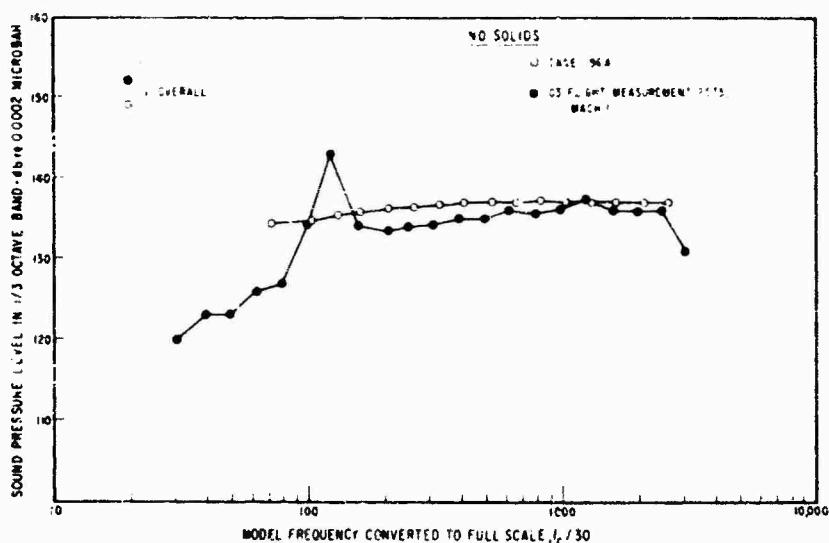


Fig. 13. Comparison of model and full-scale sound pressure level spectra

configuration. The peak in the flight data just above 100 Hz is considered spurious by comparison with all other available model and flight results. This peak also contributes to the rather high overall level of 148.5 db, equal to the 120-in. solid -07 flight result for the same measurement point.

Figure 14 presents a comparison of the pressure level spectra at Station 567 for the Titan IIC -07 flight and the corresponding model test data for the same location (gage Station A, see Fig. 2) with core-only, 120-in.

solid booster, and 156-in. booster configurations. This presentation demonstrates the good agreement between the model and full-scale levels and also the slight but consistent increase in level for the progression from no solids to 120-in. solids, and to 156-in. solids.

These results indicate that the effects of the solid booster bow shock upon the surface pressure fluctuations on the open or target side are not very great, at least for the conditions examined in this study. However, the question of the influence of the booster bow shock

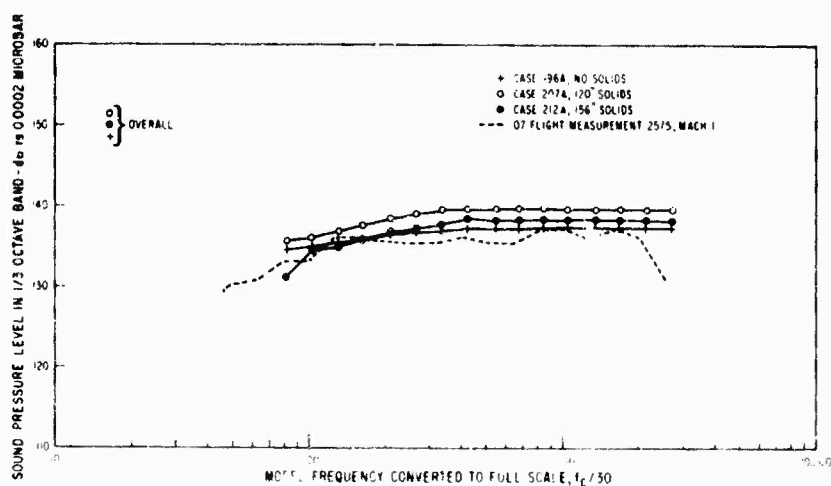


Fig. 14. Comparison of model and full-scale sound pressure level spectra with and without solids

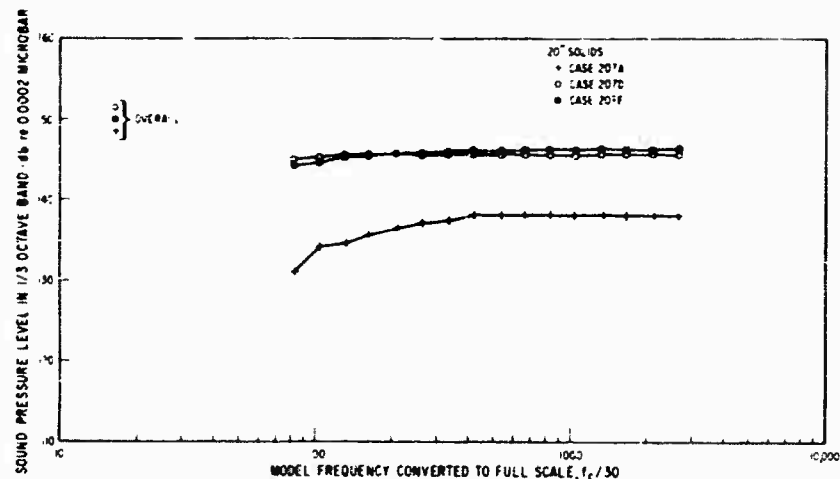


Fig. 15. Model sound pressure level spectra showing effect of transducer location

interaction with that part of the core directly under the booster remains to be answered. The pertinent data on this point, the results from the six gage locations in the model tests, are presented in Table 1 in terms of the overall sound pressure level and the effects of location upon 1/3-octave-band sound-pressure-level spectra shown in Fig. 15. The target- or open-side locations A, C, and E give levels only slightly higher than for the core-only configuration. On the other hand, the fluctuations at the locations under the rocket motors, B, D, and F, are about 5-10 db above the open-side values. Thus there is strong enhancement of the fluctuating pressures under the booster bodies and directly behind the interaction of the boundary layer with the strongest portion of the booster nose shock, and there is a much weaker enhancement over the open-side regions. Some modifications to this general picture are noted below.

The limited number of measurement stations makes it hard to determine the effect of strong local peaks in fluctuation near the intersection of the booster bow shock with the core-body boundary layer. Values for boundary-layer-shock wave interaction reported in the literature [7] would lead to the expectation of higher values than those measured here in a limited region near the shock wave. The finite-size pressure transducers, the fixed axial increments by which they could be moved, and the limited time available to search for the various regions of maximum effect all acted to suppress the appearance of the local peaks in the results presented here. However, some of the higher readings at the C and E locations may result

from picking up at least some of the fluctuation field in the neighborhood of the shock-boundary layer interaction. The effects of the strong interaction region upon the spectral distribution can be observed in Fig. 15, where the data from the 120-in. solid case 207 exhibit both a higher overall level for the D and F locations when contrasted with the A location, and a strongly enhanced low-frequency content probably resulting from upstream separation-reattachment effects.

It should be noted that the restriction on the lowest measurable frequencies, established by the limited duration of the tests and referred to above, does not affect the comparison between the model and the full-scale flight results. The lowest 1/3-octave-band center frequency, when scaled on the basis of body diameter Strouhal number and the 1:30 model scale, results in a value of 83 Hz, which is close to the lowest available flight test result.

## CONCLUSIONS

The method of determining the surface pressure fluctuations on a model during the brief flow in a low-speed shock tunnel appears to provide a good simulation of full-scale flight test conditions. The results correlated well with expectations based upon general continuous-flow studies and with comparable flight test results when scaled to the latter conditions. The relative ease and low cost of obtaining data in a short-duration facility suggest that this method can become a useful tool in the pursuit

of answers to some of the yet unexplained basic aspects of surface pressure fluctuation phenomena (particularly the separated flow and strong interaction cases) and can assist in obtaining information for design purposes.

The data obtained from tests of core-only Titan IIIA configuration, 120-in. SRM Titan IIIC configuration, and 156-in. SRM Titan IIIC configuration models indicated that the interaction of the booster-rocket-motor-body bow shock with the core boundary layer led to a small increase in surface pressure fluctuation

(aerodynamic noise) for locations on the target or open sides, whereas a substantial increase (of 150-160 db) was found on the booster-body sides. For the single Station 567 open-side location, flight test results closely resembled the scaled model results.

Dynamic-pressure scaling for the pressure fluctuation amplitude appears to give consistent results, but the choice of the proper length scale for Strouhal number scaling of frequencies in such complicated interactions as those considered here requires additional study.

## Appendix

### SCALING LAWS FOR PRESSURE FLUCTUATIONS

Dimensional analysis of the basic parameters influencing the static-pressure fluctuations on the surface of a body indicates that the amplitude of the fluctuations should scale with some characteristic pressure (or force per unit area) and the frequency scale according to the dimensionless grouping,  $FL/U$ , the Strouhal number. However, the choice of which reference pressure or force to use and the choice of length and velocity scales is not indicated by the procedure of dimensional analysis, but must be supplied on the basis of additional physical information. Furthermore, for relatively complex flow fields and interactions as considered in this report, it is quite possible that two or more parameters are involved and that two or more length scales with corresponding dimensionless groupings are required. The following discussion amplifies these points and presents the rationale for the particular choice of normalizing parameters chosen for the present investigation.

The amplitude scaling of the pressure fluctuations is more easily treated than the frequency scaling and is discussed first. In the relatively uncomplicated case of an attached turbulent boundary layer, the process of turbulent energy transfer from the energy source, the mainstream dynamic head, through the interaction between mean-flow gradients and fluctuating quantities and thence to solid surface shear-stress dissipation is well documented in such works as Refs. 9 and 10. Intuition and experience indicate that either the readily measured free-stream-flow dynamic pressure (a measure of the available energy) or the laminar sublayer surface-shear stress (a good measure of the actual turbulent energy

near the surface, just beyond the sublayer) would be likely candidates for the role of normalizing quantity for the fluctuating static pressure at the surface. Moreover, the long history of experimental boundary-layer investigations discloses that the ratio of surface shear to free-stream dynamic pressure (the skin-friction coefficient  $C_f$ ) is a slowly varying function of Reynolds number for turbulent flow. These facts suggest that the use of surface-shear stress as the normalizing quantity would remove the Reynolds number trend, and the experience of most workers in the study of near-field boundary-layer noise (Kistler and Chen [11], and others) confirms this fact. However, in those cases where strong external effects (such as surface discontinuities and shock waves) interfere with the turbulent boundary layer, the picture must be drastically modified. In these strong-interaction cases the boundary-layer assumptions are frequently invalid, and new sources of fluctuating pressure production appear in the form of pressure gradients and the large eddy structure of separated flows, shock-wave pressure fields, and similar phenomena. In these complex cases, the direct approach consists of employing the free-stream dynamic pressure  $q$  as the normalizing quantity and letting the resultant magnitude express the fraction of available kinetic energy which has been measured as a surface pressure fluctuation, and therefore serve as an indication of the interaction severity. An indication of the failure of wall-shear-stress scaling when applied to these more complicated phenomena can be seen from the case of separated flow, where the wall-shear stress is essentially zero, but larger surface pressure fluctuations have been measured than for attached flow cases.

Therefore,  $\eta$  scaling was selected for this study, since it would be applicable to the complex interactions found therein.

The frequency scaling by means of the dimensionless grouping  $fL/U$  (the Strouhal number) requires that a reasonable choice be made for the length scale,  $L$ , and the velocity scale,  $U$ . Two fairly obvious choices for length scales are a characteristic body length (such as body diameter  $D$ ) or the thickness of a fluid shear zone (the boundary layer thickness,  $\delta$ , or the width of a wake). The body scale should have a connection with unsteady phenomena influenced by the potential flow field, such as some types of shock wave oscillation, while the width of a shear zone should be closely connected with the scale of the large eddies and the eddies of greatest energy. The body scale is, of course, easily determined, while the shear zone thickness must be either measured or calculated under conditions which frequently lead to considerable doubt as to the accuracy of the result. The obvious and most easily determined velocity is that of the free stream, while arbitrarily defined physical velocities (such as the  $x$  velocity component at the height of the momentum thickness of a boundary layer) or arbitrary groupings of terms having the dimensions of velocity (like the "friction velocity,"  $v_* = \sqrt{\tau_w/\rho}$ ) have significance in certain cases, but are much less readily determined.

Physical dimensions (body diameter, step height, cavity dimension, etc.) have been used with success in some strong-interaction cases and failed in others. The use of boundary-layer thickness, together with free-stream velocity, is nearly universal in reporting fluctuations in flat-plate or smooth-body boundary-layer cases.

The relationship between the boundary-layer thickness and  $x$  distance (proportional to  $D$  for geometrically similar bodies) for fully turbulent flat-plate boundary layers is expressed by the Blasius relation:

$$\frac{\delta}{x} = 0.37 \text{Re}_x^{-0.2}$$

For the full-scale flight results, the appropriate Reynolds numbers are in the  $10^7$ - $10^8$  range. The corresponding model Reynolds number is about  $10^6$ . The relative boundary-layer thicknesses for these cases are shown:

| $\text{Re}_x$ | $\delta/x$ | $\frac{(\delta/x)}{(\delta/x)_{10^6}}$ |
|---------------|------------|--|
| $10^6$        | 0.023      | 1.00                                   |
| $10^7$        | 0.0147     | 0.64                                   |
| $10^8$        | 0.0093     | 0.40                                   |

On the basis of these figures, the values of  $x$  for the model and full-scale vehicle differ by about a factor of 2. This will influence the relative Strouhal number as follows:

$$\frac{\text{St}_f}{\text{St}_m} = \frac{\frac{f_f L_f}{U_f}}{\frac{f_m L_m}{U_m}} = \left(\frac{f_f}{f_m}\right) \left(\frac{L_f}{L_m}\right) \left(\frac{U_m}{U_f}\right)$$

For a fixed Strouhal number and equal fluid velocities in each case (realized in practice), the frequencies are related as follows:

$$\frac{f_m}{f_f} = \frac{L_f}{L_m} \left(\frac{L_f}{L_m}\right) \left(\frac{U_m}{U_f}\right) = \left(\frac{L_f}{L_m}\right) \left(\frac{U_m}{U_f}\right)$$

$$\frac{f_m}{f_f} = 2 \left(\frac{U_m}{U_f}\right)$$

Thus for a geometrically similar model, the difference between model and full-scale frequencies scaled on the basis of the boundary-layer thickness or the body diameter would differ by about a factor of 2. The extended noise and boundary-layer trips shift the effective origin of the turbulent boundary layer compared to a smooth, exact-scale model. It is estimated that the latter effect will tend to reduce slightly the aforementioned factor of 2.

These uncertainties in the proper frequency scaling for such complex interactions as those considered here, together with the difficulty of determining the boundary-layer thickness in this experiment, led to the use of the body diameter  $D$  to specify the Strouhal number  $fD/U$ . In addition, the reported energy spectra are nearly flat when reported in terms of 1/3-octave-bandwidth integration intervals of the power spectral density (the latter is a



monotonically decreasing function of frequency). Therefore, a moderate error due to the use of the readily measured body diameter would not have a serious influence on the practical utility of these results.

## NOMENCLATURE

|                 |  |
|-----------------|--|
| $C_f$           | skin friction coefficient, dimensionless   |
| dB              | sound pressure level in decibels referenced to 0.0002 $\mu\text{bar}$                |
| D               | body diameter of cylindrical shell   |
| $G(f)$          | power spectral density as a function of frequency $f$ ((amplitude) <sup>2</sup> /Hz) |
| Hz              | frequency in hertz (cps)   |
| kHz             | frequency in kilohertz (kc/sec)  |
| M               | Mach number, dimensionless   |
| $p'(t)$         | fluctuating pressure component as a function of time                                 |
| $\overline{p'}$ | mean value of the fluctuating pressure   |
| $q$             | dynamic pressure ( $\rho/2$ ) $U^2$  |
| Re              | Reynolds number $UL/\nu$   |
| $r(\tau)$       | correlation coefficient as a function of time lag $\tau$                             |
| SPL             | sound power level (db)   |
| St              | Strouhal number $fD/U$ or $fL/U$ , dimensionless frequency                           |
| T               | time interval  |
| $t$             | time   |
| $t_i$           | discrete sample point on the time scale  |
| $U$             | mean fluid velocity  |
| $v_w$           | friction velocity $\sqrt{\tau_w/\rho}$   |
| $x$             | axial coordinate   |

boundary-layer thickness

fluid density

time lag =  $t_2 - t_1$

wall shear stress

## MAJOR STEPS OF DATA ANALYSIS

1. Pressure transducer output was recorded on two oscilloscope traces, each of 0.5-msec duration.

2. Scope traces were photographed and enlarged to 11 in. by 14 in.

3. Enlarged traces were digitized on OSCAR machine at 2-MHz sampling rate.

4. OSCAR cards were fed into calibration and trend-removal program; second-degree polynomial least-squares mean trend was removed.

5. Resultant fluctuations about mean spectrally analyzed by wave analyzer program.

6. Power spectral density,  $(\overline{p'})^2$  per cycle, was converted to 1/3-octave band energy spectrum basis by integrating over each bandwidth:

$$\text{db}_{1/3\text{OB}} = \text{db}_{\text{cps}} + 10 \log_{10} \Delta f.$$

7. Model results were converted to full-scale basis by  $q$  scaling, i.e.,  $\overline{p'}/q \approx \text{constant}$

$$\frac{\overline{p'_m}}{q_m} = \frac{\overline{p'_f}}{q_f}$$

and

$$\text{db}_{\text{simulated full scale}} = \text{db}_{\text{model}} + 20 \log_{10} \frac{q_f}{q_m}.$$

8. Model frequency was scaled to flight results on the basis of body-diameter Strouhal number  $fD/U$ . Since  $U_m = U_f$  and  $D_m = 1/30 D_f$ ,  $f_f = 1/30 f_m$ .

## REFERENCES

1. R. L. Varwig and L. Rosenman, "A Seven Foot Diameter Shock Tube for Transonic and Supersonic Aerodynamic Testing," Aerospace Corp. Rept. TDR-469(5240-10)-13, (SSD-TR-65-79), June 1965.
2. F. R. Hama, "Boundary Layer Tripping in Super- and Hyper-sonic Flows," JPL Space Programs Summary 37-29, Vol. IV, Oct. 1964, pp. 163-175.

3. H. Holtz and Morris, "Wave Analyzer Program," Aerospace Corp. Tech. Memo. ATM (6116-40)-123, Dec. 1965
4. J. S. Bendat and A. G. Piersol, Measurement and Analysis of Random Data (Wiley, New York), 1966
5. Summary Report: Titan III. "Vibration and Acoustic Data," Bolt Beranek & Newman Rept. 1268, Dec. 1965
6. K. W. Shogren, private communication
7. H. S. Ribner, "The Noise of Aircraft," U. of Toronto, Institute for Aerospace Studies, UTIAS Review 24, AFOSR 64-B10, Aug. 1964
8. A. L. Kistler, "Fluctuating Wall Pressure Under a Separated Supersonic Flow," J. Acoust. Soc. Amer., 36(3):543 (1964)
9. J. O. Hinze, Turbulence (McGraw-Hill, New York), 1959
10. A. H. Townsend, The Structure of Turbulent Shear Flow (Cambridge University Press, Cambridge), 1956
11. A. L. Kistler and W. S. Chen, "The Fluctuating Pressure Field in a Supersonic Turbulent Boundary Layer," J. Fluid Mech., 16:41 (1963)

#### DISCUSSION

Mr. Hughes (Naval Ordnance Laboratory): Have you experienced any shock sensitivity of the pressure gages, either axial or transverse, which could possibly pick up some spurious noise?

Mr. Ross: No. These were special gages developed in the Aerospace Corporation laboratory for use in high shock environments. Tests were made with the transducers mounted both rigidly in the model and suspended in the compliant mounting. The latter mounting was employed - you may recall some white circles around the black dots in the picture of the model of the tunnel when I pointed out the transducers - these were silicone inserts which were found to give negligible acceleration effect. This was explored in some detail, not only with the models I have discussed here, but also with a large variety of other transonic buffet and aerodynamic noise models which have been tested.

Mr. Manning (Bolt Beranek & Newman): You mentioned toward the end of your talk that you were measuring crosscorrelation in the pressure field. Have you also tried to measure the sound radiated into the external environment by the turbulent boundary layer?

Mr. Ross: No, not in this particular type of test.

Mr. Mustain (Douglas Aircraft Co.): As you know, a similar model has been tested in the continuous type tunnels. What is the

advantage of your shock tunnel over the other type of tunnel? Have you correlated data on one model tested in the other type of tunnel with your type of measurements? Is yours better or is theirs better? Yours appears to be good with the flight measurements.

Mr. Ross: This is a good question. I did not point out the fact that this type of test can be performed more rapidly and with cheaper models. For one thing, the temperature problems for the model and transducer are greatly reduced. Also, it is possible to test at rather high Mach numbers and Reynolds numbers with much less expensive equipment than the continuous flow tunnel. On the second part of your question, we have made a large number of tests with modifications of the models you have seen here and special models which are precisely the NASA Ames standard test bodies that have been used by Charley Cole and his group. We are now in the process of evaluating the results and attempting to compare them with Cole's results to see if we get good correspondence between continuous flow tests and the short duration tests. There are problems in each regime. The continuous flow test has the problem of the noise from the compressors upstream being convected down and contaminating the result, and we have problems with wave reflections from the sides and also the rather severe problems in data reduction and instrumentation imposed by the few milliseconds of effective test time available. This question is being investigated and possibly we can report on this in the near future.

\* \* \*

## IMPACT TESTING WITH A FOUR-INCH AIR GUN AND LEAD TARGETS

Harry J. Davis  
Harry Diamond Laboratories  
Washington, D.C.

Fuzes and fuze components are tested for ruggedness at the Harry Diamond Laboratories by mounting them in projectiles and firing them from an air gun into lead blocks. An evaluation of this method of testing is reported.

The air gun is 96 ft long and has a 4-in. bore. The projectile is 11 in. long, has a round nose, and with a standard fuze cargo weighs 17.5 lb. The muzzle velocity of this projectile ranges from 100 to 650 fps. The target consists of 3 to 10 lead blocks, each of which is 6 by 8 by 1 in. The deceleration of the projectile upon striking this target provides the test.

The analysis depends upon two years of accumulating routine test data. The measured quantity of primary interest is the peak acceleration obtained from copper ball accelerometers. The advantages and disadvantages of copper ball accelerometers are presented. These measurements indicate that structures or components with natural frequencies of hundreds of hertz experience 5000 to 50,000 g. Accelerations of the order of hundreds of thousands of g's, however, have been measured at natural frequencies greater than 10 kHz. Such measurements may differ by a factor of 2 at different points within the projectile.

The air gun design and the test technique are discussed briefly. Target penetration phenomena are also discussed since they provide the force pulses experienced by the projectile. The usual law which assumes a constant retarding force and the Poncelet solid penetration law are applied to the present study.

It is concluded that, although the impact test is a convenient and inexpensive means of subjecting fuzes to high force levels, quantitative interpretation of the results must be made with caution.

### INTRODUCTION

The modern ordnance fuze is so complex that its dynamic response to impacts cannot be exactly specified by theoretical analysis. Therefore, since a fuze is subjected to accelerations during shipment and while being fired, its dynamic behavior must be determined experimentally before it can be treated as a reliable part of a weapons system.

Air gun techniques have long been used by the Harry Diamond Laboratories (HDL) to shoot heavy projectiles containing fuzes into lead targets, resulting in high decelerations that may cause structural failures within the fuze. These deficiencies are corrected before the fuze is field tested. This paper examines the phenomena occurring during the lead impact to evaluate the shock testing performed.

### EXPERIMENTAL APPARATUS AND TECHNIQUE

In a test, the shell containing the fuze is placed in the breech of the air gun. A tank is filled with air at the pressure necessary to achieve the desired projectile velocity. This pressure ranges from 2 to 125 psig. A solenoid-operated valve connecting the gun to the tank is opened and the shell is fired through a 36-ft-long, 4-in.-inner-diam tube. Further details of the gun are given in Ref. 1.

After leaving the gun the shell travels approximately 5 ft and hits a stack of 6-in. by 8-in. by 1-in. lead blocks, which deform plastically while decelerating the shell. This constitutes the impact test. When setting up the test, newly set blocks are pressed together by hand and no attempt is made to fasten them down.

The nose of the shell is usually greased or oiled to ease removal from the lead.

A typical projectile is 4 in. in diameter and 11 in. long. It weighs 16.3 lb without fuze cargo and is made of 4140 steel. There are three sections screwed together: the nose, cargo section, and end cap (Fig. 1). The hemispheric nose constitutes approximately half of the total weight of the projectile. The nose shown in Fig. 1 has a 2-in. radius. Cone-shaped and flattened noses have been used but are not discussed because of insufficient test data. The threaded cargo-carrying portion of the vehicle is integral with the 3/16-in.-thick walls of the cargo or test specimen section.

The measurements routinely made in the course of a run are listed in Table 1 with an estimate of their accuracy. Experimental data gathered over a period of years were fitted to the function  $X = cY^n$ , where suitable pairs of quantities listed in Table 1 could be substituted for  $X$  and  $Y$  (see Nomenclature). Some of the resulting relations are used here, while others are of general interest in air gun design work. Details of the fitting technique and its results are given in Appendix A and in Tables 2 and 3.

Several laws are described in the literature in connection with penetration mechanics. The impact speed and penetration depth data gathered in HDL air gun testing were fitted using a least-squares technique to the expression predicted by some of these laws. The results (Appendix B) bear on the evaluation of the 4-in. air gun test and yield data basic to penetration phenomena.

#### FORCES ACTING ON THE PROJECTILE AND TEST SPECIMEN

The peak  $g$  impact-velocity fit described in Appendix A for 17.5-lb projectiles is plotted in Fig. 2 for the three different copper ball accelerometers used. It can be seen that there are three distinct curves (solid lines), although the reading of any one accelerometer is often interpreted as being indicative of the peak force acting upon the system. The 95 percent confidence limits are also shown in Fig. 2 by the broken lines. The broad range indicated by the confidence limits results from variations in the test conditions and the inaccuracy of the copper ball accelerometer measurements. As discussed in Appendix C, copper ball accelerometers approximate spring-mass systems whose response depends upon the ratio of the natural period of the system and a characteristic time, usually the input pulse duration. In the test, the copper ball accelerometers do not measure the peak of the driving forces acting on the accelerometer but measure the response of the accelerometer as a function of its natural period. This response is called the shock spectrum of the system. The copper ball accelerometer may be used, then, as a test specimen whose response is known, at least to the limits described in Appendix C.

To investigate the response further, a model 8 copper ball accelerometer [2] was obtained from the U.S. Naval Ordnance Laboratory. This device consists of nine copper balls of different masses, and provides a group of peak-reading accelerometers with natural periods ranging from 67.5 to 295  $\mu\text{sec}$ , i.e., natural

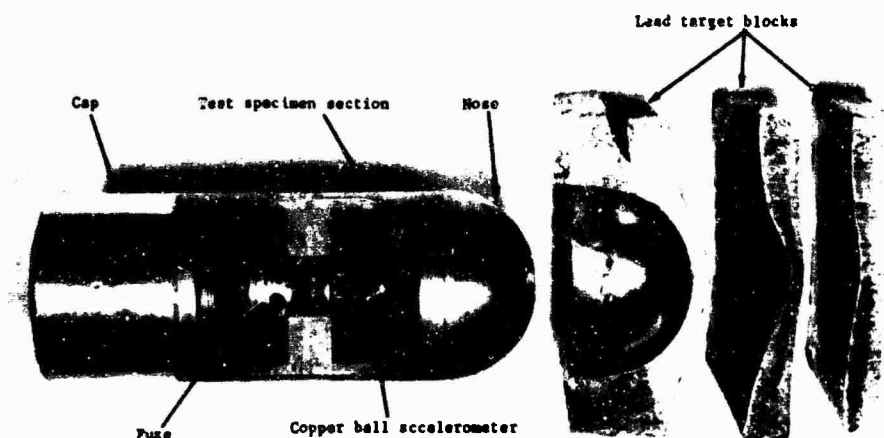


Fig. 1. Projectile and target blocks used in HDL 4-in. air gun

TABLE 1  
Air Gun Measurements

| Quantity                   | Estimated Accuracy | Remarks  |
|----------------------------|--------------------|--|
| Projectile weight          | $\pm 0.25$ lb      | Weight estimate usually made by operator of gun                                |
| Initial gas pressure       | $\pm 2$ psi        | Bourdon tube gage  |
| Projectile muzzle velocity | $\pm 1\%$          | Light screen technique [1]   |
| Peak deceleration force    | Unknown            | Model 1 copper ball accelerometer [2]  |
| Peak penetration depth     | $\pm 0.25$ in.     | Machinist's scale inserted in crater (accuracy better in shallow penetrations) |

TABLE 2  
Empirical Fit of Air Gun Data to Function  $X = cY^n$

| $w = 17.5$ lb;<br>Shallow Penetration <sup>a</sup> |          | $t_n = 460 \mu\text{sec}^b$ |       |                      |
|--|----------|-----------------------------|-------|----------------------|
| X  | Y        | c                           | n     | $t_n$                |
| $G_{pk}$   | p        | $1.631 \times 10^{-3}$      | 0.610 | $5.5 \times 10^{-2}$ |
| $G_{pk}$   | $v_0$    | $3.791 \times 10^{-1}$      | 1.012 | $4.3 \times 10^{-2}$ |
| $x_M$  | $G_{pk}$ | $5.516 \times 10^{-5}$      | 1.123 | $6.3 \times 10^{-2}$ |
| $x_M$  | $v_0$    | $1.656 \times 10^{-3}$      | 1.267 | $4.5 \times 10^{-2}$ |
| $v_0$  | p        | $3.902 \times 10^{-1}$      | 0.625 | $4.0 \times 10^{-2}$ |
| $G_{pk}$   | $x_M$    | $6.345 \times 10^{-3}$      | 0.738 | $4.1 \times 10^{-2}$ |
| $w = 23.0$ lb                                      |          | $t_n = 340 \mu\text{sec}^c$ |       |                      |
| X  | Y        | c                           | n     | $t_n$                |
| $G_{pk}$   | p        | $3.517 \times 10^{-3}$      | 0.451 | $6.6 \times 10^{-2}$ |
| $G_{pk}$   | $v_0$    | $1.112 \times 10^{-2}$      | 0.893 | $1.3 \times 10^{-1}$ |
| $x_M$  | $G_{pk}$ | $2.275 \times 10^{-4}$      | 0.977 | $1.4 \times 10^{-1}$ |
| $x_M$  | $v_0$    | $1.821 \times 10^{-4}$      | 1.705 | $8.6 \times 10^{-2}$ |
| $v_0$  | p        | $5.017 \times 10^{-1}$      | 0.491 | $1.4 \times 10^{-2}$ |
| $G_{pk}$   | $x_M$    | $1.036 \times 10^{-4}$      | 0.502 | $7.2 \times 10^{-2}$ |

Note.—See Nomenclature; pressure in pounds per square inch, penetration in inches.

<sup>a</sup> $x_M = D/2$ .

<sup>b</sup>Velocity range = 81-276 fps; number of points = 68.

<sup>c</sup>Velocity range = 267-422 fps; number of points = 52.

TABLE 3  
Empirical Fit of Air Gun Data to Function

| $w = 17.5$<br>lb     |          | $t_n = 460 \mu\text{sec}$ |       |                       | $t_n = 340 \mu\text{sec}$ |       |                      | $t_n = 270 \mu\text{sec}$ |       |                      |
|----------------------|----------|---------------------------|-------|-----------------------|---------------------------|-------|----------------------|---------------------------|-------|----------------------|
| X                    | Y        | c                         | n     | $\sigma_n$            | c                         | n     | $\sigma_n$           | c                         | n     | $\sigma_n$           |
| $G_{pk}$             | p        | $1.22 \times 10^3$        | 0.685 | $2.7 \times 10^{-2}$  | $1.124 \times 10^4$       | 0.206 | $3.5 \times 10^{-2}$ | $1.600 \times 10^3$       | 0.744 | $4.2 \times 10^{-2}$ |
| $G_{pk}$             | $v_0$    | 3.678                     | 1.421 | $5.4 \times 10^{-2}$  | $2.263 \times 10^2$       | 0.782 | $9.1 \times 10^{-2}$ | 1.263                     | 1.684 | $9.6 \times 10^{-2}$ |
| $x_M$                | $G_{pk}$ | $4.03 \times 10^{-3}$     | 0.697 | $3.0 \times 10^{-2}$  | $1.830 \times 10^{-1}$    | 0.316 | $4.7 \times 10^{-2}$ | $3.0 \times 10^{-2}$      | 0.488 | $3.5 \times 10^{-2}$ |
| $x_M$                | $v_0$    | $6.4 \times 10^{-4}$      | 1.458 | $2.7 \times 10^{-2}$  | $8.4 \times 10^{-4}$      | 1.414 | $4.0 \times 10^{-2}$ | $7.86 \times 10^{-3}$     | 1.054 | $3.9 \times 10^{-2}$ |
| $v_0$                | p        | $6.064 \times 10^1$       | 0.478 | $0.55 \times 10^{-2}$ | $1.183 \times 10^2$       | 0.316 | $1.1 \times 10^{-2}$ | $7.17 \times 10^1$        | 0.435 | $0.7 \times 10^{-2}$ |
| $G_{pk}$             | $x_M$    | $5.303 \times 10^3$       | 0.886 | $3.78 \times 10^{-2}$ | $1.436 \times 10^4$       | 0.400 | $6.0 \times 10^{-2}$ | $3.956 \times 10^3$       | 1.422 | $3.2 \times 10^{-2}$ |
| Velocity Range (fps) |          | 250-467                   |       |                       | 355-505                   |       |                      | 370-630                   |       |                      |
| No. of Points        |          | 336                       |       |                       | 310                       |       |                      | 88                        |       |                      |

Note.—See Nomenclature; pressure in pounds per square inch, penetration in inches.

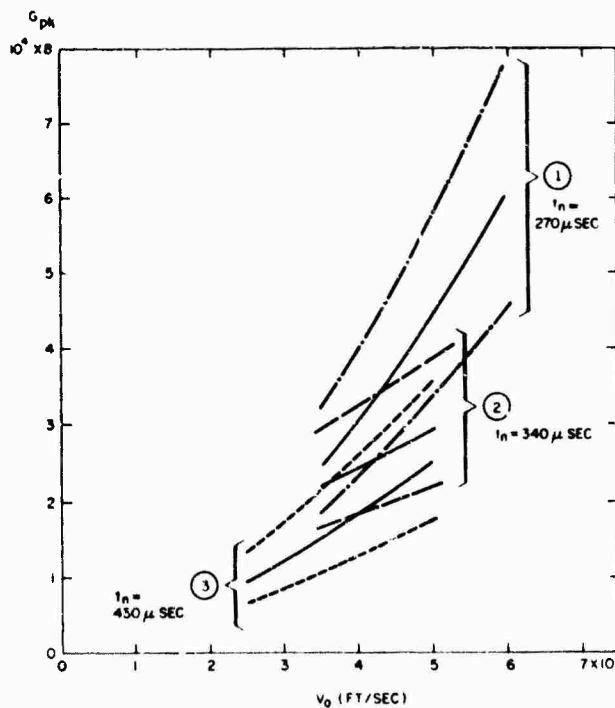


Fig. 2. Peak g measured at projectile nose (and 95 percent confidence limits) vs impact velocity

frequencies from 15,000 to 3400 Hz. A series of runs at different velocities was made using the model 8 accelerometer, and the results for each are shown in Fig. 3 where peak accelerations are plotted against the natural period and frequency of the accelerometer. The projectile weighed 17.0 lb. Also shown are the results of curve fitting listed in Table 2, determined from the model 1 accelerometer data (National Bureau of Standards calibration) described in Ref. 2.

The agreement between the two runs made at 413 fps speaks well for the precision of the measurement. The disagreement between the two types of accelerometers in the overlap region of the 400-fps curves amounts to 10,000 g but lies within the precision indicated by the confidence limits of Fig. 2. Within these limits the difference in the projectile weights (17.0 lb for the model 8 data vs a nominal 17.5 lb for the fitted data) has no effect. Figure 3 verifies the fact that the forces experienced by the copper ball accelerometer and any component tested in the 4-in. air gun are quite sensitive to the component's natural period. The cause of the large acceleration levels at the short periods is unknown; but it may be the ringing of the nose and projectile, sharp impulses generated by relative motion between sections of the projectile, or sudden, sharp blows experienced by the projectile in the course of the penetration process or the rebound into the catch box walls.

The copper ball data in the previous discussion were taken from accelerometers

mounted on the nose. A series of runs was made to compare these data with data taken from copper balls mounted in the cargo section. Figure 4 shows the two different 413-fps shock spectra shown in Fig. 3 together with a 412-fps shock spectrum obtained from the model 8 accelerometer mounted in the cargo section. At short natural periods, the readings of the nose accelerometer are considerably higher than those of the cargo accelerometer, and at longer periods, the readings approach each other.

To determine shell response for periods longer than those shown in Fig. 4, model 1 copper ball accelerometers were placed in the nose and cargo section. In addition, the total number of lead blocks was varied. The projectile weight was 17.0 lb, and the impact velocity was kept constant at 300 fps. The results are shown in Fig. 5. It can be seen that the peak g's experienced at the cargo section are consistently higher than those at the nose section. It is inferred that the trend of the curves in Fig. 4 continues for smaller  $\tau_n$ , resulting in the reversal of levels experienced at the shorter period.

The data of Fig. 5 indicate that, within the limits of the accuracy and the range of blocks tested, the target thickness has no consistent effect on the peak g level. A statistical correlation of the 17.5-lb projectile peak g with target thickness, however, does show a dependence. The reason for the change in g levels on different days is unknown. The resolution of these inconsistencies depends upon more accurate measurements.

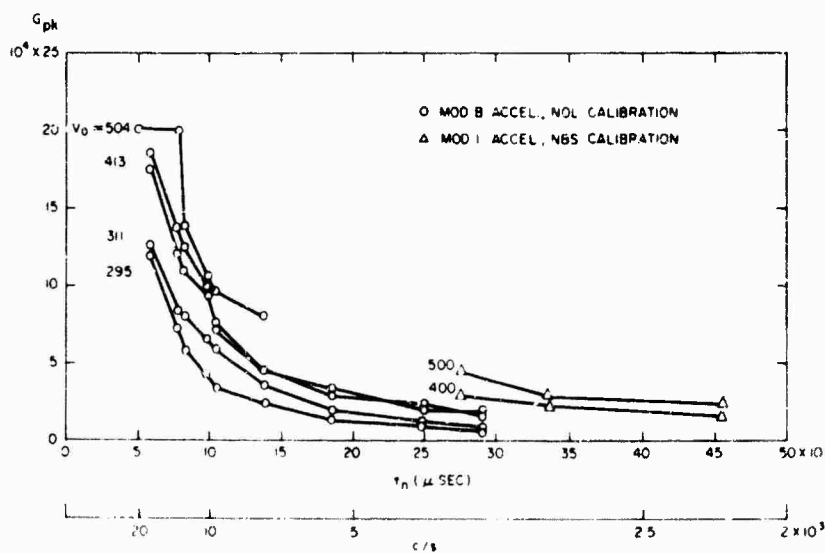


Fig. 3. Peak g for different impact velocities measured at projectile nose vs natural period

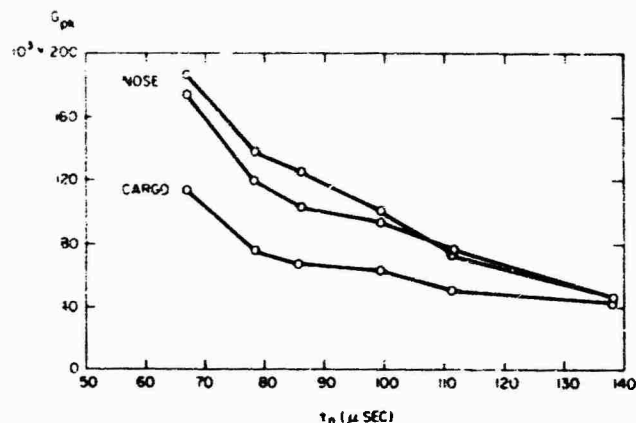


Fig. 4. Peak  $g$  measured at nose and at cargo sections as a function of natural period of accelerometer

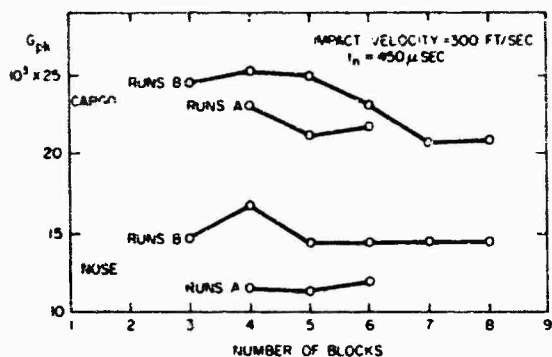


Fig. 5. Peak  $g$  measured at the projectile nose and cargo sections as a function of the number of lead target blocks (runs A and B refer to sets of runs made on different days)

## SUMMARY AND CONCLUSIONS

The primary measuring instrument used in this evaluation study was the copper ball accelerometer. The data generated by this device must be questioned when they are used in such undefined situations as previous air gun impact tests.

The copper ball accelerometer with high natural frequency indicates peak accelerations up to 200,000  $g$  (Fig. 3). It is unlikely that the peak retarding force offered by the target material has this magnitude. The accelerometer measurements still yield valid information, however, if they are interpreted as a shock spectrum, i.e., as the response of structural members. The deformation of the copper ball in these accelerometers may result from a

pulse of extremely high amplitude and short duration, or from the cumulative effect of a number of low-amplitude impulses. Whichever the cause, the response is a complicated one and the use of the impact test for high-frequency components is questionable. The center of mass of the projectile and its cargo follows the trajectory demanded by the target's retarding force. The difference between the copper ball accelerometer readings in the nose and in the cargo section shows that the structure of the projectile significantly affects the pulse experienced by the test specimen. Various theories were applied to the lead target penetration process; the measured penetration depth and impact velocity are compared with the theoretical expressions in Appendix B. But because none of these theories had previously been applied to the penetration of lead in the velocity range under study, their validity is unknown. Despite this uncertainty, a study of the data and various comparisons allows the drawing of the following conclusions:

1. A constant pressure model evaluated with the assumption of shallow penetration predicts a penetration time independent of impact velocity. Without the shallow penetration approximation, this model would predict a penetration time that would vary with impact velocity. Although a closed-form solution to this model was not obtained, it deserves further attention, particularly in the case of low-velocity impacts.
2. The Poncelet equation, widely used to predict penetration depths, is of questionable value since peak force is reached at the instant the projectile contacts the target. This is not



the case for projectiles with blunt noses ([3], p. 306).

3. The crude assumption of a constant force is widely used to get estimates of peak forces in impact testing. In the study made here, this assumption predicts penetration times (Fig. 6) and peak g's (Fig. 7) which are in fair agreement with the measured penetration times (Fig. 6) and the peak g's measured by the low-frequency accelerometers (Fig. 3).

4. The penetration time is an insensitive measure of the force laws described here.

#### NOMENCLATURE

$a$  = Acceleration

$A$  = Barrel or projectile base area

$D$  = Projectile diameter

$g$  = Acceleration due to gravity

$G_{pk}$  = Peak acceleration expressed in multiples of  $g$

$l$  = Length of barrel

$m$  = Projectile mass

$p$  = Dynamic flow pressure of target material

$p_0$  = Initial driving pressure of gas

$t_M$  = Duration of penetration process

$t_n$  = Natural period of accelerometer

$T$  = Target thickness

$v$  = Instantaneous projectile velocity

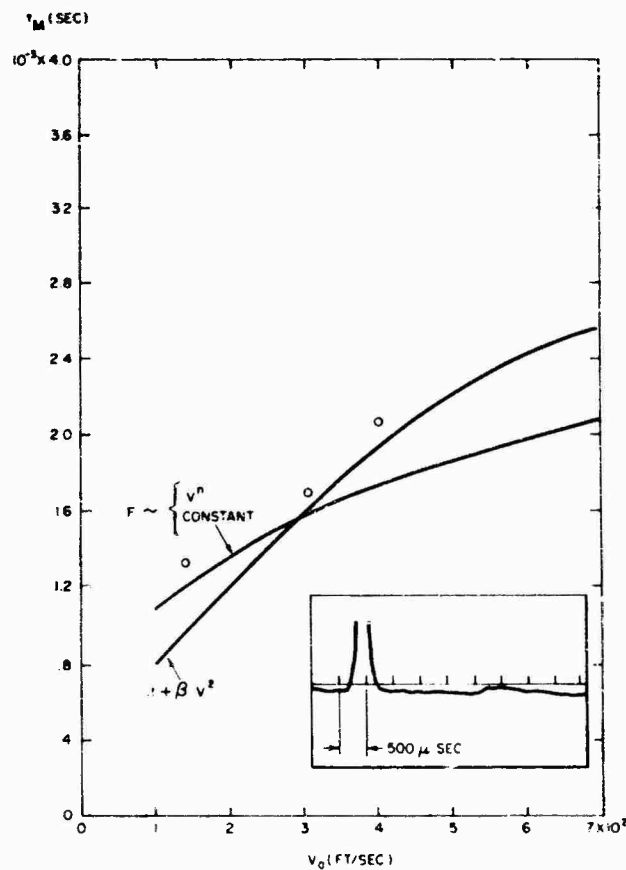


Fig. 6. Penetration time calculated for various penetration models together with measurements

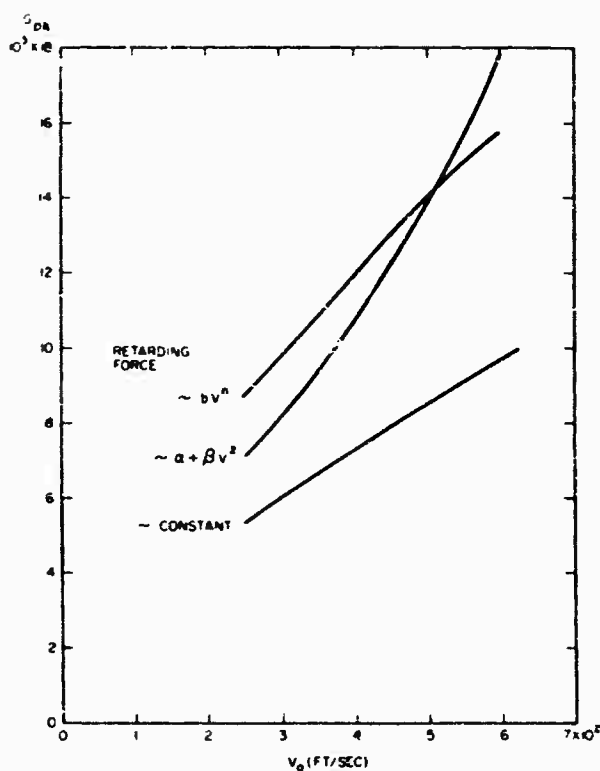


Fig. 7. Peak g calculated for various force equations

- $v_0$  = Projectile muzzle velocity
- $w$  = Projectile weight
- $x_M$  = Maximum target penetration
- $\gamma_n$  = Standard deviation of exponent  $n$

#### ACKNOWLEDGMENTS

The advice and assistance of H. Curchack, C. Rich, I. Smith, R. Woodall, and H. Wyllie of the Harry Diamond Laboratories and of V. DeVost of the Naval Ordnance Laboratory is gratefully acknowledged.

#### Appendix A

##### FIT OF EXPERIMENTAL DATA

The data accumulated in 4-in. air gun tests over a 2-year period were punched on cards and computer fitted by a least-squares technique to curves of the form  $X = cY^n$ . The actual fit was made to the straight line formed by taking the logarithm of the above expression.

The results are shown in Tables 2 and 3. The number of points used in each fit together with the velocity range covered by the data are

also given. The results of the fit for projectiles weighing 17.5 and 23.0 lb, respectively, are shown, as are the results for 17.5-lb projectiles which penetrated less than 2 in., i.e., less than the radius of the projectile's nose. The standard 17.5-lb projectile data are subdivided into three parts in Table 3 since three different copper ball accelerometers were used, each with its own natural period as shown in the table.

## Appendix B

### PENETRATION PHENOMENA

The retarding force experienced by the projectile is determined by the phenomena encountered while penetrating the lead target. Since there were no dynamic force measurements, the available data were used to gain some insight into these phenomena. The 734 experimentally determined penetration depths for the 17.5-lb projectiles, on which Tables 2 and 3 are based, were fitted to the impact velocity, yielding

$$x_M = 1.167 \cdot 10^{-4} v_0^{1.33}$$

where  $x_M$  is in feet and  $v_0$  is in feet per second.

The value of 1.33 for the exponent of  $v_0$  has been noted in other investigations [4] as characteristic of relatively low velocity penetrations. The observation has also been made [4] that the exponent tends toward values less than 1.33 with increasing impact velocity. As can be seen in Tables 2 and 3, the fitted data show this trend. The residual of this fit is -0.7078, the standard deviation of the residual being  $2.76 \times 10^{-7}$ .

The number of lead blocks used in each run is varied in the interests of economy. The minimum thickness of unpenetrated target is usually more than 0.5 in. The penetration-depth vs target-thickness data for the 17.5-lb projectiles already discussed were fitted to a straight line. The resulting correlation coefficient for this fit was 0.86, indicating that the

penetration depth is dependent upon the target thickness.

Visual inspection of the craters indicates that the spherical nose of the projectile always matches the contour of the crater in the vicinity of the nose. The surface of this part of the crater is smooth and bright and has a different appearance from that of the after part of the crater. The crater diameter at the surface of entry is greater than the diameter of the projectile, the diameter at the entrance of a 6-1/2-in.-deep crater being 5-3/8 in. These effects can be seen in Fig. B-1. Table B-1 gives data pertinent to Fig. B-1.

The jagged lip around the edge of the crater (as typified by those of Fig. B-1 and small particles of lead on the catch box floor indicate that the lead flows or melts during the penetration process. The surface of the crater appears to be a very thin layer of lead, which may be picked off in strips. This can also be seen in Fig. B-1.

It was noted after a series of shots that there was a flattening of the projectile nose. As the flattening for a single run was very slight this effect was ignored.

These observations show that the kinetic energy of the projectile is being dissipated in several ways: the plastic deformation of the target and projectile material, the melting of the target material, and the transmission of



Fig. B-1. Target craters resulting from different velocity impacts (numbered 1-6 left to right; see Table B-1)

TABLE B-1  
Characteristics of Target Blocks

| Fig. B-1<br>Target<br>Number <sup>a</sup> | $v_0$<br>(fps) | $x_M$<br>(in.) | Number of<br>Lead Blocks<br>Used | Diameter<br>at Entrance<br>to Crater<br>(in.) | Angle of<br>Climb<br>(deg) |
|---|----------------|----------------|----------------------------------|---|----------------------------|
| 1   | 223            | 1-1/2          | 6                                | 3-7/8   | 0                          |
| 2   | 390            | 4              | 6                                | 4-1/2   | 5-1/2                      |
| 3   | 521            | 4-3/4          | 7                                | 4-7/8   | —                          |
| 4   | 520            | 5-1/2          | 6                                | 4-7/8   | 6-1/2                      |
| 5   | 538            | 6              | 10                               | 5-3/8   | 11-1/5                     |
| 6   | 558            | 5-1/8          | 7                                | —   | 0                          |

<sup>a</sup>Numbered 1-6 from left to right.

energy to far parts of the target system by various types of waves. Although it is reasonable to assume that the predominant dissipative mechanism varies with the kinetic energy of the projectile, an attempt was made to find a single force law describing the penetration of the projectile over the entire velocity range.

One approximate assumption was that the velocity of the projectile decays linearly as it progresses through the target, when the retarding force is constant. Integrating the equation of motion using  $x = 0$  and  $\dot{x} = v_0$  when  $t = 0$  and applying the necessary condition that  $\dot{x} = 0$  when the penetration process is over yields

$$x_M = \frac{v_0^2}{2a} \quad (B-1)$$

and

$$t_M = \frac{v_0}{a} \quad (B-2)$$

The Poncelet equation has been used to express penetration processes of ordnance material since the early 19th century [5]. In its classic form this equation of motion can be expressed as

$$-m \frac{d^2x}{dt^2} = \alpha + \beta v^2 \quad (B-3)$$

where  $\alpha$  and  $\beta$  are constants.

Integrating and using the same initial conditions yields

$$x_M = \frac{m}{2\beta} \ln \left( 1 + \frac{\beta}{\alpha} v_0^2 \right) \quad (B-4)$$

$$t_M = \frac{m}{(\alpha\beta)^{1/2}} \tan^{-1} \left[ \sqrt{\frac{\beta}{\alpha}} v_0 \right] \quad (B-5)$$

$$\left( \frac{dv}{dt} \right)_{pk} = -\frac{1}{m} (\alpha + \beta v_0^2) \quad (B-6)$$

Another law assumes that the force acting on the projectile depends on the instantaneous velocity raised to a power. Yielded as the equation of motion is

$$m \frac{d^2x}{dt^2} = -b v^n \quad (B-7)$$

with the result after integration:

$$x_M = \frac{m}{(2-n)b} v_0^{(2-n)} \quad (B-8)$$

$$t_M = \frac{m}{(1-n)b} v_0^{(1-n)} \quad (B-9)$$

$$\left( \frac{dv}{dt} \right)_{pk} = -b v_0^n \quad (B-10)$$

This law is discussed for the sake of completeness, a velocity-dependent law of this nature being primarily applicable to gases and granular solids [5].

Using the  $x_M$  obtained from the  $v_0$  fit for the 17.5-lb projectile given here, the acceleration for the constant force law was evaluated using Eq. (B-1) while the constants for the velocity-dependent force law were obtained by equating this fit to Eq. (B-8). The Poncelet predicted depths (Eq. (B-4)) were fitted from the original 17.5-lb projectile data. The constants resulting from these fits are:

| $F = bv^n$ | $F = \frac{1}{2} \rho v^2$ |
|------------|----------------------------|
| b = 293.9  | $\rho = 8.52 \cdot 10^4$   |
| n = 0.670  | $\rho = 0.628$             |

The peak forces calculated from Eqs. (B-1), (B-6), and (B-10) are shown in Fig. 7. The peak g predicted by the constant force law is less than that predicted by the other laws.

Another theory used to describe low-velocity penetration processes assumes that the target material exerts a constant dynamic flow pressure  $p$  on the projectile as the penetration process takes place. Although a highly speculative assumption, it yields interesting results. The equation of motion for a round-nosed projectile becomes

$$m \frac{d^2x}{dt^2} = -p(Dx - x^2)$$

$$\approx -pDx$$

The last step is an approximation valid when  $x \leq D/2$ . Integrating this equation, we obtain

$$x_M = v_0 \left( \frac{m}{pD} \right)^{1/2} \quad (B-11)$$

$$t_M = \frac{1}{2} \left( \frac{m}{pD} \right)^{1/2} \quad (B-12)$$

$$\left( \frac{dv}{dt} \right)_{p_0} = v_0 \left( \frac{pD}{m} \right)^{1/2} \quad (B-13)$$

Table 2 gives data for 68 points where  $x_M \leq D/2$ . The average pressure obtained from these data using Eq. (B-11) was 13,000 psi. This compares favorably with the 12,000-psi figure given in Ref. 3 (p. 96). It also agrees with the 13,000 psi obtained by McCarty and Carden [6], who fitted peak acceleration-impact velocity data; however, their fit of penetration depth-impact velocity data yielded 21,000 psi. The constant pressure theory as developed here predicts a penetration time independent of impact velocity. This time is 0.82 msec for the 17.5-lb projectile if  $p = 13,000$  psi.

A measurement of the penetration time was made by placing a commercial strain gage on a steel block behind the lead target blocks. No attempt was made to interpret the strain amplitude obtained, but the duration is believed to be close to the projectile deceleration time. One of the traces is sketched as the insert of Fig. 6. Three data points were obtained by this means and are shown in Fig. 6 together with the durations predicted by constant-force, velocity-dependent, and Poncelet-force laws. The times predicted by the first two laws are identical; indeed, the penetration times predicted by all three laws are quite similar. However, the fact that there is a variation in penetration time rules against the constant-pressure law.

When one cut open various target blocks, it was shown that the projectile had moved away from the steel table as it moved through the target. In addition, the tops of the blocks were splayed apart but the bottoms had a compressed appearance. The climbing angle was measured by taking the horizontal distance to the end of the crater and the vertical distance from the center at the entrance of the crater to the center of the crater at its end. These angles are listed in Table B-1.

The effect of the climbing angle on the final target-penetration depth is believed small and was ignored in this analysis. An estimate of the transverse forces acting on the projectile was made, using an expression based on a constant-force model

$$F = \frac{8y}{t_M^2}$$

where  $y$  is the measured transverse displacement of the projectile and  $t_M$  is the time duration of the corresponding constant force, taken from Fig. 6. The result is an estimate of 16,000 to 20,000 peak g acting transversely on the projectile in the velocity range of 400 to 500 fps.

Based on the climbing of the projectile and the assumption that the nonsymmetrical deformation of the target were caused by wave phenomena, the target blocks were placed on rails, allowing only a small portion of the target's bottom surface to contact the steel surface of the support table. The climbing and nonsymmetry were eliminated. Figure B-1, blocks 5 and 6, are targets used with and without rails.

## Appendix C

### COPPER BALL ACCELEROMETERS

Copper crusher gages have been in use since the 19th century. Intensive development of these devices took place during and after the world wars. Gages have been designed to measure pressures generated by waves in underwater explosions [7] and pressures generated in artillery weapon firings [8]. The U.S. Navy has made considerable use of copper crusher accelerometers in connection with underwater demolition work. The series of gages developed by the U.S. Naval Ordnance Laboratory [2] has found wide acceptance.

Figure C-1 is a schematic of the essentials of one of these gages. The proof mass is designed so that it may be varied. The radius of the surface in contact with the copper ball is nominally 1-1/2 in. The crushed element is an annealed copper ball 5/32 in. in diameter. A rubber sleeve is used to hold the ball to the anvil, which is rigidly fixed to the projectile. In simple models, a small screw is made finger-tight behind the proof mass to prevent the system from rattling in the container. Conceptually, this gage is taken to be a spring-mass system, the analogy being shown in Fig. C-1.

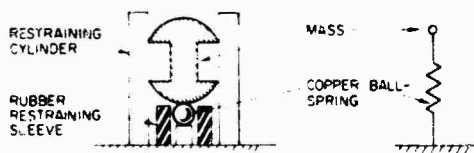


Fig. C-1. Model of copper ball accelerometer and spring-mass analogy

The plastic deformation taking place when the mass crushes the copper ball is assumed to be linear with the applied force. The slope of a static calibration curve then yields the spring constant  $k$ . This, together with the proof mass, yields the natural frequency  $f_n$  of the gage. To obtain the peak forces acting on the system, the deformation of the ball is obtained by measuring the diameter of the ball before and after the run. Then using the expressions

$$F_{\text{Dynamic}} = m' a_{\text{Dynamic}} = \frac{w'}{g} a_{\text{Dynamic}} = k X_{\text{Dynamic}}$$

we obtain

$$G_{pk} = \frac{a_{\text{Dynamic}}}{g} = \frac{k}{w'} X_{\text{Dynamic}}$$

where

$w'$  = weight of proof mass

$m'$  = proof mass.

Note that

$$\frac{k}{w'} X_{\text{Dynamic}} = \frac{F_{\text{Static}}}{w'} \frac{X_{\text{Dynamic}}}{X_{\text{Static}}}$$

and therefore the measured  $G_{pk}$  is proportional to the displacement response normally obtained from a shock spectrum analysis.

The copper ball accelerometer has the advantages that it is rugged and capable of measuring peak forces in the range of hundreds of thousands of g's. It is a highly reliable instrument in that it seldom fails to operate, and it is relatively inexpensive to build and use.

One of the disadvantages of the copper ball accelerometer is that the static force-deformation curve is nonlinear, as seen from Fig. C-2. Calibration curves of four different batches of 5/32-in. balls are shown: one from the Harry Diamond Laboratories (HDL); one from the National Bureau of Standards (NBS); and two from the Naval Ordnance Laboratory (NOL) — curve (1) from Ref. 2 and curve (2) from the slowest applied force curve in Ref. 9. Drawing straight lines through these curves decreases the accuracy of measurement, but the nonlinearity is slight, particularly when the deformation of the ball is kept small.

Another disadvantage is that copper is a rate-sensitive material; i.e., its final deformation is a function of the rate at which the deforming force is applied. Accurate copper ball accelerometer measurements, then, should take note of the rate of application of the force. Determining this rate is very difficult. Some work on this problem has been done at the Naval Ordnance Laboratory [9,10] and additional work is planned. Present estimates show static calibration curves to be 40 percent lower than dynamic curves; slopes vary by 15 percent.

An often-neglected characteristic of the copper ball accelerometer is its natural

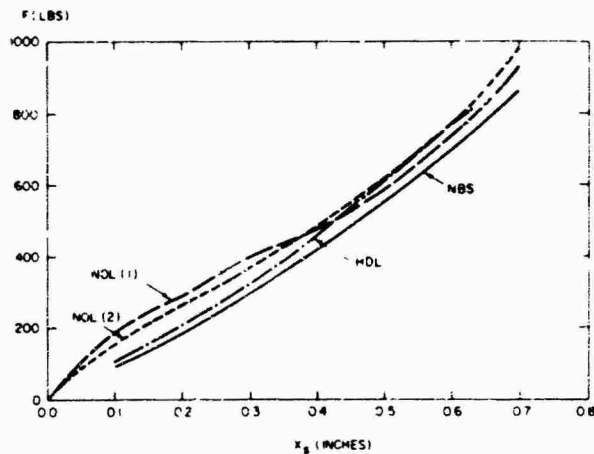


Fig. C-2. Copper ball static calibration curves (ball diameter, 5/32 in.)

frequency. The maximum amplitude of its response, as shown by the shock spectrum of a spring-mass system, is dependent upon this natural frequency. This characteristic can be used to advantage when several copper ball gages with different natural frequencies are used together. The resulting deformation can be plotted as a function of the natural frequencies to obtain the shock spectrum of the system.

Multiple shocks acting upon a copper ball accelerometer will cumulatively deform the

copper ball. Large errors can result if the duration or repetition times of the shocks are comparable to the natural period of the accelerometer. This situation can be overcome by using restraints that fall into place during the application of the force. The design of such devices is discussed in Ref. 2. Information useful in design work can be obtained from copper ball accelerometers even in this situation, particularly if a shock spectrum is generated by the means described in the preceding paragraph.

#### REFERENCES

1. H. R. Kollmeyer, "Light Gas Gun for Production of Shock Pressure in Solids," Diamond Ordnance Fuze Lab. Rept. TR-933, 1961
2. V. F. DeVost, "NOL Copper Ball Accelerometers," U.S. Naval Ordnance Laboratory, White Oak, Md., NAVORD Rept. 6925, 1960
3. W. Goldsmith, Impact (Edward Arnold, London), 1960
4. W. Herrman and A. H. Jones, "Survey of Hypervelocity Impact Information," M.I.T. Aeroelastic and Structures Res. Lab. Rept. 99-1, 1961
5. W. A. Allen et al., "Dynamics of Projectile Penetrating Sand," J. Appl. Phys., 28:370 (1957)
6. J. L. McCarty and H. D. Carden, "Impact Characteristics of Various Materials Obtained by Acceleration Time-History Technique Applicable to Evaluating Remote Targets," NASA-TN-D-1269, 1962
7. H. Hilliar, "Experiments on the Pressure Wave Thrown Out by Submarine Explosions," in, Underwater Explosion Research, Vol. 1, Department of the Navy, Washington, D.C., 1950
8. Anon., "Interior Ballistics of Guns," U.S. Army Materiel Command Pamphlet AMCP-706-150, 1956
9. H. M. Cole, "An Investigation of the Dynamic Deformation of Small Copper Balls," U.S. Naval Ordnance Laboratory, White Oak, Md., NOL TR 65-189, 1965
10. J. L. Rand, "Dynamic Compression Testing of Crusher Gage Material," U.S. Naval Ordnance Laboratory, White Oak, Md., NOL TR-63-277, 1964